

**TRANSITION IN SEPARATION BUBBLES:
PHYSICAL MECHANISMS AND PASSIVE CONTROL TECHNIQUES**

by

Brian R. McAuliffe

A thesis submitted to the Faculty of Graduate Studies and Research
in partial fulfillment of the requirements for the degree of

Doctor of Philosophy

in Aerospace Engineering

Ottawa-Carleton Institute for Mechanical & Aerospace Engineering

Department of Mechanical & Aerospace Engineering

Carleton University

Ottawa, Ontario, Canada

©Brian R. McAuliffe

May 2007



Library and
Archives Canada

Bibliothèque et
Archives Canada

Published Heritage
Branch

Direction du
Patrimoine de l'édition

395 Wellington Street
Ottawa ON K1A 0N4
Canada

395, rue Wellington
Ottawa ON K1A 0N4
Canada

Your file *Votre référence*
ISBN: 978-0-494-27104-9
Our file *Notre référence*
ISBN: 978-0-494-27104-9

NOTICE:

The author has granted a non-exclusive license allowing Library and Archives Canada to reproduce, publish, archive, preserve, conserve, communicate to the public by telecommunication or on the Internet, loan, distribute and sell theses worldwide, for commercial or non-commercial purposes, in microform, paper, electronic and/or any other formats.

The author retains copyright ownership and moral rights in this thesis. Neither the thesis nor substantial extracts from it may be printed or otherwise reproduced without the author's permission.

AVIS:

L'auteur a accordé une licence non exclusive permettant à la Bibliothèque et Archives Canada de reproduire, publier, archiver, sauvegarder, conserver, transmettre au public par télécommunication ou par l'Internet, prêter, distribuer et vendre des thèses partout dans le monde, à des fins commerciales ou autres, sur support microforme, papier, électronique et/ou autres formats.

L'auteur conserve la propriété du droit d'auteur et des droits moraux qui protègent cette thèse. Ni la thèse ni des extraits substantiels de celle-ci ne doivent être imprimés ou autrement reproduits sans son autorisation.

In compliance with the Canadian Privacy Act some supporting forms may have been removed from this thesis.

Conformément à la loi canadienne sur la protection de la vie privée, quelques formulaires secondaires ont été enlevés de cette thèse.

While these forms may be included in the document page count, their removal does not represent any loss of content from the thesis.

Bien que ces formulaires aient inclus dans la pagination, il n'y aura aucun contenu manquant.


Canada

Dedicated to my wife

Rakhi

and to my daughter

Priya Emma.

Abstract

This thesis documents complementary experimental and computational studies aimed at identifying the physical mechanisms associated with laminar-to-turbulent transition in separation bubbles, and at examining passive techniques for manipulation of this process. Measurements were made over the suction surface of two airfoil models using particle image velocimetry (PIV), and were performed in a low-Reynolds-number tow-tank facility. One of the models, which consists of an unconventional airfoil design, was developed specifically for the purpose of examining passive manipulation of separation-bubble transition. The computational studies were performed using direct numerical simulation (DNS), providing detailed resolution of the spatial and temporal scales of the flow.

Separation-bubble transition is observed to occur in a different manner depending on the level of freestream turbulence. In a low-disturbance environment, transition is shown to be initiated by the inviscid Kelvin-Helmholtz instability mechanism. This instability results in the roll-up and subsequent shedding of vorticity in the separated shear layer, downstream of which break-down to small-scale turbulence occurs in the region of high shear between sequential rollers and initiates reattachment of the shear layer to the surface. Under low-Reynolds-number conditions, a vortex-pairing phenomenon is identified and associated with a subharmonic instability of the separated shear layer. A possible link between the inviscid Kelvin-Helmholtz and the viscous Tollmien-Schlichting instabilities is identified. Under elevated-freestream-turbulence conditions, separation-bubble transition is shown to occur through the production, growth, and merging of turbulent spots. The spots, which consist of a series of vortex loops, are shown to be initiated through a secondary inviscid instability, promoted by the presence of streamwise streaks that originate in the upstream laminar boundary layer disturbed by the freestream turbulence.

Two-dimensional surface modifications were made to the unconventional airfoil to provide passive manipulation of the separation-bubble-transition process. Most of the configurations examined are shown to provide reduced boundary-layer losses downstream of reattachment. The spatially-resolved PIV results identify various means through which the transition process can be altered to improve the performance of airfoils over which separation bubbles are common.

Acknowledgements

First and foremost, I would like to thank my research advisor, Dr. Metin Yaras, for his support, persistence, and encouragement throughout the course of the present work. His has inspired me to pursue a career in research. I also wish to gratefully acknowledge Dr. Ernest Hanff of the National Research Council of Canada for his generous support and collaboration in the work, and for providing access to the experimental facilities.

Most of all, I would like to thank my family; my wife, Rakhi, for her undying love, encouragement, and tolerance over the last few years, and my daughter, Priya, for giving me the inspiration to be the best person and father that I can be. Their love and support have been my foundation throughout the course of this research, and have instilled in me the important balance between work and family. I would like to thank my mother, Marguerite, my father, Sean, and my sister, Lisa, who have provided love and encouragement throughout my years of study. I would also like to thank my in-laws, Harish, Rita, and Nitin, for wholeheartedly treating me as a son and brother.

I would like to acknowledge the financial support of Pratt & Whitney Canada, as well as the Natural Sciences and Engineering Research Council of Canada (NSERC) for a post-graduate scholarship. Without their support, this research would not have been possible.

This work was aided through the technical support of many people. I would like to thank Todd Brown, Brian Jahraus, James Ross, and Kul Kapoor of the National Research Council of Canada for providing technical support and assistance throughout the course of the experimental research. I would also like to thank Alex Proctor and Kevin Sangster for their technical assistance in the machine shop of the Department of Mechanical and Aerospace Engineering. Dr. Donald Gauthier of Carleton University and Dr. Ali Mahallati of the National Research Council of Canada are also acknowledged for providing the computational resources for the project.

Of course, I could not have survived the lengthy process of completing my degree without the presence of friends and colleagues. Martin Conlon has been my friend and sounding-board throughout the work, and is gratefully acknowledged for reviewing this manuscript and providing insightful suggestions. The numerous coffee excursions with him over the years have helped alleviate some of the stress and frustration that comes with such a demanding project. I am indebted to Ali Mahallati for his generous friendship and help over the last few years. Through the provision of computational resources and technical knowledge, he has been instrumental in completing the project. I would also like to thank Stephen Roberts for providing a sound basis for the present research, for his technical expertise, and for his generous help with initiating the computational portion of the work.

Table of Contents

Abstract	i
Acknowledgements	iii
List of Tables	x
List of Figures	xii
List of Symbols	xix
1 Introduction	1
1.1 Motivation	1
1.2 Thesis Objectives	4
1.3 Approach	5
1.4 Overview of Thesis	8
2 Background and Literature Review	11
2.1 Chapter Overview	11
2.2 Laminar-to-Turbulent Transition in Shear Flows	12
2.2.1 Free Shear Layers	12
2.2.2 Boundary Layers	14
2.2.3 Separation Bubbles	17
2.2.4 Turbulent Spots	20
2.3 Review of Relevant Experimental and Computational Studies of Separation Bubbles	24
2.4 Transition Modelling	29

2.5	Transition Control in Separation Bubbles	36
2.5.1	Control Methods and Classification	36
2.5.2	Passive Transition Manipulation	38
3	Experimental Setup and Procedures	41
3.1	Chapter Overview	41
3.2	National Research Council Facility	41
3.2.1	Tow Tank	42
3.2.2	Airfoil Models	45
3.2.2.1	SD7003 Low-Reynolds-Number Airfoil	45
3.2.2.2	Airfoil with Curved Backward-Facing Suction-Side Ramp	46
3.2.3	Instrumentation	47
3.2.4	Camera-Model Tracking-Error Correction	49
3.2.5	Measurement Procedures	50
3.2.6	Operating Conditions	52
3.3	Carleton University Facility	54
3.3.1	Wind Tunnel	54
3.3.2	Instrumentation	55
4	Computational Setup and Procedures	57
4.1	Chapter Overview	57
4.2	Governing Equations	58
4.3	Solution Method	59
4.3.1	Basic Methodology	59
4.3.2	Discretization	59
4.3.3	Solution Strategy	63
4.3.4	Parallel Processing	66
4.4	Computational Setup	67
4.4.1	Computational Domains	67
4.4.1.1	Low-Freestream-Turbulence Domain	67

4.4.1.2	Elevated-Freestream-Turbulence Domain	69
4.4.2	Boundary Conditions	71
4.4.3	Computational Meshes	74
4.4.4	Simulation Time-Step and Duration	77
4.4.5	Solution Convergence	78
5	Data Reduction Procedures	80
5.1	Chapter Overview	80
5.2	Data Reduction of Experimental PIV Measurements	80
5.2.1	Image Correction Algorithms	81
5.2.2	Image Analysis	84
5.2.3	Displacement-Vector-Field Data Reduction	87
5.2.4	Ensemble-Averaged Parameters	89
5.2.5	Additional Parameters of Interest	92
5.2.6	Uncertainty Estimates	96
5.3	Data Reduction of Simulation Results	99
5.3.1	Time Averaging Techniques	99
5.3.2	Vorticity Calculation	102
5.3.3	Intermittency Calculation	107
5.3.4	Spectral Analysis	109
5.3.5	Turbulence Integral Length Scale	109
5.3.6	Additional Parameters of Interest	111
6	Separation-Bubble-Transition Measurements on a Low-Reynolds-Number Airfoil	112
6.1	Chapter Overview	112
6.2	Operating Conditions	113
6.3	Discussion of Measurements	114
6.4	Transition Onset Prediction	122
6.5	Conclusions	129

7	Numerical Study of Instability Mechanisms Leading to Transition in Separation Bubbles	130
7.1	Chapter Overview	130
7.2	Flow Conditions	131
7.3	Low-Freestream-Turbulence Case	133
7.3.1	Selection of Conditions	134
7.3.2	Validation of Simulation Results	137
7.3.3	Instability Mechanisms	140
7.3.4	Breakdown Mechanisms	149
7.4	Elevated-Freestream-Turbulence Case	152
7.4.1	Selection of Conditions	153
7.4.2	Comparison With Experiment	156
7.4.3	Instability Mechanisms	158
7.4.4	Breakdown Mechanisms	166
7.4.5	Validation of Turbulent-Spot Growth Models	173
7.5	Comparative Assessment	177
7.6	Conclusions	182
8	Transition in Separation Bubbles at Low Reynolds Numbers	186
8.1	Chapter Overview	186
8.2	Airfoil Design	187
8.3	Discussion of Measurement Results	192
8.3.1	Shear-Layer and Flow Characteristics	192
8.3.2	Transition Mechanisms	196
8.3.3	Ensemble-Averaged Flow Statistics	208
8.4	Conclusions	210
9	Passive Manipulation of Separation-Bubble Transition	212
9.1	Chapter Overview	212
9.2	Passive Surface Modifications	213
9.3	Discussion of Measurement Results	215

9.3.1	Separation Bubble Characteristics and Airfoil Performance	215
9.3.2	ST Configuration	222
9.3.3	SG Configuration	225
9.3.4	SR Configuration	227
9.3.5	LG Configuration	230
9.3.6	SN Configuration	233
9.4	Conclusions	235
10	Summary, Contributions and Recommendations	238
10.1	Summary	238
10.2	Contributions	246
10.3	Recommendations for Future Work	247
	References	251
A	The Particle Image Velocimetry (PIV) Measurement Technique	265
A.1	Principles of PIV	265
A.2	Digital Cross-Correlation Evaluation for PIV	268
B	Unconventional Airfoil Geometry	274
B.1	Surface Geometry	274
B.2	Engineering Drawings	277
C	Simulation Boundary Details	281
C.1	Upper Domain Shapes	281
C.2	Inlet Velocity Conditions	283
C.3	Streamwise Pressure Distributions	285
D	Detailed Results of Flow Control Study	288

List of Tables

2.1	Experimental studies of separation bubbles and separated-flow transition	25
2.1	Experimental studies of separation bubbles and separated-flow transition (continued)	26
2.2	High-resolution simulation studies of separation-bubble flows	30
3.1	Details and components of the LaVision Flowmaster PIV systems	48
3.2	Operating conditions and measurement details for each experimental test case	53
4.1	Node spacings used in DNS studies involving separation bubbles (all have $y_1^+ < 1$)	77
5.1	Image analysis details for PIV measurements	85
5.2	Maximum estimated uncertainties for reduced experimental PIV data	98
5.3	Time- and spanwise-averaged variables calculated from simulation results	99
6.1	Operating conditions for SD7003 experiments	113
6.2	Instability Strouhal numbers identified in studies involving separation bubbles	122
6.3	Separation bubble characteristics for the SD7003 airfoil	123
7.1	Flow conditions and separation-bubble characteristics for the two simulations	131
7.2	Measured separation bubble characteristics	135

7.3	Instability Strouhal numbers identified in several experimental and numerical studies involving shear layers with inflectional velocity profiles	142
9.1	Characteristics of separation bubbles and reattached boundary layers for all configurations	218
B.1	Unconventional airfoil surface coordinates	276
B.2	Coordinates of groove on upper surface of the unconventional airfoil	277
C.1	Upper-surface polynomial coefficients for low- Tu simulation in units of metres	282
C.2	Upper-surface polynomial coefficients for elevated- Tu simulation in units of metres (segments for $0.45 \leq x \leq 0.78$ same as those in Table C.1)	282
C.3	Velocity distribution specified on inlet boundary for low- Tu simulation	284
C.4	Static pressure distribution specified on upper boundary for low- Tu simulation (gauge pressure)	286
C.5	Static pressure distribution specified on upper boundary for elevated- Tu simulation (gauge pressure)	287

List of Figures

2.1	Kelvin-Helmholtz instability roll-up and pairing process in a free shear layer (adapted from Estevadeordal and Kleis, 1999)	13
2.2	Schematic of attached-flow natural transition process (adapted from White, 1991)	14
2.3	Morkovin’s boundary-layer-transition road-map (reproduced from Saric <i>et al.</i> , 2002)	16
2.4	Schematic of time-averaged separation-bubble characteristics	18
2.5	Planform photograph of a turbulent spot (reproduced from Schlichting and Gersten, 2000)	21
2.6	Schematic of a turbulent spot in a zero-pressure-gradient environment (reproduced from Schubauer and Klebanoff, 1955)	21
2.7	Vortex loop development observed in a separated shear layer (reproduced from Watmuff, 1999)	23
2.8	Classification of flow control concepts (adapted from Gad-el-Hak, 2000)	37
3.1	Schematic of low-Reynolds-number tow-tank facility	43
3.2	Photograph of low-Reynolds-number tow-tank facility	44
3.3	Schematic of the SD7003 airfoil	45
3.4	Schematic of the unconventional airfoil	46
3.5	Marker fixture with forward second LED mask removed	50
3.6	PIV measurement regions for a) the SD7003 airfoil and b) the unconventional airfoil (LED marker locations identified in body of airfoils)	52
3.7	Schematic of Carleton University closed-circuit wind-tunnel test section	55

4.1	Two-dimensional representation of finite volume definition	60
4.2	Schematic of W-cycle in ANSYS-CFX multigrid (integers represent number of solutions sweeps at the given level)	66
4.3	Schematic of computational domain for the low-freestream-turbulence simulation	68
4.4	Schematic of computational domain for the elevated-freestream-turbulence simulation	70
4.5	Streamwise pressure distributions imposed on the upper domain boundaries for both simulations	73
4.6	Computational $x - y$ mesh for BUBBLE sub-domain ($3\times$ stretching in y -direction)	76
5.1	Sample sub-regions extracted for image analysis of SD7003-airfoil experiments (dashed lines indicate sub-regions used for $Re=40,000$, $\alpha=8^\circ$ conditions)	86
5.2	Sub-set of computational grid (ϕ represents any flow variable)	104
6.1	Boundary-layer-edge velocity distributions	114
6.2	Statistical velocity fields for case R40 α 8 (contour intervals for (b),(c),(d) are 0.03 with min. level of 0.08; contour levels for (e) are 0.003 with min. level of 0.001)	115
6.3	Interpretation of separation point from PIV image recording	116
6.4	Time-averaged reattachment point for case R40 α 8 (r-reattachment point)	117
6.5	Instantaneous velocity field in the reattachment region (r - reattachment, s - separation)	117
6.6	Growth of maximum $-\langle u'v' \rangle$ for case R40 α 8	119
6.7	Growth of maximum $-\langle u'v' \rangle$ for case R65 α 4	120
6.8	Shear layer roll-up at two unrelated instances in time, (a) without K-H vortex pairing, and (b) with K-H vortex pairing	121
6.9	Integral parameters for case R40 α 8	124
6.10	Comparison of results with transition-onset model of Roberts (2005)	127
6.11	Comparison of various transition-onset prediction models	128
7.1	Boundary-layer-edge velocity distributions for both simulations in the region $0.40 \text{ m} < x < 0.78 \text{ m}$	132

7.2	Measured freestream velocity distributions	134
7.3	Sample hot-wire velocity-fluctuation time traces	136
7.4	Comparison of measured and computed velocity-fluctuation time traces for Test Case 1 ($y = 2$ mm)	138
7.5	Disturbance spectra in the separation bubble	138
7.6	Instability growth rates at the dominant frequency	139
7.7	Streamwise velocity fluctuation profiles in the separation-bubble region	139
7.8	Vorticity roll-up of the separated shear layer caused by the Kelvin-Helmholtz instability (series of temporally-spaced plots, with trajectories of two roll-up vortices shown by white lines)	141
7.9	Separation-bubble characteristics under low- Tu freestream conditions (wall-normal coordinate stretched for better visualization), a) Time-averaged velocity vector profiles with every 6 th profile shown, b) velocity fluctuation levels	144
7.10	Strouhal numbers based on the correlation of Walker (Equation 7.2) for boundary layer parameters typically observed upstream of separation bubbles	146
7.11	Effects of instability growth on velocity profiles at $x' = 85$ mm (p-peak, t-trough)	148
7.12	Instantaneous vector field through the transition region (x - y plane at $z = 30$ mm and x - z plane at $y = 4$ mm)	150
7.13	Transitional structures in the separation bubble under low- Tu freestream conditions, a) Vorticity iso-surface $\Omega = 1500$ s ⁻¹ , b) Pressure iso-surfaces $p' = -1$ Pa (blue), $p' = 1$ Pa (yellow)	151
7.14	Streamwise distributions of freestream velocity and turbulence intensity	154
7.15	Velocity profiles, intermittency distribution, and spot origin histogram through the bubble region of the elevated- Tu simulation	155
7.16	Comparison of simulated and measured velocity time-traces with an intermittency of 0.5 (experimental data from a test case of Roberts, 2005)	158
7.17	Unsteadiness of separation location, a) $z-x$ near-wall plane, b) $z-y$ plane at averaged separation location	159
7.18	Streamwise streaks in the shear layer observed in a plane where $\bar{U} \approx 1/2\bar{U}_e$, a) streamwise fluctuations, b) wall-normal fluctuations	161
7.19	Power spectra of velocity through the bubble region under elevated freestream turbulence (at $y = 0.00125$ m)	162
7.20	Vortex loops within a turbulent spot	164

7.21	Evolution of a turbulent spot through a time sequence of flow in an $x-y$ plane along the centreline of the spot (averaged vectors and spanwise-vorticity in uppermost plot)	165
7.22	Turbulent-spot growth as observed in the $y-t$ and $z-t$ planes	167
7.23	Schematic of the vortex loop structure during the early development of a turbulent spot	169
7.24	Turbulent shear stress contributions during the early development of a turbulent spot	170
7.25	Power spectra of a) velocity, b) static pressure in the separated shear layer	172
7.26	Spot spreading half-angles	174
7.27	Identification of spot celerities, a) leading edge, b) trailing edge	176
7.28	Comparison of streamwise intermittency distribution, boundary layer growth characteristics, and velocity-fluctuation correlations for the two cases examined	178
7.29	Turbulent boundary-layer properties downstream of the separation bubble	181
8.1	Concepts for new test model	188
8.2	Ensemble-averaged streamlines over the unconventional airfoil	193
8.3	Shear layer property distributions over the unconventional airfoil, a) shear layer edge velocity, b) displacement and momentum thicknesses, c) shape factor	195
8.4	Instability growth in the separated shear layer for $Re=39,000$	198
8.5	Fluctuation growth rates and transition onset location for $Re=39,000$	200
8.6	Vortex pairing phenomenon observed at $Re=28,000$	202
8.7	Subharmonic pairing phenomenon observed at $Re=39,000$	204
8.8	Streamwise correlation function of wall-normal velocity fluctuations at $x/C = 0.426$, $y/C = 0.061$ for $Re=39,000$	206
8.9	Streamwise correlation of dominant wavelengths for $Re = 39,000$, a) wavelength distribution, b) correlation peak distribution	207
8.10	Mean streamlines and contour plots of velocity correlations at $Re = 39,000$ (dividing streamline overlaid on contour plots)	209
9.1	Geometry of surface modifications (dashed line indicates extent of flexible vinyl strip)	214

9.2	Dominant wavelengths observed in the separated shear layer for all configurations	216
9.3	Separation, transition onset, and reattachment locations for all configurations	219
9.4	Transition onset and reattachment lengths, relative to separation, for all configurations	220
9.5	Momentum-thickness Reynolds numbers for all surface configurations at $x/C = 0.85$	221
9.6	Velocity-vector profiles and $\langle u'v' \rangle$ distributions at a Reynolds number of 39,000 for a) the clean airfoil, and b) the ST configuration	223
9.7	Velocity-vector profiles and $\langle u'v' \rangle$ distributions at a Reynolds number of 101,000 for a) the clean airfoil, and b) the ST configuration	224
9.8	Streamwise correlation of dominant wavelengths for SG and CL configurations for $Re = 28,000$, a) wavelength distributions, b) correlation peak distributions	226
9.9	Variation in instability growth and wavelength for the SR configuration at $Re = 39,000$ for unrelated instants in time	228
9.10	Velocity-vector profiles and $\langle u'v' \rangle$ distributions at a Reynolds number of 51,000 for a) the clean airfoil, and b) the SR configuration	229
9.11	Velocity-vector profiles and $\langle u'v' \rangle$ distributions at a Reynolds number of 51,000 for a) the clean airfoil, and b) the LG configuration	232
9.12	Unsteady separation observed downstream of the groove of the LG configuration at $Re = 101,000$	232
9.13	Velocity-vector profiles and $\langle u'v' \rangle$ distributions at a Reynolds number of 28,000 for a) the clean airfoil, and b) the SN configuration	234
9.14	Unsteady separation observed downstream of the surface modification for the SN configuration at $Re = 101,000$	235
A.1	Typical arrangement for a PIV measurement system (reproduced from Raffel <i>et al.</i> , 1998)	266
A.2	Example of Cross Correlation Evaluation for a 4×4 Pixel Interrogation Window (shaded region is window 1, reproduced from Raffel <i>et al.</i> , 1998)	269
A.3	Advanced Techniques for PIV Cross-Correlation Evaluation, (a) Window Overlap, (b) Window Shifting, (c) Window Deformation	272
B.1	Schematic of unconventional airfoil	275
B.2	Side view of the unconventional airfoil (dimensions in inches, scale=0.30)	278

B.3	Isometric views of the unconventional airfoil (dimensions in inches, scale=0.125)	278
B.4	Bottom, front, and top views of the unconventional airfoil (dimensions in inches, scale=0.15)	279
B.5	Detail for the mounting-hole and wire-passage arrangements of the unconventional airfoil (dimensions in inches, scale=0.50)	280
B.6	Lower-surface cover plate for the unconventional airfoil; two required (dimensions in inches, scale=0.125)	280
C.1	Velocity distribution specified on inlet boundary for low- Tu simulation .	283
C.2	Static pressure distributions specified on upper domain boundaries . . .	286
D.1	Detailed results for CL configuration at $Re=28,000$	289
D.2	Detailed results for CL configuration at $Re=39,000$	290
D.3	Detailed results for CL configuration at $Re=51,000$	291
D.4	Detailed results for CL configuration at $Re=101,000$	292
D.5	Detailed results for ST configuration at $Re=28,000$	293
D.6	Detailed results for ST configuration at $Re=39,000$	294
D.7	Detailed results for ST configuration at $Re=51,000$	295
D.8	Detailed results for ST configuration at $Re=101,000$	296
D.9	Detailed results for SG configuration at $Re=28,000$	297
D.10	Detailed results for SG configuration at $Re=39,000$	298
D.11	Detailed results for SG configuration at $Re=51,000$	299
D.12	Detailed results for SG configuration at $Re=101,000$	300
D.13	Detailed results for LG configuration at $Re=28,000$	301
D.14	Detailed results for LG configuration at $Re=39,000$	302
D.15	Detailed results for LG configuration at $Re=51,000$	303
D.16	Detailed results for LG configuration at $Re=101,000$	304
D.17	Detailed results for SN configuration at $Re=28,000$	305
D.18	Detailed results for SN configuration at $Re=39,000$	306
D.19	Detailed results for SN configuration at $Re=51,000$	307

D.20 Detailed results for SN configuration at $Re=101,000$ 308
D.21 Detailed results for SR configuration at $Re=28,000$ 309
D.22 Detailed results for SR configuration at $Re=39,000$ 310
D.23 Detailed results for SR configuration at $Re=51,000$ 311
D.24 Detailed results for SR configuration at $Re=101,000$ 312

List of Symbols

a	Solution coefficient matrix; Turbulent spot leading-edge celerity.
A	Combined solution coefficient matrix.
b	Solution coefficient matrix; Turbulent spot trailing-edge celerity.
$cc_{v'}$	Streamwise correlation of wall-normal velocity component (Equation 5.36).
C	Airfoil chord length.
C_p	Pressure coefficient = $\frac{p-p_{ref}}{\frac{1}{2}\rho U_{ref}^2}$.
$C_{P_{tke}}$	Normalized turbulence-kinetic-energy production = $\frac{P_{tke}C}{U_\infty^3}$.
C_{Ω_z}	Normalized spanwise vorticity = $\frac{\Omega_z C}{U_\infty}$.
d	Characteristic length of hyperbolic-tangent velocity profile.
f	Frequency.
$f(\Delta x)$	Longitudinal correlation function = $\frac{\overline{u'(x)u'(x+\Delta x)}}{u'^2}$.
h	Height of curved backward-facing ramp.
H	Shape factor = δ^*/θ .
I	Particle image intensity level.
k_{rms}	Surface-roughness RMS height.
K	Spanwise extent for spanwise averaging.
L	Characteristic surface length.

L_b	Separation bubble length = $x_r - x_s$.
L_p	Length of solid wall in the simulations.
L_r	Length of curved backward-facing ramp.
L_t	Transition length = $x_{te} - x_{ts}$.
\dot{m}	Mass-flow rate.
n	Turbulent spot production rate (per unit time, per unit span).
N	Number of Samples; Non-dimensional turbulent spot production rate = $n\sigma\theta_{ts}^3/\nu$.
N_n	Finite-element shape factor for node n .
p	Static pressure.
p_0	Total pressure = $p + \frac{1}{2}\rho U^2$.
P_{tke}	Turbulence kinetic energy production = $-\overline{u'v'}S_{xy}$.
$R(\Delta t)$	Longitudinal correlation function = $\frac{\overline{u'(t)u'(t+\Delta t)}}{u'^2}$.
$R(x, y)$	Cross-correlation function for PIV image evaluation.
Re	Flow Reynolds number = $\frac{C U_\infty}{\nu}$.
Re_{crit}	Boundary-layer critical Reynolds number for instability growth.
Re_r	Reattachment Reynolds number = $\frac{x_r U_{er}}{\nu}$.
Re_s	Separation Reynolds number = $\frac{x_s U_{es}}{\nu}$.
Re_{sp}	Simulation flow-Reynolds-number based on suction peak velocity = $\frac{L_p U_{sp}}{\nu}$.
Re_{s-ts}	Separation-to-transition Reynolds number = $\frac{(x_{ts}-x_s)U_{es}}{\nu}$.
Re_{ts}	Transition-onset Reynolds number = $\frac{x_{ts} U_{ets}}{\nu}$.
Re_{δ^*}	Displacement-thickness Reynolds number = $\frac{\delta^* U_e}{\nu}$.
Re_θ	Momentum-thickness Reynolds number = $\frac{\theta U_e}{\nu}$.
s	Distance along surface from leading edge.
S	Surface area.
SF	Particle-image geometric scaling factor [pixel/m].

SF_C	Chord-based particle-image geometric scaling factor [pixel/ C].
Sr_θ	Instability Strouhal number = $\frac{f \theta}{\Delta U}$.
Sr_{θ_s}	Instability Strouhal number at separation = $\frac{f \theta_s}{U_{es}}$.
S_{xy}	Strain rate = $\frac{1}{2}(\frac{\partial u}{\partial y} + \frac{\partial v}{\partial x})$.
t	Time.
t^*	Normalized time = $t U_\infty / C$.
T	Time period for time-averaging procedure.
Δt	Time between laser pulses in PIV experiments; Simulation time-step.
Tu	Turbulence intensity.
TF	Taylor's turbulence factor = $Tu_{ref}(L/\Lambda_f)^{0.2}$.
u	x -velocity component.
u^*	Friction velocity = $\sqrt{\tau_w / \rho}$.
u^+	x -velocity component in wall units = u/u^* .
U	Velocity magnitude = $\sqrt{u^2 + v^2 + w^2}$.
U_c	Instability convection speed.
U_0	Reference velocity for hyperbolic-tangent velocity profile.
ΔU	Velocity difference across a free shear layer.
v	y -velocity component.
V	Volume.
w	z -velocity component.
x	Coordinate direction.
x'	Separation-reference x coordinate = $x - x_s$.
Δx	x -component of particle displacement vector.
X	Particle image coordinate.
x^+	x -coordinate in wall units = xu^*/ν .

y	Coordinate direction.
Δy	y -component of particle displacement vector.
Y	Particle image coordinate.
y^+	y -coordinate in wall units = yu^*/ν .
z	Coordinate direction.
z^+	z -coordinate in wall units = zu^*/ν .
α	Airfoil angle of attack; Spot-spreading half-angle.
β	Flow-state parameter for intermittency calculation.
γ	Intermittency.
δ	Boundary-layer/Shear-layer thickness.
δ^*	Displacement thickness.
η	Acceleration parameter = $\left(\frac{\nu}{U_e^2}\right) \frac{dU_e}{dx}$.
θ	Momentum thickness; Angular coordinate.
κ	Wavenumber = $2\pi/\Lambda_x$.
λ_θ	Pressure gradient parameter = $\left(\frac{\theta^2}{\nu}\right) \frac{dU_e}{dx}$.
Λ_f	Integral length scale of turbulence.
Λ_x	Instability wavelength.
μ	Dynamic viscosity.
ν	Kinematic viscosity.
ρ	Density.
σ	Turbulent spot propagation parameter = $\tan(\alpha)\left(\frac{1}{b} - \frac{1}{a}\right)$.
τ_w	Wall shear = $\frac{\partial u}{\partial y}\Big _{y=0}$.
ϕ	Simulation solution matrix; Random variable.

$\hat{\phi}$	Random simulation flow variable interpolated on to $x - z$ plane.
ψ	Random variable.
Ω	Vorticity magnitude = $\sqrt{\Omega_x^2 + \Omega_y^2 + \Omega_z^2}$.
Ω_x	x -direction vorticity = $\frac{\partial w}{\partial y} - \frac{\partial v}{\partial z}$.
Ω_y	y -direction vorticity = $\frac{\partial u}{\partial z} - \frac{\partial w}{\partial x}$.
Ω_z	z -direction vorticity = $\frac{\partial v}{\partial x} - \frac{\partial u}{\partial y}$.

Subscripts

c	Centroid.
e	Boundary-layer/Shear-layer edge.
le	Turbulent spot leading edge.
i, j, k	Coordinate-direction identifier.
ip	Integration point.
MA	Maximum amplification.
max	Maximum.
$meas$	Measured value.
min	Minimum.
$pred$	Predicted value.
r	Reattachment.
ref	Reference value.
rms	Root-mean-square.
s	Separation.
sp	Suction peak.
$s - ts$	Separation to transition.
te	End of transition; Turbulent spot trailing-edge.

<i>thresh</i>	Threshold value.
<i>ts</i>	Start of transition.
∞	Reference velocity (airfoil towing speed).
0	Original; Reference for curved backward-facing ramp.
<i>0eff</i>	Effective origin.

Superscripts

'	Fluctuation quantity.
+	Adjacent point; Wall-scale quantity.
-	Adjacent point.

Mathematical Descriptions

$\langle \phi \rangle$	Ensemble average of ϕ .
$\bar{\phi}$	Time average of ϕ .

Abbreviations

CCD	Charge-coupled device.
CFD	Computational fluid dynamics.
CPU	Central processing unit.
CU	Carleton University.
DNS	Direct numerical simulation.
FFT	Fast Fourier transform.
HWA	Hot-wire anemometry.
ILU	Incomplete-lower-upper.

K-H	Kelvin-Helmholtz.
LED	Light-emitting diode.
LES	Large eddy simulation.
LPT	Low-pressure turbine.
LST	Linear stability theory.
MAV	Micro air vehicle.
MEMS	Micro-electro-mechanical system.
NATO	North Atlantic Treaty Organization.
Nd:Yag	Neodymium-doped yttrium aluminium garnet.
NRC	National Research Council of Canada.
PIV	Particle-image velocimetry.
PSD	Power spectral density.
PTU	Programmable timing unit.
RAM	Random-access memory.
RMS	Root-mean-square.
T-S	Tollmien-Schlichting.

Chapter 1

Introduction

1.1 Motivation

Laminar separation bubbles occur in many practical aerodynamic applications, particularly at low-Reynolds-number operating conditions. Generally when laminar separation occurs on a streamlined body such as an airfoil, the aerodynamic performance of the body is degraded. This is a result of decreased lift and increased form drag due to separation of the boundary layer. Laminar-to-turbulent transition of the separated shear layer is what causes the flow to reattach to the airfoil surface. The general characteristics of a laminar separation bubble are described in Chapter 2.

Recent interest in low-Reynolds-number aerodynamics has been driven by aircraft-engine design, and in particular the design of high-bypass-ratio turbofan engines. The low-pressure turbines (LPTs) of modern turbofan engines operate under low-Reynolds-number conditions during high-altitude flight (Mayle, 1991). At these low Reynolds numbers ($Re \sim O(10^5)$), much of the airfoil suction-surface shear-layer remains laminar and is thus susceptible to separation in regions of strong adverse pressure gradients. At very low Reynolds numbers,

transition may commence sufficiently far downstream of separation that reattachment of the shear layer may not occur. The airfoil is then said to “stall”. The effects of stall in an LPT are decreased flow turning and higher pressure losses, which in turn reduce the available power output and the component efficiency. It is therefore desirable to prevent stall by ensuring that reattachment of a separated shear layer occurs over the airfoil surfaces.

Weight reduction is the current focus in LPT design, and is primarily achieved by reducing the number of airfoils per stage, as well as reducing the number of stages in an engine. This requires that each airfoil in a stage carry a greater aerodynamic load and by extension have a greater susceptibility to laminar separation and stall. In fact, most LPTs of modern design have laminar separation bubbles present over the airfoil suction surfaces throughout much of the operating envelope. It is therefore important to understand the transition process in a laminar separation bubble in order to better optimize modern LPTs for weight and performance. This was the prime motivation for the research.

Another example of where low-Reynolds-number effects are becoming increasingly important is the emerging field of Micro Air Vehicle (MAV) research. MAVs are a new class of very-small flight vehicles being developed primarily for military reconnaissance purposes in an effort to increase the situational awareness of ground-based soldiers by providing them with information on their surroundings. By sending a small, almost undetectable, unmanned aircraft into the field ahead of the soldiers, the battlefield can be assessed *a priori*, and tactics can be implemented to minimize casualties.

MAVs have been categorized as any flight vehicle with a maximum length dimension of 15 cm (McMichael and Francis, 1997). This takes them down to the size of small birds and large insects, where Reynolds numbers are in the laminar and transitional regimes ($Re \sim O(10^4)$), and where boundary layers are very susceptible to laminar separation. A very limited understanding of aerodynamics and flight in this regime has been developed over

the past century, and the physical behaviour of such vehicles is currently unpredictable.

In recent years, numerous transition models have been developed and published in the open literature. These models approach the problem through various means but all are semi-empirical in nature. It is important that any modelling effort used in the design of airfoils which are prone to separation be able to capture the characteristics of the separation bubbles and the ensuing transition process. One such model has been developed by the research group in which the present work has been performed (Roberts and Yaras, 2005*b*).

Although still many years or decades away from becoming practical for design purposes, large eddy simulation (LES) and direct numerical simulation (DNS) are becoming viable options for modelling the process of laminar-to-turbulent transition. The benefit of applying such methods to transitional flows is not only the accuracy with which they resolve the flow characteristics, but the simultaneous availability of the spatial and temporal nature of the flow from which a better understanding of the underlying physics can be obtained.

At the current state of aerodynamic design, limitations to lift and drag improvements are being reached by way of shape and configuration optimization. Currently, flow control, otherwise known as flow manipulation, is a popular research topic. Many types of flow control systems have been studied, from simple geometric modifications such as vortex generators (Lin *et al.*, 1990) to high-order feedback control schemes using Micro Electro Mechanical Systems (MEMS) (Gad-el-Hak, 2001). Although active forms of flow control, which require some form of energy expenditure, are very effective at achieving a specific result, the penalty associated with the control method can outweigh the benefits of its use. It is therefore desirable to develop methods of control that increase the system performance as a whole.

It is relatively easy to develop a passive control technique to prevent stall, or a significant loss of lift, due to separation at a specific operating condition. This can be

accomplished by placing a trip wire or a series of vortex generators near the separation point to enhance transition and entrainment of freestream fluid towards the surface, thus eliminating separation. Problems with these methods arise if the airfoil is required to perform under a wide range of operating conditions. For example, Lake *et al.* (2000) used a trip wire to prevent stall of an LPT airfoil at a low-Reynolds-number operating condition, reducing the cascade total pressure losses by more than 50%. However, at a higher Reynolds number where the standard airfoil behaved well, the presence of the trip wire increased the total pressure loss by more than 100%.

Due to complexity and reliability issues, practical application of all but the simplest active flow control techniques is many years away. It is likely that simpler passive techniques will dominate the aeronautic and gas turbine industries in the coming years.

1.2 Thesis Objectives

There are three main objectives to the research project described herein, all concerned with low-Reynolds-number aerodynamics and, in particular, separated-flow transition. The focus for these efforts is the Reynolds number range encountered by LPTs and MAVs. These objectives are described briefly in this section.

The first objective of the current research initiative is to further validate aspects of a transition model developed at Carleton University (Roberts and Yaras, 2005*b*). The model under consideration was developed based on measurements made on a flat test surface with an imposed pressure distribution at Reynolds numbers in the range 100,000 to 500,000. One goal is to validate the model for lower Reynolds numbers and for the effects of surface curvature. The model also makes use of previously-published empirical correlations for the growth of turbulent spots based on experiments of artificially-generated turbulent spots

under low-freestream-turbulence conditions. Another goal is to validate the accuracy of these correlations for spots that occur under elevated-freestream-turbulence conditions.

The second objective is to improve our understanding of the physical mechanisms of separation-bubble transition, and to examine variations in the associated processes under different levels of freestream turbulence. As with attached-boundary-layer transition, the mechanisms associated with the transition process are dependent on the disturbance environment in which the flow develops. Many experimental studies have examined such phenomena, however lack of simultaneous spatial and temporal data limit the development of a complete picture of the transition process. The objective of the current research is to overcome these limitations and to develop a better physical understanding of the process.

The third objective is to examine a variety of passive techniques for manipulating the transition process of a separated shear layer in a low-disturbance environment. The goal is to develop a simple, practical method of transition manipulation that improves the performance of airfoils under poorly-behaved low-Reynolds-number conditions without compromising the performance under well-behaved conditions.

1.3 Approach

The research objectives have been met using complementary experimental and computational approaches. Data from two different experimental facilities are examined in the present work: a low-Reynolds-number tow-tank facility at the National Research Council of Canada (NRC), and a closed-loop wind-tunnel facility at Carleton University (CU). Numerical simulations were performed using the ANSYS-CFX commercial CFD package (versions 5.7.1 and 10.0).

Data from a previous research project using the CU wind-tunnel facility have been used to validate the numerical simulation components of the current research initiative. The CU facility consists of a flat-plate test surface in a closed-circuit wind tunnel. To simulate the environment in which a boundary layer develops over an airfoil, a contoured test-section ceiling is used to impose a streamwise pressure distribution over the flat plate. Passive turbulence-generating grids can also be placed upstream of the test section to elevate the freestream turbulence to levels encountered in gas-turbine engines. The Reynolds number range for this facility, based on plate length and incoming flow velocity, is approximately 10^5 to 10^6 . Freestream turbulence intensities on the order of 0.5% to 9% can be achieved, which is typical of the range observed in gas-turbine engines.

The primary measurement technique used in the CU facility is hot-wire anemometry (HWA), a well-established method for performing measurements within a separation bubble. HWA is a single-point measurement technique which enables velocity measurements with high frequency resolution ($O(100 \text{ kHz})$ is possible). HWA measurements can provide very accurate velocity measurements and the high frequency response ensures full coverage of the turbulence spectrum for the range of Reynolds numbers possible in the CU facility. However, single-point hot-wire measurements provide minimal information regarding the spatial structure of turbulence, and the inability of single-sensor hot-wires to differentiate flow direction precludes identification of the reverse flow region in a separation bubble. Greater details regarding the test section, the measurement techniques, and the data processing techniques used in the CU facility will be discussed in Chapter 3, Section 3.3.

Although HWA is currently the primary method of studying separation-bubble transition, it can be difficult to examine instability mechanisms directly using single-point measurements. This deficiency, coupled with the desire to study the spatial structure of the transition process has led to the use of the NRC facility for studying such flows.

The NRC Low-Reynolds-Number Facility consists of a water tow-tank with a particle image velocimetry (PIV) measurement system, both of which will be discussed in Chapter 3, Section 3.2. The advantage of PIV over HWA is the ability to provide details regarding the spatial nature of the transition process.

The NRC facility consists of an enclosed tank in which a model can be towed through water or glycerin. The tank has a roof to prevent the problems associated with a free surface, and the roof features a sealed slot through which the test-model-support strut can travel. Water was used as the working medium for the present research. Two test models were examined in the facility. One of them, which is a typical low-Reynolds-number airfoil, was used for validation of the transition model developed at Carleton University. The other was designed specifically for the purposes of the passive flow control study.

Advantages of the NRC facility over the CU facility are the excellent “inflow quality” due to the stagnant freestream conditions (0% freestream turbulence intensity and zero end-wall boundary layer blockage), and the low Reynolds number range ($Re \leq 100,000$) for the test models used. Disadvantages of the NRC facility are the inability to increase the level of freestream turbulence (without significant modifications) and the low sampling rate of the PIV system, the latter of which can prevent detailed temporal analysis of the results.

Prior to initiating this research program, another doctoral student within the same research group at Carleton University performed a three-dimensional, time-dependent numerical simulation of a separation bubble using a large eddy simulation (LES) model, and achieved promising results (Roberts, 2005). Part of the current work is a continuation of these simulations, at refined resolution such that the present simulations were performed in a direct numerical simulation (DNS) framework. Thus, the simulations provide detail regarding the three-dimensional nature of the transition process. The flows simulated are representative of those previously studied in the CU facility, and therefore results from the

hot-wire measurements in that facility can be used for validation of the DNS results.

To summarize, the approach taken towards achieving the objectives of the present research consist of complementary experimental measurements and numerical simulations. Experiments were performed in a low-Reynolds-number tow-tank facility using two different airfoil models in an attempt to examine the characteristics of separation-bubble transition at low Reynolds numbers, and to examine various passive techniques for manipulating this transition process. Direct numerical simulation was used to examine the physical mechanisms associated with transition in separation bubbles, and made use of experimental data previously collected in a closed-circuit wind-tunnel facility.

1.4 Overview of Thesis

A substantial amount of research regarding separation bubbles and transitional flows has been accomplished by the engineering and scientific research communities prior to the initiation of this research project. The objectives of the present work have been identified by examining the open literature on these topics, and a review of the pertinent literature is given in Chapter 2.

Chapter 3 provides a description of the experimental facilities and measurement techniques used in the course of the research. The NRC tow-tank facility, its measurement system, and the test models examined are described first, followed by details of the CU wind-tunnel facility and its measurement system.

The numerical setup and procedures for the computational aspects of the research are described in Chapter 4. This includes a brief outline of the numerical methods used in the ANSYS-CFX solver, and a detailed description of the computational domains, their discretization, boundary-condition specifications, and convergence criteria.

Data reduction procedures for both the experimental and computational studies are outlined in Chapter 5, along with a discussion of measurement uncertainties.

As noted in Section 1.2, there are three main objectives to the present work. There are various ways in which the results could be presented, but the method chosen is a chronological approach based on the order in which the work was accomplished. Although there may appear to be some discontinuity between the individual chapters, the chronological treatment best represents the incremental knowledge gained during the multitude of studies performed.

Chapter 6 presents the first experimental study performed in the NRC tow-tank facility using a typical low-Reynolds-number airfoil. This study established confidence that the facility could be used for examining separation-bubble transition, and helped develop the procedures and requirements for the later experiments that involved control of the transition process in separation bubbles. The spatial nature of the PIV measurements has revealed the dominant flow structures associated with separation-bubble transition at low Reynolds numbers and low freestream turbulence. Further validation of the transition model developed at Carleton University is also presented in this chapter. In particular, the model is validated for an extended low-Reynolds-number range, and for the influence of surface curvature.

The nature of instability mechanisms and the resultant breakdown to turbulence in separation bubbles are discussed in Chapter 7 in regards to the direct numerical simulations performed. Two simulations are presented based on experiments performed in the CU wind-tunnel facility. The simulations represent the flow over a flat plate with an imposed streamwise pressure distribution representative of the suction surface of modern low-pressure-turbine airfoils. The primary difference between the two simulations is the level of freestream turbulence, with turbulence intensities at the streamwise location of separation

of 0.1% and 1.45%. Transition to turbulence in the separated shear layer occurs through different paths for each case. Each of these mechanisms are identified for their respective cases, and the differences in the resulting transition processes are identified.

Chapters 8 and 9 present results from experiments using an airfoil with a curved backward-facing ramp on its suction side, designed specifically for the purposes of examining passive manipulation of the transition process in a separation bubble. In Chapter 8, the transition process is examined through PIV measurements for the airfoil without flow control, and provides additional insight to the transition process occurring under low-Reynolds-number conditions. Chapter 9 presents the PIV measurement results for the cases with passive surface modifications, and identifies various means through which the transition process can be manipulated by passive control.

Chapter 2

Background and Literature Review

2.1 Chapter Overview

This thesis is concerned with the process of laminar-to-turbulent transition in separated shear layers. In particular, the research is focused on separated shear layers for which transition results in reattachment of the layer to the surface, thus forming a separation bubble. This chapter reviews the background and literature pertinent to the research. Section 2.2 begins with a discussion of laminar-to-turbulent transition by reviewing the various modes and mechanisms of transition that occur in not only separation bubbles, but also in boundary layers and free-shear layers with which separation bubbles share characteristics. This is followed by a review of experimental and computational studies of interest regarding separation-bubble transition (Section 2.3), and a review of current models for predicting this transition process (Section 2.4). Section 2.5 reviews control of laminar-to-turbulent transition by first providing a general classification of flow-control methods, followed by a description of various passive techniques for manipulating the transition process in separated shear layers.

2.2 Laminar-to-Turbulent Transition in Shear Flows

Separation bubbles have been shown to share strong commonalities with boundary-layer and free-shear-layer flows (Malkiel and Mayle, 1996; Roberts, 2005), and as such the characteristics and transition mechanisms of these flows are described in Sections 2.2.1 and 2.2.2, respectively, followed by a discussion of separation-bubble characteristics in Section 2.2.3. The structure of turbulent spots, as observed in both boundary layers and separated shear layers, are then discussed in Section 2.2.4.

2.2.1 Free Shear Layers

In free shear layers such as jets, wakes, and mixing layers, the predominant form of transition is through the Kelvin-Helmholtz (K-H) instability mechanism. The K-H instability is considered an inviscid mechanism associated with inflectional velocity profiles, as it can be predicted through linear stability analysis even when viscous terms are neglected (Schlichting and Gersten, 2000). This mechanism is present in many natural flows. In fact, any parallel flow in which a transverse gradient of velocity or density exists may be susceptible to the K-H instability (Chandrasekhar, 1961). For example, stratified shear layers in the atmosphere are susceptible to this mechanism, as are channel and oceanic flows (Abdeljabar and Safi, 2001). Chandrasekhar provides an inviscid stability analysis for a hyperbolic-tangent velocity profile ($U = U_0 \tanh(y/d)$), which is a reasonable approximation to the velocity profiles of planar free-shear layers and separated shear layers. He demonstrated that the hyperbolic-tangent velocity profile is inviscidly unstable to disturbances in the range of $0 < \kappa d < 1$, where κ is the wave number.

Through receptivity of a free shear layer to small disturbances, the K-H instability gives rise to the roll-up of vorticity into discrete two-dimensional vortices, often called “Kelvin cat-eyes”, connected by a line of concentrated vorticity called a “braid”, as described by

Estevadeordal and Kleis (1999). The frequency of maximum amplification with which this instability develops has been identified by Ho and Huerre (1984) to correspond to a Strouhal number of 0.016, based on the momentum thickness and the velocity difference across the shear layer ($Sr_\theta = f \cdot \theta / \Delta U$). Chandrasekhar's stability parameter, κd , and the Strouhal-number equivalent, Sr_θ , are related to each other, and it can be readily demonstrated that the κd range of 0 to 1 for a hyperbolic-tangent velocity profile corresponds to a range of 0 to 0.0398 for Sr_θ . Once the spanwise-oriented vortices grow to a sufficient size, a subharmonic pairing instability then develops where two sequential vortices begin to orbit and agglomerate, through mutual induction of their vorticity fields, into a larger vortex, from which a subharmonic of the fundamental instability frequency develops. The vorticity roll-up and pairing process is shown schematically in Figure 2.1, as observed by Estevadeordal and Kleis (1999). As was pointed out by Ho and Huang (1982), the change of the local length scale of the shear layer as a result of the vortex merging makes the original subharmonic become neutrally stable, and the new subharmonic becomes the wave of most rapid amplification. This pairing of vortices is suggested as the dominant mechanism associated with the growth of planar free-shear layers (Ho and Huerre, 1984). As the roll-up of spanwise vorticity begins, the shear layer becomes unstable to streamwise vorticity and thus quickly becomes three-dimensional in nature. Huang and Ho (1990) have shown

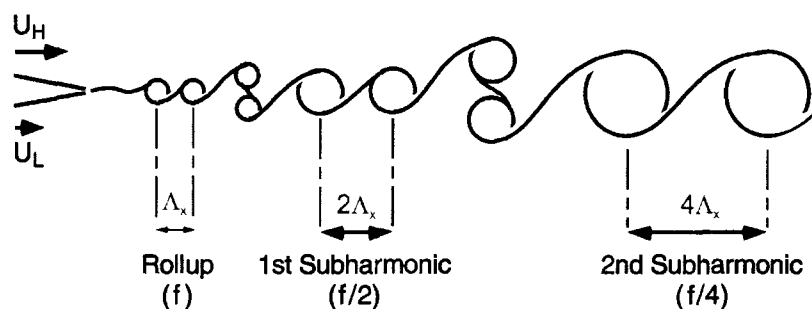


Figure 2.1: Kelvin-Helmholtz instability roll-up and pairing process in a free shear layer (adapted from Estevadeordal and Kleis, 1999)

that the generation of small scale turbulence, hence transition, occurs at a location where both streamwise vorticity and an agglomerating vortex pair are first present. Despite the small-scale breakdown to turbulence, the large-scale vortical structures remain coherent for a significant distance downstream (Ho and Huerre, 1984; Esteveordal and Kleis, 1999).

2.2.2 Boundary Layers

Under conditions with mild pressure gradients and low levels of environmental disturbances, the process of transition from a laminar to a turbulent boundary layer is well known (Schlichting and Gersten, 2000). Figure 2.2 shows a schematic representation of this process for a boundary layer developing over a flat plate. As a laminar boundary layer develops downstream of the plate leading-edge, a point is reached where amplification of

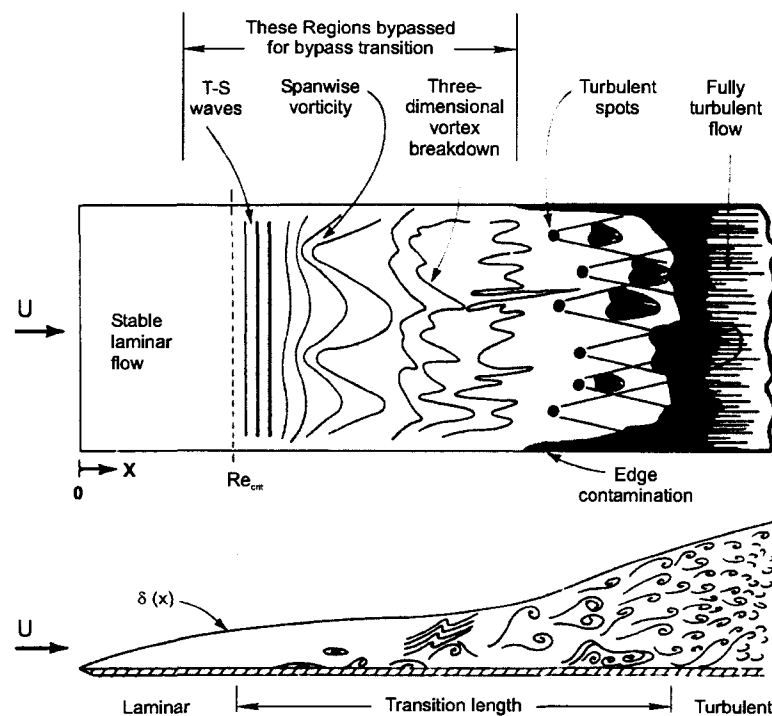


Figure 2.2: Schematic of attached-flow natural transition process (adapted from White, 1991)

two-dimensional instability waves within the shear layer begins. This occurs at a critical Reynolds number, Re_{crit} , which defines the earliest location at which the waves can be amplified, based on linear stability theory. These instability waves are known as Tollmien-Schlichting (T-S) waves, and the range of amplified frequencies of this instability can also be predicted from stability theory. As these instability waves grow and convect downstream, secondary instabilities lead to the development of streamwise vorticity, from which three-dimensional vortical structures form. These structures, often referred to as Λ -vortices, eventually breakdown into turbulent spots which appear irregularly over the surface, spread downstream in a wedge-shaped pattern and eventually coalesce forming a fully-turbulent boundary layer in a manner originally proposed by Emmons (1951). Details regarding the structure of turbulent spots are described in Section 2.2.4.

The transition process shown in Figure 2.2, which occurs in environments with low levels of freestream turbulence, smooth surface conditions, and mild streamwise pressure gradients, is referred to as “natural transition,” and is only one of the various modes through which transition to turbulence can occur in a boundary layer. The presence of environmental disturbances, such as elevated freestream turbulence, surface roughness, noise, vibrations, or unsteadiness of the freestream flow, has been shown to promote transition in a boundary layer (Mayle, 1991). Under such conditions, which are common in turbomachinery flows, disturbances that penetrate the shear layer can undergo an algebraic growth followed by viscous decay, unless they manage to grow to sufficiently large amplitudes to yield a turbulent spot. This path to transition is referred to as transient growth or non-modal growth, with the latter referring to the fact that this mode is not predicted as one of the eigenmodes of the solution of linearized theories based on the Orr-Sommerfeld equation (Saric *et al.*, 2002). In the turbomachinery-aerodynamics community, this category of transition modes is often referred to as “bypass transition”, as T-S waves are not observed and the linear-instability-growth phase is bypassed. However, “road-maps” to turbulence

have been developed over the years which provide a more refined classification of the various modes observed to occur for different amplitudes and types of disturbances. In the transition road-map of Morkovin (1993), described qualitatively in Figure 2.3, bypass transition is a mode where breakdown to turbulence occurs very quickly through the direct production of turbulent spots in the shear layer, and is associated with very strong disturbances. Between the natural and bypass modes of transition (paths A and E in Figure 2.3, respectively), transient-growth modes provide various paths to transition (paths B, C, and D) for which different physical mechanisms prevail. These transient-growth mechanisms are often associated with streamwise streaks in the laminar boundary layer that provide conditions under which secondary instabilities lead to small-scale breakdown to turbulence (Klebanoff, 1971; Matsubara and Alfredsson, 2001; Jacobs and Durbin, 2001).

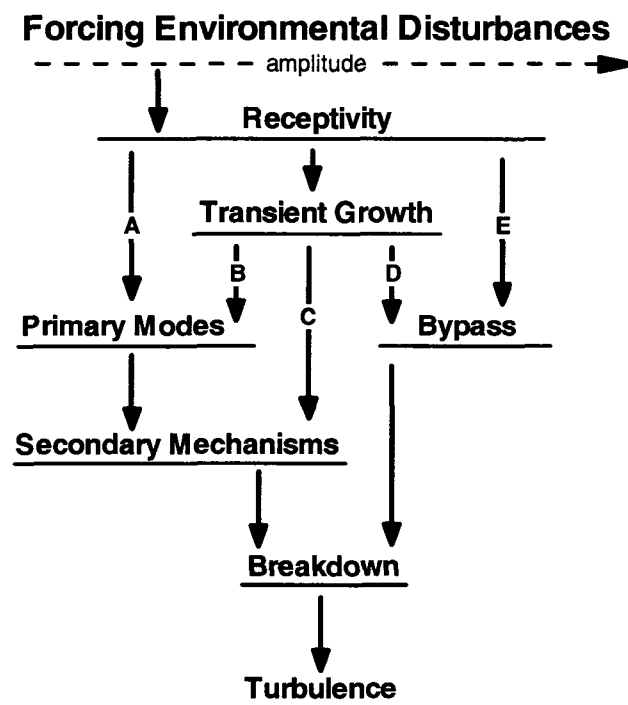


Figure 2.3: Morkovin's boundary-layer-transition road-map (reproduced from Saric *et al.*, 2002)

There are no definitive thresholds for when transient-growth or bypass mechanisms begin to dominate, but they are strongly influenced by the magnitude of the disturbances as well as the receptivity of the shear layer to these disturbances (Morkovin, 1993).

Regardless of the mode through which transition of a boundary layer occurs, the process is first initiated through receptivity of the shear layer to disturbances. This receptivity process governs not only the locations at which disturbances are initiated in the shear layer, but also the amplitude and spectral characteristics of these disturbances which influence the mode through which transition will occur. Saric *et al.* (2002) provide a review of receptivity mechanisms for boundary-layer flows, and identify the ways in which various disturbance sources can affect the ensuing transition process. In general, receptivity sites occur where the mean flow changes rapidly relative to the scales of the boundary layer.

2.2.3 Separation Bubbles

As already noted, separation bubbles and their transition characteristics share commonalities with the two types of flows discussed thus far: free shear layers and boundary layers. The basic flow characteristics of two-dimensional separation-bubble phenomena are described in the following, based on the level of understanding at the outset of the present research.

The time-averaged characteristics of a separation bubble are shown in Figure 2.4. As a laminar boundary layer develops in a region of increasing pressure in the streamwise direction, the shear-layer velocity profile becomes inflectional and thus more susceptible to disturbances (Schlichting and Gersten, 2000). If the near-wall fluid in the laminar boundary layer possesses insufficient momentum to overcome the pressure rise, the flow adjacent to the surface may be brought to rest and the trajectory of the shear layer deviates from that of the surface. The boundary layer is then said to “separate” from the surface (at x_s in

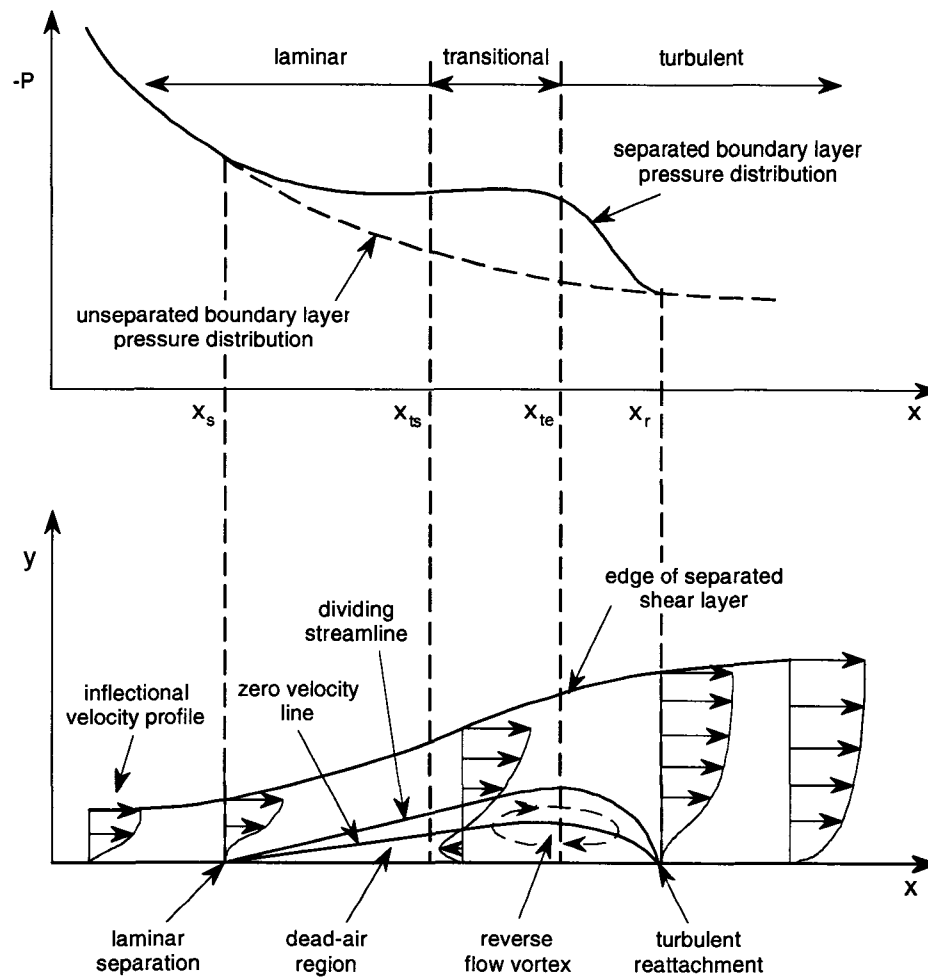


Figure 2.4: Schematic of time-averaged separation-bubble characteristics

Figure 2.4), downstream of which the direction of the near-wall fluid is reversed. The separated shear layer is directed in a manner such that, as it can no longer support a traverse pressure-gradient ($\partial p/\partial y$) to sustain the streamwise pressure gradient ($\partial p/\partial x$), a plateau in the streamwise pressure distribution is normally seen. Initially, the region below the separated shear layer, in which the flow is reversed, possesses sufficiently-low momentum that it is considered stagnant and is sometimes referred to as the “dead-air” region (Tani, 1964). Transition to turbulence is initiated in the separated shear layer, at x_{ts} , and provides a mechanism for enhancing the wall-normal momentum exchange,

which subsequently may result in reattachment of the shear layer to the surface. When the flow field is examined in a time-averaged manner, a reverse-flow vortex develops upstream of the reattachment point, x_r , and reattachment of the shear layer is accompanied by a region of strong pressure recovery. Instances of additional time-averaged vortices have been observed within a separation bubble (Hatman and Wang, 1998*b*; Ripley and Pauley, 1993), including the presence of a smaller secondary vortex with a direction opposite to that of the reattachment vortex. These secondary vortices are similar to those that occur in the lower corner behind a backward-facing step (Hall *et al.*, 2003). Transition completion, x_{te} , is shown in Figure 2.4 to occur upstream of reattachment, however this is not consistently observed and sometimes occurs downstream of reattachment (Roberts, 2005).

The transition process in a separation bubble has been observed to occur through different physical mechanisms. The Kelvin-Helmholtz (K-H) instability has been shown to initiate transition by means of the roll-up, shedding, and subsequent breakdown of large-scale, spanwise-oriented vortical structures that develop in the separated shear layer (Spalart and Strelets, 2000; Bao and Dallmann, 2004), similar to that which occurs for planar free-shear layers. These vortical structures originate from an inviscid instability of the shear layer, initiated by receptivity of the layer to small environmental disturbances. The Tollmien-Schlichting (T-S) viscous instability mechanism, associated with boundary-layer transition, has also been shown to initiate transition in separation bubbles (Volino, 2002*b*; Roberts, 2005; Gostelow and Thomas, 2006). This mechanism provides the conditions under which turbulent spots are observed in the late stages of the transition process and provide the final breakdown to small-scale turbulence. Under elevated levels of environmental disturbances (for example: freestream turbulence, surface roughness, periodic wake passing, etc.), the K-H and T-S instabilities may be bypassed with the breakdown to small-scale turbulence occurring through either a transient-growth or bypass mode of transition. This has been observed experimentally in separation bubbles by Volino (2002*a*)

and Roberts (2005). A discussion of these and other studies of separation-bubble transition is provided in Section 2.3.

Separation bubbles that occur over airfoils have typically been classified into one of two categories, “short” or “long”, each defined by their effects on the airfoil pressure distribution, according to Mayle (1991). Short bubbles have only a local effect on the airfoil surface pressure distribution, as is the case in Figure 2.4, whereas long bubbles significantly alter the pressure distribution over the entire airfoil. The transition from a short to a long bubble is referred to as “bursting” and is sometimes the process to which airfoil stall is attributed.

2.2.4 Turbulent Spots

The structure of turbulent spots in attached boundary layers has been examined by many researchers dating back to the work of Emmons (1951) and Schubauer and Klebanoff (1955). Early work consisted of identifying the shape and growth characteristics of spots in mild pressure gradients and providing conceptual ideas regarding the cause for spot growth and turbulence generation. Yaras (2007) provides a brief review of turbulent-spot research in regards to attached boundary-layer transition. Recent studies such as those of Schröder and Kompenhans (2004) and Yaras (2007) have focused on identifying coherent substructures within turbulent spots. These studies provide strong evidence of the presence of organized patterns of hairpin vortices and associated streaky patterns in the streamwise velocity field within a turbulent spot.

Figure 2.5 shows a photograph of the planform view of a turbulent spot developing in an undisturbed laminar boundary layer (reproduced from Schlichting and Gersten, 2000). The small-scale turbulent fluctuations generated within the spot are clearly evident in Figure 2.5, as is the calmed-region that trails the spot on the left-hand-side of the photograph. This calmed region has been shown to provide a damping mechanism for wall-turbulence, as

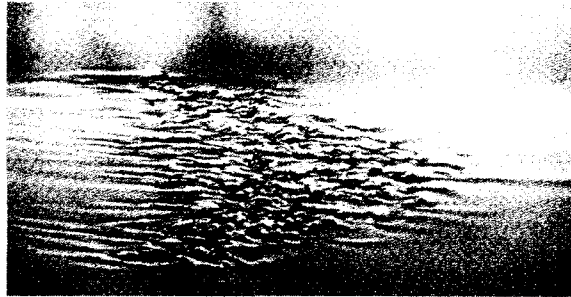


Figure 2.5: Planform photograph of a turbulent spot (reproduced from Schlichting and Gersten, 2000)

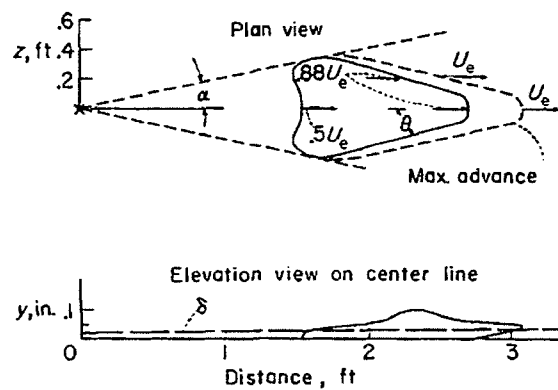


Figure 2.6: Schematic of a turbulent spot in a zero-pressure-gradient environment (reproduced from Schubauer and Klebanoff, 1955)

it has a velocity-profile shape similar to that of a turbulent boundary layer, without the associated turbulence (Gostelow *et al.*, 1996). The calmed region is therefore much less susceptible to disturbance growth. The general structure of a turbulent spot developing in an undisturbed, zero-pressure-gradient boundary layer, based on the artificially-generated-spot experiments of Schubauer and Klebanoff (1955), is shown schematically in Figure 2.6. This basic structure, consisting of a triangular planform arrangement with an overhang at the downstream end, has been confirmed through many experimental studies since the work of Schubauer and Klebanoff. However, the presence of freestream acceleration or

deceleration modifies this shape, and has also been shown to be affected by the manner in which the artificially-generated spots are produced (Yaras, 2007).

The presence of turbulent spots in a separated shear layer has been observed under conditions with elevated environmental disturbances (Volino, 2002*a*; Volino, 2002*b*; Roberts, 2005). The internal structure of such turbulent spots has been documented mainly based on artificially-generated spots through phase-averaged measurements. Averaging of phase-locked measurements tends to smear-out details of the sub-structure, unless the spots develop under strongly-favorable pressure gradients, relatively-low flow Reynolds numbers, and with low levels of environmental disturbances such as freestream turbulence (Yaras, 2007). Artificially-generated spots in separated shear layers have been examined by D'Ovidio *et al.* (2001*a*) and by Watmuff (1999) through excitation of a wave packet introduced upstream of separation, although Watmuff refers to them as “vortex loops” rather than “turbulent spots.” In both of these studies, a dominant frequency emerges from the wave packet as it convects through the separated shear layer. Watmuff identifies a roll-up of vorticity from this amplified instability, which leads to a series of vortex loops, the structures of which remain coherent as they convect through the reattached turbulent boundary layer. Figure 2.7, reproduced from Watmuff (1999), shows the spatial and temporal development of these vortex loops as measured by means of phase-averaged flying-hot-wire measurements. The presence of a dominant frequency within the turbulent spot has also been identified in the measurements of D'Ovidio *et al.* (2001*a*).

One question that remains, regarding turbulent-spot growth in separated shear layers, is how their development is affected by the presence of elevated freestream turbulence. Studies such as those of Volino (2002*a*) and Roberts (2005) have provided evidence of turbulent spots under such conditions, however the nature of the single-point measurement techniques used in these studies do not provide a means for examining the streamwise development of individual spots.

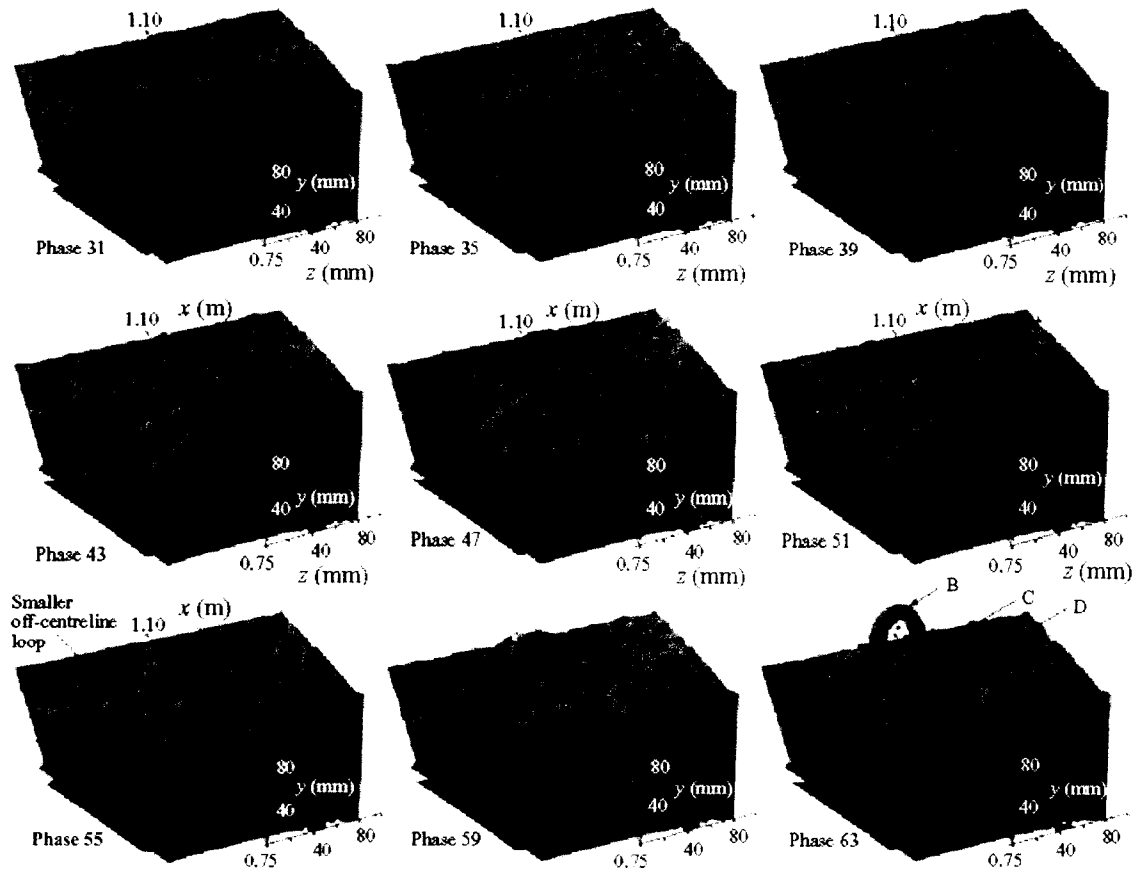


Figure 2.7: Vortex loop development observed in a separated shear layer (reproduced from Watmuff, 1999)

2.3 Review of Relevant Experimental and Computational Studies of Separation Bubbles

Separation-bubble transition has been examined by many researchers over the past few decades. Many of these studies are in the context of flows over modern high-lift low-pressure-turbine (LPT) airfoils, where separation bubbles can be present over most of their operating regimes. This section begins by reviewing many of the experiments concerned with separation bubbles, followed by a review of numerical studies performed in the same context. To prevent extended discussions of the conditions and measured parameters, the experimental studies of relevance are tabulated in Table 2.1. This is by no means a comprehensive list of all the studies that have been performed in the context of separation-bubble transition, but represents those that have been found most useful by the author in understanding the state-of-the-art in regards to separation-bubble transition at the outset of this research program. The abbreviations used in Table 2.1 are listed below:

Type of experiment:	SA	single airfoil experiment
	FP	flat plate experiment with imposed pressure gradient
	SPC	single passage cascade experiment
	LCS	linear cascade experiment
	WTT	water tow-tank experiment
Measurements details:	SH	single hot-wire probe
	XH	two-component hot-wire probe (X-wire)
	SP	surface pressure taps
	HF	surface-mounted hot-film sensors
	PV	particle image velocimetry (PIV)
	FV	flow visualization
Parameters investigated:	Re	Reynolds number
	Tu	freestream turbulence intensity
	PD	pressure distribution
	SR	surface roughness
	PU	periodic freestream unsteadiness

Table 2.1: Experimental studies of separation bubbles and separated-flow transition

Reference	Type	Measurement Details						Parameters Investigated					Conditions		Comments
		SH	XH	SP	HF	PV	FV	Re	Tu	PD	SR	PU	$Re \times 10^{-3}$	Tu[%]	
Tani (1964)	SA			•			•	•	•				42 – 8400 ₁	N/A	-SB characteristics examined for various airfoils
Arena and Mueller (1980)	SA			•			•	•	•				150 – 470 ₁	0.1	-Airfoil SB examined for various Re and α
Batill and Mueller (1981)	SA						•	•	•				50 – 120 ₁	N/A	-Airfoil SB examined for various Re and α -K-H and pairing instabilities observed
Cherry <i>et al.</i> (1984)	FP	•		•			•	•					32 ₂	0.07	-Separation induced by rectangular leading-edge -Vorticity shedding identified from fluctuating SP
Schmidt and Mueller (1989)	SA	•					•	•	•				50 – 200 ₁	0.11-0.3	-Examined the applicability of various SB models
Malkiel and Mayle (1996)	SA	•		•									29 ₂	0.3	-Detailed examination of SB transition process
Qui and Simon (1997)	SPC	•		•			•	•					50 – 300 ₃	0.5-10	-Examined SB in simulated LPT environment
Hatman and Wang (1998b)	FP		•	•			•		•				N/A	0.45-0.9	-Examined SB characteristics -Detailed Reynold stresses in near-wall region
Murawski and Vafai (1999)	LCS	•		•			•		•				50 – 300 ₃	0.54-1.08	-Examined SB in LPT cascade environment -PD varied using trailing-edge extensions
Watmuff (1999)	FP	•	•	•									860 ₄	0.1	-Examined instability induced by wave packet -Flying hot-wires used to resolve reverse flow
Lou and Hourmouziadis (2000)	FP	•		•			•				•		290 – 1400 ₄	0.5	-PU generated by oscillating downstream flap -SB examined for steady and unsteady conditions
Shyne <i>et al.</i> (2000)	FP	•		•	•		•	•	•				100 – 250 ₃	0.8-3.0	-Examined SB in simulated LPT environment
Howell <i>et al.</i> (2001)	LCS	•		•	•		•		•		•		130 – 210 ₃	N/A	-Examined high-lift PD using inserts and flaps -Focus is wake-induced SB transition
Volino and Hultgren (2001)	FP	•					•	•					50 – 300 ₃	0.2-7	-Examined SB in simulated LPT environment
Yaras (2001)	FP	•		•			•		•				350 – 1020 ₄	0.22-0.65	-Examined SB characteristics for various PD -Importance of pressure gradient history noted
Talan and Hourmouziadis (2002)	FP	•		•			•				•		115 – 506 ₄	< 0.6%	-PU generated by oscillating downstream flap -vortex shedding observed for $Re_{\theta_s} < 125$
Volino (2002a)	SPC	•		•			•	•					25 – 300 ₃	0.5-8,7	-Examined SB in simulated LPT environment
Volino (2002b)	SPC	•		•			•	•					25 – 300 ₃	0.5-8.7	-Part 2 of Volino (2002a) -Examined turbulence spectra in SB

continued on page 26

Table 2.1: Experimental studies of separation bubbles and separated-flow transition (continued)

Reference	Type	Measurement Details						Parameters Investigated					Conditions		Comments
		SH	XH	SP	HF	PV	FV	Re	Tu	PD	SR	PU	$Re \times 10^{-3}$	Tu[%]	
Yaras (2002)	FP	•		•				•	•	•			350 – 470 ₄	0.5-9.0	-Examined dependence of SB on Tu -Trans. onset and reattach. correlation
Volino and Murawski (2003)	LCS	•		•	•			•					50 – 200 ₃	1.3-1.4	-Examined SB characteristics and turbulence spectra
Roberts and Yaras (2003)	FP	•		•				•	•	•		•	350 – 470 ₄	0.6-3.2	-PU generated by oscillating flap -Examined SB characteristics
Breear and Hodson (2003)	LCS	•		•			•	•	•			•	130 ₃	0.6-3.9	-Examined effect of Tu on pressure surface SB -Varied incidence (-10°,0°, +10°)
Bao and Dallmann (2004)	WTT					•	•	•					8 – 100 ₅	0	-Examined SB instability and vortex dynamics
Lang <i>et al.</i> (2004)	FP					•	•						≈ 65 ₄	< 0.05	-LDA and PIV compared with DNS -Stability and trans. mechanism examined
Roberts and Yaras (2005a)	FP	•						•			•		350 – 470 ₄	0.5 – 4.5	-Examined effects of surface roughness on SB
Roberts and Yaras (2006a)	FP	•						•		•	•		350 – 470 ₄	< 1	-Examined effects of surface roughness on SB
Gostelow and Thomas (2006)	FP	•		•				•		•	•		1400 ₄	0.2	-Examined instability growth in SB -Examined SP flucs. using surface microphones
Mahallati <i>et al.</i> (2007)	LCS			•	•			•	•				25 – 150 ₆	0.4-4.0	-Examined SB in LPT cascade environment

¹ Reynolds number based on undisturbed freestream velocity and true chord length

² Reynolds number based on undisturbed freestream velocity and leading edge dimension (thickness, radius)

³ Reynolds number based on exit velocity and surface length

⁴ Reynolds number based on inlet velocity and surface length

⁵ Reynolds number based on undisturbed freestream velocity and surface length upstream of separation

⁶ Reynolds number based on inlet velocity and axial chord length

Based on the experimental studies outlined in Table 2.1, several important conclusions regarding separation-bubble transition have been reached and are discussed in the following. In the presence of undisturbed freestream conditions, separation generally occurs at a fixed streamwise location on the solid surface. The reattachment location, on the other-hand, is unsteady in nature and can wander from the time-averaged reattachment location by up to 50% of the time-averaged bubble length. This wandering is caused by the growth and subsequent shedding of vorticity that occurs in the reattachment region, and is what causes major difficulties in developing models to predict time-averaged separation bubbles. The length of the transition region within a bubble is also much shorter than that for attached-flow transition at the same Reynolds number. This is attributed to the rapid three-dimensional deformation of the separated-shear layer, which is partially damped by the wall in attached flows, and is similar to the process observed in free-shear layers.

The onset of transition in a separated shear layer appears to be dependent on both local and upstream flow conditions. Many of the studies presented in Table 2.1 have reported that the transition onset location can be correlated well with the boundary-layer momentum thickness at separation, a parameter that represents the growth of the boundary layer prior to separation. Also, the level of freestream turbulence can greatly affect both the onset of transition and the mode of transition (natural, transient-growth, or bypass). It is not only the level of turbulence intensity that affects the transition process but the scales of the freestream turbulence as well. Mayle *et al.* (1998) show that the growth of pre-transitional laminar fluctuations is promoted in a narrow band of frequencies, with a corresponding band of freestream turbulence length scales comparable to the scale of the energy-dissipating eddies in the boundary layer. Surface roughness can also promote the onset of transition through a similar mechanism as freestream turbulence.

In general, the transition process in a separated shear layer is promoted and enhanced by an increase in the flow Reynolds number, an increase in the strength of the adverse pressure

gradient prior to separation, an increase in the freestream turbulence intensity, an increase in the level of surface roughness, and the presence of periodic freestream unsteadiness. Although not discussed above or represented thoroughly in Table 2.1, the periodic passing of turbulent wakes also has an effect on the transition process in a separated shear layer, whereby the turbulence of the passing wake promotes the growth of instabilities in the shear layer. This wake-induced transition process is not a focus of the present work, but a thorough review of the subject is given by Mahallati (2003). Also, many of the publications by the Whittle Laboratory at Cambridge University, under the supervision of Howard Hodson (e.g. Stieger and Hodson, 2004; Hodson and Howell, 2005; Zhang and Hodson, 2005) have provided significant contributions to the understanding of wake-induced transition phenomena.

Although many of the more recent studies presented in Table 2.1 have included spectral analysis of time-dependent hot-wire measurements, there does not appear to be a clear distinction between the appearance of either the K-H or T-S instabilities. Talan and Hourmouziadis (2002) have, however, observed the shedding of large-scale vortices from separation bubbles in periodic unsteady freestream flow only for cases in which the momentum thickness Reynolds number at separation was below a certain threshold ($Re_{\theta_s} \leq O(100)$). This may indicate a distinction between the two mechanisms.

The studies of Roberts and Yaras identified in Table 2.1 were performed during an earlier phase of the current research program, and were aimed at identifying and modelling the transitional behaviour of attached and separated boundary-layers. All of these studies are documented in the thesis of Roberts (2005), and therefore, for the sake of conciseness, any further reference to this material is made through citation of Roberts' thesis.

Despite the significant number of experimental studies performed in the context of examining separation-bubble transition, most of the experimental methods used have

limitations such that they cannot provide simultaneous spatial and temporal resolution of the flow. The advances in computing power over recent years has permitted the use of Large Eddy Simulation (LES) and Direct Numerical Simulation (DNS) for examining transition in both attached and separated shear layers. The major benefit of these methods is the ability to capture both the spatial and temporal variation in the flow field. Some simulation studies of interest to the present work are listed in Table 2.2, and the pertinent information from these studies is discussed in detail in Chapter 7 with regards to the DNS studies performed during this research program. The important information regarding shear-layer transition gained from these studies is the identification of the coherent structures involved in the transition process.

The following section reviews several prediction models for separated-flow transition, many of which have been developed based on observations and measurements from the studies presented in Table 2.1.

2.4 Transition Modelling

The end-result of transition research is typically a description, or model, of the transition process with which the performance of an airfoil can be predicted. As discussed by Roberts (2005), the most promising methods for predicting low-Reynolds-number transition are at the opposing ends of the complexity spectrum. Direct Numerical Simulation (DNS) provides the most detailed and complete description of transition, by virtue that all of the scales of turbulence are resolved with high spatial and temporal resolution, through direct numerical simulation of the Navier-Stokes equations. This requires significant computing resources. At the other end of the spectrum falls the semi-empirical models based in part on the physics of transition but adjusted to reproduce experimental measurements. Although these models generally represent a “best-fit” to the data and most often cannot

Table 2.2: High-resolution simulation studies of separation-bubble flows

Reference	Simulation Type		Comments
	LES	DNS	
Ripley and Pauley (1993)		•	<ul style="list-style-type: none"> - 2D-DNS performed for three cases of separating flows over a flat-plate - Streamwise pressure distributions imposed by transpiration through upper domain surface - K-H and vortex-pairing instabilities observed in separation bubbles
Muti Lin and Pauley (1996)		•	<ul style="list-style-type: none"> - 2D-DNS performed for an Eppler 387 airfoil - 6 cases in range $60,000 \leq Re_C \leq 200,000$ and $0^\circ \leq \alpha \leq 7^\circ$ - K-H and vortex-pairing instabilities observed in separation bubbles
Wilson and Pauley (1998)	•		<ul style="list-style-type: none"> - 2D and 3D LES performed a separation bubble over a flat-plate - Various subgrid models examined (constant and dynamic Smagorinsky constants) - Three-dimensional vortex structures observed in transition region
Spalart and Strelets (2000)		•	<ul style="list-style-type: none"> - 3D-DNS performed for a separation bubble over a flat-plate - Instabilities promoted by temporal- and spanwise-periodic aspiration through surface upstream of separation - Λ-vortices observed to provide breakdown to turbulence
Alam and Sandham (2000)		•	<ul style="list-style-type: none"> - 3D-DNS performed for a separation bubble over a flat-plate - K-H instability observed to initiate transition in a low-disturbance environment - Transition is quick and vortex-pairing is not observed
Yang and Voke (2001)	•		<ul style="list-style-type: none"> - 3D-LES performed for a separation bubble at the circular leading edge of a flat plate - K-H instability observed to initiate transition - Secondary instability leads to three-dimensional vortex-structures downstream of transition
Abdalla and Yang (2004)	•		<ul style="list-style-type: none"> - 3D-LES performed for a separation bubble at the blunt leading edge of a flat plate - K-H instability observed to initiate transition, with primary and secondary pairing events observed - Helical-pairing instability noted to cause breakdown to turbulence
Roberts and Yaras (2006b)		•	<ul style="list-style-type: none"> - 3D-DNS performed for a separation bubble over a flat plate - Identified as LES, but no subgrid model used and resolution sufficient for DNS - K-H instability observed to initiate transition

be extrapolated, they are currently the most efficient means of predicting transition with reasonable accuracy. This section briefly discusses the most recent models that have appeared in the literature. The mathematical description of the models is not provided in this section, but those suited to transition under low-freestream-turbulence conditions are provided in Chapter 6, where an assessment of the suitable models is made against experimental results for separation bubbles over a low-Reynolds-number airfoil.

Based on his critical review of transition phenomena in gas turbines, Mayle (1991) provided correlations for predicting the transition process in a separation bubble. He provided two correlations for the onset of transition, one for short bubbles and one for long bubbles, and a correlation for the length of the transition region. All three correlations are based on a small database of experimental data and do not account for the effects of freestream turbulence, which Mayle admits is an important parameter. The purpose of Mayle's paper was to present the available knowledge-base for transition in turbomachinery flows, and concluded that more research was required to provide accurate prediction models, especially for separated-flow transition. In a response to Mayle's paper, Walker (1993) provides similar conclusions.

Hatman and Wang (1999) have developed a set of correlations based on an extensive set of experimental data gathered over a range of Reynolds numbers and pressure distributions. They categorized the types of bubbles they observed and developed correlations for each. The main deficiencies of the Hatman and Wang model are that the effect of pressure gradient history upstream of separation has not been accounted for and that it is only valid for low-freestream turbulence levels ($< 0.9\%$). Despite these shortcomings, Yaras (2002) showed that the transition-onset model of Hatman and Wang works well for his set of low-freestream-turbulence cases.

Praisner and Clark (2007) present a set of new models for attached- and separated-flow transition, each based on the concept of dynamic similarity (for a description of dynamic similarity, see White, 1994). Their separated-flow transition model predicts the location of transition onset based on an extensive database of published and proprietary experimental data, and it is assumed that transition is instantaneous. Praisner *et al.* (2007) present data from numerical Reynolds-Averaged-Navier-Stokes (RANS)-based simulations using this separated-flow transition model, and show good agreement between experiment and simulation for modern low-pressure-turbine airfoils.

Redford and Johnson (2004) present a model for the prediction of both attached- and separated-flow transition, which is a modified version of a previous attached-flow model (Johnson and Ercan (1999)). These models are based on certain observations regarding the physics of attached-flow transition, which they have divided into three processes, each of which are predicted. First, the model predicts the susceptibility of the pre-transitional laminar boundary layer to freestream disturbances and determines where turbulent spots may form. Second, the model predicts the streamwise location where production of turbulent spots is most likely to occur and the corresponding spot-production rate. Third, the model predicts the growth and merging of the spots with downstream distance. Comparison with experimental data show that this model accurately predicts the onset and progression of separated-flow transition when the freestream turbulence intensity is greater than 1%, which corresponds to the flow regime where transition occurs through a transient-growth or bypass mode.

Volino and Bohl (2004) have also developed a model based on the growth of pre-transitional velocity fluctuations. Their model predicts only the onset of transition, which is assumed to occur instantaneously, as with the model of Praisner and Clark (2007). The model of Volino and Bohl has been developed from measurements performed in a simulated low-pressure-turbine environment where a relatively long accelerated-flow region precedes

the adverse pressure gradient region where separation occurs. Therefore, to extend the range of applicability of this model, it should also be validated for conditions in which the suction peak occurs immediately downstream of the stagnation point, as with an isolated airfoil.

During a previous phase of the present research program, Roberts and Yaras (2005b) developed a new model that predicts the onset and progression of transition for both attached and separated shear-layers. This model was developed from an extensive set of experimental measurements performed in various experimental facilities. Any further reference to this model will be made through citation to Roberts' thesis (Roberts, 2005), as it contains not only a description of the model development but also much of the experimental results upon which the model is based.

In the model of Roberts (2005), transition is predicted in a two-step process using an algebraic semi-empirical scheme. The first step is the prediction of the location of transition inception, and the second is the prediction of the length of the transition zone. For transition in attached boundary layers, Roberts recommends the transition inception model of Abu-Ghannam and Shaw (1980). A new model for separated-flow transition-inception was developed by Roberts due to the inability of published models to provide reliable predictions for the extensive set of experimental data examined. This model, which relates the separation-to-transition-inception distance to the boundary-layer state at separation, uses the same functional form as those of Mayle (1991) but include additional parameters to account for the effects of turbulence intensity, turbulence length-scale, and surface roughness. This model is given as follows:

$$Re_{s-ts} = \left[785 - 30TF(\%) - (1400 - 25e^{0.45TF(\%)}) \frac{k_{rms}}{\theta_s} \right] Re_{\theta_s}^{0.7} \quad (2.1)$$

where $TF = Tu_{ref}(L/\Lambda_f)^{0.2}$ is Taylor's turbulence factor and accounts for freestream

turbulence intensity (Tu) and length scale (Λ_f), both of which are important parameters describing the freestream turbulence field. Equation 2.1 accounts for surface roughness, through the RMS roughness height (k_{rms}).

Prediction of the transition length is accomplished using an intermittency-based modelling approach describing the fraction of time the boundary layer is turbulent at a given streamwise location. The model accounts for the production, growth and merging of turbulent spots using the intermittency function of Solomon *et al.* (1996), defined as follows:

$$\gamma(x) = 1 - \exp \left[-n \int_{x_{ts}}^x \frac{\sigma}{\tan(\alpha)} \left(\frac{dx}{U_e} \right) \int_{x_{ts}}^x \tan(\alpha) dx \right] \quad (2.2)$$

In Equation 2.2, x_{ts} is the transition onset location, n is the spot inception rate, σ is the spot propagation parameter, α is the lateral spot spreading half-angle, and U_e is the local freestream velocity. The first and second integrals represent the effects of streamwise and spanwise spreading of turbulent spots, respectively. Equation 2.2 assumes that turbulent spots appear only at one streamwise location on the surface, which is known as the “concentrated breakdown” model as first proposed by Dhawan and Narasimha (1958). Roberts proposes a new correlation for n based on an extensive set of experimental measurements. His model relates the non-dimensional inception-rate parameter, $N = n\sigma\theta_{ts}^3/\nu$, with the shear layer shape factor at the location of transition onset, H_{ts} . The new model for the spot inception rate is:

$$\log_{10}(N) = \frac{0.55H_{ts} - 2.2}{1 - 0.63H_{ts} + 0.14H_{ts}^2} \quad (2.3)$$

To model the effects of streamwise and spanwise spreading of turbulent spots, which affect the length of the transition region, Roberts makes use of the previously-developed model of D’Ovidio *et al.* (2001b) for the spot propagation parameter, σ , and that of Gostelow *et al.* (1996) for the spot spreading half-angle, α . The spot propagation parameter

is defined as

$$\sigma = \tan(\alpha) \left(\frac{1}{b} - \frac{1}{a} \right) \quad (2.4)$$

where $a = U_{le}/U_e$ and $b = U_{te}/U_e$ are the leading edge and trailing edge celerities of the spot, respectively. The models provide the spot growth parameters as a function the local pressure gradient parameter, $\lambda_\theta = (\theta^2/\nu)dU_e/dx$, and are based on measurements of artificially-generated turbulent spots under accelerating and decelerating freestream conditions. The spot spreading half angle is modelled as

$$\alpha = 4 + \frac{22.14}{0.79 + 2.72e^{(47.63\lambda_\theta)}} \quad (2.5)$$

and the spot propagation parameter is modelled as

$$\sigma = 0.024 + \frac{0.604}{1 + 5e^{(66\lambda_\theta)}}. \quad (2.6)$$

These models have been validated in the range $-0.12 \leq \lambda_\theta \leq 0.06$ by D'Ovidio *et al.* (2001b). These turbulent-spot-growth models do not account for the potential influence of freestream turbulence and, despite being shown to provide accurate transition lengths for such conditions through the use of Equation 2.2, should therefore be further validated for such purposes.

Roberts (2005) shows that his transition-rate model, consisting of Equations 2.2 through 2.6, maintains the prediction accuracy of existing models for attached-flow transition but also provides promising results regarding transition prediction in separated-flows.

2.5 Transition Control in Separation Bubbles

As discussed in the introduction to this document, the operating range for low-pressure turbines (LPTs) and micro air vehicles (MAVs) encompasses the laminar and transitional boundary-layer flow regimes ($Re \approx 10^4 - 10^6$). Laminar separation is a general occurrence over the suction surface of these aerodynamic devices, and it is desired that reattachment occurs shortly thereafter to prevent a large degradation of the airfoil performance. LPTs and MAVs are therefore prime candidates for flow control, where an attempt can be made to improve the performance through manipulation of the flow field. Classification of flow control methods is discussed in Section 2.5.1, and Section 2.5.2 reviews passive methods of transition control for separated flows.

2.5.1 Control Methods and Classification

Gad-el-Hak (2000) describes many ways of classifying flow-control methods. The classification scheme adopted by the present author considers the energy expenditure and the control loop involved. Figure 2.8 shows this classification scheme. If no energy input is required, the control method is considered *passive* and there is no control loop involved. If energy input is required, the control method is considered *active* and involves a control loop. *Active* flow control is further sub-divided, depending on the control loop and controlled flow variable. If steady or unsteady energy input is used without regard for the state of the flow (fixed-input), then the method is considered *predetermined* and uses open-loop control, whereas if the control input is continually adjusted based on a measured flow variable (variable-input), then the method is considered *reactive*. Two different types of control loop can be used for reactive control. In a *feedforward* control loop, the measured and controlled flow variables differ. In a *feedback* control loop, the measured and controlled variables are the same. The complexity of these control methods increases with the order

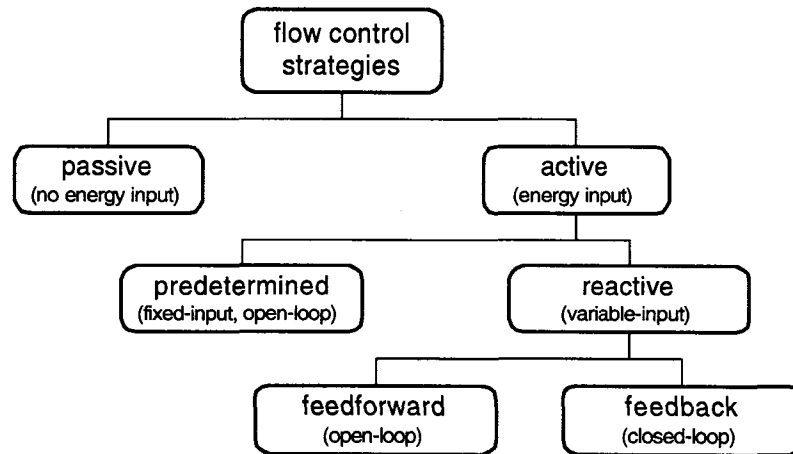


Figure 2.8: Classification of flow control concepts (adapted from Gad-el-Hak, 2000)

in which they were discussed. Therefore, if *passive* control works well for a given objective, it will likely be the simplest method of control for the given application.

The major benefit of active control over passive control is that the specific control technique can be activated only when required. This is beneficial when the aerodynamic device must operate over a wide range of conditions, only part of which requires flow control to either improve or maintain desired performance levels. A problem arises when the penalty associated with the active control method (energy expenditure) outweighs the benefits of its use. Due to this effect, it is then desired to develop methods of control that increase the system performance as a whole. Passive control is therefore highly desirable because any improvement in aerodynamic performance will cause a direct increase in the system efficiency, be it an LPT or an MAV. The next section reviews some methods of passive transition flow-control for low-Reynolds-number applications.

2.5.2 Passive Transition Manipulation

The primary focus of the proposed research, with regards to flow control, is to maintain or improve the performance of low-Reynolds-number airfoils by preventing the formation of long separation bubbles or full-scale stall. This becomes an exercise in manipulating the separation and transition process over the airfoil suction surface. Although separation can occur over the pressure surface of airfoils at design incidence, particularly on modern LPT airfoils (Brear and Hodson, 2003), the effect on the performance is secondary as compared to the effect of suction-surface separations. This was shown by Denton (1993) who argued that the entropy generation within a boundary layer is proportional to the cube of the local freestream velocity. Therefore, for moderate to high levels of lift, the suction surface boundary layer will likely account for most of the viscous losses, even if separation is present on the pressure surface.

There are two approaches to maintaining high-lift and preventing high boundary-layer losses when laminar separation is present. One method is to prevent separation altogether by initiating transition such that the boundary layer is turbulent at the expected location of laminar separation and is therefore much less susceptible to separation. This technique works well to maintain lift but high viscous losses result from the longer turbulent boundary layer. The second method is to ensure that separated-flow transition occurs soon after separation, which would result in a short separation bubble with low form and skin-friction drag/losses.

The majority of passive separation-control methods are of the first type described above, whereby transition is initiated before separation. The primary method of passive separation manipulation has been vortex generators (Lin, 2002; Kerho *et al.*, 1993), which consist of surface protrusions that generate vortical entrainment of freestream fluid down to the surface. When these devices are used to prevent separation at off-design conditions,

parasitic drag is typically increased at design conditions unless the devices can be retracted into the surface (Gad-el-Hak, 2000). This effect is seen for many types of separation-control devices. In studies by Lake *et al.* (2000) and Volino (2003), the use of surface protrusions on a modern LPT airfoil reduced low-Reynolds-number separation losses, but generated higher losses at higher Reynolds numbers typical of take-off conditions. Lin *et al.* (1989) and Lin *et al.* (1990) examined various passive methods of turbulent-flow separation control over a backward-facing ramp. They found that vortex generators, transverse grooves, longitudinal grooves, large-eddy breakup devices, and arches were all effective at either preventing or reducing the length of turbulent separation. Lin (2002) describes the development of “low-profile” vortex generators that generate lower losses than conventional vortex generators, while effectively suppressing or reducing separation of turbulent boundary layers.

Recently, some studies involving the manipulation of laminar separation over LPT airfoils have identified methods of separation control that fall into the second category discussed above, whereby separated-flow transition is triggered within the separated shear layer sooner than would be expected in the absence of any manipulation. Lake *et al.* (2000) present results indicating that recessed surface modifications such as dimples and longitudinal v-grooves can promote separated-flow transition at low-Reynolds numbers while providing a negligible change in, or even improved, performance at high-Reynolds numbers. A similar effect is seen in the data of Volino (2003) for the smallest of his surface protrusions, which extend from the surface approximately $1/3$ of the local boundary layer thickness, at the highest Reynolds number examined. In a previous study by the present author (McAuliffe, 2003) in which active separation control by means an inclined plane wall jet was examined for an LPT airfoil, the presence of the wall-jet slot without any injection promoted transition in the downstream separated shear layer and improved the performance of the airfoil as compared to the baseline smooth airfoil for all cases examined.

Sieverding *et al.* (2004) show similar results for partial slots on the suction surface of a high-pressure turbine airfoil at low-Reynolds numbers. In fact, McAuliffe (2003) showed that the presence of the slot with no blowing prevented full-scale stall of the LPT airfoil for one of the operating conditions examined. Although no details regarding the velocity spectra are given for the above-mentioned studies, it is expected that instabilities were promoted within the separated shear layer due to the small disturbances initiated by the upstream surface modifications.

In a series of studies regarding the effect of surface modifications on the transition process of separation bubbles in the presence of periodic wake-passing, Zhang and Hodson (2005) and Zhang *et al.* (2005) showed that a variety of surface protrusion and indentation methods placed upstream of separation provided decreased separation-lengths and decreased losses over the suction surface of highly-loaded LPT airfoils. They concluded that surface modifications that provide additional disturbances upstream of separation, consisting primarily of small backward-facing steps, promoted the transition process occurring in the downstream separation bubbles.

At the moment, passive control techniques appear best suited for application in the aeronautics industry, primarily because they require no energy expenditure and no complex control system. Therefore, passive manipulation of separation-bubble transition was examined during the last phase of the present research, and is documented in Chapter 9.

Chapter 3

Experimental Setup and Procedures

3.1 Chapter Overview

This chapter describes the experimental facilities used during the course of the present research. Section 3.2 provides details of the National Research Council (NRC) Low-Reynolds-Number facility, its measurement system, and the test models used. Section 3.3 describes the Carleton University wind-tunnel facility from which experimental measurements were used to perform validation of numerical simulation results.

3.2 National Research Council Facility

The Low-Reynolds-Number Pilot facility at the National Research Council of Canada (NRC) was developed with the intent of studying low-Reynolds-number flows in a test medium that allows the use of macro-scale models. Conventional wind or water tunnels

which recirculate the working fluid have disadvantages: to achieve low-Reynolds-number operating conditions ($Re < 100,000$) either the models must be very small or the flow must have a very low velocity. This generally results in poor spatial resolution of the flow features of interest and insufficient measurement accuracy of the aerodynamic loads. To avoid these issues, the NRC facility consists of a tow-tank in which an airfoil model can be towed through an aqueous solution of water and glycerin. By changing the concentration of glycerine, the kinematic viscosity of the test medium can be varied over three orders of magnitude (Hanff, 2004). With this level of flexibility, for a test model with a characteristic length of 30 cm, a Reynolds number range of 25 to 250,000 can be achieved in the facility. However, for the purposes of the present study, pure water was used and the flow-Reynolds-number range over which the experiments were performed is 28,000 to 101,000. Particle image velocimetry (PIV) is the primary measurement technique used in the facility. This measurement system consists of a data acquisition computer, a set of two lasers, and a digital camera. Details regarding the specific systems used and their components are provided in Section 3.2.3.

3.2.1 Tow Tank

The NRC facility consists of an enclosed tank of 3 m working length with a 1 m \times 1 m cross-section in which an airfoil model can be towed. A schematic of the facility is shown in Figure 3.1, which depicts the locations of the PIV system components relative to the tow tank. Since the test models move in relation to the main structure, the lasers and camera of the PIV system must track accordingly. A motion system has been designed for the facility that makes use of servo-motors to provide accurate registration between the system components. The test models are supported by a stem attached to a traverse system mounted above the tank. The stem is inserted through a slot in the roof of the tank, and a flexible seal within this slot provides low resistance to the moving stem.

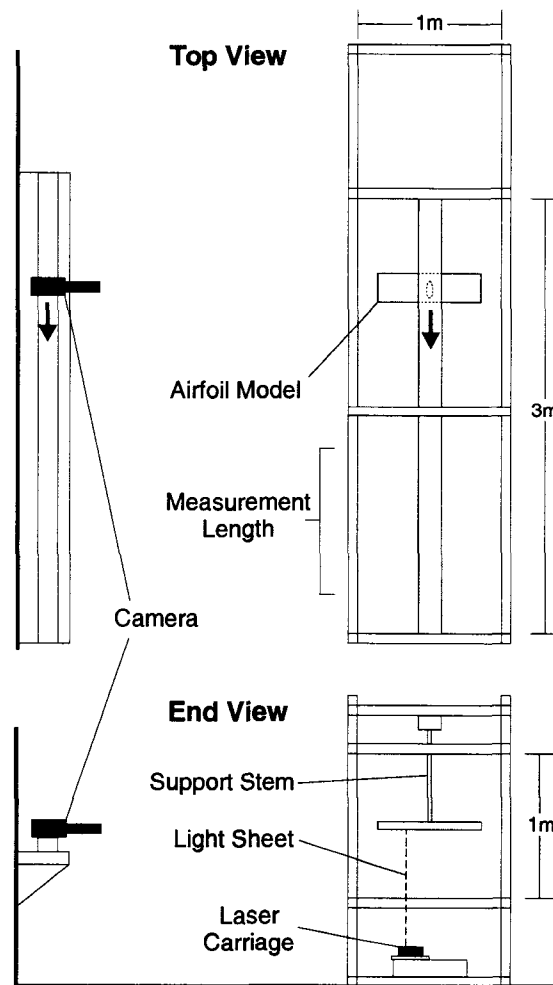


Figure 3.1: Schematic of low-Reynolds-number tow-tank facility

Glycerine is highly hygroscopic and the seal prevents infiltration of moisture from ambient air, ensuring constant and unchanging properties of the test medium. When glycerine is used as part of the working fluid, the model-insertion portion of the tank is also sealed by means of a door. Figure 3.2 shows a photograph of the facility with various components of the system labelled. Greater detail regarding the facility development is presented in a North Atlantic Treaty Organization (NATO) Research and Technology Organization (RTO) technical report (Hanff, 2006).

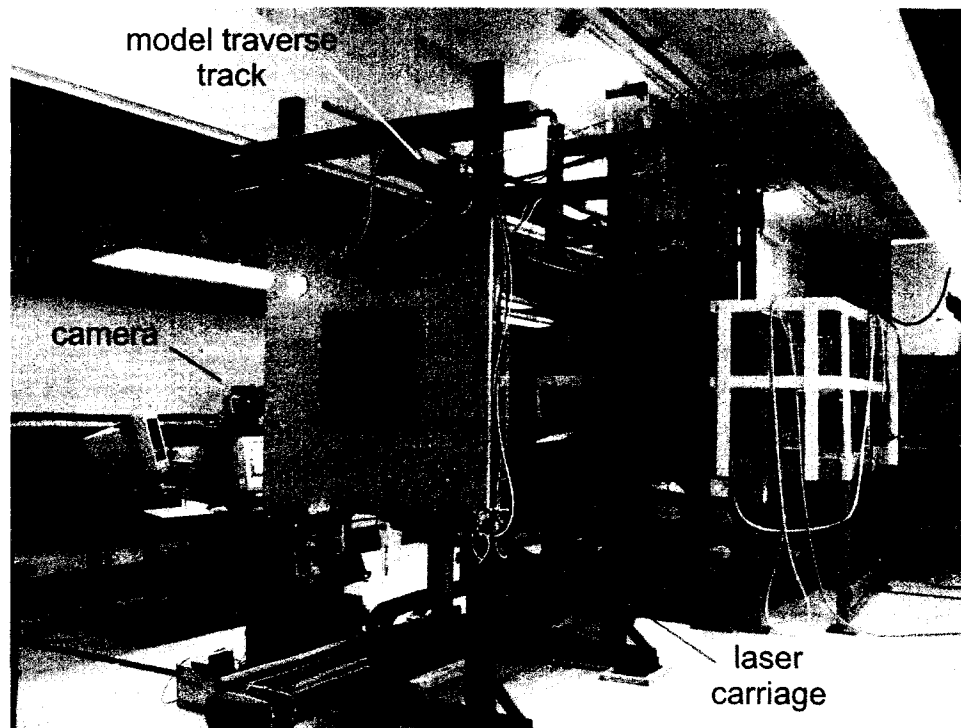


Figure 3.2: Photograph of low-Reynolds-number tow-tank facility

Apart from the low-Reynolds-number advantage, another major advantage of the NRC facility over conventional wind or water tunnels is the excellent “inflow quality” due to the stagnant freestream conditions, namely 0% freestream turbulence intensity and zero end-wall boundary-layer blockage. Also, the roof of the tank prevents the effects associated with a free surface.

This pilot facility has been a test-bed for developing a larger-scale facility with a 25 m working length, which is currently under construction. Initially, detailed experiments such as those presented in this thesis were not planned for the pilot facility because of its relatively short working length. However, after some initial development work it was realized that the tow tank had sufficient length for the required measurements. The only major disadvantage of the short working length is the short measurement window within which the airfoil is operating at “steady-state” (≈ 1 m). Overcoming this limitation requires many

measurement runs to collect sufficient data for statistical averaging. Between measurement runs, the working fluid must return to a stagnant condition before collecting more data. The settling time between runs is approximately 10 minutes, and was determined by examining the temporal decay of wake turbulence after returning the airfoil model to its start position.

3.2.2 Airfoil Models

Two airfoil models have been studied in the NRC facility. The first, described in Section 3.2.2.1, was used to examine the effectiveness of studying separation-bubble transition in the facility. The second, described in Section 3.2.2.2, was designed for the purpose of studying passive control of transition in a separation bubble.

3.2.2.1 SD7003 Low-Reynolds-Number Airfoil

The first study performed in the NRC facility used a low-Reynolds-number airfoil that has been the focus of an international collaborative research program initiated to study the behaviour of Micro Air Vehicles (Hanff, 2006). The model geometry is that of the SD7003 airfoil (Selig, 1995), which is documented to have a suction-surface separation bubble present over much of its low-Reynolds-number operating range ($Re < 100,000$). A schematic of the airfoil is given in Figure 3.3.

The SD7003 test model is a two-dimensional wing with a chord length of 20.3 cm and an aspect ratio of 3.6, spanning the middle 72% portion of the tank. It has been manufactured

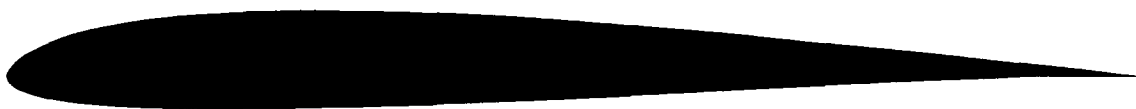


Figure 3.3: Schematic of the SD7003 airfoil

in two sections and is made of stainless steel to prevent corrosion issues. Although the airfoil has a small aspect ratio, two-dimensional flow has been documented over much of the airfoil suction surface. While the geometry of the airfoil differs from a typical turbomachinery blade, this does not diminish the relevance of the present study to turbomachinery design since its focus is on the details of the transition process in a separated shear layer. The results of the study are applicable to a variety of low-Reynolds-number airfoils including those used for turbomachinery blades, for the control surfaces of aircraft, and for the wings of unmanned aircraft.

3.2.2.2 Airfoil with Curved Backward-Facing Suction-Side Ramp

The main disadvantage of using conventional airfoils for a parametric flow-control study of separation-bubble transition is the streamwise movement of the separation location with variations in operating conditions. This has been observed for the SD7003 airfoil, as will be shown in Chapter 6. An unconventional airfoil has been designed to alleviate this problem while still providing a pressure distribution consistent with those observed over airfoils for which laminar separation bubbles are common. A schematic of the unconventional airfoil is provided in Figure 3.4 and details regarding its development and design are discussed in Chapter 8, Section 8.2. Since the airfoil has a thick cross-section relative to the SD7003 test model, the use of stainless steel for its manufacture was precluded, as the inertial forces on the traverse motors and the mounting stem would exceed their specifications. The airfoil

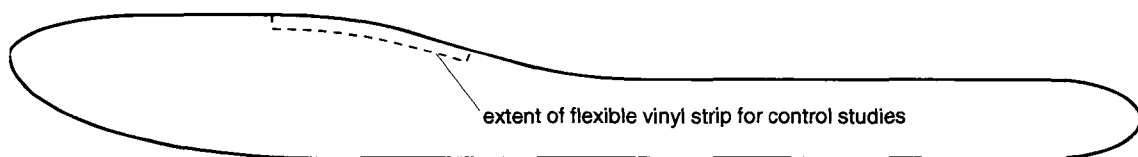


Figure 3.4: Schematic of the unconventional airfoil

was instead manufactured from a machinable fibreglass material (Green Glass G-10). The surface geometry and engineering drawings are provided in Appendix B.

The test model is two-dimensional, with a chord length of 25 cm and an aspect ratio of 3.0, spanning the middle 76% portion of the tank. Despite the low aspect ratio, the low level of lift produced by the airfoil at the tested angle-of-attack provides a large spanwise extent over which the flow is two-dimensional.

The flow control study described in Chapter 9 makes use of two-dimensional surface modifications to the airfoil in the vicinity of separation. The geometry of the surface modifications are provided in Chapter 9, Section 9.2. The recessed surface modifications were machined into thin, flexible vinyl strips 47 mm wide and 3.2 mm thick, which were then mounted in a matching groove machined into the airfoil surface, shown with dashed lines in Figure 3.4. One of the modifications consists of a surface protrusion which is made of the same vinyl material and mounted on the airfoil surface. The vinyl strips inserted into the groove on the airfoil were mounted using a combination of Crazy Glue and multiple layers of 3M water-resistant double-sided tape. Along the leading and trailing edges of the strips, plasticine was inserted in the small-gaps and much care was taken to ensure a continuously smooth surface.

3.2.3 Instrumentation

Particle image velocimetry (PIV) is used as the primary measurement technique in the NRC facility. A background to the theory of PIV measurement techniques and its practical implementation are provided in Appendix A. Two different LaVision Flowmaster PIV systems have been used during the experiments, each consisting of a data acquisition computer with a programmable timing unit (PTU), a set of two Nd:Yag lasers, and a digital CCD camera. The PTU provides synchronization between the lasers, the camera, and the

data acquisition system. Both systems were used in a two-frame cross-correlation mode, and Table 3.1 provides basic characteristics of the two systems, the details of which are discussed in the following. System 1 was that used for the SD7003 experiments presented in Chapter 6 and System 2 was that used for the experiments with the unconventional airfoil presented in Chapters 8 and 9.

Most currently-available PIV systems have low sampling rates such as those identified in Table 3.1, primarily due to limitations of the Nd:Yag lasers. This is the limiting factor for System 2. The factor limiting the sampling rate of System 1 is the time required for the camera to download the image data to the computer, which in full-frame mode is approximately 0.25 s. However, the sampling rate was increased to 7.5 Hz by utilizing only a portion of the camera's CCD sensor, effectively decreasing the total measurement time by almost a factor of 2 over the measurement time in full-frame mode. For the measurements presented in Chapter 6, the image resolution was reduced to 1280×480 pixels which was still sufficient to capture the shear layer developing over the airfoil surface. Although the CCD sensor for System 2 has a greater number of pixels, it is physically larger than that

Table 3.1: Details and components of the LaVision Flowmaster PIV systems

	System 1	System 2
Processor	Dual <i>Intel Pentium 2</i>	Dual <i>Intel Xeon</i>
RAM	256 MB	1 GB
Lasers	<i>New Wave</i> Nd:Yag	<i>Big Sky</i> Nd:Yag
Camera Resolution	1280×1000 pixels	1600×1200 pixels
Lens	<i>Nikon</i> 150-300mm zoom	<i>Nikon</i> 300mm
Sampling Rate	4 Hz / 7.5 Hz	14.8 Hz
Maximum Samples per Run	45	83

for System 1 and both provide almost identical spatial resolution in the captured images ($\approx 14,400$ pixel/m for the current experiments). As a note, fast-response PIV systems with sampling rates on the order of 1 kHz are becoming available as a result of new laser technology. However, these systems are much more expensive than their Nd:Yag counterparts and have issues related to reduced illumination of the seeding particles, with an associated uncertainty in the processed data.

DANTEC 20- μm polyamide particles have been used as the seeding material for the experiments, which result in particle-image diameters of approximately 2-4 pixels. The seeding particles are almost neutrally buoyant with a specific gravity of 1.03, which ensures that they closely follow the motion of the fluid.

3.2.4 Camera-Model Tracking-Error Correction

As a result of small vibrations of the camera-lens assembly combined with the notable distance between the camera traverse system and the tow-tank (see Figure 3.1), image-to-image variations in the location of the airfoil could not be neglected. The error introduced by this jitter is on the order of the freestream particle displacements between two sequential images in any image pair. If not corrected for, this level of error would prevent a quantitative analysis of the PIV results. To correct for this error, a fixture containing light-emitting diodes (LEDs) is placed in a cavity inside the wing. Figure 3.5 shows a picture of the four-LED version of the fixture used for the SD7003 experiments. An eight-LED version has been used in the unconventional-airfoil experiments. The cavity in which the fixture is placed is open at the side of the wing allowing the camera to capture the image of the LEDs, whose spanwise location is coincident with the focus plane of the lens. A mask with an orifice of approximately 10 μm diameter is placed over each LED, providing a marker of approximately 10 pixel diameter in the PIV images. For each measurement region examined,

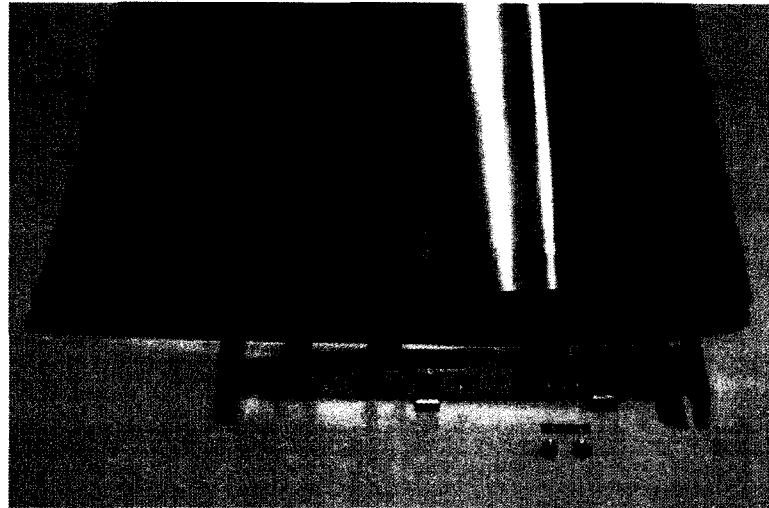


Figure 3.5: Marker fixture with forward second LED mask removed

two markers are selected as reference and a marker identification algorithm is used to locate the centroids of these markers within each image. From these marker-centroid locations, displacement and rotation corrections are performed to align the markers with a reference image. These algorithms are described in Chapter 5, Section 5.2.1. As a result of non-uniformity in the marker intensity distributions, uncertainty in the location of the airfoil in the corrected images is approximately 0.5 pixels.

3.2.5 Measurement Procedures

During the experiments, the motion system was controlled by a technician, and the data acquisition system was controlled by the author. Due to the short working length of the tow tank, quick acceleration to the model operating speed was required to ensure that the shear layers over the airfoil surface reach a “steady-state” condition prior to data acquisition. By “steady-state,” it is implied that the ensemble-averaged statistics of the flow over the airfoil are unaffected by the period during which the measurements are made, and are therefore stationary and ergodic (Tennekes and Lumley, 1972). Based on an estimate of the time-

to-“steady-state” for a laminar boundary layer, using an analytical solution described by Schlichting and Gersten (2000), the shear layers developing over the airfoil models were expected to reach “steady-state” during the first half of each measurement run. This was subsequently confirmed through a running-average analysis of the PIV measurements in the separated shear layers. The typical acceleration at the start of a measurement run was 0.5 m/s^2 , which ensures that for the highest towing speed examined ($\approx 0.36 \text{ m/s}$) the airfoil reaches the towing speed within 0.72 s, which corresponds to a distance of 0.13 m ($\approx 1/2$ of the unconventional-airfoil chord length). The same level of deceleration was used at the end of each measurement run. After each measurement run, the model was immediately returned to its start position and a minimum waiting time of ten minutes was required to allow the water in the tank to settle.

Data acquisition with the PIV system was initiated once the airfoil passed the structural member at the mid-portion of the tank (see Figures 3.1 and 3.2). This provided approximately 1 m of length over which measurements could be made. Depending on the PIV system used and the Reynolds number examined, anywhere from 24 to 83 image pairs could be captured during a measurement run. The lower limit represents the experiments using System 1 at the highest towing speed examined, whereas the upper limit represents the maximum number of images that could be captured by System 2 system during a measurement run constrained by random-access-memory (RAM) restrictions.

For each test case, multiple overlapping regions were examined over the suction surface of the airfoils. This was done in order to achieve adequate spatial resolution of the shear layer. The measurement regions, which are shown in Figure 3.6 for the two airfoils, were selected such that they provided overlap between adjacent regions, that they captured at least two markers within each image, and that the overall measurement time is minimized.

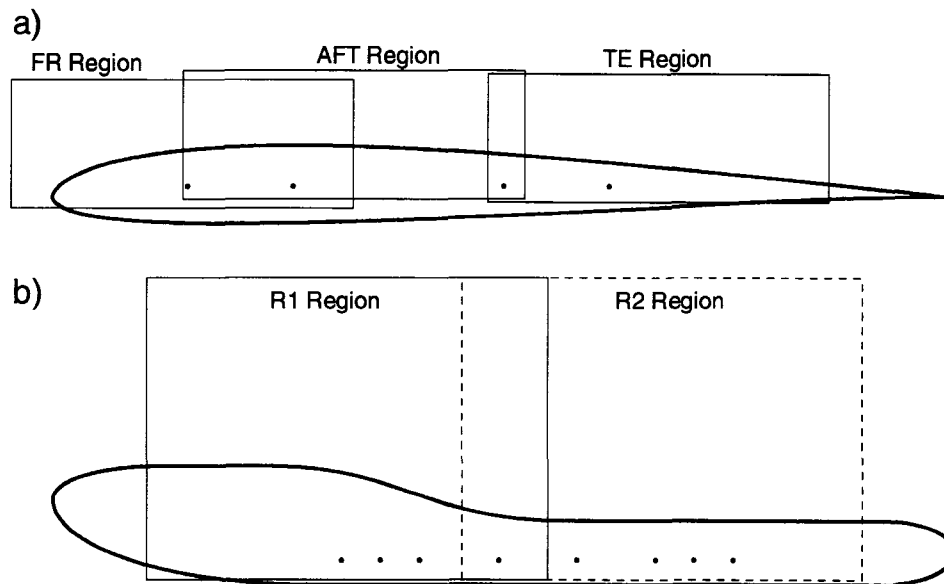


Figure 3.6: PIV measurement regions for a) the SD7003 airfoil and b) the unconventional airfoil (LED marker locations identified in body of airfoils)

3.2.6 Operating Conditions

The operating conditions examined for the two PIV studies are provided in Table 3.2, which includes the Reynolds number, angle-of-attack, towing speed, and time between laser pulses. For each of these operating conditions, the number of measurement regions examined, the number of measurement runs required, the number of image-pairs acquired during each run, the total measurement time, and the required data storage capacities are also identified in Table 3.2. The number of configurations for each operating condition is identified in Table 3.2 to indicate that multiple flow-control configurations were examined with the unconventional airfoil. The noted measurement times assume a waiting time between runs of 11 minutes, as this is an average of the actual waiting time during the experiments. The storage capacities are based on the image-pair file sizes, which for the SD7003 experiments was 4 MB/file and for the unconventional-airfoil experiments was

Table 3.2: Operating conditions and measurement details for each experimental test case

Case	Re	α [°]	U_∞ [m/s]	Δt [ms]	Regions	Runs	Samples/Run	Meas. Time [hr]	Storage [GB]	Configs
R40 α 8	40,000	8	0.1793	2.25	3	27	40	14.6	13	1
R40 α 10	40,000	10	0.1793	2.25	2	14,25 [†]	42	7.2	7	1
R65 α 4	65,000	4	0.2967	1.5	3	27,44 [†]	24	17.2	9	1
R28	28,000	-0.4	0.1008	10.5	2	10	83	3.7	20	6
R39	39,000	-0.4	0.1412	7.5	2	10	83	3.7	20	6
R51	51,000	-0.4	0.1816	5.8	2	10	83	3.7	20	6
R101	101,000	-0.4	0.3630	2.9	2	8	40	2.8	8	6

[†] number of runs is dependent on number of image pairs acquired for a given region

12 MB/file. The total measurement times required for the studies were 39 hr and 83 hr for the SD7003 and the unconventional-airfoil experiments, respectively. This however does not include the time required for setup and daily preparation, as well as the time taken for identifying the conditions to examine. The times allocated to final measurement runs identified in Table 3.2 were approximately one-third of the total time spent for each experimental test case.

3.3 Carleton University Facility

Experimental results from wind-tunnel tests performed prior to the current research have been used for validation of the numerical simulations. This section briefly describes the experimental facility and measurement system used for these measurements. Greater detail regarding this facility and the experiments performed therein are provided in the thesis of Roberts (2005).

3.3.1 Wind Tunnel

Over the past decade, numerous experiments on attached- and separated-flow transition have been performed in a closed-circuit wind-tunnel at Carleton University. The measurements of interest were performed using hot-wire anemometry over a flat-plate test surface of 1220 mm length and 762 mm width, in a test section of 1830 mm length, 762 mm width and 508 mm height. Streamwise pressure gradients were imposed on the test surface using a contoured wall that forms the ceiling of the test section. The test cases used for the present research have a streamwise pressure distribution similar to that encountered over the suction surface of a low-pressure-turbine airfoil, for which a separation bubble forms in a region of adverse pressure gradient. A schematic of the test section is shown in Figure 3.7. The level of freestream turbulence was increased in the wind tunnel by means of passive

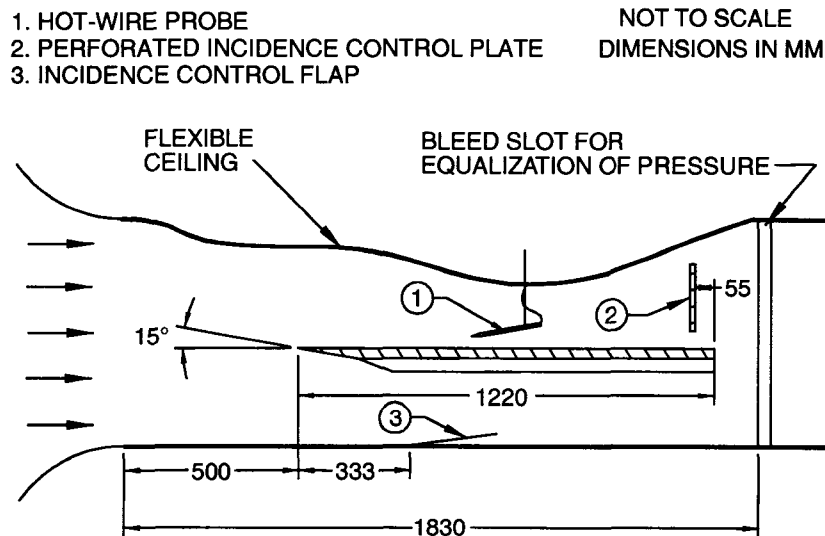


Figure 3.7: Schematic of Carleton University closed-circuit wind-tunnel test section

turbulence-generating grids, providing various freestream turbulence intensities in the range 0.5% to 9% at the test-plate leading edge.

3.3.2 Instrumentation

Boundary-layer measurements were made at mid-span of the test surface using a hot-wire probe with a single tungsten sensor of $5\ \mu\text{m}$ diameter and 1.3 mm length. The separation bubble and the upstream and downstream boundary layers were measured through wall-normal traverses at multiple streamwise locations, complemented by streamwise traverses performed within the separation-bubble region.

Calibration of the hot-wire was performed for a velocity range of 0 to 18 m/s using a 9th-order polynomial curve fit and was regularly verified to account for slight drifts in the output of the anemometer signal-conditioning circuitry. Uncertainty in the measured velocity has been estimated by Roberts (2005) to be $\pm 2\%$ of the local velocity except for small velocity magnitudes near the wall ($< 0.5\ \text{m/s}$) for which the uncertainty is estimated to

be $\pm 4\%$. Compensation for temperature drifts were also accounted for in the measurements using the method of Bearman (1971).

The anemometer output was sampled using an Analog Devices RTI834-H data acquisition system with a sampling rate of 8 kHz. The data was low-pass filtered at 3.8 kHz prior to A/D conversion. At each measurement location, 20 sets of 8192 samples were collected.

Chapter 4

Computational Setup and Procedures

4.1 Chapter Overview

As noted in the introduction and literature review chapters, recent advancements in computational power have permitted the use of direct numerical simulation (DNS) for studying transitional flows at Reynolds numbers typical of those encountered in the low-pressure turbine of gas turbine engines. This chapter documents the simulations performed during the present research, for which the ANSYS-CFX commercial software package was used. Section 4.2 presents the governing equations that are solved in the simulations, and Section 4.3 provides details of the numerical techniques implemented in the ANSYS-CFX solver. Descriptions of the computational setup for the present simulations are provided in Section 4.4.

4.2 Governing Equations

The major benefit of DNS is the ability to capture all the dominant spatial and temporal scales of a flow, without the use of modelling assumptions for sub-grid turbulence. Therefore, only solutions of the time-dependent continuity and Navier-Stokes equations, which govern the physics of the flow of interest, are required.

For the present simulations, the Mach numbers are sufficiently low ($M \approx 0.02$) that the incompressible form of the continuity and Navier-Stokes equations can be solved without use of the energy equation. Constant fluid properties can also be assumed such that modelling of the density, ρ , and dynamic viscosity, μ , is not required. The incompressible, time-dependent form of the continuity and Navier-Stokes equations are:

$$\frac{\partial}{\partial x_j}(\rho u_j) = 0 \quad (4.1)$$

$$\frac{\partial}{\partial t}(\rho u_i) + \frac{\partial}{\partial x_j}(\rho u_j u_i) = -\frac{\partial p}{\partial x_i} + \frac{\partial}{\partial x_j} \left[\mu \left(\frac{\partial u_i}{\partial x_j} + \frac{\partial u_j}{\partial x_i} \right) \right] \quad (4.2)$$

The ANSYS-CFX solver uses a finite-volume approach to solve the above equations. Integrating these equations over a control volume and using Gauss' divergence theorem for converting volume integrals into surface integrals, Equations 4.1 and 4.2 become:

$$\int_S \rho u_j dn_j = 0 \quad (4.3)$$

$$\frac{d}{dt} \int_V \rho u_i dV + \int_S \rho u_j u_i dn_j = - \int_S p dn_i + \int_S \mu \left(\frac{\partial u_i}{\partial x_j} + \frac{\partial u_j}{\partial x_i} \right) dn_j \quad (4.4)$$

where S and V represent the surface and volume regions of integration, respectively, and dn_j denotes the outward-normal surface vectors associated with each integration surface.

4.3 Solution Method

4.3.1 Basic Methodology

ANSYS-CFX provides solutions of the governing equations using a coupled, unstructured, finite-volume method (ANSYS, 2004). Solution of the linearized equations is accelerated by use of an algebraic multigrid strategy. For the present simulations, which are time-dependent, the discretized forms of the governing equations are converged through multiple iterations within each time-step. The ANSYS-CFX User Manual (ANSYS, 2004) provides brief descriptions of the discretized equations and numerical techniques implemented in the code. Greater detail regarding the techniques and the derivations thereof are provided in the Theory Documentation Manual for CFX-TASCflow (AEA-Technology, 2001). ANSYS-CFX and CFX-TASCflow share the same discretization schemes and therefore the CFX-TASCflow Theory Documentation Manual, with its greater detail, is an informative source for understanding the numerical techniques implemented in the solver.

4.3.2 Discretization

Discretization of the volume-integral form of the governing equations (Equations 4.3 and 4.4) is performed by generating a finite volume for each of the nodes associated with the computational mesh. An example mesh is shown in Figure 4.1, which identifies the points, surfaces, and regions of importance for a given computational volume. A collocated-grid technique is used such that the solution variables (u , v , w , and p) are all stored at the

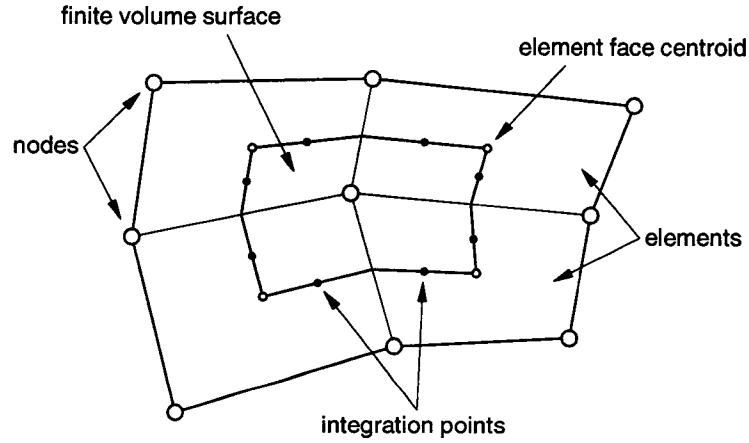


Figure 4.1: Two-dimensional representation of finite volume definition

nodes. The discretized forms of the governing equations are given as:

$$\sum_{ip} (\rho u_j \Delta n_j)_{ip} = 0 \quad (4.5)$$

$$V \frac{\Delta(\rho u_i)}{\Delta t} + \sum_{ip} \dot{m}_{ip} (u_i)_{ip} = \sum_{ip} (p \Delta n_i)_{ip} + \sum_{ip} \left[\mu \left(\frac{\partial u_i}{\partial x_j} + \frac{\partial u_j}{\partial x_i} \right) \Delta n_j \right]_{ip} \quad (4.6)$$

where V is the volume of the discrete control volume, Δt is the time step, Δn_j is the discrete outward surface vector, and ip denotes the integration points at the volume surfaces.

For the present simulations, the temporal derivative in Equation 4.6 is solved using the following second-order accurate formulation:

$$\frac{\Delta(\rho u_i)}{\Delta t} = \frac{1}{\Delta t} \left[\frac{3}{2} (\rho u_i)_t - 2 (\rho u_i)_{t-\Delta t} + \frac{1}{2} (\rho u_i)_{t-2\Delta t} \right] \quad (4.7)$$

which makes use of the two previous time-steps ($t - \Delta t$ and $t - 2\Delta t$).

The mass-flow term in Equation 4.6, \dot{m}_{ip} , is the mass flow rate through the control

volume surface associated with the particular integration point, and is defined as:

$$\dot{m}_{ip} = (\rho u_j \Delta n_j)_{ip}|_{t-\Delta t} \quad (4.8)$$

This mass flow rate is based on data from the previous time-step. For an unsteady solution, such as those performed in this work, this mass flow term is based on the previous iteration within a time-step, thus linearizing the discretized equation. Therefore, as the solution converges within a time-step, the mass flow terms will tend towards the current time-step values.

For the purpose of evaluating the velocities and pressures at the volume integration points, finite-element-based shape functions are used. The variation of any variable ϕ within an element can be expressed as:

$$\phi = \sum_{n=1}^{N_{node}} N_n \phi_n \quad (4.9)$$

where N_n is the the shape function for node n and ϕ_n is the value of ϕ at node n . The shape functions used in the code are linear in terms of parametric element-based coordinates. The same shape functions are also used to calculate geometric properties, such as integration-point coordinates, within an element according to:

$$x = \sum_{n=1}^{N_{node}} N_n x_n \quad , \quad y = \sum_{n=1}^{N_{node}} N_n y_n \quad , \quad z = \sum_{n=1}^{N_{node}} N_n z_n \quad (4.10)$$

The velocities and pressures in the advection and pressure gradient terms in Equation 4.6 are evaluated using the shape functions according to a standard finite-element approach:

$$\phi_{ip} = \sum_n N_n(r_{ip}, s_{ip}, t_{ip}) \phi_n \quad (4.11)$$

where the summation is performed over all the shape functions for the element under consideration. In Equation 4.11 (r_{ip}, s_{ip}, t_{ip}) represents the element-based coordinates of the integration points. For the advection terms, Equation 4.11 represents a second-order central difference approximation.

The diffusion terms in Equation 4.6 are also evaluated using the shape functions. At a particular integration point, ip , the derivative of ϕ with respect to the coordinate direction x_i is given as:

$$\left. \frac{\partial \phi}{\partial x_i} \right|_{ip} = \sum_n \left. \frac{\partial N_n}{\partial x_i} \right|_{ip} \phi_n. \quad (4.12)$$

The continuity and momentum equations are a coupled set, and are solved simultaneously within each iteration of the solution. The coupling is performed through the continuity equation (Equation 4.5) using a formulation for the mass-carrying velocities derived from discrete forms of the momentum equation. These mass-carrying velocities are evaluated using the following expressions that make use of velocities and pressures at both the local integration point as well as the surrounding node locations:

$$u_j|_{ip} = \bar{u}_j|_{nodes} + f \left(\left. \frac{\partial p}{\partial x_j} \right|_{ip} - \left. \frac{\partial p}{\partial x_j} \right|_{nodes} \right) - c \cdot f \left(u_j|_{ip} - \bar{u}_j|_{nodes} \right)_{t-\Delta t} \quad (4.13)$$

where

$$f = \frac{d_{ip}}{1 - c \cdot d_{ip}}, \quad c = \frac{\rho}{\Delta t}, \quad \text{and} \quad d_{ip} = - \frac{V_{element}}{\sum_{element} |\dot{m}_{ip}| + 8\mu \frac{|\Delta n_{ip}|}{\Delta_{ip}}}$$

In the denominator of d_{ip} , the summation is performed for the absolute value of the mass flow rate through all integration points within the element. The term $|\Delta n_{ip}|/\Delta_{ip}$ represents the magnitude of the local surface vector divided by the distance across the element, normal to the local surface, and through the integration point location. Equation 4.13 shows that the mass-carrying velocities at the integration points are expressed as an average of the surrounding nodal velocities and adjusted by a redistribution of pressure gradients and

previous time-step velocities. The derivation of Equation 4.13 is provided in the CFX-TASCflow Theory Documentation Manual (AEA-Technology, 2001).

Using the mass-carrying integration-point velocities defined by Equation 4.13 in the continuity equation (Equation 4.5) provides a velocity-pressure coupling that permits use of a single-cell, un-staggered, collocated grid. These velocities are also used to evaluate the momentum-equation mass-flow terms, defined by Equation 4.8.

4.3.3 Solution Strategy

The discrete linearized forms for the continuity and momentum equations (Equations 4.5 and 4.6) are a set of coupled equations for the three components of velocity and the pressure, and can be cast in a matrix form as follows:

$$\sum_{nb_i} a_i^{nb} \phi_i = b_i \quad (4.14)$$

where

$$a_i^{nb} = \begin{bmatrix} a_{uu} & a_{uv} & a_{uw} & a_{up} \\ a_{vu} & a_{vv} & a_{vw} & a_{vp} \\ a_{wu} & a_{wv} & a_{ww} & a_{wp} \\ a_{pu} & a_{pv} & a_{pw} & a_{pp} \end{bmatrix}_i^{nb}, \quad \phi_i = \begin{bmatrix} u \\ v \\ w \\ p \end{bmatrix}_i, \quad b_i = \begin{bmatrix} b_u \\ b_v \\ b_w \\ b_p \end{bmatrix}_i$$

In Equation 4.14, i is the identifying number of the finite volume and nb represents the central node and all neighbouring nodes upon which the solution at i depends. The a and b matrices represent the equation coefficients for the left and right sides of the equation, respectively.

The linearized system of discrete equations, which includes Equation 4.14 for all nodes

in the simulation, can be represented by:

$$[A] [\phi] = [b] \quad (4.15)$$

This equation is solved iteratively within the ANSYS-CFX solver using an Incomplete Lower Upper (ILU) factorization technique. Starting with an approximate solution $[\phi^n]$, the solution is to be improved by a correction $[\phi']$ such that:

$$[\phi^{n+1}] = [\phi^n] + [\phi'] \quad (4.16)$$

Substitution of Equation 4.16 into Equation 4.15 provides the following equation representing the solution for the correction term:

$$[A] [\phi'] = [b] - [A] [\phi^n] \quad (4.17)$$

Iteration on the solution to this equation will reduce the correction term such that it tends towards zero and the actual solution of the discretized equations is approached. The right-hand-side of Equation 4.17 represents the residual of the governing equation in question, and is used as a criterion for assessing convergence of the solution.

To improve the performance and convergence rates of the solution algorithm, a multigrid technique is applied. This technique performs multiple solution passes on subsequently coarsened grids such that, during these passes, the larger-wavelength errors are reduced more efficiently on the coarser grids, while the iterations on the finer grid levels serve to efficiently dissipate the shorter-wavelength errors. An algebraic multigrid scheme which makes use of the Additive Correction Method (ACM) of Hutchinson and Raithby (1986) for coarse-grid equation-generation is used in the ANSYS-CFX solver. This technique has been documented to significantly improve the performance of the CFX-TASCflow solver (Raw, 1996).

The basic idea behind algebraic multigrid is to coarsen the computational grid primarily in the direction for which small-wavelength errors are quickly dissipated. The method provides an automated process for coarsening which compiles the finer grids into larger grids based on the relative strengths of the coefficients a_i multiplying the solution variables. In the ANSYS-CFX solver, the $a_{pp}|_i$ coefficient from the continuity equation is used by the coarsening algorithm which, according to Raw (1996), best represents the behaviour of the coupled set of equations.

The method used to generate the coarse-grid equations (ACM), is based on conservation principles such that it represents an agglomeration of fine grid volumes into larger virtual grid volumes. The coarsened-grid equations can then be cast in an identical form to those of the fine-grid equations such that their solution provides corrections to the fine-grid solutions and ensures that conservation is enforced for all grid levels. The mathematical details of this technique are not given here, but they can be found in the paper by Raw (1996) and in the CFX-TASCflow Theory Documentation Manual (AEA-Technology, 2001).

A fixed W-cycle is used for the multigrid strategy implemented in ANSYS-CFX, which is represented schematically in Figure 4.2. During each solver iteration, the solution results are first passed down to subsequently coarser grids. For these “restriction” passes, one solution sweep is performed on the set of equations for each grid level. A coarsening rate, defined as the ratio of fine mesh-to-coarse mesh volumes during a coarsening pass, between 9 and 13 is used after each of these steps, and is stopped once the number of coarse grid volumes is below 20. As the solution is passed back up to the finer grids, where three solution sweeps are performed for each of these “prolongation” passes, control is passed back to the next coarsest grid once before it is allowed to continue back up. This allows the solution to concentrate more on the coarser grids to reduce the large-wavelength errors. With more levels than those shown in Figure 4.2, the pattern is recursively repeated.

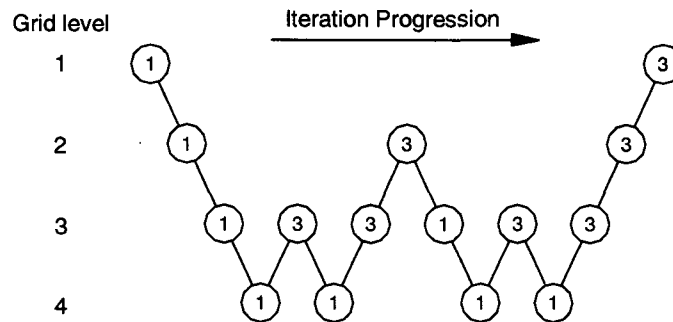


Figure 4.2: Schematic of W-cycle in ANSYS-CFX multigrid (integers represent number of solutions sweeps at the given level)

4.3.4 Parallel Processing

As direct numerical simulation is computationally expensive, given the large number of nodes, parallel processing was used to reduce the simulation time. Parallel processing is implemented by partitioning, or dividing, the computational domain into smaller partitions such that the solution for each partition is performed by a different processor (CPU). A master process, performed by a single processor, manages the flow of data to the slave processes and ensures solution-connectivity between them.

The ANSYS-CFX solver makes use of the automated MeTiS partitioning method, which is an open-source partitioning package based on the Multilevel Graph Partitioning Algorithm (ANSYS, 2004). Other partitioning algorithms are available in the solver, because the MeTiS method requires significant memory resources. However, the MeTiS method is recommended and was used for the present simulations. Parallel processing makes use of partition-overlap to provide connectivity between the different partition-solutions. For the present simulations, the level of overlap varied between 5% and 20%, depending on the domain region associated with a particular partition.

For the low-freestream-turbulence simulation, which has 1.2×10^6 nodes, a cluster of four

Intel Pentium 4 processors was used. For the elevated-freestream-turbulence simulation, which has 4.3×10^6 nodes, a cluster of six Intel Pentium 4 processors was used. For both simulations, 2 GB of RAM was dedicated to each processor.

4.4 Computational Setup

Two simulations have been performed to examine the nature of transition in separation bubbles under different levels of freestream turbulence intensity. The simulations are based on experimental test cases examined in the closed-circuit wind tunnel at Carleton University, described in Section 3.3. The low-freestream-turbulence simulation has been performed using version 5.7.1 of the ANSYS-CFX solver, and the elevated-freestream-turbulence simulation using version 10.0. Also, each simulation has used a different computational domain tailored for the specific case under consideration.

4.4.1 Computational Domains

4.4.1.1 Low-Freestream-Turbulence Domain

The computational domain for the low-freestream-turbulence simulation was selected to capture a separation bubble developing in a region of adverse pressure gradient over a flat plate with an imposed streamwise pressure distribution. To reduce the computational effort, experimental measurements were used as inlet conditions to the domain and therefore only the region from slightly upstream of the suction peak to downstream of the separation bubble was modelled. A schematic of the domain is shown in Figure 4.3. The domain width is 60 mm, and was selected based on the assumption that the transition process occurs through either the production, growth, and merging of turbulent spots, or breakdown of spanwise-oriented vortices resulting from the Kelvin-Helmholtz instability in the separated shear

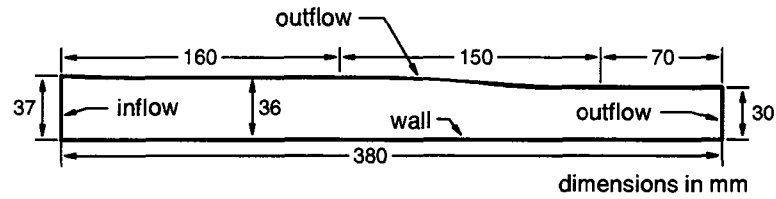


Figure 4.3: **Schematic of computational domain for the low-freestream-turbulence simulation**

layer. Based on the experimentally determined transition length, this width was selected by assuming that a turbulent spot generated at the experimental location of transition onset would span half the domain once it has convected to the experimental location of transition completion. As spanwise-periodic boundary conditions are applied to the domain, this would ensure minimal spanwise influence of a spot on itself through these boundaries. The boundary conditions are discussed in greater detail in Section 4.4.2. For the purpose of sizing the domain, the width of a turbulent spot was estimated based on Gostelow *et al.*'s correlation for the spot spreading angle (Equation 2.5 in Section 2.4, page 35). The domain inflow plane is located 0.4 m downstream of the test-plate leading edge. This location is slightly upstream of the suction peak, and therefore allows for the growth of instabilities in the adverse-pressure-gradient boundary layer prior to separation.

In the experimental setup upon which the simulation is based, the pressure distribution was imposed upon the flat test surface through the use of a contoured shape for the ceiling of the wind-tunnel test section. For computational efficiency, the computational domain does not extend up to this contoured ceiling in the y -axis direction. Instead, the upper boundary of the computational domain has been set to an outflow condition with a prescribed static pressure distribution (described in the section on boundary conditions, Section 4.4.2). The upper boundary was shaped such that fluid does not enter the domain through this boundary. This shaping was accomplished by first estimating the contraction

and expansion required by a wall-bounded domain based on the desired freestream velocity distribution, using a one-dimensional flow assumption. The surface shape selected for the upper domain boundary provides a greater contraction than that estimated by the one-dimensional flow assumption, ensuring no streamlines enter the upper domain surface. The upper surface shape consists of a series of streamwise-distributed polynomials and flat sections. The polynomial coefficients that define this upper domain boundary are provided in Appendix C. The slight contraction near the domain inlet prevents fluid from entering the domain as the freestream flow is accelerated prior to encountering the adverse pressure gradient at around $x = 0.45$ m (0.05 m into the domain). The second contraction is required as a result of reattachment of the separated shear layer to the surface. If not contracted, the quick reattachment that results from transition in the separated shear layer, where streamlines move closer to the surface, would cause inflow through the upper boundary.

4.4.1.2 Elevated-Freestream-Turbulence Domain

As with the low-freestream-turbulence simulation, the domain for the elevated-freestream-turbulence simulation is based on experimental measurements over a flat plate with an imposed streamwise pressure distribution. However, this simulation required physically-representative turbulence to prevail in the freestream flow. Initially, several ways of imposing freestream turbulence on the inlet-plane flow for the domain in Figure 4.3 were considered, including the use of random fluctuations imposed on the mean velocity, the use of a mathematical representation for isotropic turbulence superimposed on the mean flow, and the use of simulated turbulence from a separate simulation of grid-generated turbulence. This last method was attempted, however due to the mathematical nature of the subsonic inlet boundary condition applied in ANSYS-CFX, which allows only the specification of a velocity distribution. The solver was thus unable to resolve the small-scale pressure fluctuations associated with the turbulence. Based on the promising results from

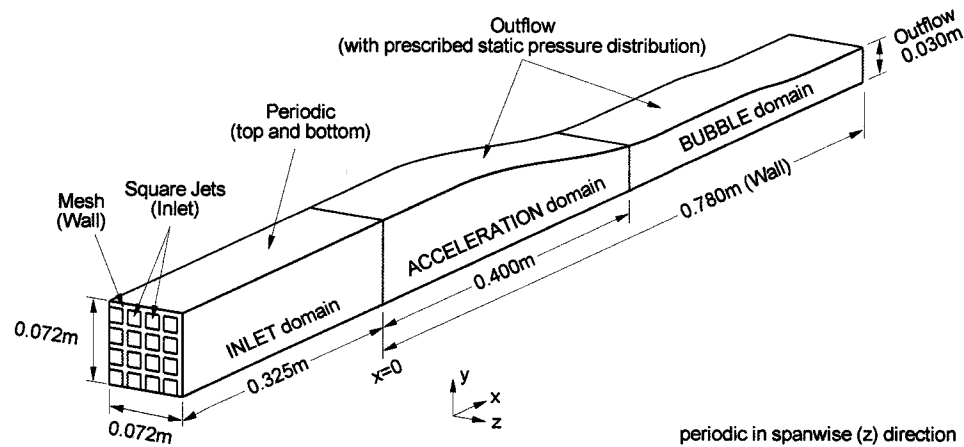


Figure 4.4: Schematic of computational domain for the elevated-freestream-turbulence simulation

the grid-generated-turbulence simulation, it was decided to extend the domain upstream to include an inlet plane representing the turbulence grid in the experiments, with a region for turbulence decay upstream of the flat plate, and with the entire flat plate up to the same outlet position as in the low-freestream-turbulence simulation. This computational domain is shown in Figure 4.4. The inlet plane of the domain consists of a 4×4 array of square openings that simulate a turbulence-generating grid used in the wind-tunnel experiments. These openings are 13 mm wide with a spacing of 18 mm.

The computational domain shown in Figure 4.4 consists of three sub-domains: the INLET domain, the ACCELERATION domain, and the BUBBLE domain. The ACCELERATION and BUBBLE domains extend over the wall region, and the INLET domain provides a region where the turbulence intensity can decay to the desired level near the flat-plate leading edge (approximately 5% turbulence intensity at $x = 0$). The shape of the upper domain boundary over the “wall” region was selected, as with the low-freestream-turbulence case, such that fluid should not enter these domains over the length of the flat plate. The acceleration required over the upstream portion of the flat plate

was the defining reason for the strong streamwise contraction of the ACCELERATION domain. Also, it was desired that the BUBBLE domain have approximately the same shape as the low-freestream-turbulence domain. The polynomials that define the upper domain surface are provided in Appendix C. The width of the domain is greater than that of the low-freestream-turbulence domain (72 mm as opposed to 60 mm) based on the geometric requirements for the square openings at the inlet plane of the computational domain.

4.4.2 Boundary Conditions

Many of the boundary conditions are similar between the two simulations. As the experimental test-section upon which the simulations are based has a much greater spanwise extent than the computational domains, periodic boundary conditions were imposed on the surfaces bounding the domain in the spanwise direction. The selected domain widths are sufficient to prevent the artificial influence of a given flow structure, such as a turbulent spot, by its periodic neighbour (effectively itself) through the periodic boundary.

The flat-plate test surface from the experiments has been simulated by applying a no-slip wall to the lower surface of the low-freestream-turbulence domain and the lower surfaces of the ACCELERATION and BUBBLE domains in the elevated-freestream-turbulence simulation.

An area-averaged constant static pressure condition was specified for the outflow boundary at the downstream end of the computational domains. The location of these boundaries was chosen such that the absence of a convective boundary condition, which allows transient flow structures to leave the domain with minimal deformation, does not affect the flow field within and immediately downstream of the region of interest.

Velocity-based inlet boundary conditions have been applied for both simulations. For the low-freestream-turbulence simulation, where the inlet is located 0.4 m downstream of

the flat-plate leading edge, an experimentally-measured wall-normal velocity profile has been used for the inflow condition (provided in Appendix C). The ANSYS-CFX solver linearly-interpolates the specified distribution over the computational mesh at the inlet plane. The freestream turbulence and laminar boundary layer fluctuations associated with this measured velocity profile were not explicitly imposed on the inflow and freestream boundaries of the computational domain. Instead, the simulated freestream turbulence of 0.1% intensity was allowed to develop through round-off errors associated with the finite-precision computations. In the experiments, the turbulence intensity in the freestream flow over the separation bubble was 0.7%. Based on earlier experimental studies (Yaras, 2002), the effect of this difference in freestream turbulence intensity on the transition process is expected to be small. The integral length scale associated with this simulated freestream turbulence is 20 mm, which is on the same order as the measured value of 40 mm. As well, the simulated freestream-turbulence frequency spectrum has a distribution similar to that of the experiment, albeit with a lower energy content.

The inflow boundary condition for the elevated-freestream-turbulence simulation consists of a 4×4 array of square, uniform-velocity jets of 13 mm width and 18 mm spacing to simulate the flow through a turbulence-generating grid that was used in the experiments. The jet velocity was set to 8.13 m/s which provides a mixed-out mean velocity of 4.24 m/s upstream of the plate leading edge. The leading edge of the flat-plate was placed 325 mm downstream of the inflow boundary. Over this streamwise distance, the simulated grid turbulence decayed to 5% intensity with an integral length scale of 7 mm, thereby approximating the conditions measured at the test plate leading-edge in the experiments. Over this initial turbulence-decay region, the computational domain is bounded in the y (wall-normal) and z (spanwise) directions by surfaces with periodic flow conditions.

In both simulations, a streamwise static pressure distribution was imposed on the upper surfaces of the domains with no-slip walls as their lower surfaces. This was done

through the use of an outflow boundary condition. As already noted, these upper domain surfaces were shaped such that fluid should not enter the domain over its length. The imposed pressure distributions for both simulation are provided in Figure 4.5, in pressure-coefficient form, with the actual discrete pressure distributions provided in Appendix C. These distributions were inferred by fitting polynomials through data from surface static-pressure measurements obtained from the experiments upon which the simulations are based. The pressure coefficient plotted in Figure 4.5 is defined as follows:

$$C_p = \frac{p - p_{sp}}{\frac{1}{2}\rho U_{x=0}^2} \quad (4.18)$$

where p_{sp} is the suction peak pressure and $U_{x=0}$ is a reference velocity at the leading edge of the flat plate. For the low-freestream-turbulence simulation, $U_{x=0}$ is inferred from the measurements upon which the simulation is based.

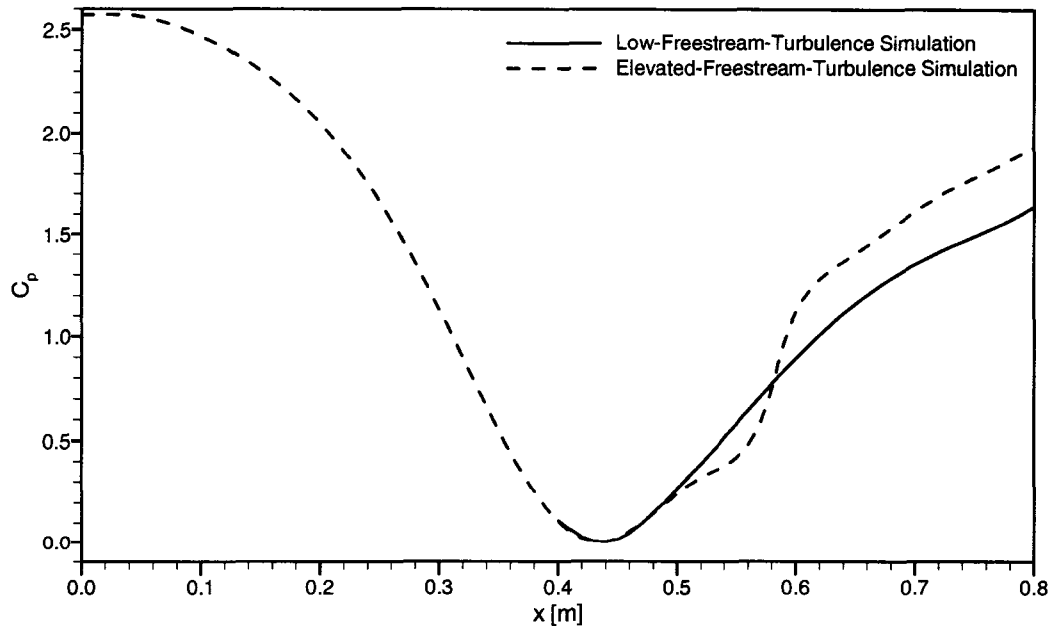


Figure 4.5: **Streamwise pressure distributions imposed on the upper domain boundaries for both simulations**

For the low-freestream-turbulence simulation, the effect of the separation bubble on the pressure distribution was not modelled, and the pressure distribution provides a smooth change in pressure gradient along the upper domain boundary. This decision was made because the effect of the bubble on the streamwise pressure distribution diminishes with increasing distance from the surface, and it was desired that the separation bubble result from an effective streamwise expansion of the simulated flow passage. This is similar to the approaches used by Ripley and Pauley (1993), Alam and Sandham (2000), and Marxen *et al.* (2003) in their simulations of separation bubbles, and has resulted in a separation bubble that closely resembles the experiments.

For the elevated-freestream-turbulence simulation, the use of a continual adverse pressure gradient over the separation-bubble region produced some numerical challenges due to the presence of freestream turbulence. Therefore, the effect of the separation bubble on the streamwise pressure distribution was modelled for this case. As the influence of the bubble diminishes with increasing distance from the surface, a combination of the surface pressure measurements and the shear-layer-edge velocity measurements were used to develop a streamwise pressure distribution that would better represent that at the upper domain boundary. This is the distribution shown in Figure 4.5.

4.4.3 Computational Meshes

The low-freestream-turbulence domain shown in Figure 4.3 was discretized using a structured grid of 381, 61, and 51 nodes in the streamwise, spanwise, and wall-normal directions, respectively (total of 1.2×10^6 nodes). Equal node spacing of 1 mm was used in the streamwise and spanwise directions, and the nodes were distributed with an expansion factor of 1.1 in the wall-normal direction. Based on the resulting turbulent boundary layer near the domain outlet, y^+ of the first node off the wall is about 0.6. The corresponding

Δx^+ and Δz^+ value is 24. A grid refinement study was performed, whereby the spanwise spacing was reduced to $\Delta z^+ = 16$, the streamwise spacing in the transition region was reduced to $\Delta x^+ = 12$, and the nodes were clustered towards the separated shear layer. This refinement did not yield any significant changes in the characteristics of the separation bubble.

For the elevated-freestream-turbulence domain shown in Figure 4.4, different node spacings and numbers were used in each of the sub-domains, with a total node count of 4.3×10^6 . At the interface between the ACCELERATION and BUBBLE domains, a one-to-one node correspondence was used, whereas the nodes on interface planes between the INLET and ACCELERATION domains do not match. This was done to maintain the rectilinear node distributions for the decaying turbulence in the INLET region while clustering the nodes towards the wall in the ACCELERATION domain where the boundary layer begins to grow. The ANSYS-CFX solver provides a means for interfacing two dissimilar mesh distributions by interpolating the results across the domains to conserve the flow properties. This interface is called a General Grid Interface (GGI) connection. The results were checked to ensure continuity in the flow properties across this interface.

The INLET sub-domain was discretized using 262, 57, and 57 nodes in the streamwise, spanwise, and wall-normal directions, respectively. Equal node spacing of 1.25 mm was used in the streamwise direction for the first 315 mm and a reduction factor of 0.977 was used in the last 10 mm to ensure minimal streamwise node-spacing discontinuity at the plate leading edge. A near-uniform node spacing of 1.263 mm was used in the transverse directions, with slight variations in spacing to conform to the boundaries of the jets at the inflow plane.

The ACCELERATION domain was discretized using 401, 73, and 59 nodes in the streamwise, spanwise, and wall-normal directions, respectively. Equal node spacing of 1 mm

was used in the streamwise and spanwise directions, and nodes in the wall-normal directions were clustered closer to the wall to ensure a sufficient number of nodes in the boundary layer.

The BUBBLE domain was discretized using 404, 73, and 59 nodes in the streamwise, spanwise, and wall-normal directions, respectively. The streamwise node spacing in the regions $0.40 \text{ m} < x < 0.55 \text{ m}$ and $0.64 \text{ m} < x < 0.78 \text{ m}$ was set to 1 mm, and was reduced to 0.75 mm in the region $0.576 \text{ m} < x < 0.626 \text{ m}$. Between these regions, a node-spacing stretch factor no greater than 2% was used. The wall-normal spacing was varied along the streamwise direction to ensure nodes were clustered within the shear layer. This variation in the wall-normal spacing distributions is evident in Figure 4.6 which shows the computational x - y mesh in the BUBBLE domain. The y -axis coordinate has been stretched in Figure 4.6 to allow better visualization of the node distributions.

For the elevated-freestream-turbulence simulation y^+ of the first node off the wall is about 0.5, based on the turbulent boundary layer near the domain outlet. The corresponding Δz^+ value is 19 and the Δx^+ value varies between 14 and 19 through the separation bubble region.

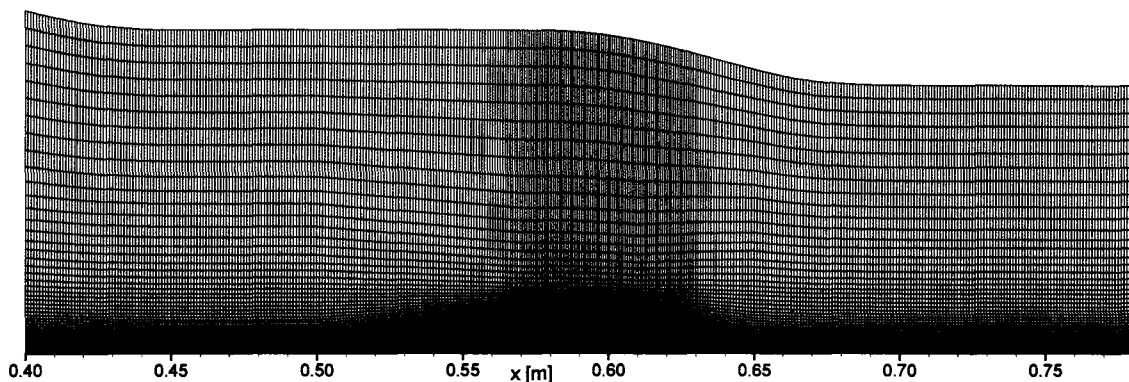


Figure 4.6: Computational $x - y$ mesh for BUBBLE sub-domain (3 \times stretching in y -direction)

Table 4.1: Node spacings used in DNS studies involving separation bubbles (all have $y_1^+ < 1$)

Simulation/Investigators	Δx^+	Δz^+
Low-Freestream-Turbulence	24	24
Elevated-Freestream-Turbulence	19	19
Na and Moin (1998)	18	11
Alam and Sandham (2000)	14,20	6
Michelassi <i>et al.</i> (2002)	10	3
Kalitzin (2003)	28	19

Table 4.1 provides the mesh spacings for the two present simulations in wall-coordinates, and compares them to the spacings in other published DNS studies involving separation bubbles. The streamwise node-spacings are comparable to the other studies and the spanwise spacing is slightly greater. However, the selected spatial resolution has been found to be adequate in resolving the transitional flow structures associated with the separation bubbles, as will be discussed in Chapter 7.

4.4.4 Simulation Time-Step and Duration

Time steps of 0.20 ms and 0.15 ms were used for the low- and elevated-freestream-turbulence simulations, respectively, which correspond to a Courant number ($U\Delta t/\Delta x$) in the separated shear layers of approximately 1.0. The simulations were started on two-dimensional grids with slip-walls replacing the no-slip walls to establish the freestream velocity and pressure fields, which were then used as initial conditions for the computations in the three-dimensional domains. With these initializations, the solutions reached a “steady-state” within approximately 2000 and 5600 time steps for the low- and elevated-

freestream turbulence simulations, respectively. Here, “steady-state” refers to the condition for which the large-scale properties of the separation bubble did not change. After reaching “steady-state”, the simulations were continued for another 2048 and 4100 time steps, respectively.

Averaging for the low-freestream-turbulence case was accomplished through spanwise and time averaging of data from five evenly-spaced $x - y$ planes over 2048 time steps. For the elevated-freestream-turbulence case, spanwise and time averaging was accomplished over the entire BUBBLE domain over 3200 time steps. Over these periods, running averages of the auto- and cross-correlation of velocity fluctuations within the transition regions show variation by no more than a few percent, providing confidence that the dominant physical aspects of the transition processes were captured.

4.4.5 Solution Convergence

Solutions of the continuity and momentum equations at each time step were converged within eight iterations such that the maximum residuals at the end of each time step were lower than 6×10^{-5} , except very near the inlet boundaries where the maximum residuals were on the order of 10^{-4} . RMS residual levels were on the order of 10^{-6} after each time step. As a check on the effects of convergence level on the simulation results, the elevated-freestream-turbulence simulation was restarted from an intermediate time step and continued for 300 time steps using 15 iterations within each time step. There were no significant differences in the solution after 300 time steps, providing further confidence in the results. The multigrid method implemented in ANSYS-CFX required 5 grid levels for the low-freestream-turbulence simulation (with 1.2×10^6 nodes on the finest grid) and 6 grid levels for the elevated-freestream-turbulence simulation (with 4.3×10^6 nodes on the finest grid).

The spatial and temporal resolutions described in the last section were chosen such that the turbulence scales in the turbulent boundary layer downstream of the separation bubbles are resolved down to about 35 times the Kolmogorov scale. Through comparison with experimental data, Chapter 7 shows this resolution to be adequate for capturing the turbulence associated with transition and reattachment of separated shear layers. The selected spatial and temporal resolutions are also consistent with recent direct numerical simulations involving separation bubbles, performed by other research groups (Na and Moin, 1998; Alam and Sandham, 2000; Kalitzin, 2003).

Chapter 5

Data Reduction Procedures

5.1 Chapter Overview

This chapter describes the data reduction procedures used for analysis of the experimental and computational results. Section 5.2 provides descriptions of the procedures used for reducing the experimental particle image velocimetry (PIV) measurements, along with estimates of the experimental uncertainties. The data reduction procedures for the direct numerical simulation (DNS) results are presented in Section 5.3.

5.2 Data Reduction of Experimental PIV Measurements

Of the experimental studies presented in this document, two sets of experimental measurements were performed during the research program. The first study, described in Chapter 6, was performed early in the program to assess the effectiveness of applying PIV in studying separation bubbles. The second was the last study performed during the program, described in Chapters 8 and 9, approximately two years after the first, and

utilized a different PIV system, with variations in the analysis procedures. Section 3.2.3 has already described the two PIV systems used; each uses a variant of the LaVision DaVis data reduction software (versions 6 and 7, respectively). This software was used to perform the image corrections required as a result of the relative motions between the camera and model, and to evaluate the image data, from which particle displacement vectors were extracted. The extracted particle displacement fields were then analyzed using custom data reduction programs developed specifically for the respective studies.

In the following, the image correction algorithm is first described (Section 5.2.1), followed by descriptions of the image analysis procedures (Section 5.2.2), the post-processing data reduction procedures (Sections 5.2.3 through 5.2.5), and the uncertainty estimates analysis (Section 5.2.6).

5.2.1 Image Correction Algorithms

As noted in Section 3.2.4, image-to-image variations in the location of the airfoil model are caused by small vibrations of the camera-lens assembly combined with the notable distance between the camera traverse system and the tow-tank. If unaccounted for, errors in the particle-displacement vectors would be on the order of the true freestream particle displacements and would therefore negate the use of the reduced data for reliable statistical analysis. Section 3.2.4 described a marker fixture that is mounted inside the models and provides a reference from which corrections can be made to align all measurement images. The markers consist of light-emitting-diodes (LEDs) over which masks are placed. These masks have an orifice of approximately 10 μm diameter, such that the light permitted through the mask provides a marker in the image with a diameter of approximately 10 pixels. At least two markers were active for each measurement region examined.

The intensity distribution of each marker peaks at its centroid, and identification of this centroid is required for performing the image corrections. Identification of a marker centroid is accomplished through an intensity-weighted average of the spatial coordinates, as follows:

$$X_c = \frac{1}{\bar{I}'} \sum_{i=X_{\min}}^{X_{\max}} \sum_{j=Y_{\min}}^{Y_{\max}} X(i, j) I'(i, j) \quad (5.1a)$$

$$Y_c = \frac{1}{\bar{I}'} \sum_{i=X_{\min}}^{X_{\max}} \sum_{j=Y_{\min}}^{Y_{\max}} Y(i, j) I'(i, j) \quad (5.1b)$$

where

$$\bar{I}' = \sum_{i=X_{\min}}^{X_{\max}} \sum_{j=Y_{\min}}^{Y_{\max}} I'(i, j) \quad (5.2)$$

and $(X_{\min} : X_{\max}, Y_{\min} : Y_{\max})$ defines the search-area over which the averaging is performed, in pixel coordinates. In Equations 5.1 and 5.2, $I'(i, j)$ is defined as:

$$I'(i, j) = \begin{cases} 0 & \text{if } I(i, j) < I_{\text{thresh}} \\ I(i, j) & \text{if } I(i, j) \geq I_{\text{thresh}} \end{cases} \quad (5.3)$$

to filter any background noise in the images. Although typical background noise associated with the CCD sensors is below an intensity value of 100 (total dynamic range is 4096), a threshold value of 500 was used as reflections from particles near the marker generally provide a wide, non-uniform intensity distribution around the marker.

Once the locations of two markers in an image are known, the intensity distribution can be shifted and rotated to align the marker centroids with those of a reference image. For the SD7003 experiments in Chapter 6, the reference marker locations were selected by averaging the centroid locations calculated from all images in the first measurement run (typically 20-40 image pairs). For the experiments conducted with the unconventional

airfoil (documented in Chapters 8 and 9), the reference locations were selected such that once corrected, the images were oriented to coincide with the airfoil coordinate system. That is, the X -direction has been aligned with the flat sections over the upper and lower surfaces of the airfoil.

Three coordinate parameters are required to align each image with the reference. These are the X and Y coordinates of one marker, and the angle of the line that connects the two markers in an image, θ . This angle is defined as:

$$\theta = \tan^{-1} \left(\frac{Y_2 - Y_1}{X_2 - X_1} \right) \quad (5.4)$$

where subscripts 1 and 2 represent the respective markers. The following coordinate transformation can then be used to align the image with the reference image:

$$X' = X_{ref} + (X - X_{c1}) \cdot \cos(\theta_{ref} - \theta) - (Y - Y_{c1}) \cdot \sin(\theta_{ref} - \theta) \quad (5.5a)$$

$$Y' = Y_{ref} + (Y - Y_{c1}) \cdot \cos(\theta_{ref} - \theta) + (X - X_{c1}) \cdot \sin(\theta_{ref} - \theta) \quad (5.5b)$$

In the above equations, X_{ref} , Y_{ref} , and θ_{ref} represent the coordinates in the reference image to which the marker #1 location will coincide and the angle to which the marker connecting-line will be oriented.

To maintain sub-pixel accuracy in the PIV image analysis procedure, discussed in the next section, the transformation of the image intensity distribution is done such that the intensity centroid of a shifted pixel is placed at the correct sub-pixel location in the transformed image. This is accomplished by “smearing” the original pixel intensity over the four surrounding pixels in the transformed image. The intensity at each of the surrounding

pixels is given in terms of the original unshifted pixel intensity, I_O , by:

$$I(X^-, Y^-) = (X^+ - X)(Y^+ - Y)I_O \quad (5.6a)$$

$$I(X^+, Y^-) = (X - X^-)(Y^+ - Y)I_O \quad (5.6b)$$

$$I(X^-, Y^+) = (X^+ - X)(Y - Y^-)I_O \quad (5.6c)$$

$$I(X^+, Y^+) = (X - X^-)(Y - Y^-)I_O \quad (5.6d)$$

where X and Y are the coordinates of the intensity centroid and the superscripts $+$ and $-$ denote the bounding integer values, representing the surrounding pixels.

The above-described image-correction algorithms were implemented in the LaVision DaVis software through user-defined macros. Predefined macros for image shifting and rotation were used, which perform the intensity-smearing algorithm defined in Equation 5.6.

5.2.2 Image Analysis

Particle-image analysis was performed using the LaVision DaVis software provided with the data acquisition systems. For the present experiments, a double-frame cross-correlation technique has been used to evaluate the pixel displacement fields for each image pair. Table 5.1 identifies important parameters for the analysis of each of the two experimental studies.

For the SD7003 experiments of Chapter 6, Version 6 of the DaVis software was used. Approximately 500 image pairs were collected in the *FR* region of the airfoil where the boundary layer remained laminar, and approximately 1000 image pairs were collected for the other measurement regions. The time between laser pulses was selected such that the freestream particle displacements for each image pair were approximately 8-10 pixels. To ensure adequate spatial resolution while maintaining minimal cross-correlation errors,

Table 5.1: Image analysis details for PIV measurements

Parameter	SD7003 Study	Unconventional-Airfoil Study
freestream particle displacements	8-10 pixels	15-20 pixels
final interrogation window size	16 × 16 pixels	32 × 32 pixels
final window overlap	75%	75%
final vector spacing	4 pixels (0.116% C)	8 pixels (0.222% C)
intermediate multigrid techniques	smoothing	smoothing
	filtering	filtering
	window deformation	image reconstruction

an iterative multigrid processing technique has been used, similar to that described by Scarano and Riethmuller (2000). For each image pair, three cross-correlation passes were first performed using 32×32 pixel interrogation windows with 75% overlap, followed by ten passes using 16×16 pixel windows with 75% overlap. Window deformation, intermediate smoothing, and intermediate filtering has been used to reduce errors in the particle-displacement vector fields. The final grid spacing is 4 pixels (0.116% of chord length), which results in at least ten velocity vectors across the transition region of the shear layer, in the wall-normal direction, for the three cases examined.

The suction surface of the SD7003 airfoil is curved, over which a stepped vector grid is produced by the PIV image analysis. This can be undesirable, particularly for the thin boundary layers that develop near the leading edge of the airfoil. To reduce errors associated with this stepping effect, sub-regions of the image pairs were extracted and rotated prior to processing such that the surface appears horizontal in the analyzed images. Figure 5.1 shows an example of the sub-regions used for the SD7003 experiments in the case for which

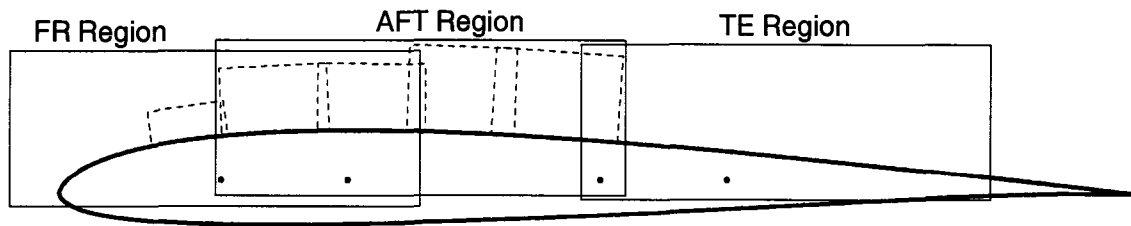


Figure 5.1: Sample sub-regions extracted for image analysis of SD7003-airfoil experiments (dashed lines indicate sub-regions used for $Re=40,000$, $\alpha=8^\circ$ conditions)

$Re=40,000$ and $\alpha=8^\circ$. For the unconventional-airfoil experiments, the images were aligned correctly to airfoil-coordinates during the image correction phase of the analysis, described in Section 5.2.1, and the airfoil was designed such that sub-region extraction is unnecessary since the curved ramp is located in the region of stagnant flow beneath the separated shear layer. The unconventional airfoil was also designed such that the boundary layer near separation is sufficiently thick at the desired Reynolds numbers that the stepping effect would not cause undesired uncertainty in the resulting vector fields and integrated boundary-layer parameters.

For the experiments with the unconventional airfoil presented in Chapters 8 and 9, approximately 300 PIV image pairs were collected for the highest Reynolds number (101,000) and approximately 500 image pairs were collected for the remaining three Reynolds numbers (28,000, 39,000, and 51,000). Initial checks were performed to ensure that the number of samples collected were sufficient for reliable statistical averaging. Version 7 of the DaVis software was used to evaluate the recorded image data. The time between laser pulses for these experiments was selected such that the freestream particle displacements for each image pair are approximately 15-20 pixels. This increased displacement, over that of the SD7003 experiments, was selected to ensure that the low-velocity flow in the reverse-flow region of the separation bubble was adequately captured as difficulties arose in capturing this

region for the previous SD7003 experiments. An iterative multigrid processing technique was also used for the new-airfoil experiments. For these experiments, approximately 50 image pairs were evaluated prior to detailed processing and the average of the resulting vector fields were then used as an initial condition for the detailed processing. Using the initial averaged vector field as a start, four cross-correlation passes were performed using 32×32 pixel interrogation windows with 75% overlap. A new feature in Version 7 of the DaVis software is an image reconstruction technique that replaces the window deformation technique used in Version 6, both of which are used to reduce errors associated with shear across an interrogation window. The image reconstruction technique uses the pixel displacement field from the previous evaluation pass to deform the second image of an image-pair such that its new particle image field closely matches that of the first image. This process reduces correlation-peak identification errors associated with large particle displacements and strong shear, and allows for quicker convergence of the correlation algorithm. The final vector spacing for the unconventional-airfoil experiments is 8 pixels (0.222% of chord length), which results in at least 5 velocity vectors across the shear layer at the location of transition onset for the highest Reynolds number tested, and at least 15 velocity vectors for the remaining three Reynolds numbers.

5.2.3 Displacement-Vector-Field Data Reduction

The result of the particle-image analysis discussed in the previous section is a particle displacement field representing the motion of the fluid during the time interval between laser pulses. Particle displacements $(\Delta x(x, y), \Delta y(x, y))$ are converted to velocities using the geometric scaling factor ($SF = \# \text{pixels/unit length}$) and the time delay between laser

pulses (Δt), as follows:

$$u(x, y) = \frac{\Delta x(x, y)}{SF \Delta t} \quad (5.7a)$$

$$v(x, y) = \frac{\Delta y(x, y)}{SF \Delta t} \quad (5.7b)$$

The geometric scaling factor, SF , has been evaluated based on the location of the LED markers in the image pairs. As the true locations of these markers are known *a priori*, both the image scaling and the true location of the airfoil in the images are readily assessed. For the purposes of the present study, the velocity magnitudes were reduced and normalized based on the airfoil towing speed, U_∞ . The actual form of Equation 5.7 used in the data reduction procedures, is as follows:

$$\frac{u}{U_\infty} = \frac{\Delta x}{SF_C \cdot C \cdot \Delta t \cdot U_\infty} \quad (5.8a)$$

$$\frac{v}{U_\infty} = \frac{\Delta y}{SF_C \cdot C \cdot \Delta t \cdot U_\infty} \quad (5.8b)$$

where C is the airfoil chord length and SF_C is the geometric scaling factor based on this chord length ($SF_C = \text{\#pixels}/C$).

Conversion of the displacement-vector locations from image coordinates (pixels) to airfoil coordinates ($x/C, y/C$) was accomplished using a similar transformation to that used for the image corrections described in Section 5.2.1. However, the geometric scaling factor SF_C is included to re-scale the vector locations:

$$\frac{x}{C} = \frac{x}{C} \Big|_{ref} + \frac{(X - X_{ref})}{SF_C} \cdot \cos(\theta) - \frac{(Y - Y_{ref})}{SF_C} \cdot \sin(\theta) \quad (5.9a)$$

$$\frac{y}{C} = \frac{y}{C} \Big|_{ref} + \frac{(Y - Y_{ref})}{SF_C} \cdot \cos(\theta) + \frac{(X - X_{ref})}{SF_C} \cdot \sin(\theta) \quad (5.9b)$$

where θ is the angle through which the rotation is to be performed, and *ref* refers to

a reference location that is known in both coordinate systems, typically an LED marker location.

If a rotation of the vector field is required, as it is for the SD7003 experiments, the velocity vector components are transformed into the new coordinate system orientation using the following:

$$\left. \frac{u}{U_\infty} \right|_{rotated} = \frac{u}{U_\infty} \cdot \cos(\theta) - \frac{v}{U_\infty} \cdot \sin(\theta) \quad (5.10a)$$

$$\left. \frac{v}{U_\infty} \right|_{rotated} = \frac{v}{U_\infty} \cdot \cos(\theta) + \frac{u}{U_\infty} \cdot \sin(\theta) \quad (5.10b)$$

5.2.4 Ensemble-Averaged Parameters

With the particle-displacement vectors converted to normalized velocity components, averaging was then performed on the reduced vector fields. Aliasing can be a problem when the sampling rate is much lower than the time scales of the flow. However due to the multiple measurement runs required to collect sufficient data for averaging purposes, the potential effects of aliasing are greatly reduced and have not caused any significant uncertainty in the resulting data. For the purpose of examining the flow-field and turbulence characteristics in the shear layers over the airfoils, ensemble averaging was performed to calculate the mean velocities and the velocity correlations associated with the turbulence Reynolds stresses. These parameters are defined as follows:

$$\langle u \rangle = \frac{1}{N} \sum_{i=1}^N u_i \quad (5.11)$$

$$\langle v \rangle = \frac{1}{N} \sum_{i=1}^N v_i \quad (5.12)$$

$$\langle U \rangle = \frac{1}{N} \sum_{i=1}^N \sqrt{u_i^2 + v_i^2} \quad (5.13)$$

$$\langle u'u' \rangle = \frac{1}{N} \sum_{i=1}^N (u_i - \langle u \rangle)^2 \quad (5.14)$$

$$\langle v'v' \rangle = \frac{1}{N} \sum_{i=1}^N (v_i - \langle v \rangle)^2 \quad (5.15)$$

$$\langle u'v' \rangle = \frac{1}{N} \sum_{i=1}^N (u_i - \langle u \rangle)(v_i - \langle v \rangle) \quad (5.16)$$

where N is the number of vector fields used in the averaging process. The RMS velocity was also calculated, according to:

$$U_{rms} = \sqrt{\frac{1}{N} \sum_{i=1}^N (U_i - \langle U \rangle)^2} \quad (5.17)$$

For the SD7003 experiments presented in Chapter 6, the streamwise and wall-normal fluctuations are presented in RMS form:

$$u_{rms} = \sqrt{\langle u'u' \rangle} \quad (5.18)$$

$$v_{rms} = \sqrt{\langle v'v' \rangle} \quad (5.19)$$

The above-identified definitions for the ensemble-averaged parameters require two passes of the data to complete the averaging process: one pass to calculate the mean values ($\langle u \rangle$, $\langle v \rangle$, and $\langle U \rangle$) and a second pass to calculate the RMS (U_{rms}) and fluctuation correlations ($\langle u'u' \rangle$, $\langle v'v' \rangle$, and $\langle u'v' \rangle$). As each vector field contains a large amount of information, it is computationally inefficient to read all of the data for a particular case into memory prior to processing. It is also inefficient to individually read each vector-field data file into memory twice for the procedure. Another form of Equations 5.14 through 5.17 can be formulated such that the data for each file can be read into a single array and replaced for each subsequent data file, thus requiring only one pass of the data. These forms, the proof

of which are not given, have been used in the data reduction procedures and are as follows:

$$\langle u'u' \rangle = \frac{1}{N} \sum_{i=1}^N u_i^2 - \langle u \rangle^2 \quad (5.20)$$

$$\langle v'v' \rangle = \frac{1}{N} \sum_{i=1}^N v_i^2 - \langle v \rangle^2 \quad (5.21)$$

$$\langle u'v' \rangle = \frac{1}{N} \sum_{i=1}^N u_i v_i - \langle u \rangle \langle v \rangle \quad (5.22)$$

$$U_{rms} = \sqrt{\frac{1}{N} \sum_{i=1}^N U_i^2 - \langle U \rangle^2} \quad (5.23)$$

A parameter that is useful in examining turbulent shear layers is the rate of production of turbulence kinetic energy, which takes its form from a specific term in the turbulence kinetic energy equation derived from the Navier-Stokes equations (White, 1991). For a two-dimensional shear layer developing in an $x - y$ plane, the production of turbulence kinetic energy can be described as the energy transfer facilitated by the $\langle u'v' \rangle$ Reynolds shear stress component through the strain rate, S_{xy} . This strain rate is defined as:

$$S_{xy} = \frac{1}{2} \left(\frac{\partial v}{\partial x} + \frac{\partial u}{\partial y} \right) \quad (5.24)$$

where the partial derivatives have been calculated using a second-order central-difference formulation:

$$\frac{\partial v}{\partial x}(x, y) = \frac{v(x + \Delta x, y) - v(x - \Delta x, y)}{2\Delta x} \quad (5.25a)$$

$$\frac{\partial u}{\partial y}(x, y) = \frac{u(x, y + \Delta y) - u(x, y - \Delta y)}{2\Delta y} \quad (5.25b)$$

In Equation 5.25, Δx and Δy are vector spacings in the x and y directions, respectively, and are equal for the PIV measurements. At the edges of the vector fields and at

the airfoil surface, where the central difference formulation cannot be applied, first-order backward/forward differences are used. The production of turbulence kinetic energy is then defined as:

$$P_{tke} = - \langle u'v' \rangle S_{xy} \quad (5.26)$$

which can be normalized using the airfoil towing speed and chord length as the characteristic velocity and length scales:

$$C_{P_{tke}} = \frac{P_{tke} \cdot C}{U_{\infty}^3} \quad (5.27)$$

Vorticity is another parameter of interest for shear flows and can readily be calculated from the spatially-resolved PIV data. As only velocities in the x-y plane are captured in the measurements, only the out-of-plane vorticity component can be calculated. The spanwise vorticity is thus defined as:

$$\Omega_z = \frac{\partial v}{\partial x} - \frac{\partial u}{\partial y} \quad (5.28)$$

where the partial derivatives are the same as those provided in Equation 5.25. As the velocity parameters reduced from the particle-displacement fields are normalized based on a characteristic velocity, the vorticity is similarly normalized. The airfoil speed and chord length have also been used here as the characteristic velocity and length scales for this normalization:

$$C_{\Omega_z} = \frac{\Omega_z \cdot C}{U_{\infty}} \quad (5.29)$$

5.2.5 Additional Parameters of Interest

Apart from the ensemble-averaged parameters defined in the previous sections, several other parameters are of interest in the study of shear layers.

The shear layer characteristics and growth can be evaluated by integral parameters that define the mass and momentum deficits in the layer as a result of viscous drag. The displacement thickness defines the mass deficit in the shear layer, which for a wall-bounded flow is defined as:

$$\delta^* = \int_0^\delta \left(1 - \frac{U}{U_e}\right) dy \quad (5.30)$$

where δ is the thickness of the shear layer and U_e is the velocity at the edge of the shear layer. Similarly, the momentum thickness represents the momentum deficit in the shear layer and is defined as:

$$\theta = \int_0^\delta \frac{U}{U_e} \left(1 - \frac{U}{U_e}\right) dy \quad (5.31)$$

These thicknesses have been calculated from the velocity vector measurements using trapezoidal integration. The ratio of displacement thickness to momentum thickness is also a useful parameter and provides a quantitative measure of the shear-layer shape, from which information regarding the susceptibility of the layer to separation and whether the layer is laminar or turbulent can be inferred, provided information regarding the streamwise pressure gradient is known. This shape factor is defined as:

$$H = \frac{\delta^*}{\theta} \quad (5.32)$$

One major benefit of using PIV to study separation bubbles is the ability to resolve the reverse flow below the separated shear layer. In Chapter 6, the effects of calculating the above-defined shear-layer parameters with and without accounting for the reverse flow are assessed. This has been done since many of the studies of separation bubbles in the open literature have examined the flow using hot-wires that cannot properly resolve the reverse-flow due to rectification errors.

The instability frequencies observed in separated-shear layers are often expressed as a non-dimensional Strouhal number based on conditions at separation, defined as:

$$Sr_{\theta_s} = \frac{f \cdot \theta_s}{U_{es}} \quad (5.33)$$

Frequency analysis of the PIV measurements is not possible, as a result of the low sampling rates. However knowledge regarding the nature of such instabilities can provide an estimate based on measured properties of the flow. The instability frequency observed in a shear layer arises from the convection of vortical structures that roll-up as a result of the instability. Knowing the spatial wavelength in the streamwise direction, Λ_x , and the convection speed of the vortical structures, U_c , the frequency can be estimated by:

$$f = \frac{U_c}{\Lambda_x} \quad (5.34)$$

from which the Strouhal number in Equation 5.33 can be defined as:

$$Sr_{\theta_s} = \frac{U_c \cdot \theta}{\Lambda_x \cdot U_{es}} \quad (5.35)$$

As the instability frequency arising in the shear layer is a result of the convecting vortical instability, its convection rate can be estimated as the velocity in the shear-layer corresponding to the maximum observed value of vorticity. This represents the location from the surface through which the cores of the vortical structures pass, and for thin inflectional velocity-profiles also corresponds to the location of maximum shear.

For the two experimental PIV studies performed during the course of this research, the instability wavelengths have been identified by different means. For the SD7003 experiments presented in Chapter 6, the streamwise wavelengths have been inferred by identifying the core-to-core distance between the large-scale vortical structures developing in the transition

region of the separated shear layers. The wavelengths identified in Chapter 6 are based on an average of the measured wavelengths after examining many instantaneous vorticity fields ($N > 50$).

For the unconventional-airfoil experiments presented in Chapters 8 and 9, the streamwise wavelengths associated with the instabilities have been calculated by means of a spatial correlation of the wall-normal velocity fluctuations. This was done in order to automate the process as 24 test cases were examined for this study compared to the 3 cases for the SD7003 experiments of Chapter 6. Correlation using the wall-normal velocity fluctuations, v' , was found to provide stronger and more distinct correlation peaks than those using the streamwise fluctuations, u' . The correlation coefficient $cc_{v'}$ is defined as:

$$cc_{v'}(x, x + \Delta x) = \frac{1}{N} \sum_i^N \frac{v'_i(x)}{\sqrt{\langle v'v'(x) \rangle}} \frac{v'_i(x + \Delta x)}{\sqrt{\langle v'v'(x + \Delta x) \rangle}} \quad (5.36)$$

where N is the number of vector fields used in the ensemble average. Normalization of the instantaneous fluctuation values by the local ensemble-averaged RMS values is required since the fluctuation levels change with streamwise distance and this ensures that the correlation value remains below 1. From the correlation functions calculated using Equation 5.36, distinct peaks provide estimates of the dominant wavelengths prevailing in the separated shear layers. More details regarding the correlation functions and identification of the dominant wavelengths are provided in Chapter 8.

5.2.6 Uncertainty Estimates

There are multiple sources of uncertainty in the PIV measurements. This section describes these sources and the resulting uncertainty estimates for the reduced data. Uncertainties in the particle displacement vectors are due to two primary errors: camera-model tracking errors, and image-processing uncertainty.

The first source of uncertainty is a result of small errors in the image-correction algorithm described in Section 5.2.1. Although the algorithm significantly reduced the effect of camera-model tracking errors by co-locating the marker centroids of an image pair, non-uniformity in the marker intensity-distributions can cause an error in the calculated centroid locations. The net result is a maximum uncertainty in the image location, relative to the reference image, of ± 0.5 pixel.

The second source of uncertainty in the particle-displacement vector fields is due to the image-processing algorithm. The uncertainty in the cross-correlation algorithm is estimated to be approximately ± 0.1 pixel in the freestream flow, which is consistent with current state-of-the-art FFT-based PIV algorithms (Westerweel, 2000). This has been assessed by examining the variation in particle-displacement magnitudes along a line for which the mean velocity should not change (as a result of the zero intensity of freestream turbulence in the tow-tank). Small vector-to-vector variations in the displacement magnitudes along these lines are on the order of 0.1 pixel. In regions of high shear with negligible out-of-plane particle loss, the uncertainty is estimated to be below 0.5 pixel based on examining image pairs for which the image reconstruction technique noted in Section 5.2.2 has been applied using the converged particle displacement field. The use of iterative multi-pass, intermediate filtering, and intermediate smoothing techniques for image analysis provides reduced uncertainty in regions of poorly correlated displacements due to out-of-plane particle motion. The resultant particle displacement vectors in these regions have

magnitudes and directions similar to the surrounding well-correlated displacements. These techniques used for reducing errors in the particle displacement fields are discussed in Appendix A and greater detail can be found in the documents by Scarano and Riethmuller (2000), Raffel *et al.* (1998), and Meunier and Leweke (2003). Outlier vectors arising from incorrect correlation-peak-identification account for less than 5% of the total vector count in a given vector field. Using spatial filtering techniques within the DaVis software, the majority of outlier vectors were removed and replaced with locally-interpolated vectors. The final count of obvious outlier-vectors is less than 1% of the total number in each vector field.

In the SD7003 experiments of Chapter 6, near-wall bias errors are also present as a result of strong reflections of the laser-light at the model surface. Masking of this near-wall region was required during image-processing which, combined with low seeding density near the surface for these measurements, provided a bias in the displacement-vector errors towards those of the higher displacements present further from the wall. These reflections were not as pronounced in the new-airfoil experiments (Chapters 8 and 9) as the unconventional airfoil was manufactured from a less reflective material (fibreglass as opposed to stainless steel). The two-step processing technique used for these newer measurements also aided in reducing these near-wall bias errors. The initial-analysis pass, with approximately 50 image pairs, did not make use of a mask, and the self-correlated reflections provided near-zero velocities at the surface. The final-analysis pass, which did make use of a mask, was initiated using an average of the initial-pass results and therefore the analysis was started from a vector field with small displacements already present near the surface. The multigrid method used for the final-analysis-pass also made use of more strictly-defined allowances for the pass-to-pass change in particle displacement vectors, ensuring that the near-wall displacement vectors were representative of the true correlation-peak locations.

Table 5.2 provides estimates of the maximum expected uncertainties in the reduced

Table 5.2: Maximum estimated uncertainties for reduced experimental PIV data

Parameter	SD7003 (Chapter 6)	Unconventional Airfoil (Chapters 8 and 9)	
		$Re = 28,000, 39,000, 51,000$	$Re = 101,000$
Re	$\pm 1,000$	$\pm 2,000$	$\pm 2,000$
$u, v, U _{shear-layer} / U_\infty$	± 0.05	± 0.05	± 0.05
$u, v, U _{near-wall} / U_\infty$	$+0.10 / - 0.05$	± 0.05	$+0.10 / - 0.05$
$U_{freestream} / U_\infty$	± 0.03	± 0.03	± 0.03
U_{rms} / U_∞	± 0.10	± 0.05	± 0.10
$\langle u'u' \rangle, \langle v'v' \rangle / U_\infty$	± 0.005	± 0.005	± 0.010
$\langle u'v' \rangle / U_\infty$	± 0.005	± 0.005	± 0.005
x_s / C	± 0.005	± 0.005	± 0.005
x_{ts} / C	± 0.010	± 0.010	± 0.010
x_r / C	± 0.01	± 0.004	± 0.007
δ^*, θ	$\pm 15\%$	$\pm 10\%$	$\pm 15\%$
H	± 0.5	± 0.3	± 0.5
$Sr_{\theta s}$	± 0.005	± 0.003	± 0.005

experimental data, for both sets of experiments performed. For the unconventional-airfoil measurements, the uncertainties at the highest Reynolds number examined are greater than those at the lower Reynolds numbers as a result of the thinner shear layers and smaller number of vector fields used for averaging, and are therefore given as a separate set. The majority of the uncertainty in the velocity parameters, and the correlations thereof, results from errors in the camera-model-tracking correction. As these errors are uncorrelated, the uncertainty in $\langle u'v' \rangle$ is not as significant as those for the other self-correlated parameters. Also, the near-wall bias errors are biased towards those of the higher velocities away from the wall, as reflected in asymmetric uncertainties for this parameter.

5.3 Data Reduction of Simulation Results

The direct numerical simulations performed during the course of this research provide temporal and spatial solutions of the flow-field developing over a flat plate in the presence of a non-uniform streamwise pressure distribution. The temporal and spatial resolutions of the simulations have been selected such that the length- and time-scales of the flow in the separation bubbles are adequately captured, permitting the use of time-averaging for all primary flow variables and fluctuation correlations thereof. Section 5.3.1 describes the time-averaging techniques used for data processing; Section 5.3.2 describes the vorticity-calculation algorithms implemented in the data reduction procedures; Section 5.3.3 describes the intermittency-calculation algorithm; Section 5.3.4 describes the spectral-analysis used; Section 5.3.5 describes the turbulence-length-scale calculations; and Section 5.3.6 identifies other parameters of interest.

5.3.1 Time Averaging Techniques

The primary flow variables calculated by the ANSYS-CFX solver are the three components of velocity (u , v , w) and the static pressure (p). Table 5.3 provides a list of the averaged-variables calculated from the simulation results, of which not all were used for interpretation of the flow physics.

Table 5.3: Time- and spanwise-averaged variables calculated from simulation results

Variable Type	Variables
mean	\bar{u} , \bar{v} , \bar{w} , \bar{U} , \bar{p} , \bar{p}_0 , $\bar{\Omega}_x$, $\bar{\Omega}_y$, $\bar{\Omega}_z$, $\bar{\Omega}$
fluctuation correlations	$\overline{u'u'}$, $\overline{v'v'}$, $\overline{w'w'}$, $\overline{u'v'}$, $\overline{v'v'}$, $\overline{w'w'}$
root-mean-square	U_{rms} , p_{rms} , $p_{0\ rms}$, $\Omega_{x\ rms}$, $\Omega_{y\ rms}$, $\Omega_{z\ rms}$, Ω_{rms}

For any variable ϕ , the time-mean value is defined as:

$$\overline{\phi(x, y, z)} = \frac{1}{T} \int_{t=t_0}^{t=t_0+T} \phi(x, y, z, t) dt \quad (5.37)$$

where the integration is performed over the time period T . For the present simulations, where the mean flow properties are two dimensional in the $x-y$ plane, spanwise integration has also been performed, according to:

$$\overline{\phi(x, y)} = \frac{1}{T \cdot Z} \int_{z=z_0}^{z=z_0+Z} \int_{t=t_0}^{t=t_0+T} \phi(x, y, z, t) dt \cdot dz \quad (5.38)$$

where Z is the spanwise extent over which the integration is performed. If discretized based on a finite time interval Δt and finite spanwise interval Δz , Equation 5.38 can be numerically integrated according to the following formulation:

$$\overline{\phi(x, y)} = \frac{1}{(N_z + 1)(N_t + 1)} \sum_{k=0}^{N_z} \sum_{i=0}^{N_t} \phi(x, y, z_0 + k\Delta z, t_0 + i\Delta t) \quad (5.39)$$

where N_z represents the number of discrete intervals over the spanwise extent Z , and N_t represents the number of time intervals over the time period T .

Correlations of the fluctuating components of velocity are also defined using a time-averaging approach. For two variables, ϕ and ψ , the correlation of their fluctuations is defined as:

$$\overline{\phi' \psi'(x, y)} = \frac{1}{T \cdot Z} \int_{z=z_0}^{z=z_0+Z} \int_{t=t_0}^{t=t_0+T} \phi' \cdot \psi' dt \cdot dz \quad (5.40)$$

where the instantaneous fluctuations ϕ' and ψ' are defined as:

$$\begin{aligned} \phi' &= \phi(x, y, z, t) - \overline{\phi(x, y)} \\ \psi' &= \psi(x, y, z, t) - \overline{\psi(x, y)} \end{aligned}$$

The discrete form of Equation 5.40 is given as:

$$\overline{\phi' \psi'}(x, y) = \frac{1}{(N_z + 1)(N_t + 1)} \sum_{k=0}^{N_z} \sum_{i=0}^{N_t} \phi' \cdot \psi' \quad (5.41)$$

where the instantaneous fluctuations ϕ' and ψ' are defined in discrete form as:

$$\begin{aligned} \phi' &= \phi(x, y, z_0 + k\Delta z, t_0 + i\Delta t) - \overline{\phi(x, y)} \\ \psi' &= \psi(x, y, z_0 + k\Delta z, t_0 + i\Delta t) - \overline{\psi(x, y)} \end{aligned}$$

The root-mean-square variables are calculated in a similar manner:

$$\phi_{rms} = \sqrt{\frac{\sum_{k=0}^{N_z} \sum_{i=0}^{N_t} \left[\phi(x, y, z_0 + k\Delta z, t_0 + i\Delta t) - \overline{\phi(x, y)} \right]^2}{(N_z + 1)(N_t + 1)}} \quad (5.42)$$

To prevent the requirement of a two-pass data reduction algorithm for calculation of the fluctuation-based variables, a similar single-pass technique to that described in Section 5.2.3 has been used. The time-averaged form of the mean, fluctuation-correlation, and RMS equations for this single-pass technique are defined as:

$$\bar{\phi} = \frac{1}{N_t + 1} \sum_{i=0}^{N_t} \left(\frac{1}{N_z + 1} \sum_{k=0}^{N_z} \phi \right) \quad (5.43)$$

$$\overline{\phi' \psi'} = \frac{1}{N_t + 1} \sum_{i=0}^{N_t} \left(\frac{1}{N_z + 1} \sum_{k=0}^{N_z} \phi \cdot \psi \right) - \bar{\phi} \cdot \bar{\psi} \quad (5.44)$$

$$\phi_{rms} = \sqrt{\frac{1}{N_t + 1} \sum_{i=0}^{N_t} \left(\frac{1}{N_z + 1} \sum_{k=0}^{N_z} \phi^2 \right) - \frac{1}{(N_t + 1)(N_z + 1)} \bar{\phi}^2} \quad (5.45)$$

A vast amount of data must be reduced in order to calculate the time- and spanwise-averaged mean, RMS, and fluctuation correlation parameters for the simulations. For

the low-freestream-turbulence simulation, averaging was performed from data extracted at five evenly-spaced, adjacent x - y planes in the computational domain. As a result of the large spanwise spacing of these planes, the vorticity parameters Ω_x , Ω_y , Ω and their respective RMS values could not be calculated. The data for this simulation was processed as if the spanwise-separated planes were additional time periods and therefore only the time-averaged formulations were used. The elevated-freestream turbulence case, however, required data from the entire computational domain to be averaged and analyzed to capture the significant three-dimensional effects occurring in the transition region of the separation bubbles. Therefore all parameters listed in Table 5.3 were calculated for this simulation. As the extracted data files for each time-step were on the order of 100 MB each, and significant computing time was required to unzip the files prior to processing, a two-step approach was taken in order to reduce the data. The first step was to perform a spanwise-average of the data at each time-step, the results of which were written to a file associated with that particular time-step. The parameters written to these spanwise-averaged files are those enclosed in parentheses in Equations 5.43 to 5.45. After the individual spanwise-averages had been performed for every time-step in the simulation, a time-average of the spanwise-averaged data files was then performed, according to Equations 5.43 through 5.45. This two-step procedure permitted the data reduction process to occur incrementally, as opposed to all-at-once.

5.3.2 Vorticity Calculation

Unlike the PIV measurements, for which the velocity-vector results are defined on a grid with equal x and y spacings, the computational elements in the simulations are skewed as a result of the domain-height contraction in the streamwise direction. This required a more detailed algorithm than that presented in Section 5.2.3 for calculating the three components

of vorticity at the domain nodes. The required vorticity components are defined as:

$$\Omega_x = \frac{\partial w}{\partial y} - \frac{\partial v}{\partial z} \quad (5.46)$$

$$\Omega_y = \frac{\partial u}{\partial z} - \frac{\partial w}{\partial x} \quad (5.47)$$

$$\Omega_z = \frac{\partial v}{\partial x} - \frac{\partial u}{\partial y} \quad (5.48)$$

$$\Omega = \sqrt{\Omega_x^2 + \Omega_y^2 + \Omega_z^2} \quad (5.49)$$

where the partial derivatives must be evaluated numerically.

A sample sub-set of the computational grid is shown in Figure 5.2. For the domain regions from which data was extracted for processing, constant node spacings in the z -direction are found throughout, and all z - y planes are perpendicular to the x -coordinate direction. However, spacings in the x - and y -directions are not constant and the contraction of the domain height in the x -direction provides skewed computational elements. Therefore, basic finite-difference formulations for the spatial derivatives based on available velocity components at the node locations, such as those provided in Section 5.2.3, cannot be used. The following provides details of the finite difference formulations used for the spatial-derivatives found in Equations 5.46, 5.47, and 5.48.

The derivatives with respect to the spanwise coordinate, z , are evaluated using a standard central-difference formulation, as the z -spacings are equal and the z - y faces of the elements are not skewed. The following estimates for the local derivatives are therefore second-order accurate:

$$\left. \frac{\partial u}{\partial z} \right|_{i,j,k} = \frac{u_{i,j,k+1} - u_{i,j,k-1}}{z_{i,j,k+1} - z_{i,j,k-1}} \quad (5.50)$$

$$\left. \frac{\partial v}{\partial z} \right|_{i,j,k} = \frac{v_{i,j,k+1} - v_{i,j,k-1}}{z_{i,j,k+1} - z_{i,j,k-1}} \quad (5.51)$$

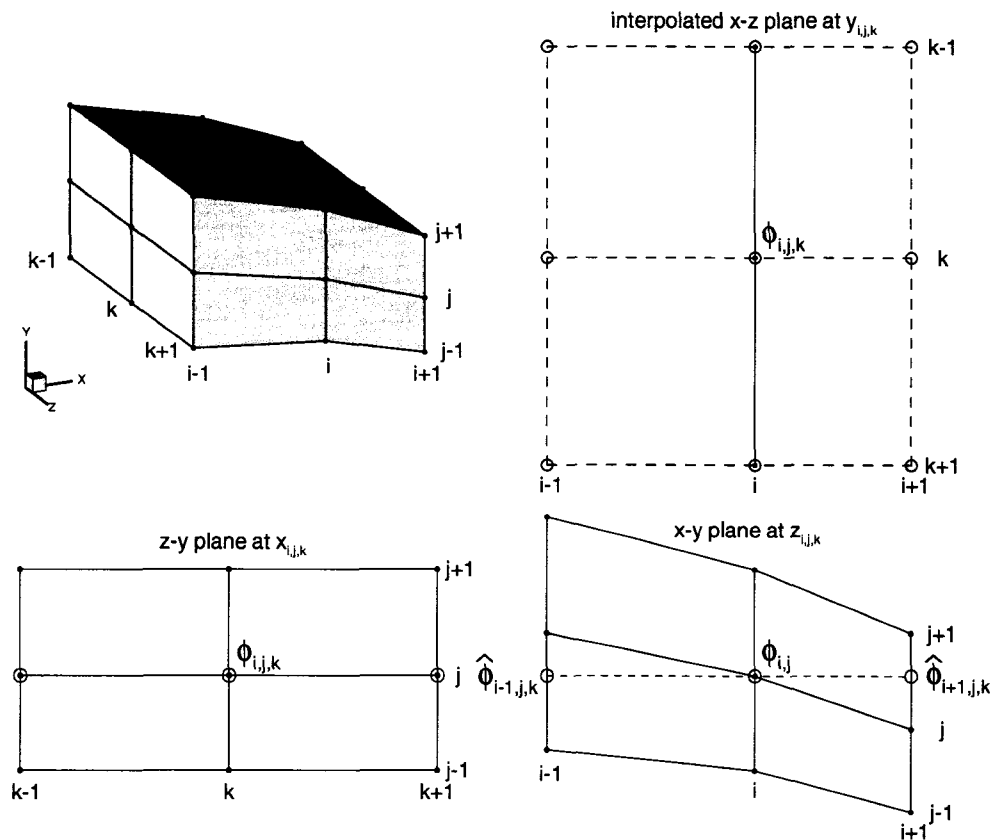


Figure 5.2: Sub-set of computational grid (ϕ represents any flow variable)

The derivatives with respect to the wall-normal coordinate, y , are evaluated using a weighted central-difference formulation to account for the unequal node distribution in this coordinate direction. The forward- and backward-difference formulations for a particular node are weighted according to the distance to the adjacent nodes, with the difference-formulation based on the closer node having a greater influence. As this method provides a weighted-average of the first-order difference formulations, it is therefore second-order

accurate:

$$\left. \frac{\partial u}{\partial y} \right|_{i,j,k} = A_y \cdot u_{i,j-1,k} + B_y \cdot u_{i,j,k} + C_y \cdot u_{i,j+1,k} \quad (5.52)$$

$$\left. \frac{\partial w}{\partial y} \right|_{i,j,k} = A_y \cdot w_{i,j-1,k} + B_y \cdot w_{i,j,k} + C_y \cdot w_{i,j+1,k} \quad (5.53)$$

where

$$A_y = \frac{1}{y_{i,j+1,k} - y_{i,j-1,k}} - \frac{1}{y_{i,j,k} - y_{i,j-1,k}}$$

$$B_y = \frac{1}{y_{i,j,k} - y_{i,j-1,k}} - \frac{1}{y_{i,j+1,k} - y_{i,j,k}}$$

$$C_y = \frac{1}{y_{i,j+1,k} - y_{i,j,k}} - \frac{1}{y_{i,j+1,k} - y_{i,j-1,k}}$$

Evaluating the partial derivatives with respect to the streamwise coordinate, x , is not as straight-forward as those for the y and z direction due to the skewed mesh (see Figure 5.2). For the purpose of evaluating these derivatives, data from the adjacent z - y planes are interpolated on an x - z grid that passes through the node of interest at location (i,j,k) . These interpolated values are denoted in Figure 5.2 by $\hat{\phi}$, and are based on linear-interpolation between adjacent nodes:

$$\hat{\phi}_{i-1,j,k} = \begin{cases} a_{i-1} \cdot \phi_{i-1,j,k} + b_{i-1} \cdot \phi_{i-1,j-1,k} & \text{if } y_{i,j,k} < y_{i-1,j,k} \\ c_{i-1} \cdot \phi_{i-1,j+1,k} + d_{i-1} \cdot \phi_{i-1,j,k} & \text{if } y_{i,j,k} \geq y_{i-1,j,k} \end{cases} \quad (5.54)$$

$$\hat{\phi}_{i+1,j,k} = \begin{cases} a_{i+1} \cdot \phi_{i+1,j,k} + b_{i+1} \cdot \phi_{i+1,j-1,k} & \text{if } y_{i,j,k} < y_{i+1,j,k} \\ c_{i+1} \cdot \phi_{i+1,j+1,k} + d_{i+1} \cdot \phi_{i+1,j,k} & \text{if } y_{i,j,k} \geq y_{i+1,j,k} \end{cases} \quad (5.55)$$

where

$$\begin{aligned}
 a_{i-1} &= \left(\frac{y_{i,j,k} - y_{i-1,j-1,k}}{y_{i-1,j,k} - y_{i-1,j-1,k}} \right) \\
 b_{i-1} &= \left(\frac{y_{i-1,j,k} - y_{i,j,k}}{y_{i-1,j,k} - y_{i-1,j-1,k}} \right) \\
 c_{i-1} &= \left(\frac{y_{i,j,k} - y_{i-1,j,k}}{y_{i-1,j+1,k} - y_{i-1,j,k}} \right) \\
 d_{i-1} &= \left(\frac{y_{i-1,j+1,k} - y_{i,j,k}}{y_{i-1,j+1,k} - y_{i-1,j,k}} \right) \\
 a_{i+1} &= \left(\frac{y_{i,j,k} - y_{i+1,j-1,k}}{y_{i+1,j,k} - y_{i+1,j-1,k}} \right) \\
 b_{i+1} &= \left(\frac{y_{i+1,j,k} - y_{i,j,k}}{y_{i+1,j,k} - y_{i+1,j-1,k}} \right) \\
 c_{i+1} &= \left(\frac{y_{i,j,k} - y_{i+1,j,k}}{y_{i+1,j+1,k} - y_{i+1,j,k}} \right) \\
 d_{i+1} &= \left(\frac{y_{i+1,j+1,k} - y_{i,j,k}}{y_{i+1,j+1,k} - y_{i+1,j,k}} \right)
 \end{aligned}$$

With the interpolated variables defined for the forward and backward x -directions, the partial derivatives with respect to x are evaluated based on a weighted central-difference, similar to that for the y derivatives. Although the weighted central difference formulation is second-order accurate, the use of linearly-interpolated values in the positive and negative x -directions provides only first-order accuracy in these derivatives:

$$\left. \frac{\partial v}{\partial x} \right|_{i,j,k} = A_x \cdot \hat{v}_{i-1,j,k} + B_x \cdot \hat{v}_{i,j,k} + C_x \cdot \hat{v}_{i+1,j,k} \quad (5.56)$$

$$\left. \frac{\partial w}{\partial x} \right|_{i,j,k} = A_x \cdot \hat{w}_{i-1,j,k} + B_x \cdot \hat{w}_{i,j,k} + C_x \cdot \hat{w}_{i+1,j,k} \quad (5.57)$$

where

$$\begin{aligned}
 A_x &= \frac{1}{x_{i+1,j,k} - x_{i-1,j,k}} - \frac{1}{x_{i,j,k} - x_{i-1,j,k}} \\
 B_x &= \frac{1}{x_{i,j,k} - x_{i-1,j,k}} - \frac{1}{x_{i+1,j,k} - x_{i,j,k}} \\
 C_x &= \frac{1}{x_{i+1,j,k} - x_{i,j,k}} - \frac{1}{x_{i+1,j,k} - x_{i-1,j,k}}
 \end{aligned}$$

Both Ω_y and Ω_z contain derivatives for the x -direction, and therefore only the Ω_x vorticity component can formally be considered second-order accurate. Despite this, the calculated vorticity fields provide sufficiently accurate results, both qualitatively and quantitatively, in regards to the spatial distribution of vorticity such that the dominant vortical structures associated with the transition process are adequately resolved.

The production of turbulence kinetic energy is also calculated from the simulation results and, as defined in Equation 5.26, requires the above-defined partial derivatives in the x and y coordinate directions for calculation of the strain rate. The strain rate is calculated based on the averaged flow-field after the time-averaging procedure has been completed.

5.3.3 Intermittency Calculation

An important parameter for studying transitional flows is the intermittency, γ , defined as the fraction of time the shear-layer flow is turbulent at a particular spatial location. In laminar flow, $\gamma = 0$, and in fully-turbulent flow, $\gamma = 1$. For the present study, the streamwise distribution of intermittency through the shear layer has been calculated from data extracted at a constant wall-normal distance. Roberts (2005) discusses that for the experimental cases upon which the simulations are based, the streamwise intermittency distribution is insensitive to the location from the wall at which the measurements were performed, as long as the measurements are made within the shear layer.

The calculation of intermittency is based on a temporal analysis of the velocity time-traces extracted from the DNS results. The method is based on an algorithm presented by Volino *et al.* (2001), which differentiates between turbulent and non-turbulent flow using the magnitudes of the first and second derivatives of the velocity time-traces (dU/dt and d^2U/dt^2). A central-difference method is used to calculate these derivatives and the algorithm uses defined thresholds of the derivatives to identify whether the flow is turbulent or not. The use of the second derivative is required to ensure turbulence identification at local minima and maxima of the time-traces, since the first derivative is zero at these instances. A flow-state parameter, β , is used to identify whether the flow is turbulent at a particular instant in time by setting its value to 1 if either of the derivatives has exceeded a specified threshold. Otherwise, if the flow is deemed non-turbulent, β is assigned a value of 0. Time-averaging of the resulting β -distribution provides the intermittency, γ .

In the present simulations, strong fluctuations have been identified in the laminar shear-layer as a result of instability growth or buffeting of freestream turbulence. To prevent the intermittency-algorithm from identifying these fluctuations as turbulent, high-pass filtering of the velocity time-traces is first performed, as the frequencies associated with these fluctuations are lower than those associated with turbulence in the shear layer. Volino *et al.*'s algorithm provides an automated method for selecting the cut-off frequency, however the method was developed based on measurements in attached-flow boundary-layer transition. Although the transition mechanisms in a separation bubble share characteristics with those in attached-flow transition, as will be discussed in Chapter 7, there are differences in the time-scales of such phenomena and therefore the cut-off frequency identified by Volino *et al.*'s algorithm has been deemed unreliable for the present results. Visual examination of the time-traces and associated spectral distributions have proved to be more reliable for identifying appropriate cut-off frequencies for the intermittency analysis.

The intermittency-calculation algorithm requires a single threshold input value, that

for the first derivative, and Volino *et al.* have proposed that this threshold scale with the local freestream velocity. This proposed threshold scale, as with the high-pass frequency cut-off scale, was based on measurements in attached-flow boundary-layer transition and the threshold values used have been modified slightly for the present simulation results. This adjustment of the threshold value was based on a visual comparison of the velocity time-traces with the calculated β -distributions. The threshold for the second-derivative is set automatically by the algorithm such that the time-averages of the β -distributions for the first- and second-derivatives are equal. The combined β -distribution, where β is set to 1 if either of the two β -distributions has a value of 1, is then low-pass filtered to eliminate drop-outs in the signal, and subsequently time-averaged to provide the intermittency value, γ .

5.3.4 Spectral Analysis

Spectral analysis of the simulation results has proved useful for identifying frequencies associated with the dominant physical mechanisms leading to transition in a separated shear layer. A Fast Fourier Transform (FFT) algorithm has been used to calculate the Power Spectral Density (PSD) distributions of velocity and pressure time-traces at various locations in the separated shear layers.

5.3.5 Turbulence Integral Length Scale

The integral length scale of turbulence is a measure of the average size of the dominant energy-containing vortical structures, or eddies, in a turbulent flow. The longitudinal integral length scale is often used as a representative measure of the spatial scales of the turbulence in a flow. This length scale is defined by Hinze (1975) as:

$$\Lambda_f = \int_0^{\infty} f(\Delta x) d\Delta x \quad (5.58)$$

where

$$f(\Delta x) = \frac{\overline{u'(x)u'(x + \Delta x)}}{\overline{u'^2}} \quad (5.59)$$

is the longitudinal correlation-coefficient function. This correlation coefficient requires simultaneous velocity data from two streamwise-separated locations. Although these data are readily available from the simulations, the approach taken to calculate the integral length scale is that most often used with single-point hot-wire measurements. This has allowed direct comparison of the calculated length scales from the simulations with those from the experiments upon which they were based. In a homogeneous turbulent flow, the longitudinal correlation-coefficient function (Equation 5.59) is equivalent to the autocorrelation coefficient function (Hinze, 1975), defined as:

$$R(\Delta t) = \frac{\overline{u'(t)u'(t + \Delta t)}}{\overline{u'^2}} \quad (5.60)$$

and requires only data from a single spatial location. Although grid-generated turbulence is not homogeneous, as there is a streamwise change in the intensity and length scales of the turbulence, the autocorrelation-coefficient function (Equation 5.60) is commonly used as a means for measuring the integral length scale of such flows (Roach, 1987; Roberts, 2005). Taylor's *frozen-turbulence approximation*, which assumes that the energy-containing eddies change very little in the time that it takes to be convected the distance Λ_f , allows an estimate of the integral length scale by means of the autocorrelation function (Pope, 2000). By assuming that the flow-field is a frozen structure moving at the local mean velocity, Taylor's *frozen-turbulence approximation* states that $R(\Delta t) \approx f(\Delta x)$, where $\Delta x = -U\Delta t$. The longitudinal integral length scale is then given by:

$$\Lambda_f = U \int_0^\infty R(\Delta t) d\Delta t \quad (5.61)$$

which has been used to calculate the integral length scales of freestream turbulence for both the simulations and the experimental measurements upon which the simulations were based.

5.3.6 Additional Parameters of Interest

As with the PIV measurement results, several parameters other than those described in the previous sections are of interest in the study of shear layers.

The shear-layer growth characteristics are examined based on the displacement thickness (δ^* , Equation 5.30), the momentum thickness (θ , Equation 5.31), and the shape factor (H , Equation 5.32).

Dominant frequencies arising in the separated shear layer are expressed as a Strouhal number (Str_{θ_s} , Equation 5.33). Unlike the PIV measurements, where the frequency is inferred based on an estimated wavelength and convection speed, the temporal resolution of the simulation results allows a direct assessment of these frequencies by spectral analysis.

Chapter 6

Separation-Bubble-Transition Measurements on a Low-Reynolds-Number Airfoil

6.1 Chapter Overview

This chapter presents results from an experimental study of the SD7003 airfoil performed in the low-Reynolds-number tow-tank facility at the National Research Council of Canada. The primary intent of this study was to assess the effectiveness of using particle-image velocimetry (PIV) to examine the transition process in a separation bubble. The promising results in this regard have provided insight into the nature of the coherent structures that develop in the transition region of a separation bubble. Additionally, the study was conducted to further validate the transition onset model of Roberts (Equation 2.1 on page 33) at Reynolds numbers lower than those for which the model was developed, and for the effects of surface curvature. Section 6.2 describes the operating conditions under

which the experiments were performed, and Section 6.3 presents the results and discussion of the PIV measurements made in the transition regions of the respective separation bubbles. Validation of the transition onset model of Roberts, as well as a comparison with other models from the open literature, is provided in Section 6.4.

6.2 Operating Conditions

The suction-surface boundary layer of the SD7003 airfoil was examined at three operating conditions, which are listed in Table 6.1. The freestream turbulence intensity is zero by virtue of the stagnant tow-tank conditions, and the Reynolds number for each case was kept constant to within $\pm 1,000$. Measurements were made at quarter-span, which provided a location free of any significant influence from the wing-tip vortices and free from any potential influence of the support stem, which was attached to the pressure surface of the wing at mid-span.

The boundary-layer-edge velocity distributions for each of the examined cases are presented in Figure 6.1. The three operating conditions result in separation bubbles ranging from a “short” time-averaged bubble length of $20\% C$ with separation slightly ($5\% C$) downstream of the suction peak ($R40\alpha 10$), to a “long” time-averaged bubble length

Table 6.1: Operating conditions for SD7003 experiments

Case Name	Reynolds Number (Re)	Angle-of-Attack (α)
R40 α 8	40,000	8°
R40 α 10	40,000	10°
R65 α 4	65,000	4°

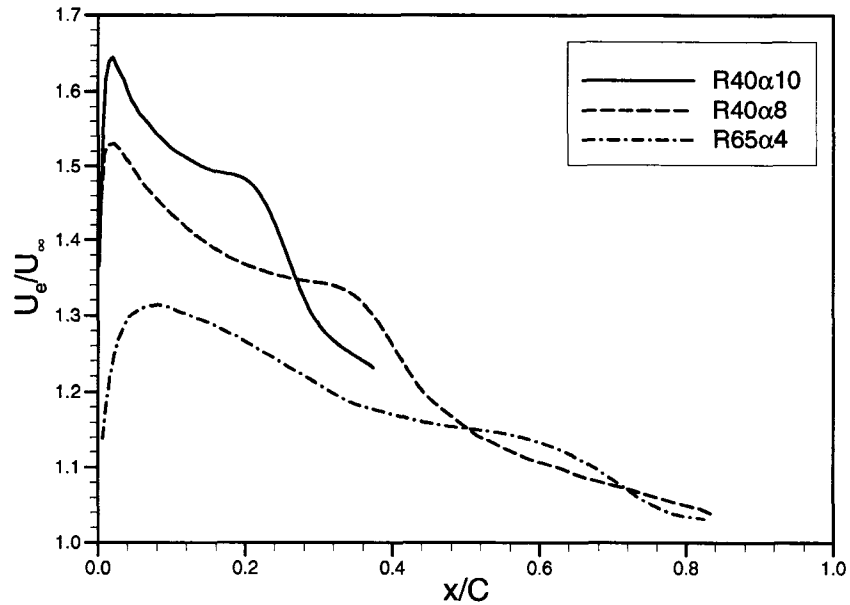


Figure 6.1: **Boundary-layer-edge velocity distributions**

of 35% C with separation 25% C downstream of the suction peak (R65 α 4). Only regions upstream of, through, and slightly downstream of the separation bubbles were examined, due to the lengthy measurement process, which explains the truncated velocity distributions of Figure 6.1.

6.3 Discussion of Measurements

For each of the operating conditions examined, the PIV measurements were reduced according to the procedures described in Chapter 5. The detailed measurements presented in the following discussions are primarily from case R40 α 8, and are representative of all three cases examined.

Figures 6.2(a)-(e) show the velocity measurements for case R40 α 8. The separation point is located at approximately $x/C = 0.09$. Due to near-wall bias errors in the PIV

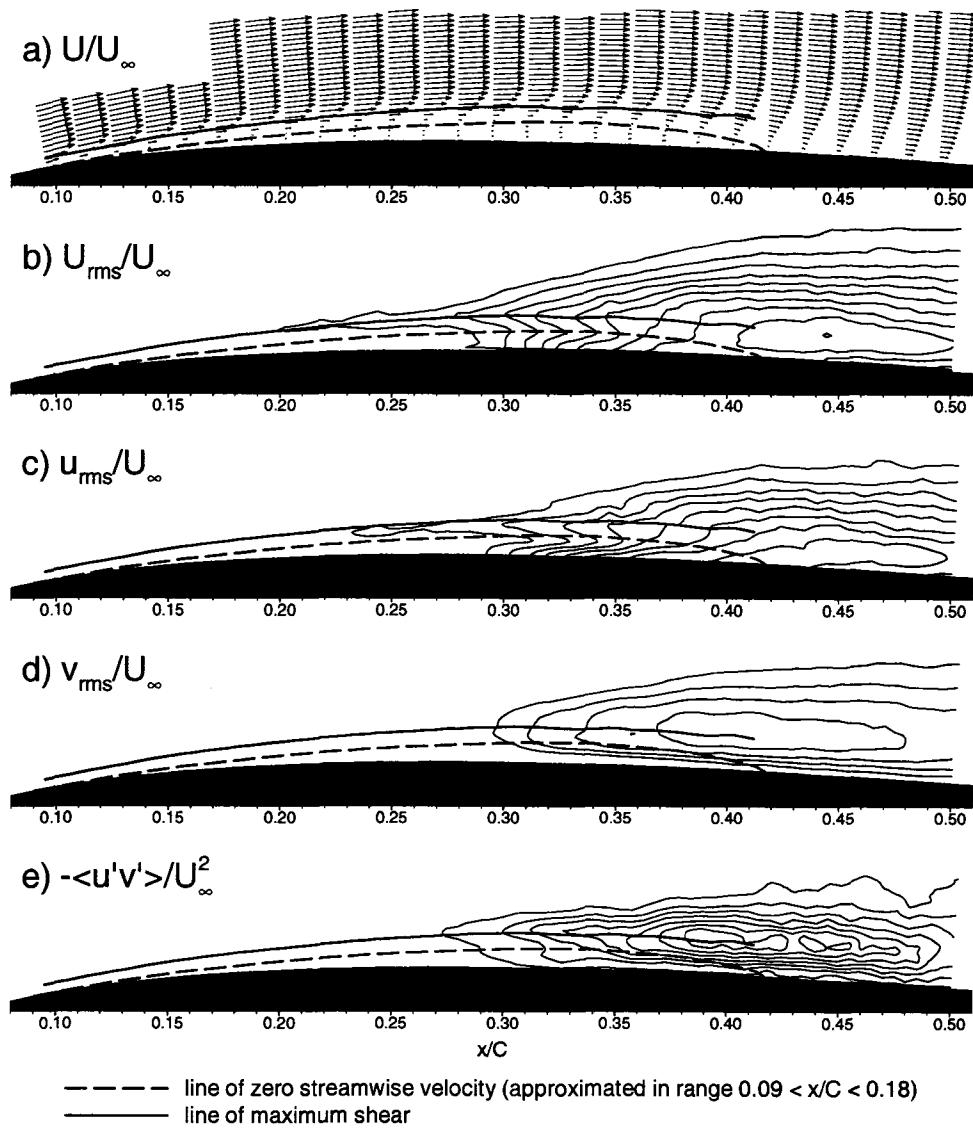


Figure 6.2: Statistical velocity fields for case R40 α 8 (contour intervals for (b),(c),(d) are 0.03 with min. level of 0.08; contour levels for (e) are 0.003 with min. level of 0.001)

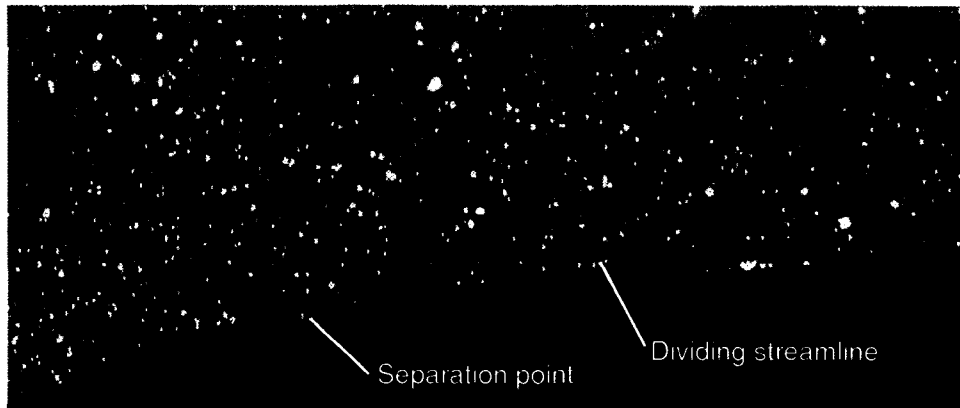


Figure 6.3: Interpretation of separation point from PIV image recording

measurements (biased towards higher velocities away from the surface) and due to the thin boundary layer at separation, the separation point cannot be evaluated from the averaged velocity vector fields. An alternative is to examine the raw PIV image recordings, which also provide information on possible time dependency of the separation location. Figure 6.3 shows one such image recording, where the dividing streamline between the stagnant/recirculating fluid within the bubble and the outer fluid is made visible by the lower seeding density inside the bubble. It is postulated that this is caused by an inertial lag of the seeding particles during the initial high-acceleration portion of the measurement run. Regardless of what causes the relatively low seeding density below the dividing streamline, extrapolating this line upstream to where it intersects the model surface provides an estimate of the separation point, to within $\pm 0.5\%$ of the airfoil chord length. The separation point established through this procedure was found to be steady.

The time-averaged velocity field yields a reattachment point at $x/C = 0.417$ with an uncertainty of $\pm 1\%$ of chord length. Although a single reverse-flow zone and a single reattachment point is observed in the time-averaged velocity field (see Figure 6.4), the temporal variation of the velocity field is substantial, as is evident from a sample instantaneous velocity field displayed in Figure 6.5. Large-scale clockwise-rotating spanwise

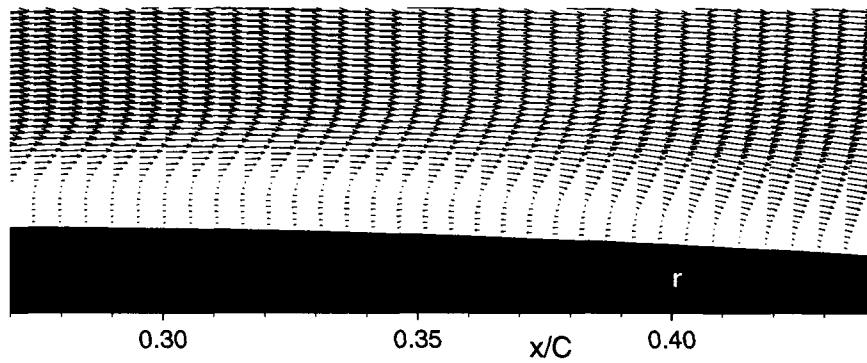


Figure 6.4: Time-averaged reattachment point for case R40 α 8 (r-reattachment point)

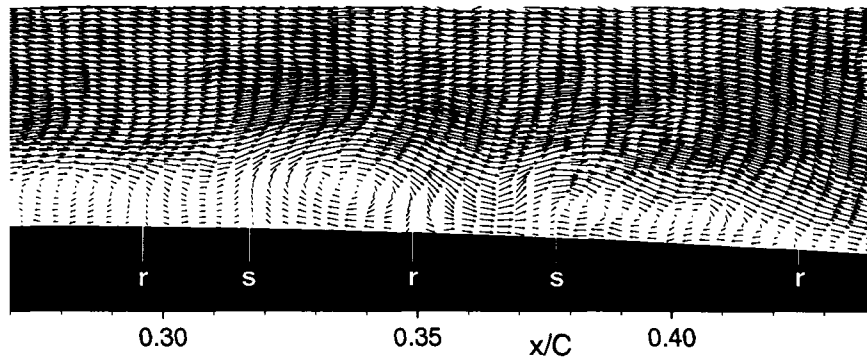


Figure 6.5: Instantaneous velocity field in the reattachment region (r - reattachment, s - separation)

vortices that are generated in the transition region of the separated shear layer induce reverse flow near the wall as they are shed downstream, resulting in secondary or tertiary reverse-flow zones. One such vortex is clearly visible in the range $0.31 < x/C < 0.36$ in Figure 6.5. Similar flow patterns have been observed by Bao and Dallmann (2004) in PIV and hydrogen-bubble flow-visualization experiments of separation bubbles.

High velocity fluctuations are present in the rear portion of the separation bubble, as seen in Figures 6.2(b)-(e). These fluctuations are due to shear-layer instability growth, transition to turbulence, and unsteadiness of the reattachment process. Limitations in the

spatial and temporal resolution of the PIV measurements do not allow the full spectrum of transition and turbulence activity to be captured. Nonetheless, correlations of the resolved velocity fluctuations, as shown in Figure 6.2, do provide qualitative information about the transition process, as well as some semi-quantitative data regarding instability growth and breakdown.

Velocity fluctuations first develop along the line of maximum shear (Figure 6.2(b)-(e)), with the streamwise fluctuations (u_{rms}) growing more quickly and attaining a higher magnitude than the wall-normal fluctuations (v_{rms}). In the rear part of the bubble ($x/C > 0.30$), high streamwise fluctuations are present in the low-velocity reverse-flow region, and are due to the highly unsteady reattachment process with multiple reattachment regions occurring over a large streamwise extent at any given time, as labelled in Figure 6.5. The $-\langle u'v' \rangle$ velocity-fluctuation correlation presented in Figure 6.2(e) represents a Reynolds Stress generated by the PIV-resolved turbulent scales. Therefore, $-\langle u'v' \rangle$ represents the strength of the large-scale turbulence in entraining freestream fluid towards the surface. The locations of maximum velocity fluctuation (U_{rms}) and maximum streamwise velocity fluctuation (u_{rms}) occur downstream of the averaged reattachment point, whereas the maxima in both wall-normal velocity fluctuation (v_{rms}) and velocity cross-correlation ($-\langle u'v' \rangle$) are centered in the vicinity of the reattachment point. The earlier maximum in v_{rms} may be due to attenuation of the wall-normal velocity fluctuations downstream of reattachment, caused by the proximity of the wall. Similar patterns are observed for the R65 α 4 and R40 α 10 cases.

The onset of transition is defined as the location where small-scale turbulence is first generated. Although not all scales of this turbulence are resolved in the present measurements, their effects on the larger-scale structures can give an indication about the onset of the transition process. Figure 6.6 presents the streamwise growth of maximum $-\langle u'v' \rangle$. An exponential growth of disturbances is noted to take place within the separated shear

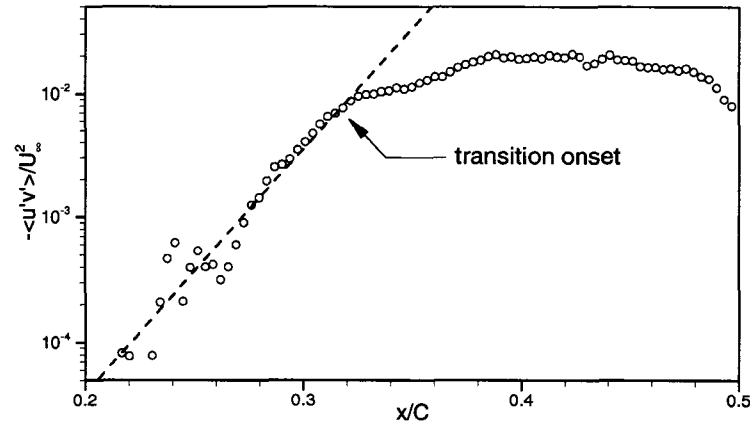


Figure 6.6: Growth of maximum $-\langle u'v' \rangle$ for case R40 α 8

layer, despite the scatter in the range $0.21 < x/C < 0.26$ as a result of PIV evaluation errors. This growth can be predicted from linear stability theory, as was done by Lang *et al.* (2004) for a controlled-transition experiment in a separation bubble. As disturbances grow, a point is reached where the growth rate deviates from the exponential path. In attached boundary layers, this is typically associated with the appearance of three-dimensional structures which, soon afterwards, break down into small-scale turbulence (turbulent spots). In the experiments of Lang *et al.* (2004), the location where the growth rate of disturbances deviated from that predicted by linear stability theory also corresponded well with the location of three-dimensional breakdown within a separated shear layer. Since this three-dimensional breakdown initiates transition, its location in the present measurements will be taken as the onset of transition. For case R40 α 8, the location where the growth of $-\langle u'v' \rangle$ deviates from exponential growth corresponds to $x/C = 0.32$ (with an uncertainty of approximately $\pm 1\%$), which is taken as the location of transition onset. A similar trend in the maximum fluctuation growth for the R65 α 4 case is shown in Figure 6.7, where transition onset is estimated to occur at $x/C = 0.65$.

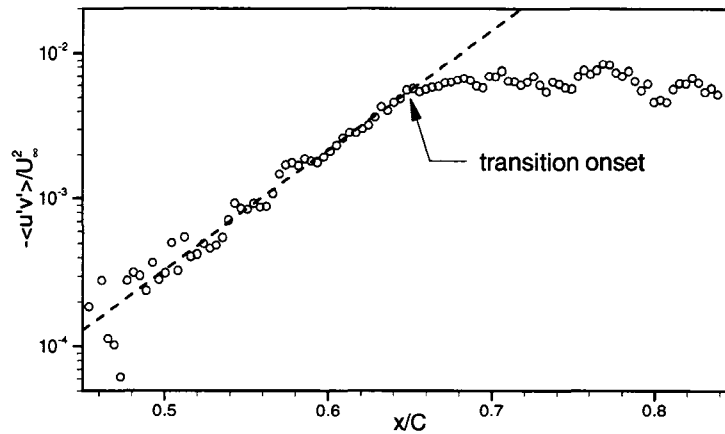


Figure 6.7: Growth of maximum $-\langle u'v' \rangle$ for case R65 α 4

For the cases examined in the present study, the Kelvin-Helmholtz (K-H) instability appears to be the dominant transition mechanism. The vortex-pairing process associated with K-H transition is observed indirectly by comparing the distance, or wavelength, between vortices generated within the separated shear layer to that between vortices downstream of reattachment. The vorticity roll-up within the separated shear-layer is clearly visible in the vorticity field of the reattachment region of the R40 α 8 bubble, presented in Figure 6.8 (black regions). In Figure 6.8(a) the spacing between all vortices is the same and is that of the fundamental instability wavelength (Λ_x). In Figure 6.8(b), which occurs at another unrelated instant in time, doubling of the fundamental wavelength between the second and third vortices indicates that vortex pairing has occurred. The close correlation between the streamwise locations of shear-layer roll-up and transition onset, and the subsequent vortex-pairing pattern suggest K-H instability as the dominant transition mechanism. The large-scale vortices shed from the bubble persist to the trailing edge of the airfoil. The same flow patterns were also observed in the remaining two test cases.

Instability frequencies have been estimated using the fundamental instability wavelength, Λ_x , and by noting that the instability convection speed, U_c , is equal to the velocity

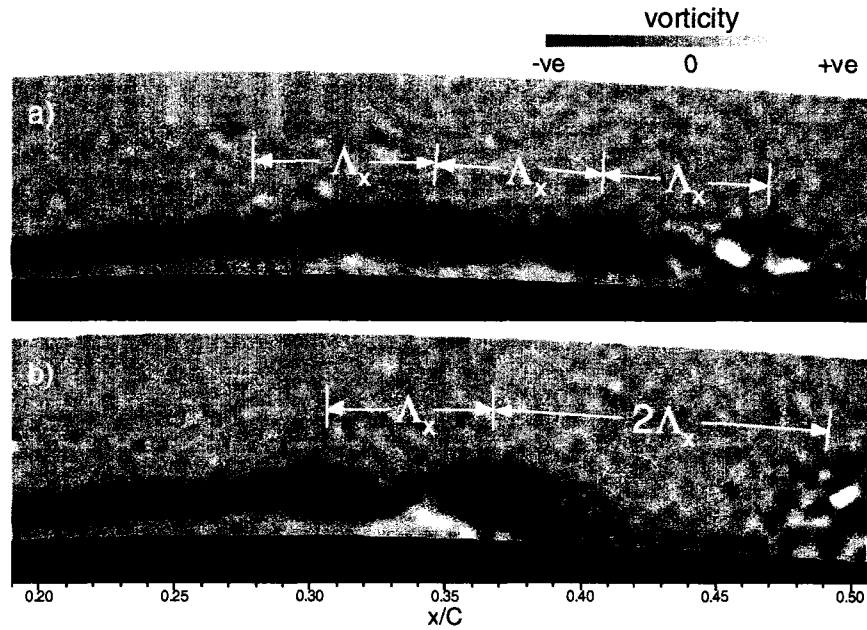


Figure 6.8: Shear layer roll-up at two unrelated instances in time, (a) without K-H vortex pairing, and (b) with K-H vortex pairing

along the line of maximum vorticity (Yang and Voke, 2001). The Strouhal number based on the instability frequency ($f = U_c/\Lambda_x$), the momentum thickness at separation (θ_s), and the freestream velocity at separation (U_{es}) falls in the range $0.008 < Sr_{\theta_s} < 0.013$ for the examined test cases. This agrees well with the range observed by others for transition initiated via the K-H instability mechanism in a separation bubble, as indicated in Table 6.2.

Table 6.2: **Instability Strouhal numbers identified in studies involving separation bubbles**

Investigators	$Sr_{\theta_s} = f\theta_s/U_{es}$
Present study	0.008-0.013
Muti Lin and Pauley (1996)	0.005-0.008
Yang and Voke (2001)	0.005-0.011
Talan and Hourmouziadis (2002)	0.010-0.014

6.4 Transition Onset Prediction

For engineering purposes, the prediction of separation-bubble transition is important for designing airfoils that exhibit adequate performance throughout their operating regimes. This section compares the measured location of transition onset for the cases examined with several empirical transition-onset prediction models proposed in the open literature.

A list of parameters useful in developing or validating transition models are given in Table 6.3. It should be noted that boundary-layer integral parameters calculated from velocity profiles with reverse flow near the wall, as in a separation bubble, may differ depending on the measurement technique used. Many of the experimental separated-flow-transition data published in the literature have been collected using single-sensor hot-wire anemometry, as noted in Section 2.3, which cannot capture reverse flow and may have significant rectification errors, as described by Watmuff (1999). Since PIV measurements can capture reverse flow, these rectification errors are not present and discrepancies between experimental data sets may exist. To estimate the potential discrepancy between boundary-layer integral parameters extracted from PIV and hot-wire measurements, the near-wall reverse-flow velocities for the R40 α 8 case were adjusted to simulate possible rectification errors. Figure 6.9 presents the streamwise distributions of displacement-thickness Reynolds

Table 6.3: Separation bubble characteristics for the SD7003 airfoil

Case	Separation				Transition Onset				Reattachment	
	x_s/C	$Re_s \times 10^{-3}$	Re_{θ_s}	H_s	x_{ts}/C	$Re_{ts} \times 10^{-3}$	$Re_{s-ts} \times 10^{-3}$	H_{ts}^\dagger	x_r/C	$Re_r \times 10^{-3}$
R40 α 8	0.09	6.3	62	3.2	0.31	17.0	12.1	8.5 (7.0)	0.42	21.0
R65 α 4	0.31	25.2	125	3.0	0.65	48.1	26.8	4.0 (4.0)	0.66	48.4
R40 α 10	0.07	5.0	57	3.4	0.21	13.4	9.4	8.7 (6.7)	0.27	15.1

[†] H evaluated with reverse flow (H evaluated with zero velocity in reverse flow region)

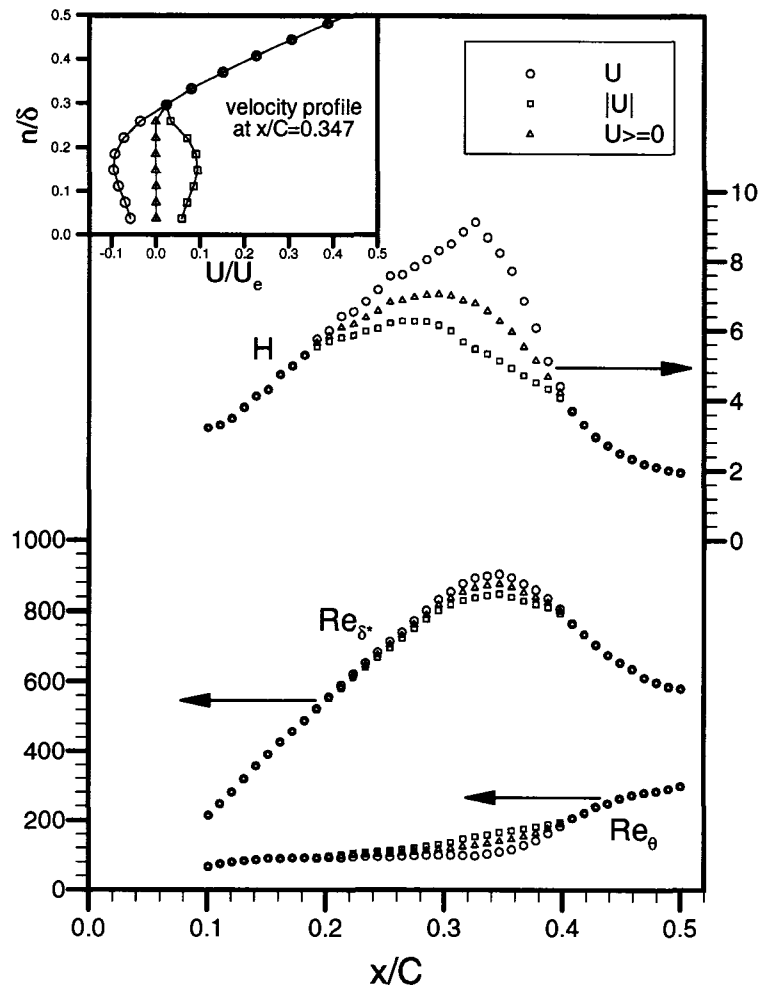


Figure 6.9: Integral parameters for case R40 α 8

number (Re_{δ^*}), momentum-thickness Reynolds number (Re_{θ}), and shape factor (H) for the R40 α 8 case using the averaged PIV data as well as with two variations on rectification errors. These variations consist of complete rectification (i.e. magnitude of velocity is used for calculation) and calculations neglecting any reverse flow. When fluctuations are present in the reverse-flow region of the bubble, hot-wire rectification errors are expected to be somewhere between these two rectification variations examined (Watmuff, 1999). As seen in Figure 6.9, significant differences for the integral parameters in the reverse-flow region are observed between the measured PIV results and the two rectification variations examined,

particularly for the shape factor, H . In Table 6.3, two values are given for the shape factor at transition onset. The first is the value calculated from the averaged PIV measurements, and includes the reverse flow. The second value assumes zero velocity for any reverse flow near the wall, which is typically seen in hot-wire measurements up to the location of transition onset (Volino and Hultgren, 2001; Volino, 2002a; Roberts and Yaras, 2003).

There have been many empirical or semi-empirical models proposed in the literature to predict transition in a separated shear layer. The models most commonly cited for the onset of transition are those by Roberts (1975), Davis *et al.* (1987), Mayle (1991), and Hatman and Wang (1999). More recently, models have been proposed by Volino and Bohl (2004), Roberts (2005), and Praisner and Clark (2007). Of the available models, those of Roberts (1975), Davis *et al.* (1987), and Volino and Bohl (2004) exhibit strong sensitivity at low freestream turbulence levels (due to singularities at $Tu = 0$), which precludes them from being used to predict separation bubble transition at negligible freestream turbulence conditions. The models examined herein were described in the Literature Review chapter (Section 2.4), and the mathematical formulations are provided here for the sake of completeness.

In his critical review of transition research for gas turbine applications, Mayle (1991) proposed two correlations to predict the onset of transition in a separated shear layer. In these correlations the distance between separation and transition onset is related to the momentum thickness at separation:

$$Re_{s-ts} = 300Re_{\theta_s}^{0.7} \quad (\text{short bubble}) \quad (6.1a)$$

$$Re_{s-ts} = 1000Re_{\theta_s}^{0.7} \quad (\text{long bubble}) \quad (6.1b)$$

Hatman and Wang (1999) proposed a set of empirical transition models based a series of experiments aimed at examining the nature of separated-flow transition at low freestream

turbulence levels (Hatman and Wang, 1998a; Hatman and Wang, 1998b; Hatman and Wang, 1998c). Their model for transition onset in a separated shear layer is:

$$Re_{ts} = 1.0816Re_s + 26,805 \quad (6.2)$$

which has been shown to work well under low freestream turbulence conditions (Yaras, 2001).

Recently, Praisner and Clark (2007) re-examined the available models for separated-flow transition and proposed a correlation based on a new set of similarity criteria. Their model, which is based primarily on a database of axial turbomachinery-type experimental data, is formulated as:

$$\frac{s_{ts} - s_s}{s_s} = 173Re_{\theta_s}^{-1.227} \quad (6.3)$$

This model is shown to work well in predicting the separation characteristics of highly-loaded low-pressure turbine cascades (Praisner *et al.*, 2007).

Roberts (2005) has proposed a set of semi-empirical transition-onset and transition-rate prediction models. His correlation for the onset of transition has the same functional form as those of Mayle (Equation 6.1) but also accounts for the effects of freestream turbulence and surface roughness, as described in Section 2.4 (Equation 2.1 on page 33). The smooth-surface form of Roberts' correlation is given as:

$$Re_{s-ts} = [785 - 30TF(\%)] Re_{\theta_s}^{0.7} \quad (6.4)$$

where TF is Taylor's turbulence factor and is set to zero for predicting the present test cases. This model was developed from a large set of experimental measurements with systematic variations in flow Reynolds number, pressure distribution, freestream turbulence levels, and surface-roughness geometry. It should be noted that the range of Reynolds numbers with which Equation 6.4 was developed are much higher than those examined in the present

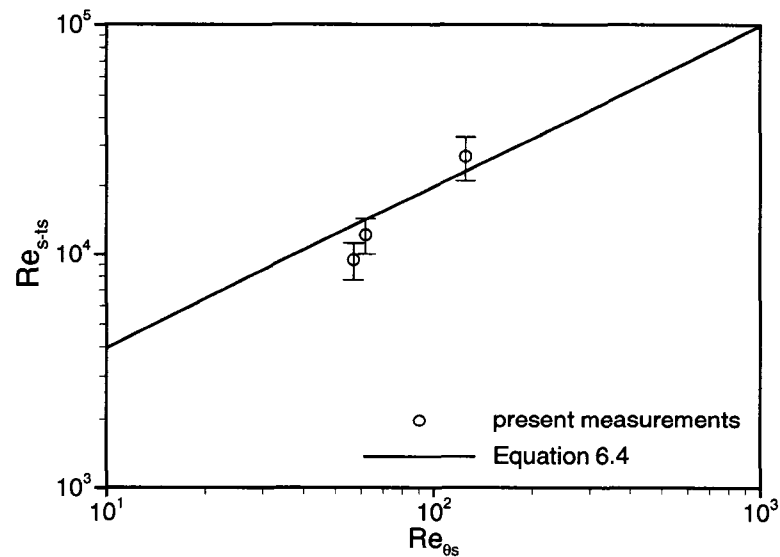


Figure 6.10: Comparison of results with transition-onset model of Roberts (2005)

experiments ($169 \leq Re_{\theta_s} \leq 444$ as compared to $57 \leq Re_{\theta_s} \leq 125$). Equation 6.4 is compared to the present experimental data in Figure 6.10 which, despite some differences, shows good agreement for all three cases. The differences between the actual and predicted transition onset locations, based on Roberts' model, fall within the scatter of the data from which the model was developed (Roberts, 2005). Therefore, the reliable prediction under the present conditions provides an extension to the Reynolds number range over which Equation 6.4 was calibrated ($57 \leq Re_{\theta_s} \leq 444$). Also, as the model was developed from experiments made over a flat test surface, the present measurements provide confidence that convex surface curvature does not play a dominant role in affecting the transition onset location in a separation bubble, at least for the levels of curvature over the SD7003 airfoil.

The empirical correlations of Mayle (Equation 6.1), Hatman & Wang (Equation 6.2), Praisner & Clark (Equation 6.3) and Roberts (Equation 6.4) are compared with the present experimental data in Figure 6.11. The dependent parameter in Figure 6.11 represents the

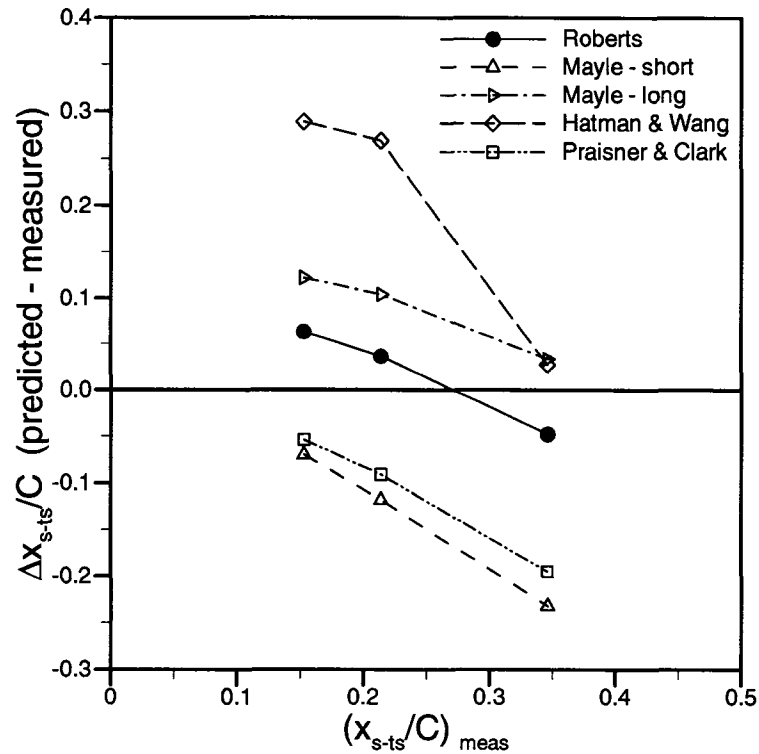


Figure 6.11: Comparison of various transition-onset prediction models

difference between the measured and predicted separation-to-transition lengths:

$$\frac{\Delta x_{s-ts}}{C} = \frac{x_{s-ts}}{C} \Big|_{pred} - \frac{x_{s-ts}}{C} \Big|_{meas} \quad (6.5)$$

The models of Mayle-short and Praisner & Clark show reasonable agreement for the shortest bubble ($R40\alpha10$ case) yet show increased under-prediction for the longer bubbles. On the other hand, the Mayle-long and the Hatman & Wang models show over-prediction for the short bubble with good agreement for the long bubble. Of all the models examined, the model of Roberts provides the most consistent prediction of the transition onset location for the present experimental data.

6.5 Conclusions

Transition in a separation bubble has been examined at low Reynolds numbers and low freestream-turbulence intensity using particle image velocimetry (PIV), and the results have provided confidence in using such techniques for separation-bubble-transition studies.

For a range of flow Reynolds numbers and streamwise pressure distributions, breakdown to turbulence in the separated shear layer over the SD7003 low-Reynolds-number airfoil is observed to be dominated by the Kelvin-Helmholtz instability mechanism. The data has allowed detailed observation of vorticity roll-up in the shear layer and the downstream shedding of this vorticity. Breakdown to turbulence is noted to occur at the most upstream location where instantaneous reattachment of the separated shear layer occurs. Secondary and tertiary reverse-flow zones, which are induced by vortices shed from the transition region of the separated shear layer, have been identified in the reattachment region. These shed vortices are generated by roll-up of spanwise vorticity within the shear layer and persist to the trailing edge of the airfoil. In some instances, the frequency of vortex shedding is noted to be the first subharmonic of the primary instability frequency prevailing in the separated shear layer, suggesting the presence of a vortex-pairing process. The Strouhal number based on the instability frequency, the momentum thickness at separation, and the freestream velocity at separation corresponds well with values identified in published literature for Kelvin-Helmholtz-induced transition in separation bubbles. The measured locations of transition onset are predicted well by the empirical model of Roberts (2005), and therefore provide further validation of this model for an extended low-Reynolds-number range and for the effects of convex surface curvature.

Chapter 7

Numerical Study of Instability Mechanisms Leading to Transition in Separation Bubbles

7.1 Chapter Overview

Through numerical simulation, this chapter examines the nature of instability mechanisms leading to transition in separation bubbles. The results of two direct numerical simulations are presented in which separation of a laminar boundary layer occurs over a flat surface in the presence of an adverse pressure gradient. The primary difference in the flow conditions between the two simulations is the level of freestream turbulence with intensities of 0.1% and 1.45% at separation. The flow conditions for both simulations are described in Section 7.2.

Separated shear layers and the process of laminar-to-turbulent transition occurring therein share characteristics with both boundary-layer and free-shear-layer flows. Despite

the extensive background and references provided in Chapter 2 regarding separation-bubble transition, this chapter re-examines the literature in an effort to provide a context for the interpretation of the simulation results. This includes a comparative analysis of separated and free shear layers in Section 7.3, with regards to transition in a low-disturbance environment. Section 7.4 describes transition of a separated shear layer under elevated freestream turbulence, and provides comparisons with transition phenomena observed in attached boundary layers. A comparison of the two cases is given in Section 7.5, which includes a discussion regarding recovery of the reattached turbulent boundary layer to an equilibrium state.

7.2 Flow Conditions

The flow conditions and some characteristics of the separation bubbles for the two simulations are compared in Table 7.1. Details regarding the numerical setup and boundary

Table 7.1: Flow conditions and separation-bubble characteristics for the two simulations

	Low- Tu	Elevated- Tu
Flow Reynolds number, $Re_{sp} = U_{sp}L_p/\nu$	440,000	390,000
Time-averaged separation location, x_s	0.514 m	0.518 m
Time-averaged bubble length, $L_b = x_r - x_s$	0.116 m	0.048 m
Transition onset location, x_{ts}	0.597 m	0.522 m
Transition length, $L_t = x_{te} - x_{ts}$	0.028 m	0.078 m
Turbulence intensity at separation, Tu_s	0.1 %	1.45 %
Turbulence integral length scale at separation, Λ_{fs}	0.020 m	0.011 m
Displacement thickness Reynolds number at separation, Re_{δ^*s}	1006	1034
Momentum thickness Reynolds number at separation, $Re_{\theta s}$	267	335
Shape factor at separation, H_s	3.77	3.08

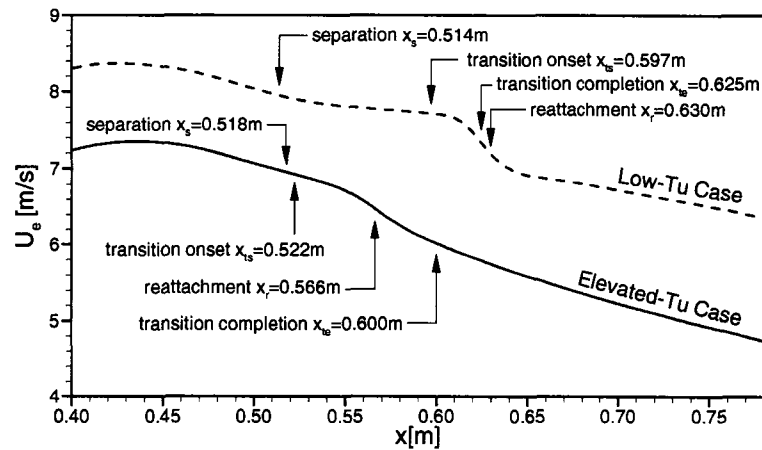


Figure 7.1: **Boundary-layer-edge velocity distributions for both simulations in the region $0.40 \text{ m} < x < 0.78 \text{ m}$**

conditions that result in these flow conditions were provided in Chapter 4. The flow Reynolds number identified in Table 7.1 is based on the suction peak velocity and the computational wall length ($L_p = 0.78 \text{ m}$). Figure 7.1 shows the boundary-layer-edge velocity distributions for both cases near and downstream of the suction peak, and provides the time-averaged locations of separation, transition onset, transition completion, and reattachment for the observed separation bubbles. The flow Reynolds numbers and streamwise pressure distributions are typical of the conditions encountered on the suction side of low-pressure turbine blades in gas-turbine engines. It is evident through the data in Table 7.1 and Figure 7.1 that the presence of freestream turbulence alters the transition process and the resultant separation-bubble characteristics. This chapter is intended to describe the physical mechanisms resulting in these differences. It should also be noted that both of the separation bubbles observed in the simulations can be classified as “short-bubbles” in that, in the experiments upon which the simulations are based, they do not significantly alter the streamwise pressure distribution, upstream and downstream of the separation bubble, from that observed in the absence of separation at higher Reynolds numbers.

7.3 Low-Freestream-Turbulence Case

In the absence of any significant levels of environmental disturbances, transition of a separated shear layer has been shown to occur through the Kelvin-Helmholtz (K-H) instability mode whereby receptivity of the layer to small disturbances results in grouping of spanwise vorticity at selective streamwise wavelengths. This was seen in the experimental results of Chapter 6, and is analogous to Tollmien-Schlichting (T-S) instability growth in attached boundary layers under such conditions. The growth of this separated-shear-layer instability leads to roll-up of the vorticity contained in the layer into discrete spanwise vortex structures, which subsequently break down to small-scale turbulence, thereby initiating reattachment to the surface. The process preceding reattachment closely resembles that which occurs in planar free shear layers, and further comparison to such processes is presented in Section 7.3.3.

As part of the ongoing transition-research at Carleton University, Roberts (2005) recently demonstrated, through a study with experimental and computational components, that transition of a separated shear layer through the K-H instability does not preclude the presence of T-S activity in the shear layer. Roberts highlighted the possibility of an interaction between the two instability modes, with the roll-up of shear-layer vorticity into vortical structures occurring at the dominant T-S frequency expected in the laminar boundary layer upstream of separation. The present effort is a follow-up of that study, focusing on numerical simulation of another separation-bubble-transition case that was expected to have, based on experimental measurements of Roberts, significantly more pronounced T-S activity. Analysis of the present findings within the context of those documented by Roberts, provides a better understanding of the relative roles of the T-S and K-H instability mechanisms in separation-bubble transition.

7.3.1 Selection of Conditions

The freestream velocity distributions for two experimentally-measured separation-bubble cases are shown in Figure 7.2. Test Cases 1 and 2 correspond to the Cp1 and Cp4 pressure distributions, respectively, identified in Roberts' experiments (Roberts, 2005). Test Case 2 is the case examined numerically by Roberts for which the potential interaction of the K-H and T-S instabilities was highlighted, and is noted to have a stronger initial acceleration and a stronger deceleration prior to separation, as compared to Test Case 1. For both cases, the flow Reynolds number based on the length of the test plate (1.22 m) and the midspan freestream velocity just downstream of the leading edge (approximately 4.2 m/s) is 350,000, and the freestream turbulence intensity at the test-surface leading edge is 0.7%.

Characteristics of the measured separation bubbles are summarized in Table 7.2. The momentum-thickness Reynolds number based on conditions at the point of separation is fairly similar for the two cases. The time-averaged bubble length, L_b , is notably shorter in Test Case 2 due to the differences in the adverse pressure gradient imposed on the boundary layer, as demonstrated by the lowest observed values of the acceleration parameter upstream

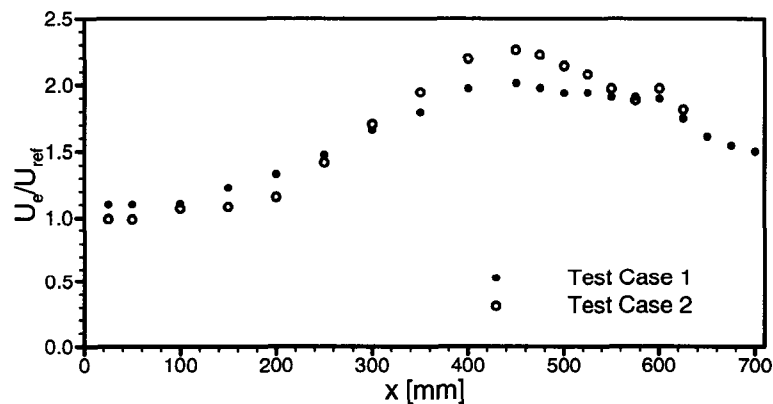


Figure 7.2: Measured freestream velocity distributions

Table 7.2: Measured separation bubble characteristics

	Test Case 1	Test Case 2
x_s (mm)	498	525
L_b (mm)	127	100
Re_{θ_s}	258	309
$\eta_{min} \times 10^6$	-1.6	-2.3
f_{MA} (Hz)	170	200
f_{MA} (Eqn. 7.1)	150	120
κd	0.40-0.44	0.34-0.41
Sr_{θ_s}	0.0106	0.0110

of separation (η_{min}). Figure 7.3 presents measured velocity-fluctuation time traces for the two cases at various streamwise locations through the separation bubble, at a fixed distance of 2 mm from the test surface. The streamwise co-ordinate used for comparison in this figure is the distance from the separation location, $x' = x - x_s$, normalized by the time-averaged length of the separation bubble, L_b . In Test Case 2, presented in the right column of the figure, a periodic wave motion is observed to develop slowly in the separated shear layer. The dominant frequency of this motion is approximately 200 Hz, which is somewhat larger than the value of 120 Hz predicted for the growth of T-S waves in the pre-separated boundary layer through the correlation of Walker (1989), defined by:

$$f_{MA} = \frac{3.2U_e^2}{2\pi\nu Re_{\delta^*}^{3/2}} \quad (7.1)$$

However, Chandrasekhar's stability parameter, κd , and the Strouhal number equivalent, Sr_{θ_s} , are both within the ranges observed in the literature for K-H dominated transition

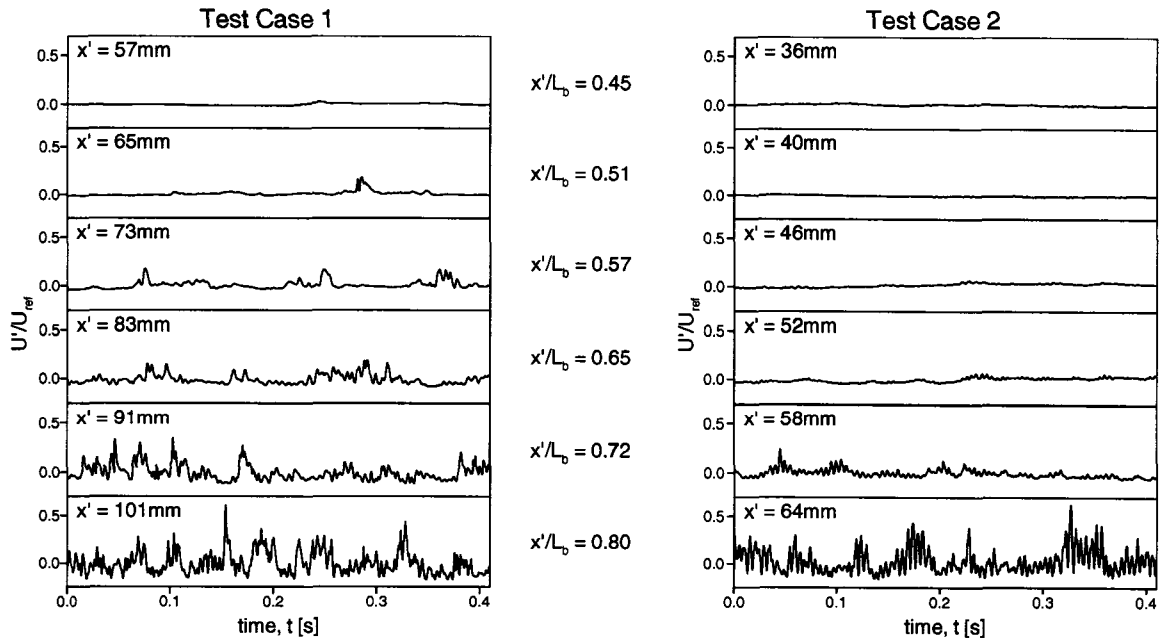


Figure 7.3: Sample hot-wire velocity-fluctuation time traces

(Section 2.2.1). The numerical study of Test Case 2 by Roberts demonstrated excellent agreement with experimental results, with respect to the time-averaged size and shape of the separation bubble, the frequency spectra of streamwise velocity fluctuations, and the location of breakdown to turbulence. Roberts used a numerical scheme similar to that used for Test Case 1 in the present study (the computational setup is described in Chapter 4). Through his simulation, the breakdown to turbulence noted in the range $0.72 \leq x/L_b \leq 0.80$ in the right column of Figure 7.3 was observed to be linked to the K-H instability. Specifically, transition to turbulence was noted to be associated with the roll-up of vortical structures near the downstream end of the separation bubble, and shed downstream periodically, similar to what was observed in the PIV measurements of the SD7003 airfoil documented in Chapter 6. The frequency of vortex shedding was found to coincide with the frequency of maximum amplification rate of the instability waves in the separated shear layer.

For Test Case 1, small-amplitude fluctuations are seen up to $x'/L_b = 0.51$, as with Test Case 2. Beyond this point, the two test cases begin to differ, with isolated regions (packets) of amplified disturbances appearing more distinctly in the time traces of Test Case 1. The frequency of maximum amplification rate in these wave packets is approximately 170 Hz, which is in reasonable agreement with the correlation of Walker (Equation 7.1) for T-S waves, yielding a value of 150 Hz. The values of Chandrasekhar's stability parameter, κd , and the Strouhal number equivalent, $Sr_{\theta s}$, are noted to be within the range of K-H instability in both test cases (Table 7.2). The present numerical simulation of Test Case 1 is intended to shed further light on the spatial and temporal development of the packets of strong instability amplification, and on their role in the breakdown of the separated shear layer into turbulence.

7.3.2 Validation of Simulation Results

Figure 7.4 presents the measured and computed velocity-fluctuation time traces at several locations along the separated shear layer for Test Case 1. The agreement between the two sets of velocity traces is good, with the exception that the packets of amplified velocity fluctuations appear somewhat later in the simulation than in the experiment. The fact that the simulated freestream turbulence intensity was slightly lower than the measured value may explain this discrepancy. Measured and predicted frequency spectra of velocity fluctuations are given in Figure 7.5 for several streamwise locations. These frequency spectra compare favorably, although the simulation results have more pronounced peaks at the dominant frequency. In both the measured and predicted spectra, the power spectral density (PSD) at the high end of the frequency range is observed to remain relatively low until about $x' = 101$ mm. This trend, and the fact that the streamwise-growth of disturbances at the dominant frequency remains close to exponential until about $x' = 90$ mm (Figure 7.6), suggests that the isolated packets of high-amplitude velocity fluctuations observed in both

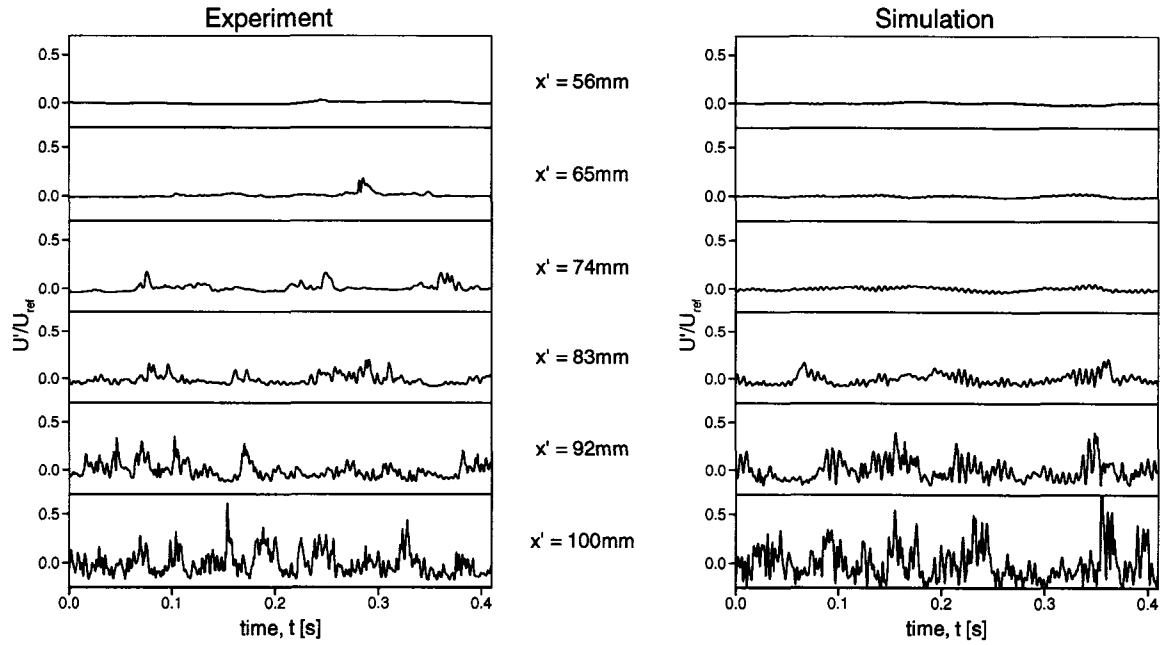


Figure 7.4: Comparison of measured and computed velocity-fluctuation time traces for Test Case 1 ($y = 2 \text{ mm}$)

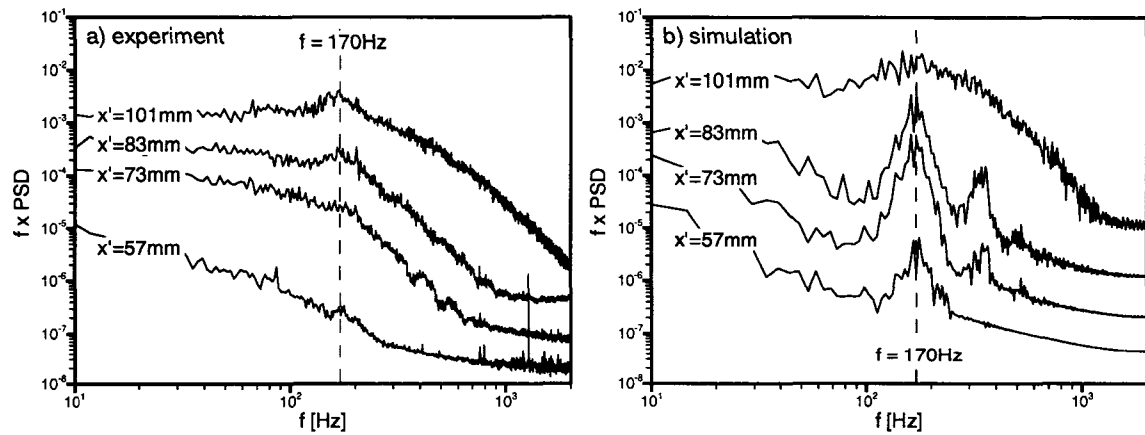


Figure 7.5: Disturbance spectra in the separation bubble

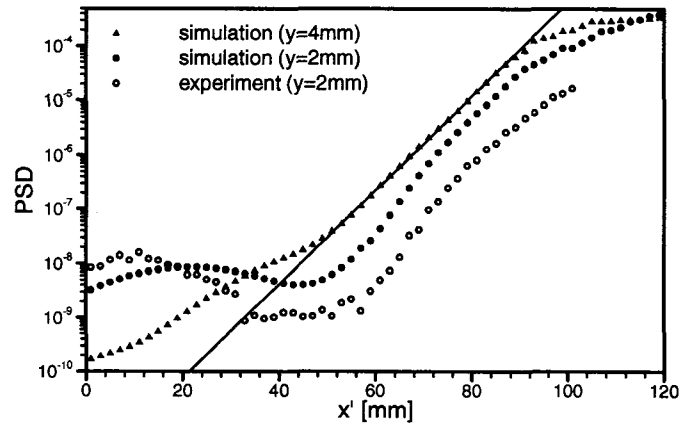


Figure 7.6: Instability growth rates at the dominant frequency

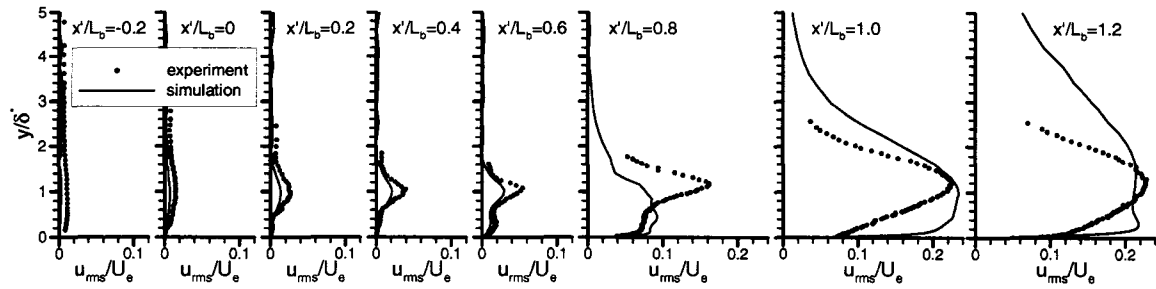


Figure 7.7: Streamwise velocity fluctuation profiles in the separation-bubble region

measured and computed velocity time traces (e.g. $x' = 83$ mm in Figure 7.4) are related to instability growth prior to breakdown into turbulence.

As shown in Figure 7.7, simulated streamwise velocity fluctuations are in reasonable agreement with experiment through the separation-bubble region. The velocity fluctuations upstream and downstream of reattachment are more dispersed, and extend farther from the wall in the simulations. This is likely caused by the higher energy content about the dominant instability frequency (Figure 7.5), which yields an over-prediction of the power spectral density across the frequency spectrum downstream of breakdown into

turbulence. The lower intensity of random fluctuations associated with the simulated freestream turbulence may have allowed for the greater concentration of energy about the dominant instability frequency.

The favorable comparison between the instability frequency and associated growth characteristics between the simulation and experiment provides confidence that the DNS results adequately capture the dominant physics of the transition process.

7.3.3 Instability Mechanisms

In planar free-shear layers, which share characteristics with separated shear layers, the process of laminar-to-turbulent transition is typically initiated through receptivity of the inflectional velocity profile to environmental disturbances. In the absence of a bounding wall, the shear layer is unstable via the inviscid Kelvin-Helmholtz (K-H) mode. Growth of the most-amplified instability frequency results in the roll-up and formation of vortices with a direction that is consistent with the vorticity of the shear layer. The dominant instability frequency has been shown to scale with the shear-layer momentum thickness through a Strouhal number, $Sr_\theta = f\theta/\Delta U$, where ΔU is the velocity difference across the shear layer. Ho and Huerre (1984) have identified the frequency of maximum amplification in an unforced planar free shear layer to correspond to $Sr_\theta = 0.016$.

The initial development of the separated shear layer in the present simulation exhibits the same characteristics as a planar free-shear layer. Downstream of separation, an instability develops that causes the vorticity in the shear layer to roll-up into distinct spanwise vortical structures. An example of the transient vorticity roll-up that occurs in the separated shear layer is shown in Figure 7.8. Approximately two periods of the dominant instability frequency are shown in this figure, and the trajectories of two distinct vortices are identified. The observed structures are similar to those identified in the

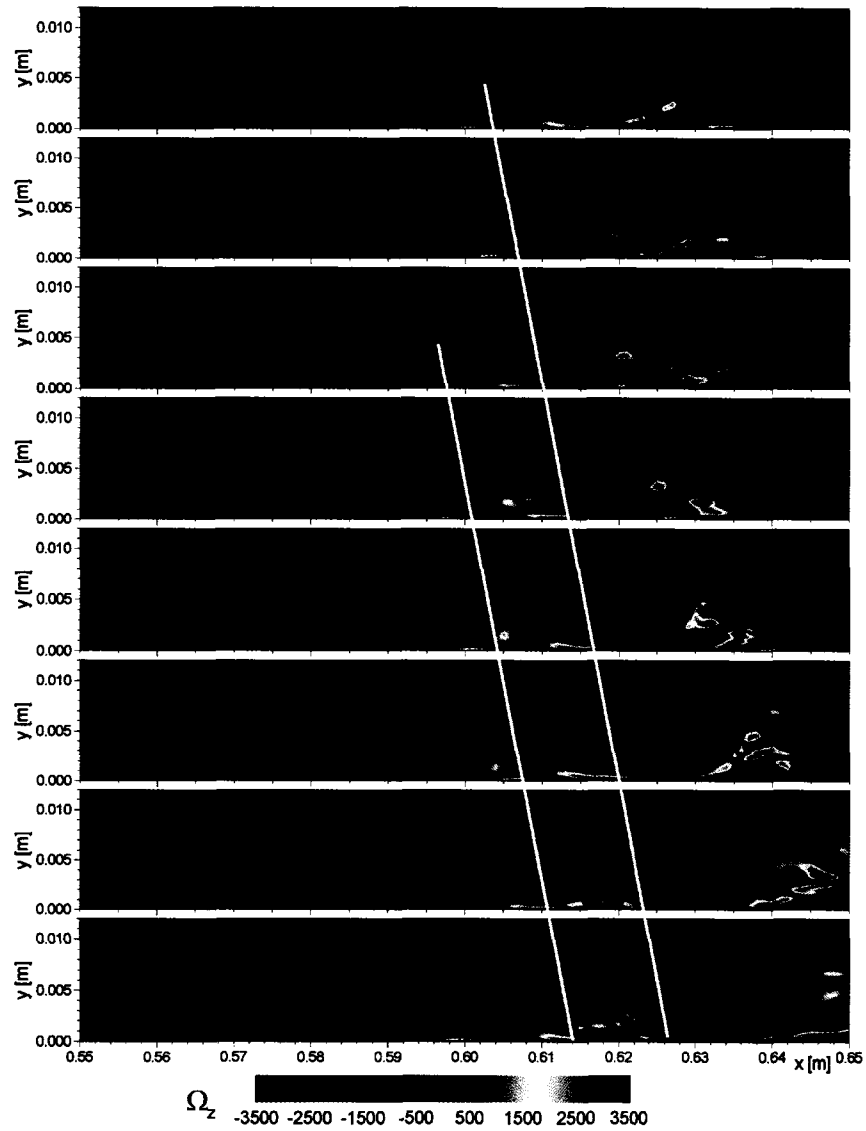


Figure 7.8: Vorticity roll-up of the separated shear layer caused by the Kelvin-Helmholtz instability (series of temporally-spaced plots, with trajectories of two roll-up vortices shown by white lines)

PIV measurements of Chapter 6. As the vortices saturate and are shed downstream of the separated shear layer, smaller-scale vortical structures are observed in Figure 7.8, indicating that transition to small-scale turbulence has been initiated. The periodicity of the convecting instability is what causes a dominant frequency (170 Hz) to emerge in the power spectra provided in Figure 7.5. For separated shear layers, the frequency associated with maximum amplification of the instability is generally in close agreement with that of planar free-shear layers and is conventionally presented as a Strouhal number based on conditions at separation ($Sr_{\theta_s} = f\theta_s/U_{es}$). Table 7.3 presents the dominant instability Strouhal number observed in the present simulation together with those of the experimental studies of Chapters 6 and 8, and other experimental and computational studies of separated shear layers. The tabulated values are consistent with the most rapidly amplified instability frequency obtained through a stability analysis as presented by Dovgal *et al.* (1994) for analytical velocity profiles similar to those prevailing in separation bubbles. The variation observed in Table 7.3 is attributed to differences in the level of reverse-flow and shape of the base-flow velocity profiles.

Table 7.3: Instability Strouhal numbers identified in several experimental and numerical studies involving shear layers with inflectional velocity profiles

Study/Investigators	$Sr_{\theta_s} = f\theta_s/U_{es}$
Present simulation	0.011
SD7003 airfoil experiments (Chapter 6)	0.008-0.013
Unconventional airfoil experiments (Chapter 8)	0.015-0.020
Muti Lin and Pauley (1996)	0.005-0.008
Yang and Voke (2001)	0.005-0.011
Talan and Hourmouziadis (2002)	0.010-0.014
Ho and Huerre (1984) (free-shear layer, Sr_{θ})	0.016

Through analysis based on linear stability theory, Rist and Maucher (2002) examined the effect of profile shape on the stability of velocity profiles with reverse flow near the surface, and found two regions in which the associated instabilities show differing characteristics. The outer “separated” part of the shear layer is unstable via an inviscid-type instability, with minimal Reynolds number influence, while in the reverse-flow region near the wall a viscous Reynolds-number-dependent instability is present. The dominance of one mode over the other was found to depend on the distance of the zero-velocity point from the surface, and on the level of reverse flow prevailing near the wall. Increased distance from the surface promotes the outer-layer inviscid mode, as well as promoting an increase in the associated frequency and growth rates of this instability. Conversely, an increase in the level of reverse flow promotes the inner viscous instability, with an associated decrease in frequency and increase in growth rate. Comparing the velocity profiles of the present simulation (Figure 7.9a) and those of the studies outlined in Table 7.3 with those examined by Rist and Maucher, with respect to distance of the shear layer from the wall and level of reverse flow, would indicate a predominance towards the outer-layer inviscid instability. In examining the fluctuation levels observed in the present simulation (Figure 7.9b), those associated with the inviscid instability in the separated shear layer appear to dominate, with co-existence of near-wall viscous instability as suggested by the near-wall fluctuation peak observed downstream of $x = 0.58$ m. This near wall peak was also observed in the SD7003 experiments of Chapter 6 (Figure 6.2, page 115). In experimental results presented by Lang *et al.* (2004) for a separation bubble in which the most unstable inviscid frequency was forced by a vibrating wire upstream of separation, similar fluctuation peaks were found in the inner and outer regions of the separated shear layer, with fluctuation profiles that were in very good agreement with linear stability analysis of the base-flow profile. These results provide evidence that although the dominant instability in separation bubbles leading to transition in a low-disturbance environment is of the inviscid Kelvin-Helmholtz type, the influence of viscous instability near the wall should not be dismissed, particularly in very

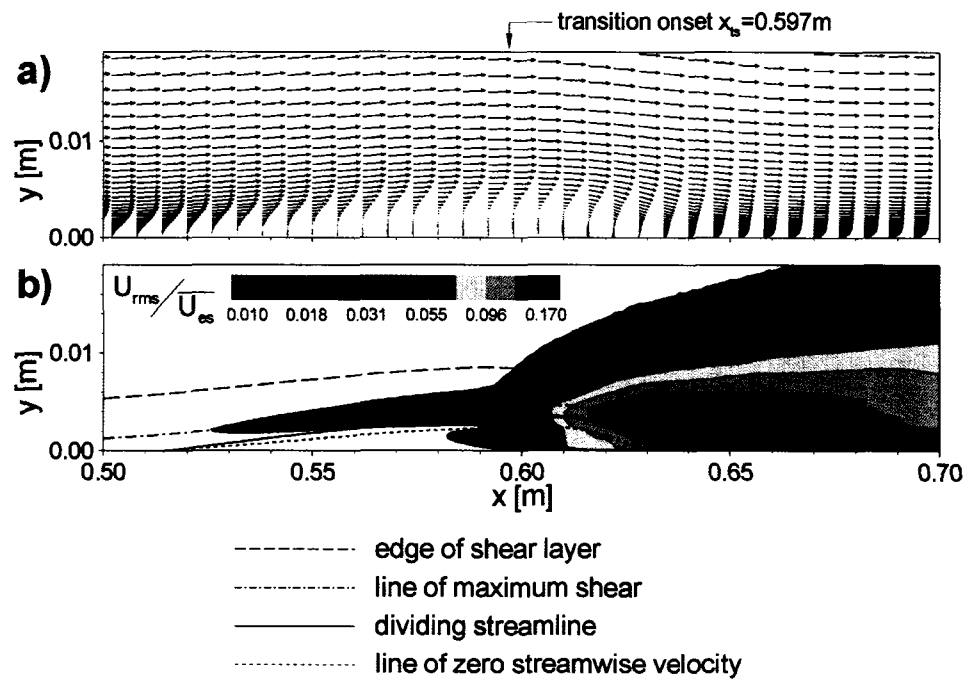


Figure 7.9: Separation-bubble characteristics under low- Tu freestream conditions (wall-normal coordinate stretched for better visualization), a) Time-averaged velocity vector profiles with every 6th profile shown, b) velocity fluctuation levels

thin separated shear layers or in those with significant levels of reverse flow.

Increased levels of reverse flow in a separated shear layer can also lead to an absolute instability for which associated fluctuations can propagate upstream and become self-sustaining. A criterion often used to assess whether an absolute instability is present in a separation bubble is the level of reverse flow in the near-wall region. Alam and Sandham (2000) identified a threshold of approximately 15-20% of the local freestream velocity, above which absolute instability prevails. However most studies, including the one presented here, indicate that laminar separation bubbles that occur over the surfaces of airfoils have reverse-flow levels much lower than this threshold, and the associated instability is therefore convective in nature. In our present simulation, for which the base-flow velocity profiles are presented in Figure 7.9a, the reverse-flow velocity in the

separation bubble remained less than 10% of the local freestream velocity.

The evidence presented thus far, in regards to the present simulation and the results of others, indicates that the K-H instability is the dominant mechanism associated with transition in a separated shear layer, in the absence of any significant level of environmental disturbances to which the shear layer is receptive. This leaves unanswered the question of whether or not the T-S instability plays a role in the process, as was proposed by Roberts based on his and others' experiments (Roberts, 2005; Volino, 2002*b*; Gostelow and Thomas, 2006). Whether or not instabilities arising in shear flows are deemed to be K-H or T-S has historically been determined by the type of flow under consideration. Specifically, K-H is generally discussed in regards to free shear layers as an inviscid phenomenon and T-S is generally discussed in regards to boundary layers as a viscous instability. Although the manner in which the instabilities are initiated differs, through either an inflectional velocity profile (K-H) or viscous effects (T-S), the general characteristic of both instabilities are very similar: amplification of infinitesimal disturbances leads to streamwise grouping of the spanwise vorticity contained in the shear layer, providing a convecting wave-pattern that amplifies, develops three-dimensional features through a secondary nonlinear instability, and eventually breaks down into three-dimensional, small-scale turbulence. These considerations indicate that there is a strong link between the two. Of course, the separate classification in regards to laminar-to-turbulent transition of boundary-layer and free-shear-layer flows has not been based solely on stability concerns alone. Breakdown to small-scale turbulence in these flows differs in both its characteristics and its resulting flow structures. In boundary layers, transition is most often associated with the production, growth, and merging of turbulent spots, whereas free-shear-layer transition is often associated with the production and diffusion of small-scale turbulence within the large-scale roll-up vortices. These differences will be discussed later in regards to the observed breakdown process seen in the simulations. As for the close agreement between

the dominant K-H frequency in the separated shear layer and the expected T-S frequency in the upstream laminar-boundary-layer, based on Walker's correlation (Equation 7.1), the above-noted considerations provide an argument that this would likely be expected under separation-bubble conditions. A Strouhal number based on the T-S frequency expressed by Equation 7.1 can be formulated as:

$$Sr_{\theta} = \frac{f \cdot \theta}{U_e} = \frac{3.2}{2\pi \cdot Re_{\theta}^{\frac{1}{2}} \cdot H^{\frac{3}{2}}} \quad (7.2)$$

which is plotted in Figure 7.10 for a range of Re_{θ} and H that can be expected upstream of separation bubbles occurring over typical airfoils. The range of Strouhal numbers observed in Figure 7.10 is in very good agreement with the range of Strouhal numbers identified in Table 7.3 for K-H instability frequencies in separated shear layers. This provides further evidence to indicate that the two mechanisms, K-H and T-S, share fundamental similarities in regards to separation-bubble transition.

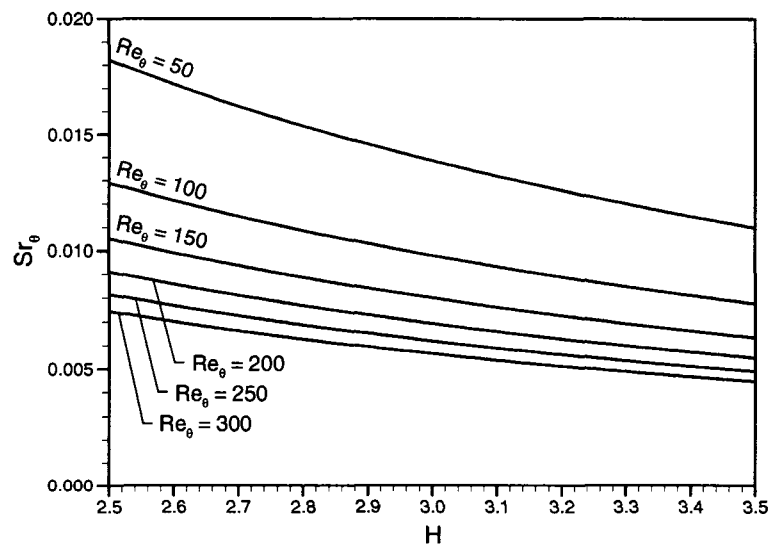


Figure 7.10: Strouhal numbers based on the correlation of Walker (Equation 7.2) for boundary layer parameters typically observed upstream of separation bubbles

One of the reasons for which Roberts (2005) assumed that there was pronounced T-S activity in the experimental test case upon which the present simulation was based was the observed “packets” of amplified instabilities, seen in the experimental velocity traces of Figures 7.3 and 7.4. It was believed that these packets were a result of turbulent spots being generated in the separated shear layer. Upon examining the results of the simulation for Test Case 1, these packets, which are present in the simulation but occur further downstream, are not a result of turbulent spots but represent periods of time in which the instability waves are more strongly amplified. The fact that the packets are more pronounced in the experimental traces is likely caused by the higher level of freestream turbulence which provides a greater level of buffeting by the large-scale freestream eddies on the shear layer, and may periodically cause earlier amplification of the instability waves. To describe the physics associated with the subsequent amplification and damping of fluctuations within these packets, profiles of instantaneous streamwise velocity and $u'v'$ during a period of amplified instability at $x' = 85$ mm are presented in Figure 7.11 along with the velocity-fluctuation time traces at 2 mm and 4 mm from the surface. The profiles shown are associated with peaks and troughs of the velocity signal at 4 mm from the surface. At the start of the period shown in Figure 7.11, the streamwise velocity profiles have relatively high levels of reverse flow (10-15% of edge velocity) with low levels of $u'v'$. The inherent instability of this velocity profile causes an increase in the amplitude of fluctuations and also results in the shear layer moving closer to the surface. The peaks of these amplified fluctuations are noted to correspond to large negative values of $u'v'$ in the region of highest vorticity, located near the velocity-profile inflection points, which facilitate cross-stream momentum exchange resulting in a diminished reverse flow, hence reduced inflectional shape of the velocity profile. This modification of the velocity profile then leads to a reduction in the amplitude of the velocity fluctuations.

In planar free-shear layers, the spanwise vortices produced by the K-H instability are

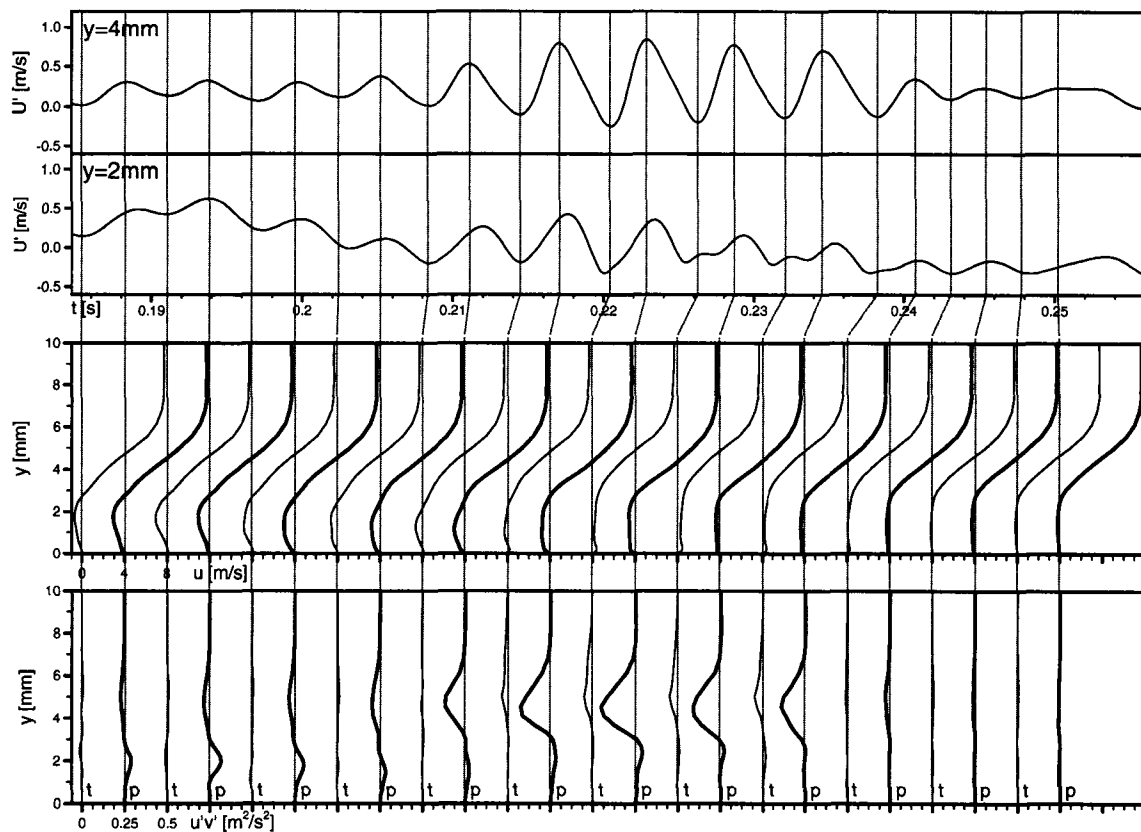


Figure 7.11: **Effects of instability growth on velocity profiles at $x' = 85\text{mm}$ (p-peak, t-trough)**

unstable to subharmonic disturbances (Kelly, 1967). This subharmonic instability leads to the vortex pairing phenomenon as observed in numerous experimental and numerical studies of such shear layers (Ho and Huerre, 1984; Huang and Ho, 1990; Esteveordal and Kleis, 1999). This pairing of vortices is suggested as the dominant mechanism associated with growth of planar free-shear layers (Ho and Huerre, 1984). The same vortex-pairing phenomenon has been observed in separation bubbles (Malkiel and Mayle, 1996; Wissink and Rodi, 2002; Abdalla and Yang, 2004), including the SD7003 experiments of Chapter 6. However, the presence of pairing has only been observed at lower Reynolds numbers (Re_{θ_s} of about 100), and was not observed in the current simulation for which $Re_{\theta_s} = 267$.

7.3.4 Breakdown Mechanisms

In planar free-shear layers, a spanwise non-uniformity is often observed, which has been tied to the development of streamwise counter-rotating vortex pairs (Ho and Huerre, 1984; Huang and Ho, 1990). It is surmised that this three-dimensionality is associated with a secondary instability superimposed on the primary two-dimensional instability (Pierrehumbert and Widnall, 1982), similar to that which occurs in boundary-layer transition when streamwise stretching of T-S waves begins (Schlichting and Gersten, 2000). The generation of small-scale turbulence in a planar free-shear layer has been associated with the interaction of these streamwise vortices with the spanwise vortices originating from the primary instability. The data of Huang and Ho (1990) revealed that small-scale fluctuations more frequently occur near the core of the streamwise vortices as they interact with a merging spanwise vortex pair. Malkiel and Mayle (1996) suggest transition in a separation bubble occurs through this interaction of streamwise and spanwise vorticity. However this interaction has not yet been identified in either spatially-resolved measurements or in numerical simulations involving separation bubbles, including the present simulation. Numerical studies performed by Spalart and Strelets (2000), Wissink and Rodi (2003), Roberts (2005), and the present simulation, indicate that in a separation bubble exposed to a low-disturbance environment, breakdown to turbulence occurs very quickly over a short streamwise distance. It should be noted that vortex-pairing is not observed in any of these cases.

Given that the packets of instability waves within the separated shear layer do not amplify to the point of bursting into turbulent spots, eventual breakdown into turbulence in the present simulation occurs as the separated shear layer rolls-up into vortical structures, as demonstrated in Figure 7.12. This figure presents instantaneous velocity vector fields in x - y and x - z planes. The level of velocity fluctuation with respect to the local time-mean velocity magnitude is illustrated through vector shading. The presence of small-scale

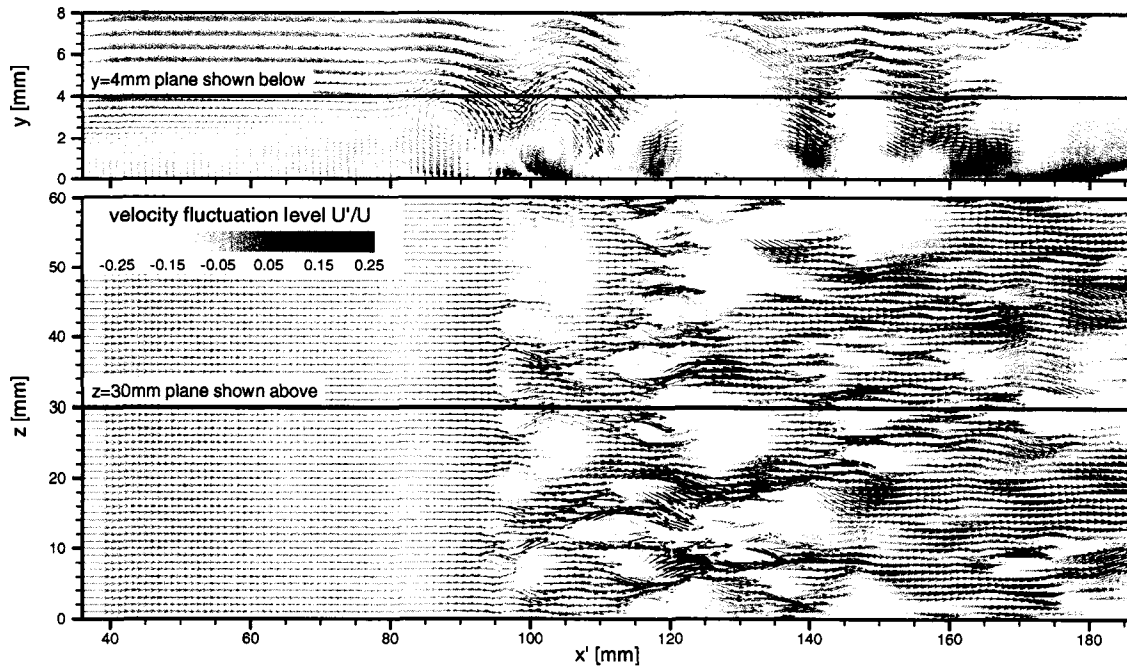


Figure 7.12: Instantaneous vector field through the transition region (x - y plane at $z = 30$ mm and x - z plane at $y = 4$ mm)

velocity fluctuations is found to correlate with the regions of high-shear that develop between pairs of spanwise-oriented vortical structures, an example of which is evident at $x' = 95$ mm in Figure 7.12. The most upstream location at which the smaller-scale structures have been detected is $x' \approx 90$ mm, which corresponds to deviation of the fluctuation growth rates from the exponential growth associated with the primary instability (Figure 7.6 on page 139). This breakdown to small-scale turbulence occurs in a time-periodic manner as the regions of high-shear, which convect with the spanwise vortices, travel through the separated shear layer, and complete breakdown occurs over approximately one wavelength of the primary instability. Figure 7.13a shows small distortions of the vorticity field, associated with this breakdown, in the roll-up region of the shear layer, and also shows the redistribution of the vorticity to progressively smaller scales downstream of reattachment. This breakdown is also seen as an increase and redistribution of the frequency content over a

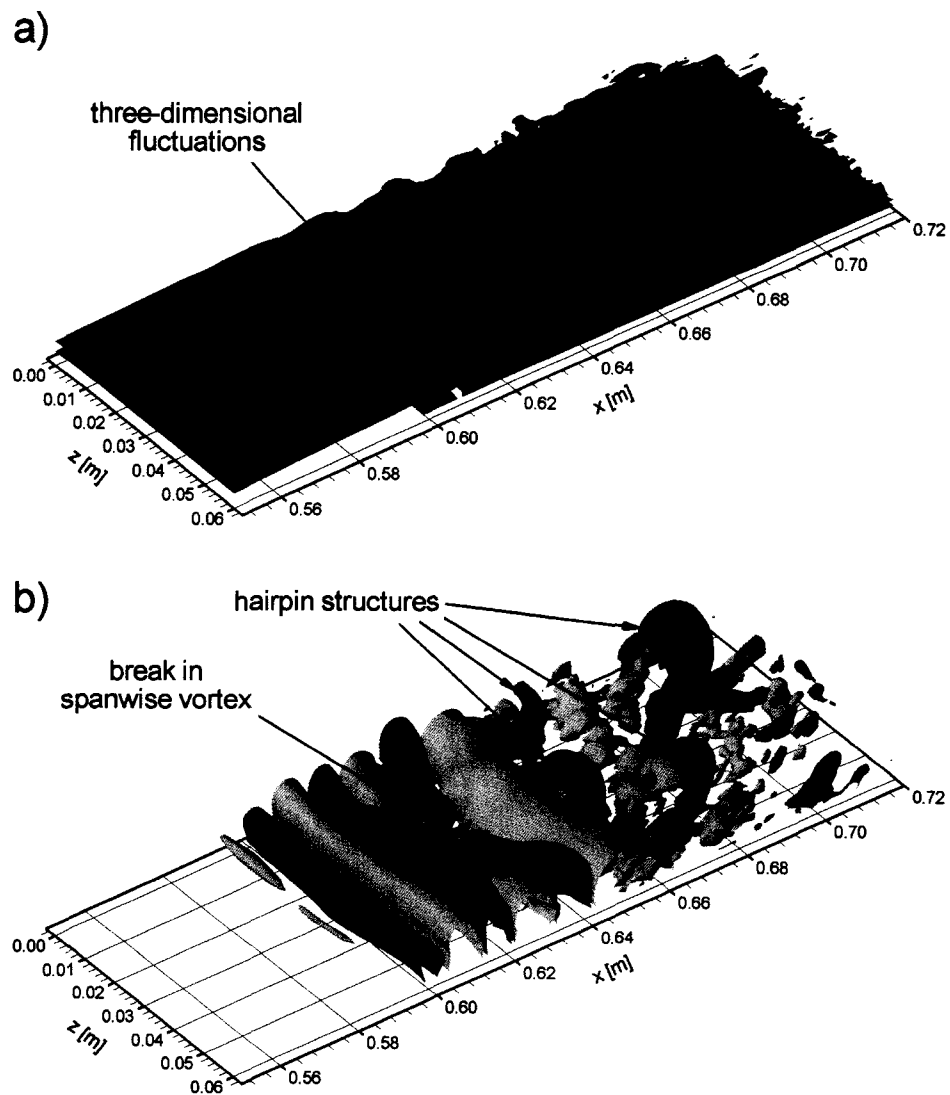


Figure 7.13: Transitional structures in the separation bubble under low- Tu freestream conditions, a) Vorticity iso-surface $\Omega = 1500 \text{ s}^{-1}$, b) Pressure iso-surfaces $p' = -1 \text{ Pa}$ (blue), $p' = 1 \text{ Pa}$ (yellow)

much wider range, as observed in the frequency spectrum near reattachment ($x' = 101$ mm) in Figure 7.5. Despite this breakdown to small-scale turbulence, coherence of the spanwise vortical structures is still observed downstream of transition, but their structure becomes distorted and stretched. These vortex structures are identified in Figure 7.13b by the blue low-pressure iso-contours. In the transition and reattachment region, stretching and reorientation of the vorticity contained in the vortical spanwise structures results in hairpin-like structures. These structures are reminiscent of those observed in turbulent boundary layers (Panton, 2001), and are also similar to those observed by Abdalla and Yang (2004) as a result of vortex pairing. The reorientation of vorticity in the streamwise direction provides enhanced momentum exchange in the wall-normal direction, and is likely a key mechanism associated with the reattachment process. Similar structures have been observed in the reattachment region of turbulent separation bubbles as well (Kiya and Sasaki, 1985).

The transition process described thus far, in regards to a low-disturbance environment, is altered significantly in the presence of elevated environmental disturbances. The next section describes the mechanisms associated with transition in a separation bubble under such conditions.

7.4 Elevated-Freestream-Turbulence Case

Laminar-to-turbulent transition of a shear layer is promoted by the presence of elevated freestream disturbances. Under such conditions, disturbances that penetrate the shear layer undergo an algebraic growth followed by viscous decay, unless they manage to grow to sufficiently large amplitudes to yield a turbulent spot. This path to transition is also referred to as transient growth or non-modal growth, with the latter referring to the fact that this mode is not predicted as one of the eigenmodes of the solution of linearized theories based on the Orr-Sommerfeld equation (Saric *et al.*, 2002). There is no definitive

threshold for when this transient-growth mechanism begins to dominate but it is strongly influenced by the magnitude of the disturbance as well as the receptivity of the shear layer to this disturbance. Once turbulent spots are produced, they grow and merge to form a fully-turbulent shear layer in a manner originally proposed by Emmons (1951). Bypass transition has been observed experimentally in separation bubbles by many researchers (e.g. Volino, 2002a; Roberts, 2005), and several studies have examined the growth of turbulent spots induced by a traveling wave-packet (Watmuff, 1999; D'Ovidio *et al.*, 2001a). In these “forced spot” cases, selectively amplified frequencies emerge from the wave packet, forming a convecting wave pattern within which breakdown to turbulence occurs. However, descriptions regarding the local flow development that leads to the creation of turbulent spots under elevated freestream turbulence conditions are scarce. Analysis of the second simulation of the present effort provides further information in this regard.

7.4.1 Selection of Conditions

As with the low-freestream-turbulence case, the present discussion of separation-bubble transition under elevated levels of freestream turbulence is focused on results of a direct numerical simulation for which the streamwise pressure distribution and flow Reynolds number are representative of those observed over the suction surface of low-pressure-turbine airfoils. The streamwise pressure distribution imposed on the upper surface of the computational domain was selected based on a test case of Roberts (2005) for which the freestream turbulence level was increased by means of a turbulence-generating grid placed at the inlet to the test section.

Figure 7.14 presents the freestream velocity distribution and turbulence-intensity levels observed in the simulation. The streamwise rate-of-decay of freestream turbulence downstream of the simulated turbulence grid at the inflow boundary is consistent with

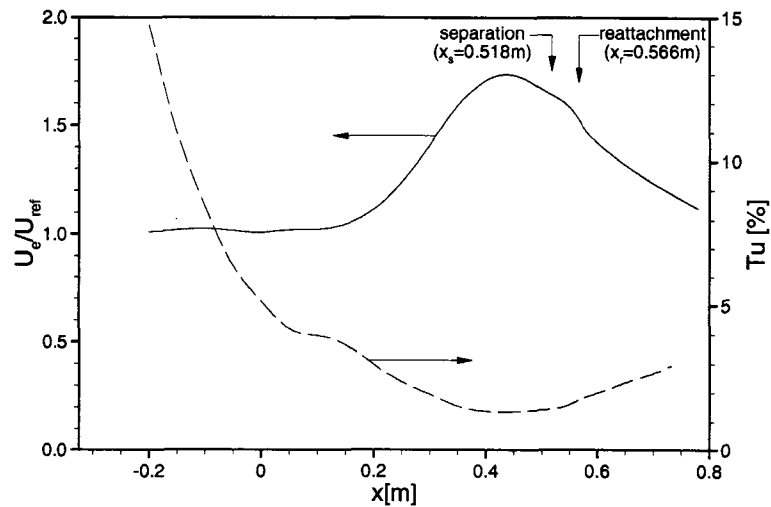


Figure 7.14: Streamwise distributions of freestream velocity and turbulence intensity

grid-generated turbulence in wind tunnels (Roach, 1987), and a slight anisotropy of the turbulence is observed. Above the plate leading edge ($x = 0$ m, $y = 0.015$ m) where the turbulence intensity is 5.1%, the streamwise fluctuation levels are 10% higher than those in the other two coordinate directions, which is consistent with the observations downstream of turbulence-generating grids of similar configuration (Roach, 1987). The strong streamwise acceleration imposed over the forward part of the flat plate causes a reduction in this streamwise turbulence intensity, providing a streamwise turbulence level over the separation bubble that is 10% lower than those associated with the wall-normal and spanwise components of velocity. As a result of the accelerating flow over the forward part of the surface, the turbulence intensity at the time-averaged streamwise location of separation is 1.45%, with a corresponding integral length scale of 0.011 m. Most studies presented in the literature, for which turbulence-generating grids were used, quote the level of turbulence intensity at the inlet of the test configuration. However, continual decay of the grid-generated turbulence, combined with the streamwise acceleration typically observed in similar turbomachinery flows, would tend to decrease the turbulence intensity upstream of separation to levels more comparable to those observed in the present case.

In the present simulation, transition in the separated shear layer is observed to occur through a transient-growth or bypass mode, whereby turbulent spots are generated as a result of disturbance growth in the laminar shear layer. Averaged velocity profiles through the bubble region, along with a line containing the reverse-flow region, are shown in the upper plot of Figure 7.15, with the coordinate normal to the surface having been stretched to better illustrate the structure of the separation bubble. The bubble is shorter and has a much thinner region of reverse flow than the low-freestream-turbulence case presented earlier. The lower plot in Figure 7.15 shows a histogram of turbulent-spot origins along with the streamwise intermittency distribution. The vertical height of bars in the histogram represents the fraction of observed spots that are produced within the streamwise range defined by the bar width. This histogram is based on the observation of more than 50 distinct turbulent spots in the separated shear layer, which is on the same order as

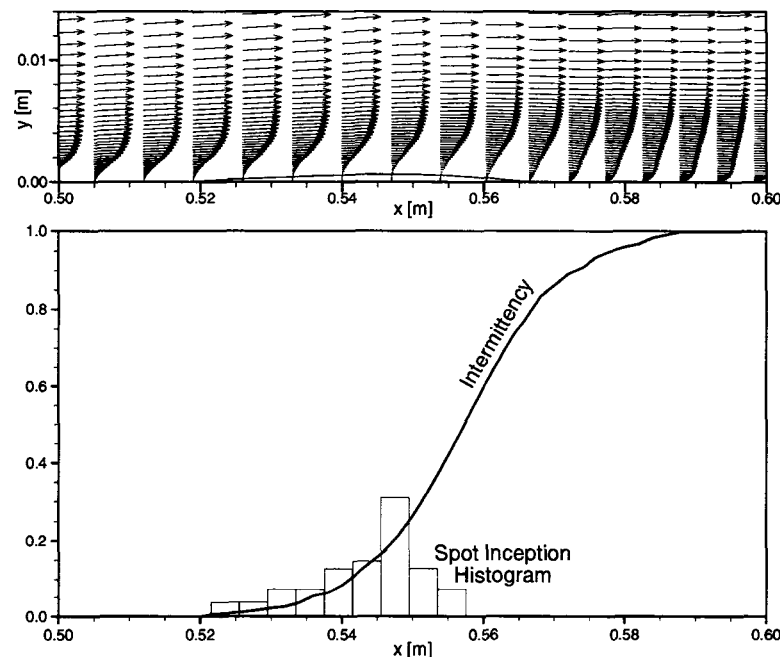


Figure 7.15: Velocity profiles, intermittency distribution, and spot origin histogram through the bubble region of the elevated- Tu simulation

the number of spots required for statistical averaging as identified by Yaras (2007) in an experimental analysis of artificially-generated turbulent spots. Turbulent spots are noted to be produced along the entire length of the reverse-flow region. This streamwise-distributed breakdown is consistent with experimental results on bypass transition in attached boundary layers (Johnson and Ercan, 1999). These observations suggest that extending the concentrated breakdown hypothesis, often utilized in the modelling of natural transition in attached boundary layers, to apply to the transient-growth or bypass modes of transition in separated shear layers cannot be readily justified, despite its widespread use. It is also noted that transition completion occurs approximately 50% of the time-averaged reverse-flow length downstream of reattachment.

7.4.2 Comparison With Experiment

As with the low-freestream-turbulence case, the elevated-freestream-turbulence simulation was based on an experimental test case of Roberts (2005). However, the present simulation provides some differences in the freestream flow conditions from those in the experimental test case. Therefore, detailed validation with the experiment cannot be performed, as was done for the low-freestream-turbulence case in Section 7.3.2. The following paragraphs discuss the two dominant effects that result in the different flow conditions.

The use of square, uniform-velocity jets at the inlet plane of the domain does not exactly mimic the flow through a turbulence-generating grid placed in a uniform flow. Although the simulated turbulence-intensity decay is consistent with that observed downstream of such grids, its decay rate is slightly higher than would be expected for the grid geometry used, but is consistent with the use of a smaller “effective” bar-width, based on the correlations of Roach (1987) developed from experimental measurements of grid-generated turbulence in

a wind tunnel. This difference in “effective” bar-width can be explained by noting that the expected streamline pattern through such a grid would provide some contraction of the core flow, as a uniform velocity profile would require infinite acceleration around the upstream edges of the openings. Despite this, the characteristics of the turbulence, including the observed anisotropy, are consistent with grid-generated turbulence. The higher decay rate of the simulated turbulence provides a turbulence intensity over the separation bubble of about 1.5%, compared with 2% in the experiments.

The second reason for differences in the simulated freestream flow properties from those in the experiments is a result of the domain-height contraction used over the initial region of the wall ($0 \text{ m} \leq x \leq 0.2 \text{ m}$). Over this region, the domain height does not contract sufficiently to ensure complete outflow at the upper domain surface. The velocity fluctuations associated with the freestream turbulence provide conditions that would require some inflow at the boundary. However, the specification of an outflow boundary does not allow inflow and hence there is an additional loss of mass-flow that is not offset by inflow. This decreases the level of freestream acceleration upstream of the suction peak, and causes a reduction in the suction-peak velocity by approximately 10% of that expected from the prescribed streamwise pressure distribution. The net effect of reduced acceleration upstream of the suction peak is a higher momentum thickness at the time-mean separation location. In the simulation, $Re_{\theta_s} = 335$, compared to a value of 285 in the experiments.

Despite these differences, the transition process proceeds as would be expected under the resultant flow conditions. The transition onset location is upstream of that for the experiment as a result of the higher momentum thickness, but is still downstream of the time-averaged separation location. Detailed velocity time-trace validation with the experiment can therefore not be performed, as was done for the low-freestream-turbulence case. However, some comparison is possible to assess whether the important flow patterns that result under such conditions are captured in the simulation. A velocity time-trace

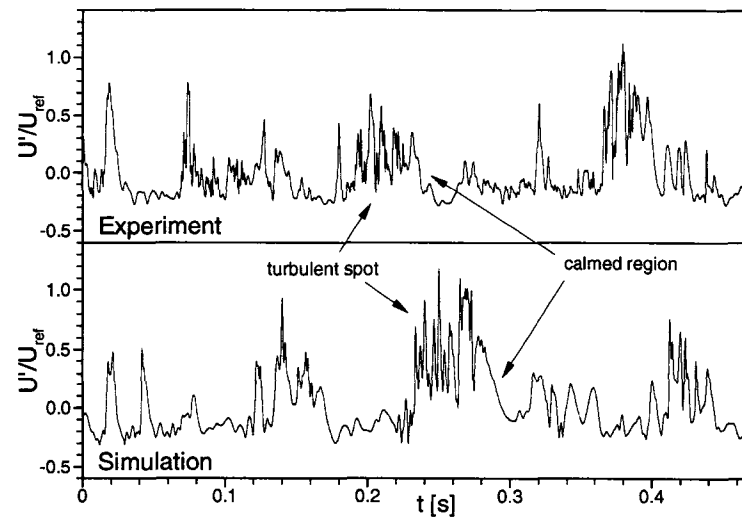


Figure 7.16: Comparison of simulated and measured velocity time-traces with an intermittency of 0.5 (experimental data from a test case of Roberts, 2005)

from within the transition region is shown in Figure 7.16 and compared with a time-trace from the experiment. The two traces in Figure 7.16 are representative of signals from their respective cases with an intermittency level of approximately 0.5. Good agreement is observed for both the occurrence, time duration, and frequency content of turbulent spots convecting past the particular location.

7.4.3 Instability Mechanisms

Unlike separated shear layers in a low-disturbance environment, where separation generally occurs at a fixed streamwise location, the instantaneous separation point under elevated freestream turbulence varies both in time and in the spanwise direction. This variation is demonstrated in Figure 7.17a which shows an $x - z$ plane corresponding to the location of the first node off the wall, and in Figure 7.17b which shows a $z - y$ plane at the time and spanwise averaged streamwise location of separation. Figure 7.17a shows streamwise streaks

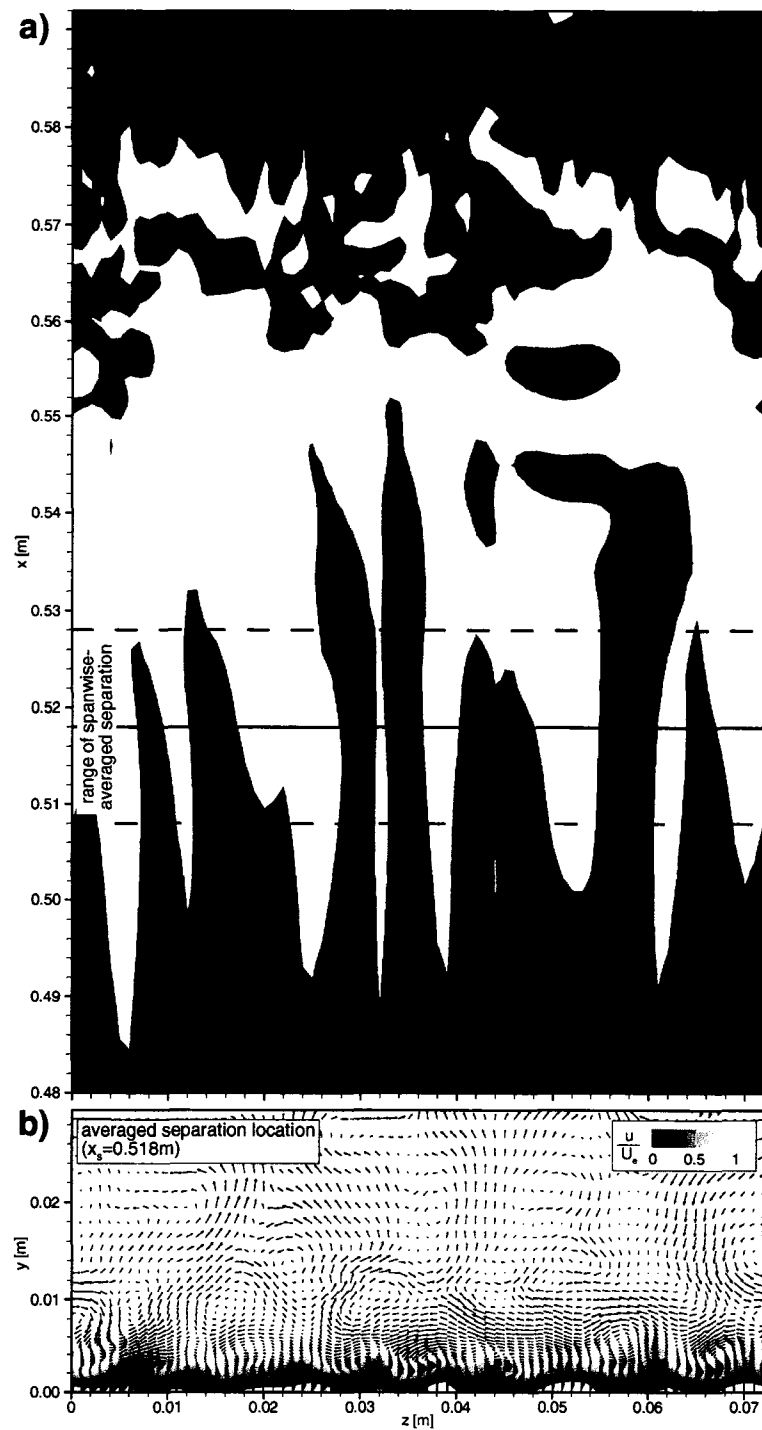


Figure 7.17: Unsteadiness of separation location, a) $z-x$ near-wall plane, b) $z-y$ plane at averaged separation location

of alternating forward and reverse flow along the averaged streamwise location of separation, with the latter represented by the white contour regions. These streaks are associated with streamwise vorticity in the shear layer which transfers low-momentum fluid away from the wall and high-momentum fluid towards the wall. The fluctuations and vortical structures associated with these streamwise streaks are identifiable in the $y-z$ plane of Figure 7.17b by the v' and w' fluctuation vectors. In this plane, the white contour regions near the surface represent reverse flow. Variation in time of the spanwise-averaged separation location is observed to occur over a range of 0.02 m (42% of time-averaged reverse-flow length). A similar variation was observed by Alam and Sandham (2000) in their DNS study of a separation bubble where perturbations were introduced through the wall upstream of separation, providing a disturbance condition similar to freestream turbulence. Figure 7.18 shows velocity fluctuations associated with the streamwise streaks in an $x-z$ plane where $\bar{U} \approx 1/2\bar{U}_e$. The strong spanwise variation and larger amplitude of the u' component compared to the v' component prior to transition is a clear indication that the streaks are comprised predominantly of fluctuations in the streamwise direction.

The streaks shown in Figures 7.17 and 7.18 have also been observed in attached laminar boundary layers exposed to freestream turbulence, starting with the work of Klebanoff (1971), hence the identification of these flow structures as “Klebanoff modes” in some of the published literature. They originate near the leading edge of the flat plate, as this is a receptivity site where the mean flow changes rapidly (Saric *et al.*, 2002). The mechanism through which the streaks are produced in a laminar boundary layer is described by Jacobs and Durbin (2001) and the references therein, and has been referred to as “shear sheltering.” In this process, the time-mean shear in a laminar boundary layer acts to filter perturbations from the freestream turbulence. Viscous stresses are able to withstand much of the perturbation spectra associated with the freestream turbulence, however low-frequency components can penetrate and are then amplified by the mean shear.

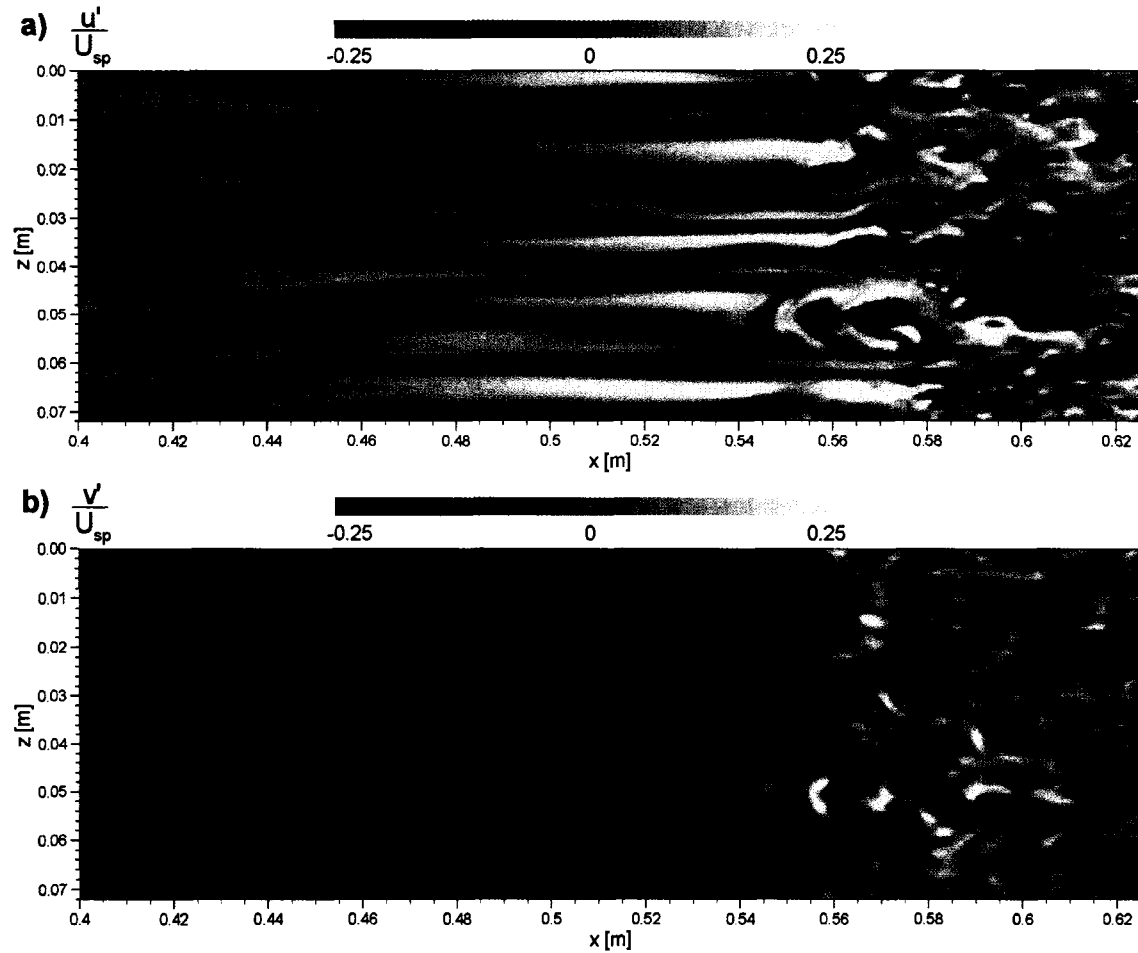


Figure 7.18: Streamwise streaks in the shear layer observed in a plane where $\bar{U} \approx 1/2\bar{U}_e$,
a) streamwise fluctuations, b) wall-normal fluctuations

This results in the energy spectrum shifting to lower frequencies. Figure 7.19 provides the frequency content of velocity fluctuations at various streamwise locations through the separation bubble region, and shows the elevated levels of low-frequency fluctuations near separation ($x = 0.52$ m) which are of similar magnitude to those downstream of the bubble where transition is near completion ($x = 0.58$ m). The elevated fluctuation spectra in the 10-20 Hz range are also observed in the laminar boundary-layer well upstream of separation, and are also apparent in the experimental measurements of Roberts (2005) under similar

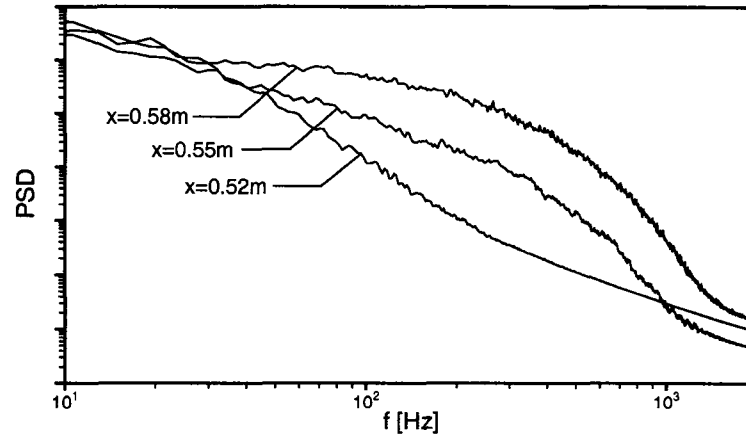


Figure 7.19: Power spectra of velocity through the bubble region under elevated freestream turbulence (at $y = 0.00125\text{m}$)

freestream-turbulence conditions. This low-frequency range is much lower than the most energetic range associated with the freestream turbulent eddies, and is also much lower than the frequency of maximum amplification for Tollmien-Schlichting waves, based on the correlation of Walker (Equation 7.1 on page 135). It is therefore assumed that these amplified low-frequencies are a result of the “shear sheltering” effect which generates the streamwise streaks in the boundary layer. This is contrary to what is observed under low-freestream-turbulence conditions, as seen earlier in Figure 7.5 (page 138), where much lower amplitudes of this low-frequency range are observed in the laminar separated shear-layer compared with those downstream of transition.

Although the laminar streaks have a long streamwise wavelength, they have a much shorter spanwise extent (Figure 7.18) which is on the order of the boundary-layer thickness ($\approx 10\text{ mm}$). This is consistent with the simulation results of Jacobs and Durbin (2001), the experiments referenced therein, and the observations of Matsubara and Alfredsson (2001). The streaks result in both forward and backward jets, relative to the mean flow profile. In Figure 7.18, a predominance towards forward jets is noted upstream of the suction peak,

however there is no bias towards either direction within the separated shear layer. This is likely a result of the adverse pressure gradient which promotes reverse flow. In this region, the laminar streamwise fluctuation levels associated with the streaks are very high, and can exceed 25% of the local edge velocity. Asai *et al.* (2002) provide evidence that this level of streamwise fluctuation is enough to bring a streak in a laminar boundary layer into a sinuous unstable mode, and initiate a secondary instability in the form of spanwise waviness of the low-speed streaks. The present simulation data provides no indication that a sinuous wavering of the streaks is a precursor to turbulent spot production, nor is the varicose wavering pattern which requires higher fluctuations levels.

As the aforementioned streamwise streaks convect through the separated shear layer, a secondary instability develops and provides conditions that are favorable for turbulent-spot generation. As a low-speed streak passes through the shear layer, a localized roll-up of vorticity occurs around the streak, resulting in a series of vortex loops which provide an exchange of momentum in the wall-normal direction. In the early stage of spot development, these vortex loops closely resemble those generated by Watmuff (1999) by way of a low-disturbance wave packet convecting through a separated shear layer. Figure 7.20 shows the structure of one such spot. The vortex loops are identified by iso-surfaces of negative pressure fluctuation (blue iso-surfaces). The small-scale structures apparent to the sides and downstream of the spot are associated with turbulence activity downstream of reattachment.

Jacobs and Durbin (2001) associate the generation of a turbulent spot with strong backward jets being lifted from near the surface towards the freestream. The present simulation results provide evidence that the generation of turbulent spots evolves more generally as a result of the strong shear associated with the streamwise streaks. The evolution of a turbulent spot is shown in Figure 7.21 in a series of vector and vorticity plots in the $x - y$ plane along the spot centreline. The wall-normal coordinate has been stretched to allow better visualization of the spot development, and only every fourth velocity vector

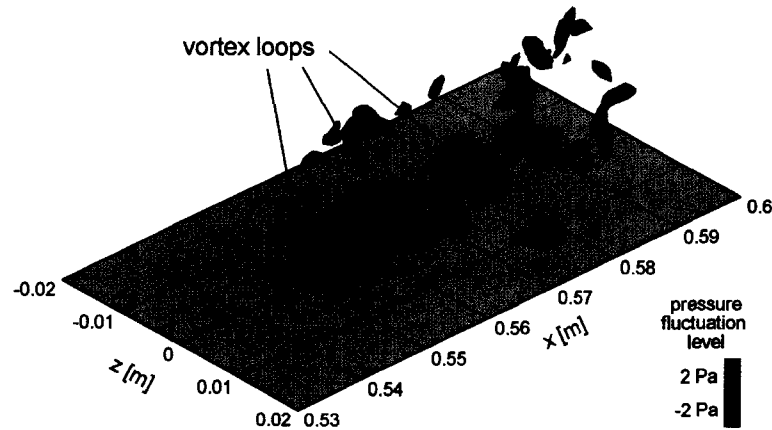


Figure 7.20: Vortex loops within a turbulent spot

profile is included in the figure as well. The planform structure of this particular spot is apparent in the $x-z$ plots in Figure 7.18 centered at about $x=0.56$ m and $z=0.05$ m. The uppermost plot in Figure 7.21 presents the time-averaged flow-field in which a discontinuity in the trajectory of maximum vorticity is observed as the shear layer transitions from a laminar separated shear layer to a turbulent reattached boundary layer. This discontinuity is caused in part by a redistribution of the spanwise vorticity to smaller scales as transition and reattachment progresses. At $t' = 0$ s, a separated laminar shear layer is present with vorticity confined to a much thinner layer than in the time-averaged case. The smaller scales observed downstream of $x = 0.57$ m are associated with the turbulence in the reattached shear layer (time-averaged reattachment is at $x_r = 0.566$ m). As the flow field evolves in time, a wave pattern becomes apparent resulting in roll-up of the vorticity contained in the shear layer. As this secondary instability grows, fluid is entrained towards the surface, resulting in a patch of reattached flow which convects downstream. The roll-up occurs in a three-dimensional manner and a series of vortex loops defines the topology of the newly formed turbulent spot, as was observed in Figure 7.20. At $t' = 0.006$ s, smaller scales are present in the shear layer indicative of the young turbulence within the spot.

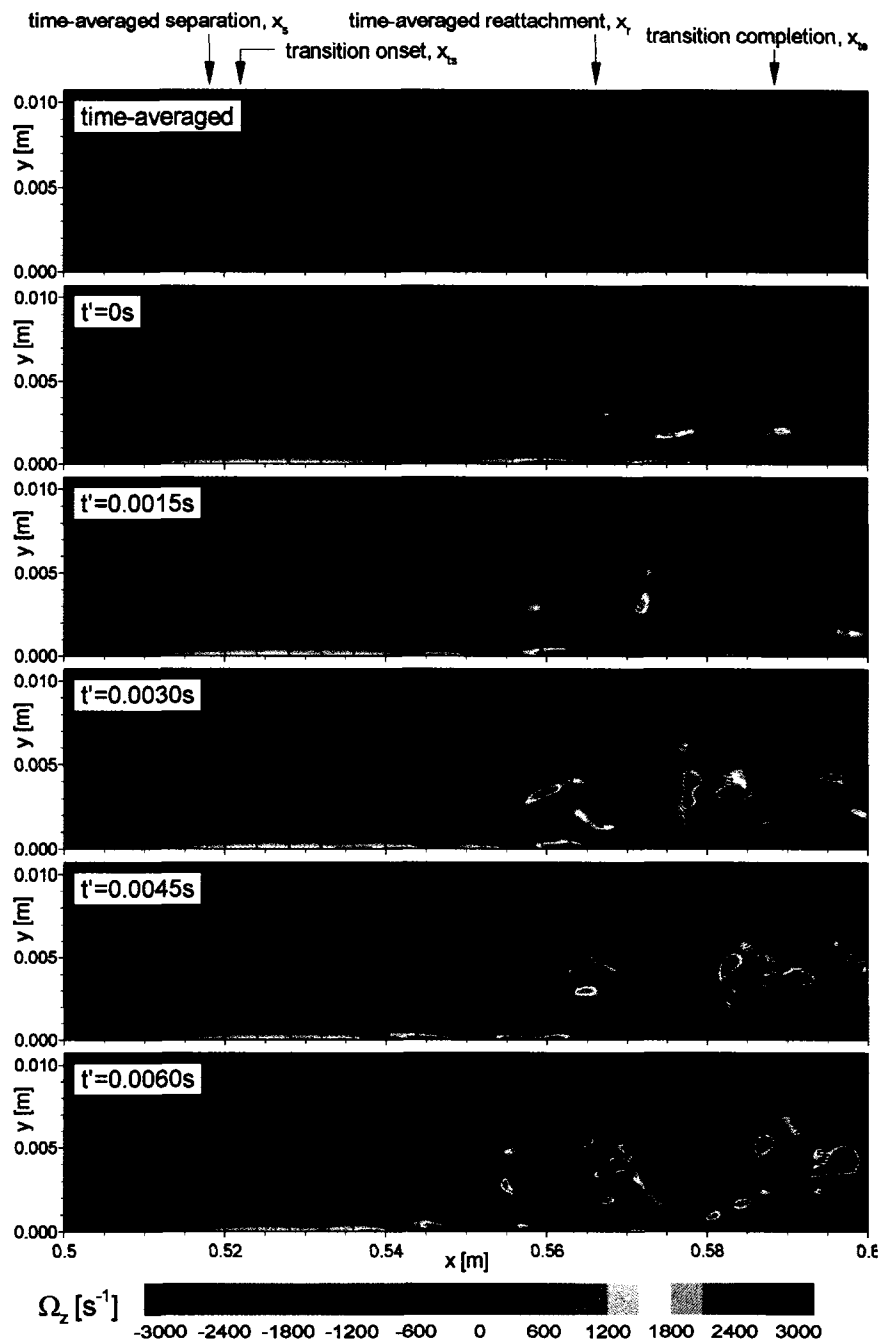


Figure 7.21: Evolution of a turbulent spot through a time sequence of flow in an $x - y$ plane along the centreline of the spot (averaged vectors and spanwise-vorticity in uppermost plot)

The instability that develops along the centreline of the spot is reminiscent of Kelvin-Helmholtz vorticity roll-up, as observed in Figure 7.8 (page 141) under low-freestream-turbulence conditions, and is in fact such an inviscid instability despite the locally three-dimensional nature of the shear layer. The Strouhal number associated with this instability, based on local conditions ($Sr_\theta = f\theta/\Delta U$), varies between 0.014 and 0.017 which is in good agreement with that for the Kelvin-Helmholtz instability in plane shear layers (see Table 7.3). Watmuff (1999) also observed similar agreement with the Kelvin-Helmholtz instability for the wave frequency from which vortex loops roll-up in his wave-packet-induced turbulent-spot study. This would suggest that turbulent spot production in a separated shear layer is the result of a local inviscid instability of the shear generated by the streamwise streaks convecting through the shear layer. A similar roll-up has been observed by Jacobs and Durbin (2001) and Wu *et al.* (1999) during the initial stages of turbulent-spot formation in simulations of freestream-turbulence-induced bypass transition and wake-induced bypass transition of a zero-pressure-gradient boundary layer, respectively.

The eventual breakdown to small-scale turbulence, which occurs as a result of the growth and development of the turbulent spots, is discussed in the next section.

7.4.4 Breakdown Mechanisms

Once a turbulent spot is initiated through the formation of vortex loops, the spot grows in the streamwise and spanwise directions as it convects downstream. Within the spot, the vortex loops provide the mechanism for momentum exchange across the shear layer. In a series of $y - t$ and $z - t$ plots, the internal structure of a turbulent spot is presented in Figure 7.22. The spot shown in Figure 7.22 is the same spot identified previously in Figures 7.21 and 7.20. A low-speed streak, or backward jet, passing through the shear layer is apparent as dark-blue regions in both the $y - t$ and $z - t$ planes. A roll-up of

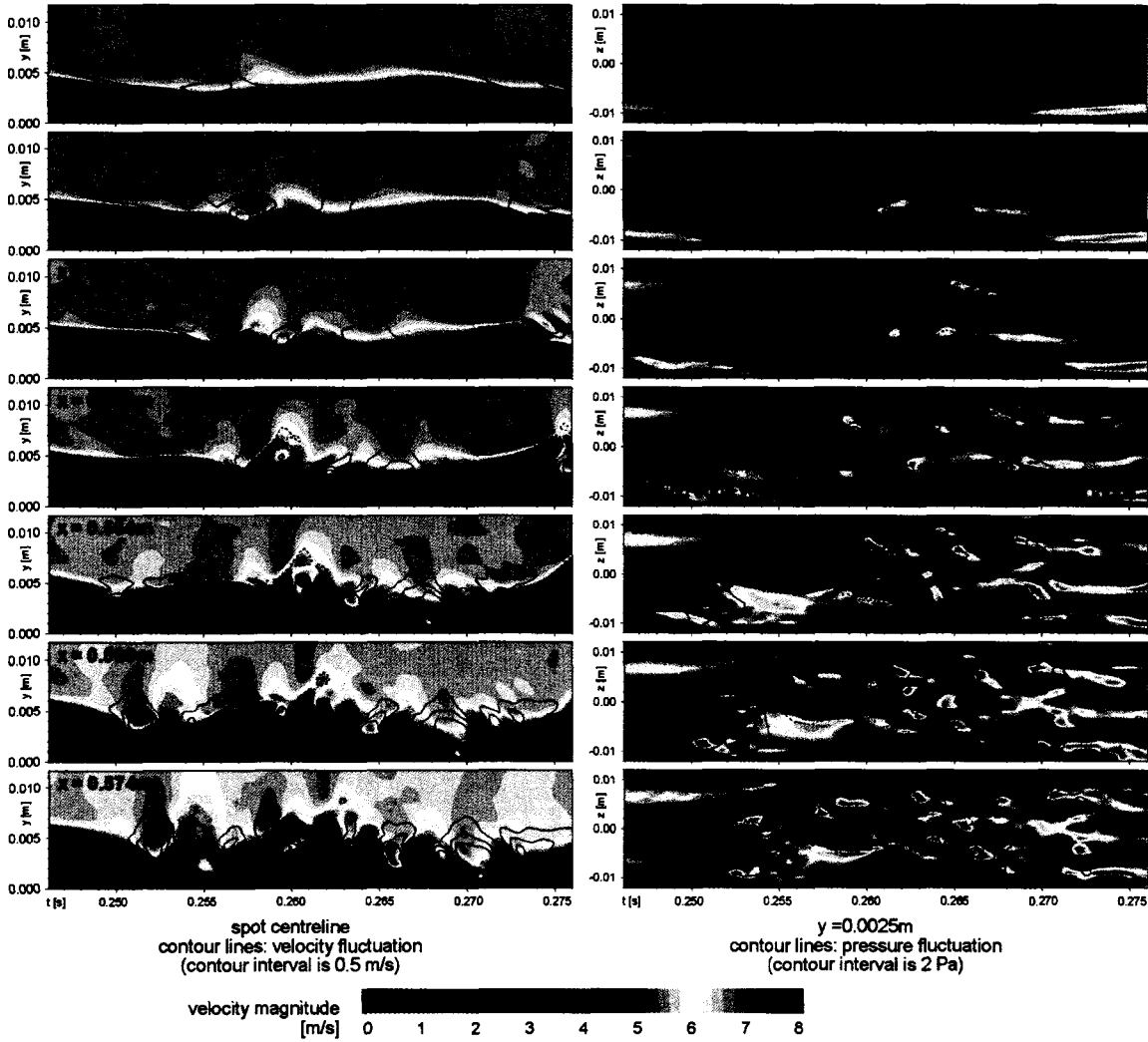


Figure 7.22: Turbulent-spot growth as observed in the $y - t$ and $z - t$ planes

vorticity occurs around this low-speed streak which pulls fluid inwards, resulting in a patch of reattached fluid that convects through the separated shear layer. This patch is identified by the time interval in the $y - t$ plots during which green contours are observed very close to the surface. The structure within the spot is dominated by the vortex loops, which can be identified by the pressure perturbation contours in the $z - t$ plots of Figure 7.22. Although the spot originates near $x = 0.54$ m, the primary vortex loop located at the leading edge of the spot is not clearly identified until after $x = 0.55$ m. In the $z - t$ plot for $x = 0.559$ m, this vortex loop is identified and the legs of the other two dominant vortex loops are visible. As the spot propagates downstream into the reattached boundary layer, its structure begins to contort and break down due to vortical diffusion within the surrounding boundary layer and freestream. However, the basic vortex-loop structure of the spot remains coherent downstream of reattachment, with loop legs still being identifiable at $x = 0.574$ m in Figure 7.22.

Of the spots observed in the simulation, generally three dominant vortex loops develop about the low-speed streak, similar to the particular spot shown in Figure 7.20. A schematic illustrating the topology of a newly-formed turbulent spot is shown in Figure 7.23. This schematic has been interpreted from examining multiple spots occurring in the present simulation. While the most frequently observed configuration consists of three vortex loops as is shown in Figure 7.23, there are also occurrences with only two distinct loops, and others with a weak fourth loop appearing on the upstream side of the spot. The primary vortex loop located at the leading edge of the spot is lifted away from the surface where it convects at a high rate due to the higher freestream velocity, thus contributing to the streamwise growth of the spot. This vortex loop is reminiscent of the hairpin vortex structures observed in near-wall regions of turbulent boundary layers (Panton, 2001). The legs of the primary vortex loop extend towards the wall where they point in the upstream direction. The downstream orientation of the legs of the secondary and tertiary loops is a result of the

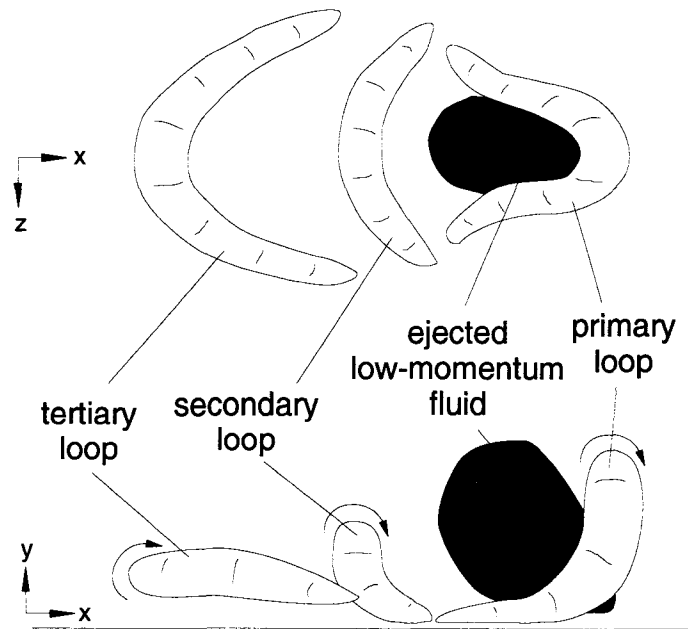


Figure 7.23: **Schematic of the vortex loop structure during the early development of a turbulent spot**

blockage created by the column of low-momentum near-wall fluid ejected away from the wall by the induced effect of the primary vortex loop. Regions within the spot that provide the greatest contribution to turbulent shear stresses ($-\overline{u'v'}$) are identified in Figure 7.24. Q2 events ($u' < 0, v' > 0$), also referred to as “ejection” processes, appear to dominate the process of wall-normal momentum exchange over the Q4 events ($u' > 0, v' < 0$) which are commonly referred to as “sweep” processes (Panton, 2001). The internal structure identified here for a turbulent spot in a separation bubble shares similarities with the vortex-loop patterns observed by Watmuff (1999) in an experiment of artificially-generated spots in a separated shear layer, and apart from consisting of vortical structures, does not show a strong resemblance to a turbulent spot developing in an attached boundary layer (Schröder and Kompenhans, 2004; Yaras, 2007).

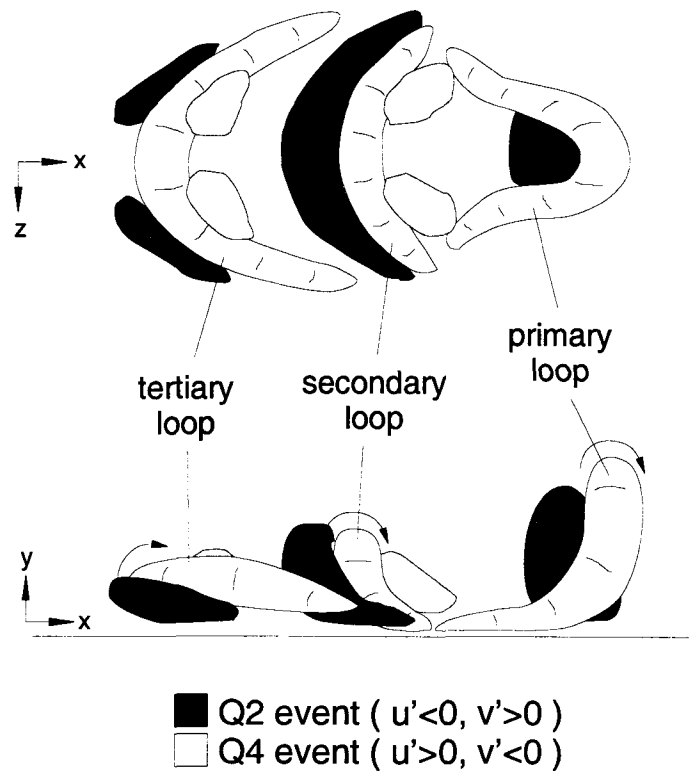


Figure 7.24: Turbulent shear stress contributions during the early development of a turbulent spot

Transition in the present case occurs through the production and growth of turbulent spots. However, the Kelvin-Helmholtz (K-H) instability mechanism, associated with the separated shear layer as a whole, is still active. Near and downstream of the time-averaged reattachment location, there are no distinct turbulent spots produced (as observed in the spot origin histogram of Figure 7.15 on page 155), but turbulence is still observed in the inter-spot regions. This turbulence may be linked to the rapid breakdown process that is typical of K-H dominated transition, as discussed earlier in Section 7.3.4. The distinct large-scale spanwise-oriented vortices generally associated with K-H instability growth are difficult to discern within the spatial structure of the shear layer. However the frequency of the K-H instability is observed in a spectral analysis of the separation bubble. Figure 7.25 presents

power spectra of both velocity and static pressure at several streamwise locations through the separation bubble region, with x' representing the streamwise distance from the averaged separation location ($x' = x - x_s$). Shortly downstream of separation ($x' = 0.016\text{m}$), during the early stages of transition, several peaks are observed and identified in the power spectra. These peaks are more pronounced in the spectrum of static pressure (Figure 7.25b) and the four most dominant peaks are identified. The frequencies about which these peaks appear are 180 Hz, 270 Hz, 360 Hz and 630 Hz and are associated with the maximum amplified frequency of the K-H instability (180 Hz) along with its harmonic (360 Hz), the vortex loop passing frequency (270 Hz) and the frequency corresponding to the integral time scale of freestream turbulence (630 Hz). The K-H frequency observed in Figure 7.25 corresponds to a Strouhal number, based on separation conditions ($St_{\theta_s} = f\theta_s/U_{es}$), of 0.018 which is in close agreement to the values provided in Table 7.3 (page 142) for separated- and free-shear layers in which the K-H instability mechanism dominates. Observance of the frequency associated with the integral time scale of freestream turbulence was not expected, as the power spectrum of the freestream turbulence is smooth with no distinct peaks. The integral time scale of freestream turbulence is a representative scale of the most energetic turbulent structures in the freestream flow, and it is conceivable that, despite the shear-sheltering effect that acts to filter frequencies at this higher range, this energetic scale may provide some penetration of fluctuations into the shear layer. There is also an additional peak at 460 Hz in the spectrum of velocity at $x' = 0.016\text{m}$. In examining the spectra for the individual velocity components, this peak is only present in that for the streamwise component of velocity, u , and it is yet unknown what causes this peak to emerge. Downstream of the time-averaged reattachment ($x' \geq 0.048\text{m}$), a broad spectrum is observed with no distinct peaks. It should also be noted that the frequency associated with the passing of vortex loops through the shear layer, as a result of the local inviscid instability discussed in the previous section, is approximately 50% higher than that of the K-H frequency associated with the large-scale properties of the shear layer.

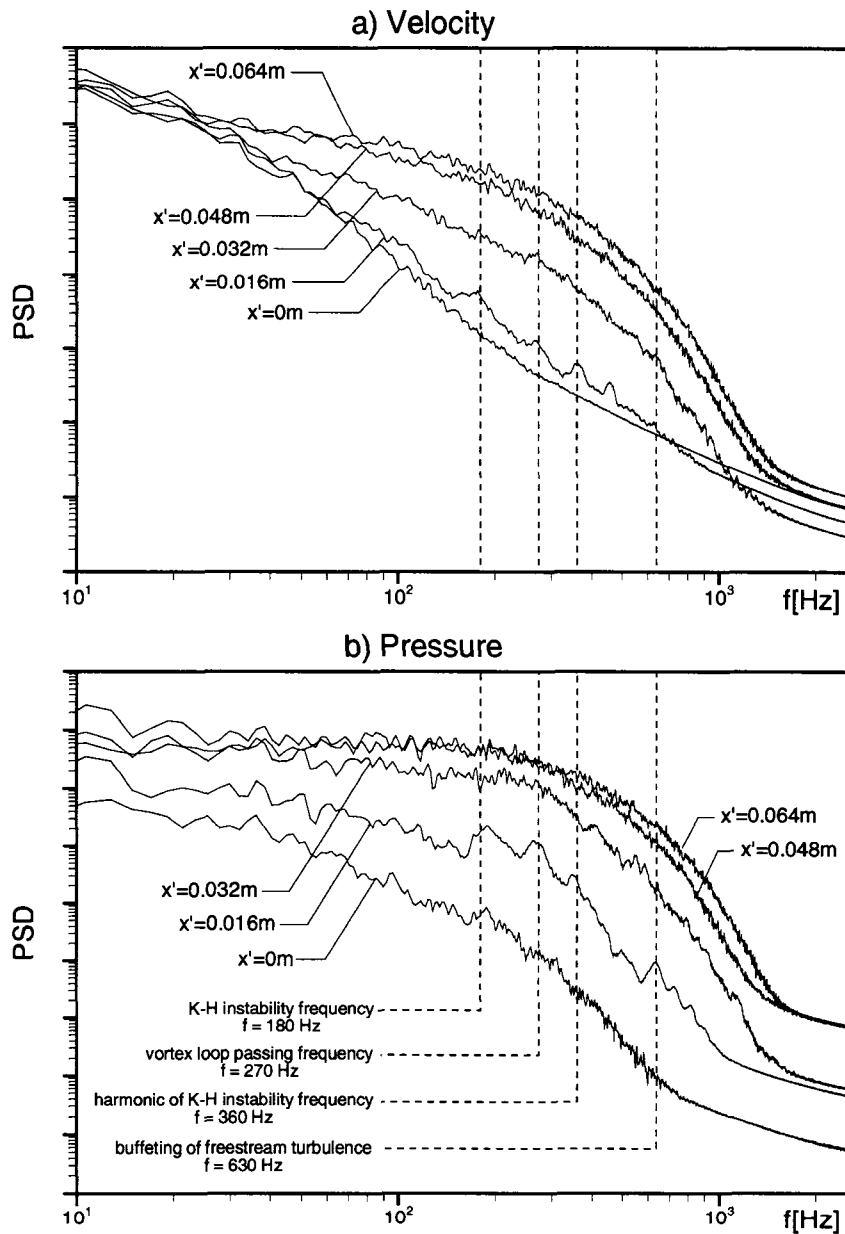


Figure 7.25: Power spectra of a) velocity, b) static pressure in the separated shear layer

7.4.5 Validation of Turbulent-Spot Growth Models

One objective of the present study was to validate the turbulent-spot growth models of Gostelow *et al.* (1996) and D'Ovidio *et al.* (2001b) used in the semi-empirical intermittency-based transition model of Roberts (2005). These spot-growth models are based on measurements of artificially-generated turbulent spots under accelerating and decelerating freestream conditions, and it is desired to assess their validity for the growth characteristics of turbulent spots generated by the presence of freestream turbulence.

The model proposed by Gostelow *et al.* (1996) for the spot spreading half-angle is

$$\alpha = 4 + \frac{22.14}{0.79 + 2.72e^{(47.63\lambda_\theta)}} \quad (7.3)$$

which is a function the local pressure gradient parameter, λ_θ . D'Ovidio *et al.* (2001b) extended the range of applicability of Equation 7.3 to include spots developing in a separated shear layer ($-0.12 \leq \lambda_\theta \leq 0.06$). Figure 7.26 shows the variation in spot spreading half-angles observed in the simulation, as compared with the value obtained from Equation 7.3. The “effective origin”, x_{0eff} , plotted on the abscissa is the streamwise location from which lines emanating at \pm the spot spreading half-angle align with the spot extremities. This is upstream of the true streamwise origin which, as identified earlier from Figure 7.22, is not a point source. However, the use of an “effective origin” allows an assessment of any spot spreading variation with downstream distance. The spot extremities have been identified using the wall-normal component of velocity fluctuation (v'), with a threshold value of ± 0.2 m/s (3% of U_e). For the levels of Thwaites' pressure gradient parameter observed in the initial part of the separation bubble ($\lambda_\theta \approx -0.2$), Gostelow *et al.*'s model predicts a spot spreading half-angle, α , of 32 degrees, whereas the average value in the present simulation is 22 degrees. Although the threshold used by Gostelow *et al.* in identifying the spot edge is slightly different (4% of U_e), they observed negligible sensitivity to this threshold over

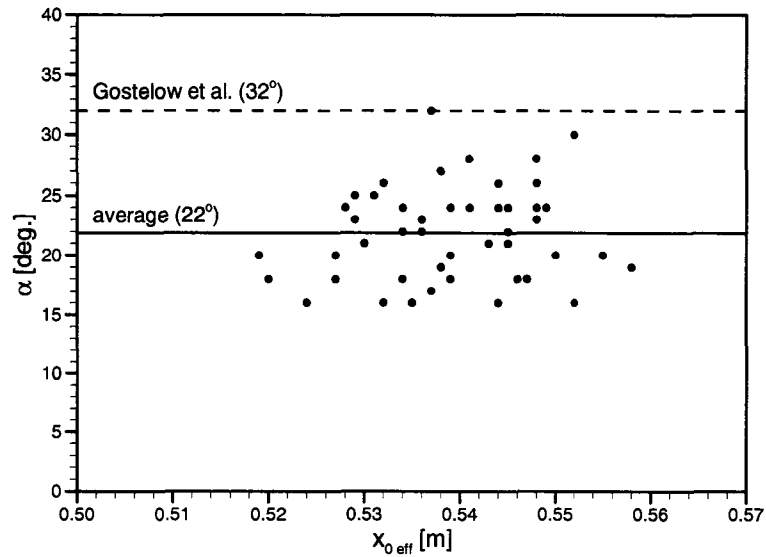


Figure 7.26: Spot spreading half-angles

a range of 2% to 15% of U_e . The spot spreading half-angles identified in the current case are consistently lower than that predicted by the model, and do not show an apparent trend with streamwise distance. In the present case, the spot spreading angles have been extracted while the spot propagates and grows in a non-turbulent region of the separated shear layer. Identifying the spot extremities in a turbulent surrounding is difficult and highly subjective. Upon closer inspection of the data from which D'Ovidio *et al.* extracted α for their separation bubble cases, the spreading angle prior to the spot entering the turbulent part of the undisturbed separation bubble is observed to be lower than that in the turbulent region by about 5 to 10 degrees. Thus, in the region of the separated shear layer where the turbulent spots grow in the absence of any other turbulence activity in the inter-spot regions, the spreading rate observed in the present simulations and that extracted from the experimental data of D'Ovidio *et al.* are in good agreement. On this basis, the present simulation results are judged to be supportive of the use of Equation 7.3 for estimating the transverse spreading rate of turbulent spots in separated shear layers.

The spot propagation parameter is defined as

$$\sigma = \tan(\alpha) \left(\frac{1}{b} - \frac{1}{a} \right) \quad (7.4)$$

where $a = U_{le}/U_e$ and $b = U_{te}/U_e$ are the leading-edge and trailing-edge celerities of the spot, respectively. These leading- and trailing-edge celerities for the turbulent spots observed in the simulation were extracted to assess the spot propagation parameter model of D'Ovidio *et al.* (2001b):

$$\sigma = 0.024 + \frac{0.604}{1 + 5e^{(66\lambda_\theta)}}. \quad (7.5)$$

The experiments from which this model was developed used phase-averaged measurements of artificially-generated turbulent spots, from which distinct spot boundaries can be identified. Such phase-averaging is not possible for the present case due to the range in streamwise spot origins and the difficulty in identifying and matching a specific phase during the spot growth period. Identification of the leading and trailing edges of the spots in the present case is therefore more difficult and subjective. Figure 7.27 shows $x-t$ plots along the centreline of a particular turbulent spot. The celerities shown as dashed lines in Figure 7.27 are a “best fit” based on many of the spots identified in the simulation, and happen to provide a very good match to the spot shown through the flood plots. The spot leading edge has been identified as the downstream side of the primary vortex-loop head, which is convected through the shear layer at the highest rate of any point in the turbulent spot. In Figure 7.27a, the primary vortex loop head is identified by high, negative, values of the spanwise component of vorticity (dark blue regions). The leading edge celerity based on this criterion is 0.8 ± 0.05 .

Gostelow *et al.* (1996) and D'Ovidio *et al.* (2001b) identified the spot trailing edge based on RMS fluctuation levels within the spot. In examining their data, the trailing edge is noted to be consistent with the trajectory of the high-velocity phase-locked perturbation peak

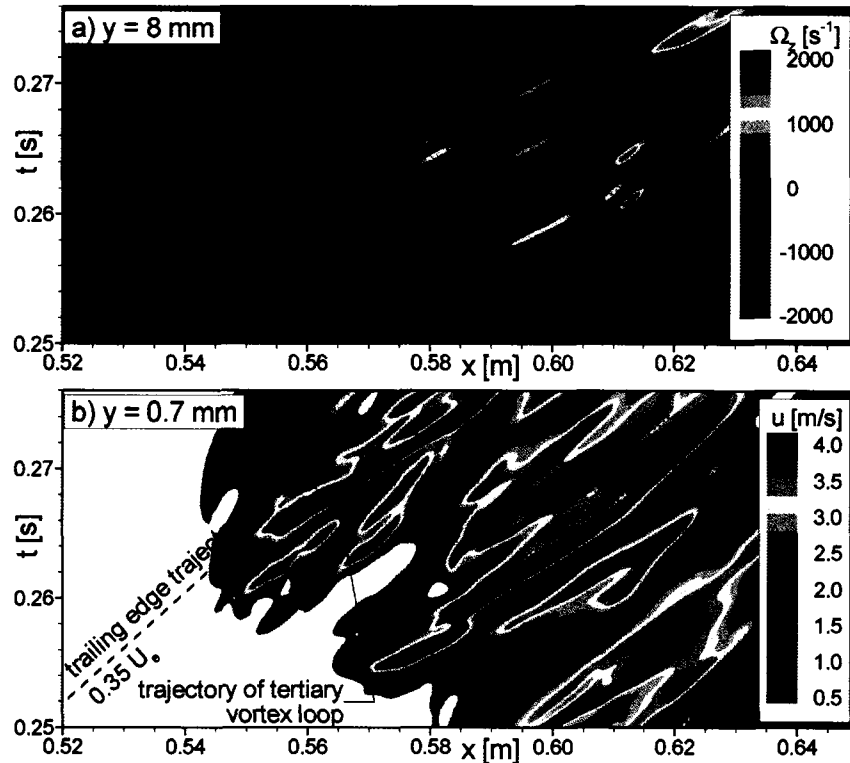


Figure 7.27: Identification of spot celerities, a) leading edge, b) trailing edge

leading the calmed region. From the spots identified in the present case (see Figure 7.27b), a distinct trajectory can be identified upstream of which near-wall streamwise velocity levels are significantly reduced from those observed within the turbulent spot. The spot trailing-edge celerity is quantified on the basis of this trajectory. While the vortex loops within the spot convect at a higher rate than the spot trailing edge, which was also observed by D’Ovidio *et al.*, weaker vortex loops and/or random fluctuations are evident between the tertiary vortex loop and the spot trailing edge. The “best fit” trailing-edge celerity of the present case is 0.35 ± 0.05

The spot propagation parameter for the present case is $\sigma = 0.65 \pm 0.2$. The high uncertainty in σ is due to subjectivity associated with identifying the leading edge and trailing edge celerities. However, the extracted value agrees well with Equation 7.5 which

predicts a value of 0.63 for the pressure gradient parameter observed through the bubble region of the present investigation ($\lambda_\theta = -0.2$). Therefore, the present simulation results are also supportive of the use of Equation 7.5 for estimating the spot propagation parameter in separation bubbles under elevated-freestream-turbulence conditions.

7.5 Comparative Assessment

The two transition mechanisms identified in the two simulations of the present effort yield some differences in the characteristics of the shear-layer development and the turbulent boundary layer downstream of the separation bubble. Figure 7.28 presents a comparison of the streamwise intermittency distributions, the boundary-layer growth characteristics, and the $x - y$ distributions of velocity-fluctuation correlations, turbulence kinetic-energy production, and pressure fluctuation levels over the aft region of the flat plate for the two cases. Under conditions of low freestream turbulence, the bubble is long and breakdown to turbulence occurs over a very short distance, with transition being complete very near the time-mean reattachment point. Conversely, the transient-growth mechanism associated with elevated freestream turbulence results in a shorter and thinner bubble with breakdown occurring over a much larger streamwise distance, and with transition being completed approximately 50% of the bubble length downstream of reattachment. This provides a more gradual change in the shear-layer growth characteristics through the bubble region.

The contour plots in Figure 7.28 also show differing characteristics between the two cases. Under low-freestream-turbulence conditions, fluctuation growth is initiated in the separated shear layer with peaks of $\overline{u'u'}$, $\overline{w'w'}$, and $\overline{u'v'}$ apparent in the separated shear layer and in the inner reverse-flow region of the bubble, consistent with the dual-mode instability discussed earlier in Section 7.3.3. The highest fluctuation levels are observed slightly downstream of the time-mean reattachment point, and the streamwise fluctuations apparent

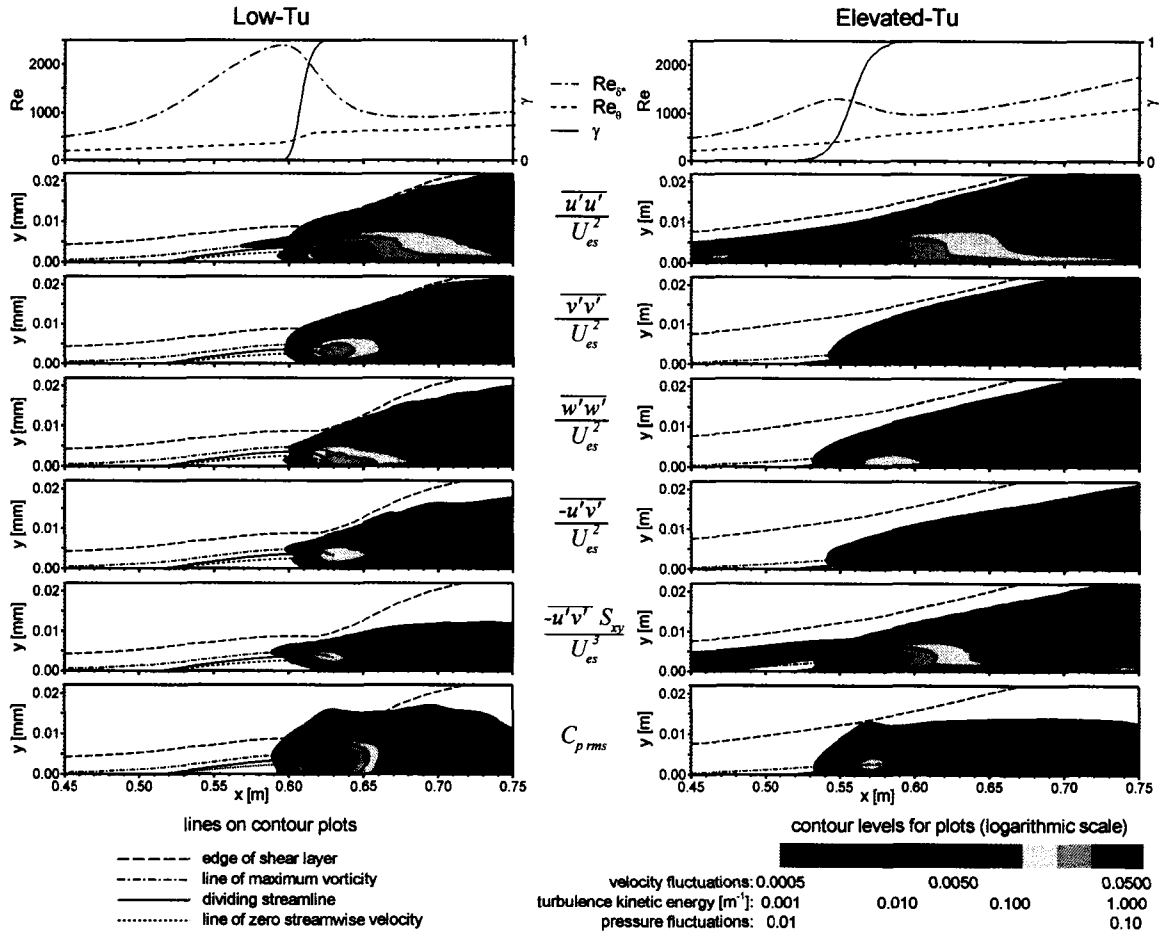


Figure 7.28: Comparison of streamwise intermittency distribution, boundary layer growth characteristics, and velocity-fluctuation correlations for the two cases examined

prior to transition onset are due to growth of the spanwise-oriented vortices resulting from the Kelvin-Helmholtz instability. The rate of growth of wall-normal fluctuations ($\overline{v'v'}$) with streamwise distance reaching a peak along the rear portion of the time-mean dividing streamline of the separation bubble is consistent with the substantial cross-stream momentum exchange that should prevail in this region to reattach the separated shear layer. Peak levels of $\overline{v'v'}$ and $\overline{w'w'}$ are of similar magnitude to that of $\overline{u'u'}$, indicating strong three-dimensionality of the resulting breakdown process. Conversely, under elevated-freestream turbulence the peak values of $\overline{v'v'}$ and $\overline{w'w'}$ are much lower than that for $\overline{u'u'}$, and occur

at a greater distance downstream of time-mean reattachment. The high levels of $\overline{u'u'}$ in this case are associated with the streamwise streaks generated in the upstream laminar boundary layer that provide the conditions under which turbulent spots are generated in the shear layer. A more gradual streamwise growth and decay of velocity fluctuations is observed under this elevated-freestream-turbulence condition.

The effects of turbulence within a wall-bounded shear layer can be characterized by an increase in the net momentum transfer towards the wall due to turbulent mixing, for which the Reynolds shear-stress component $-\overline{u'v'}$ is a measure. For the low-freestream-turbulence case, this Reynolds-shear-stress component begins to increase within the rear portion of the separated shear layer at about $x = 0.59$ m and peaks at the streamwise location of the time-mean reattachment point. In the elevated-freestream turbulence case, a small level of $-\overline{u'v'}$ is present in the laminar boundary layer prior to transition, indicating that the streamwise-oriented vortical structures associated with the streamwise streaks provide some cross-stream momentum exchange. Much higher levels of $-\overline{u'v'}$ are observed through the transition region of the separation bubble; however they are not as strong as those associated with the shorter transition process in the low-freestream-turbulence case.

The energy transfer facilitated by the $\overline{u'v'}$ Reynolds shear stress component is quantified by $-\overline{u'v'}S_{xy}$ which is the work done by this shear stress on the time-mean flow field through the strain rate S_{xy} . In regards to turbulent boundary-layers, this term is commonly referred to as the production of turbulence kinetic energy (Schlichting and Gersten, 2000; Panton, 2001). For the low-freestream-turbulence case, this energy transfer is noted to reach its peak on the line of maximum vorticity, at the streamwise location of the time-mean reattachment point. The fact that the magnitude of $-\overline{u'v'}S_{xy}$ begins to increase in the separated shear layer at about $x = 0.59$ m, which is upstream of the location of transition onset ($x \approx 0.60$ m), suggests that the packets of amplified instability waves observed within the separated shear layer are also instrumental in the cross-stream momentum

exchange. The mechanism associated with this cross-stream momentum exchange was discussed earlier in Section 7.3.3 and illustrated through instantaneous velocity profiles in Figure 7.11 on page 148. For the elevated-freestream-turbulence case, the cross-stream momentum exchange associated with the streamwise-oriented vortical structures in the laminar boundary layer provide some level of $-\overline{u'v'}S_{xy}$ prior to transition onset; however this level is more than an order of magnitude lower than that observed in the transition region.

As expected, the strong velocity fluctuations in the transition region of the separation bubbles are accompanied by pressure fluctuations ($C_{p\ rms}$). For both cases, these pressure fluctuations are observed to decrease at a faster rate downstream of reattachment than do the velocity fluctuations. The level of pressure fluctuations is also observed to be much higher in the low-freestream turbulence case, likely a result of the strong pressure variations associated with the large-scale vortical structures that develop from the Kelvin-Helmholtz instability.

In order to compare the turbulent boundary layer for the two cases, an effective bubble length has been selected such that the trailing end of this length corresponds to the location of minimum displacement thickness downstream of the bubble. This effective bubble length is representative of the region over which the bubble affects the freestream flow and its use in normalizing the streamwise coordinate provides a reasonable match in the streamwise rate of growth of the turbulent boundary layer. Figure 7.29 shows the boundary-layer velocity profile and the distribution of turbulence kinetic energy production for both cases, at various locations downstream of the time-mean point of reattachment. The distributions are plotted in wall-coordinates, with the inner layer ($u^+ = y^+$) and logarithmic law-of-the-wall ($u^+ = 1/0.41\log(y^+) + 5.0$) profiles plotted for reference.

For the low-freestream-turbulence case, only profiles up to 50% of the effective bubble

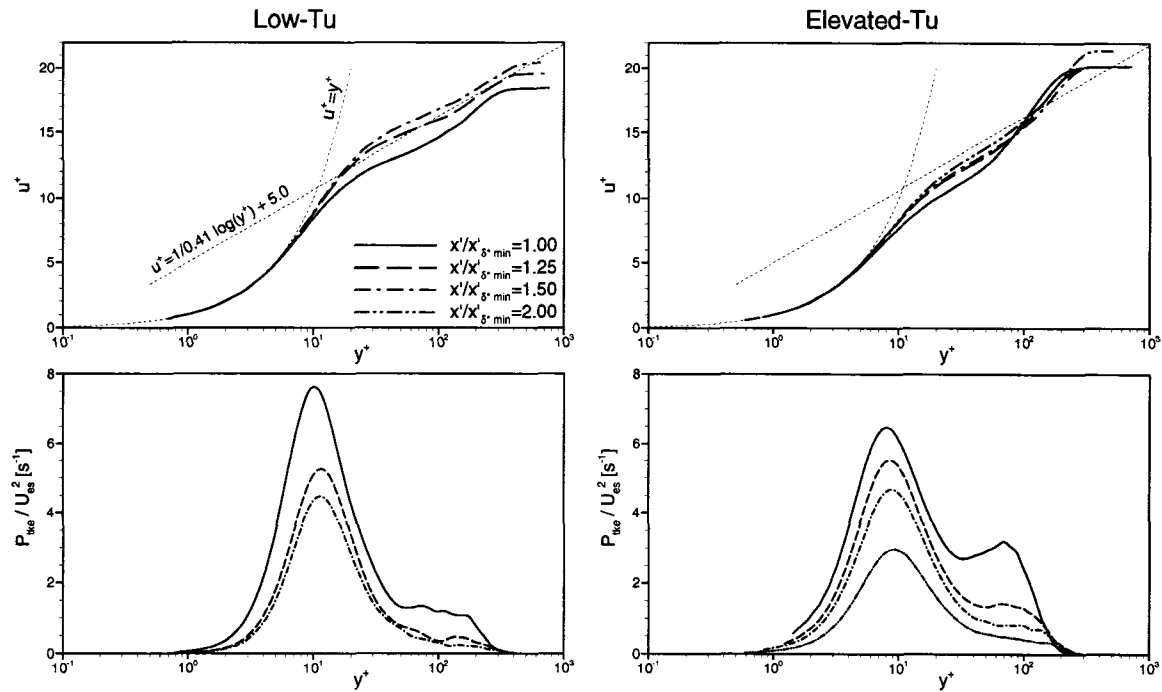


Figure 7.29: Turbulent boundary-layer properties downstream of the separation bubble

length downstream of the bubble are shown due restrictions in the length of the computational domain. At both 25% and 50% of the effective bubble length downstream, the velocity profiles show close agreement with the velocity levels of the logarithmic law-of-the-wall. The majority of turbulence kinetic energy is produced very near the wall, around $y^+ \approx 10$ (see lower left plot in Figure 7.29). This is in close agreement with the location of maximum production in an equilibrium turbulent boundary layer ($y^+ = 12$, Panton, 2001). The large-scale vortical structures shed from the separation bubble are also a source of turbulence kinetic energy, as indicated by the humps observed in the region $50 < y^+ < 300$. Alam and Sandham (2000) observed that these humps are similar to those occurring in a plane mixing layer. The humps disappear with increasing downstream distance, again indicating recovery towards a conventional turbulent boundary layer. It should also be noted that the turbulence kinetic energy production is highest in the reattachment region, and decreases with downstream distance.

Under elevated-freestream-turbulence conditions, recovery to a turbulent boundary layer occurs in a manner similar to that observed under low-freestream-turbulence conditions. The velocity profiles in Figure 7.29 are all below that for the logarithmic law-of-the-wall, but a slow relaxation toward this equilibrium state is observed. The peak in turbulence kinetic energy production also occurs near $y^+ \approx 10$. In this case however, higher production levels are observed in the outer region ($50 < y^+ < 300$) than those observed in the low-freestream-turbulence case. This is likely due to the longer transition length, resulting in transition completion being much closer to the streamwise location of minimum displacement thickness.

An assessment of the full recovery length is not possible due to limits in the length of the computational domain. However, the results presented herein are consistent with those observed by others in separation bubbles. For example, Alam and Sandham (2000) found re-establishment of the log-law required seven bubble lengths downstream of time-mean reattachment. This can be attributed to a slow decay of turbulence kinetic energy in the outer part of the layer, resulting from the larger-scale structures produced during transition of the separated shear layer, be it the large hairpin vortices observed under low-freestream-turbulence conditions or the vortex loops within a turbulent spot under elevated-freestream-turbulence conditions.

7.6 Conclusions

The mechanisms associated with laminar-to-turbulent transition in separation bubbles, and the resulting breakdown processes, have been examined in the context of direct numerical simulations performed under conditions with low and elevated freestream turbulence. The simulation results are in good agreement with experimental measurements of similar flows.

Under low-freestream-turbulence conditions, transition is initiated through receptivity of the laminar separated shear layer to small disturbances through the inviscid Kelvin-Helmholtz mechanism. Two regions of instability growth were observed, one in the separated shear layer and one in the reverse-flow region near the surface, and are consistent with the results of linear stability theory presented in the open literature. The outer inviscid mode was observed to be dominant for velocity profiles typical of those observed in laminar separation bubbles on airfoil surfaces. The frequency of this instability was found to be consistent with the dominant instability frequency of planar free shear layers. Packets associated with amplified periods of instability growth were shown to provide a mechanism for cross-stream momentum exchange prior to transition onset. Amplification of the spanwise-oriented vortex structures associated with the instability leads to small-scale fluctuations that develop within the braid region between vortices. Complete breakdown to turbulence occurs in a time-periodic manner over a short distance, corresponding to approximately one wavelength of the primary instability. The fluctuations associated with this breakdown process then lead to stretching and reorientation of the large-scale spanwise structures into hairpin vortices which are shed downstream.

The possible interdependency between the Kelvin-Helmholtz instability, generally associated with free shear layers, and the Tollmien-Schlichting instability, observed in wall-bounded shear layers, was discussed. The strong similarity in the primary-instability-growth phases was noted, and close agreement between the expected instability frequencies was demonstrated, providing further evidence that these two mechanisms share fundamental similarities in regards to separation-bubble transition.

Under elevated-freestream-turbulence conditions, the receptivity mechanism leading to shear-layer roll-up is bypassed as a result of streamwise streaks convecting through the shear layer. These streaks originate near the leading edge of the test surface and are a result of shear-filtering, which allows only low-frequency perturbations from the freestream

turbulence to enter the laminar boundary layer. The streaks are elongated in the streamwise direction, and have a spanwise length comparable to the boundary-layer thickness upstream of separation. Neither sinuous nor varicose instability of these streaks was directly observed as a precursor to the formation of turbulent spots. However, the strong shear associated with these streaks appears to provide the conditions under which turbulent spots form through a localized secondary instability, the frequency of which closely matches that of the inviscid Kelvin-Helmholtz mechanism. In this bypass mode of transition, a distributed streamwise breakdown was observed, with turbulent spots produced along the entire length of the separated shear layer. Transition completion was observed approximately 50% of the time-averaged bubble length downstream of the time-averaged reattachment location.

The internal structure of a turbulent spot in the separated shear layer has been identified as a series of vortex loops, which develop around low-speed streaks within the separated shear layer. The primary vortex loop has a structure similar to the hairpin-vortex structures observed in the inner regions of turbulent boundary layers. Unlike the primary vortex loop whose legs extend in the upstream direction, the legs of the secondary and tertiary vortex loops extend in the downstream direction as a result of being dragged and stretched around a column of low-momentum fluid ejected upwards between the legs of the primary loop. Once the spot convects into the turbulent boundary layer, much of the coherence in the vortex loops is lost due to vortex stretching, mixing with other turbulent spots, and/or mixing with turbulence generated through the Kelvin-Helmholtz breakdown process. While in this present case of elevated freestream turbulence the transition process in the separated shear layer appears to be dominated by the production of turbulent spots through the bypass mechanism, in the rear portion of the separation bubble there is evidence of breakdown in the inter-spot regions that resembles the pattern observed in Kelvin-Helmholtz type instability of separated shear layers in low-disturbance environments. In each turbulent spot, a distinct frequency has been identified with the passing of vortex loops, which in the current case

is approximately 50% higher than that associated with the Kelvin-Helmholtz instability of the separated shear layer. Agreement with the spot spreading half-angle model of Gostelow *et al.* (1996), which was subsequently validated by D'Ovidio *et al.* (2001*b*) to be applicable in separated shear layers, is expected to be good. The spot-spreading half-angles observed in the simulation, which are based on spots developing in the absence of surrounding turbulence, are consistent with the early stages of spot-development in the measurements presented by D'Ovidio *et al.* for a similar level of the pressure gradient parameter. Good agreement with the spot propagation parameter model of D'Ovidio *et al.* (2001*b*) has also been observed. These models are therefore further recommended for use in semi-empirical intermittency-based transition models, such as the one developed by Roberts (2005).

The vortex structures resulting from transition in the separated shear layer remain coherent downstream of reattachment, and provide a source for turbulence kinetic energy production in the outer part of the boundary layer. Slow recovery towards an equilibrium turbulent-boundary-layer state was observed, and is consistent with observations of long recovery lengths identified in the open literature.

Chapter 8

Transition in Separation Bubbles at Low Reynolds Numbers

8.1 Chapter Overview

Through experiments using two-dimensional particle-image velocimetry (PIV) performed in the low-Reynolds-number tow-tank facility at the National Research Council of Canada, this chapter re-examines the nature of transition in a separation bubble under low-Reynolds-number conditions. A newly-designed, unconventional airfoil that provides minimal variation in the separation location over a wide operating range was used, and the study was conducted under low freestream-turbulence conditions over a flow-Reynolds-number range of 28,000 to 101,000 based on airfoil chord. Details regarding the selection and design of the unconventional airfoil are discussed in Section 8.2. The spatial nature of the measurements has allowed identification of the dominant vortical structures associated with transition in the separated shear layer. Discussion of the results, which highlight additional flow features not identified in the SD7003-airfoil measurements of Chapter 6, is provided

in Section 8.3. The results of this study provide baseline conditions for examining passive manipulation of the transition process in a separated shear layer. This flow-manipulation study is discussed in the next chapter.

8.2 Airfoil Design

For the purpose of examining passive manipulation of the transition process in a separation bubble, it was desired to have a test configuration that would provide minimal movement of the separation location over a wide operating range. Based on the SD7003-airfoil measurements presented in Chapter 6, as well as measurements at other operating conditions not presented therein, it was observed that the use of a conventional low-Reynolds-number airfoil would not provide sufficient control of the separation location for examining the effects of transition manipulation over a wide operating range. A design study was thus undertaken to select a suitable test configuration for the flow-manipulation study.

In examining the open literature, various test-configurations could potentially provide the flow conditions necessary for the flow-manipulation study. Eight possible concepts were identified, and are shown schematically in Figure 8.1. Concept 1 is a high-lift airfoil with a profile similar to those designed by Liebeck (1978), which would provide a laminar-rooftop pressure distribution over the forward part of the suction surface, with a controlled-diffusion pressure distribution thereafter. Under moderate-to-high Reynolds-number conditions, this type of design has been used to ensure that laminar flow prevails in the freestream-acceleration region over the suction surface, with transition occurring at the start of the controlled-diffusion region. An airfoil of this type could potentially be designed such that, for the Reynolds numbers examined in the present study, separation would occur slightly downstream of the junction between the laminar-rooftop and controlled-diffusion regions.

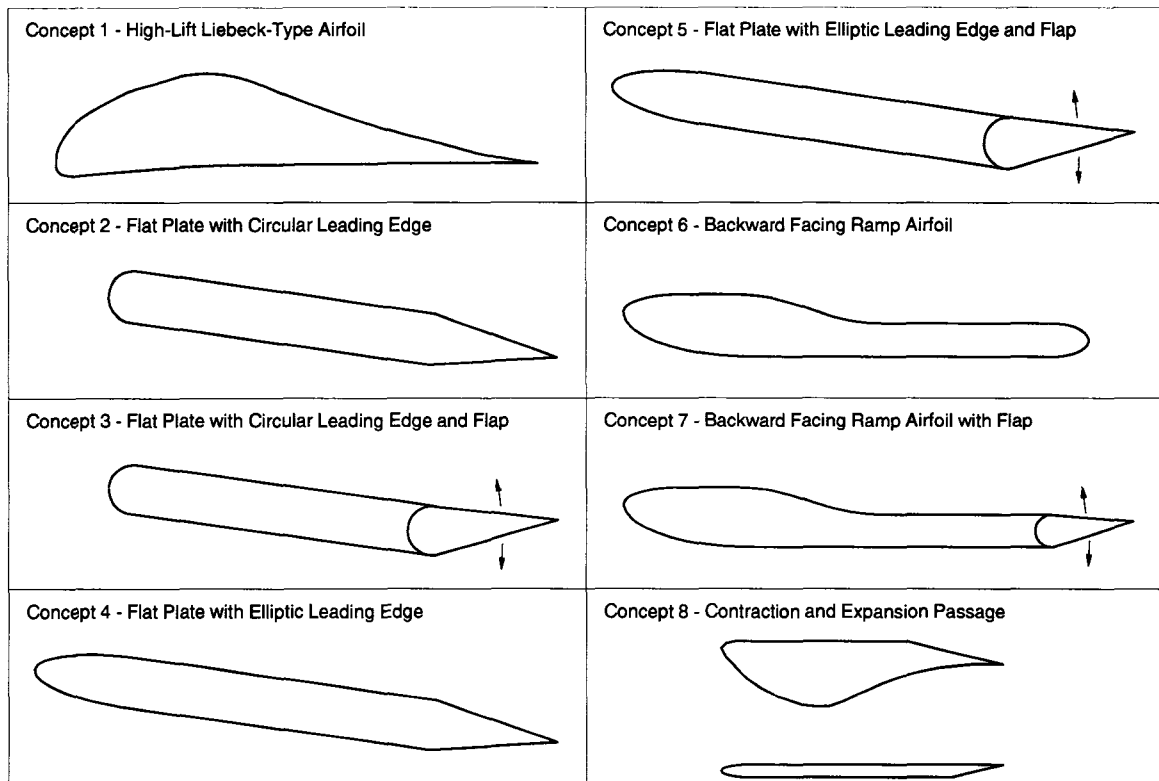


Figure 8.1: Concepts for new test model

Concept 2 is the configuration used by Malkiel and Mayle (1996) for their study of separation-bubble transition, and consists of a flat plate with a circular leading-edge. By forcing separation to occur by means of a change in surface curvature between the circular leading-edge and the flat surface, minimal movement of the separation location could be ensured over a large range of Reynolds numbers and angles-of-attack. Concept 3 is a variation on Concept 2, with the addition of a trailing-edge flap that can be used to vary the circulation, and hence the pressure distribution, over the airfoil. This configuration was used by Arena and Mueller (1980) to examine the flow characteristics typical of airfoils with separation bubbles.

Concepts 4 and 5 are similar to Concepts 2 and 3, respectively, but have elliptic rather than circular leading edges. The reduced surface-curvature change at the junction of the

leading-edge with the flat surface may provide delayed separation, with boundary-layer characteristics prior to separation that more closely resemble those over low-Reynolds-number and low-pressure-turbine airfoils. However, elliptic leading edges are generally used to suppress leading-edge separation and may provide difficulty in obtaining a fixed separation-location on the flat upper-surface over a wide range of operating conditions. The trailing-edge flap of Concept 5 would likely provide better control in this regard.

Concept 6, which is the chosen configuration for the present study, is similar to the airfoil used by Bao and Dallmann (2004) in their study of separation-bubble transition by means of hydrogen-bubble flow visualization and PIV. The region of the airfoil over which separation bubbles are observed consists of a backward-facing curved ramp fitted between two flat surfaces. A seventh-order polynomial describes the shape of the curved ramp, and provides a continuous change in surface slope and curvature over the upper surface of the airfoil. The continuous change in surface curvature at the intersection of the forward flat segment with the ramp ensures that separation occurs as a result of the induced pressure field and not due to a discontinuous change in surface curvature, as would be the case for Concepts 2 and 3. Also, to simulate the separation and transition characteristics of conventional airfoils, the continuous change in surface curvature near separation ensures that instability growth in the separated shear layer results from amplification of small-disturbances generated upstream of separation, as opposed to disturbances generated at separation by a discontinuous change in curvature. Concept 7 consists of the same airfoil shape as Concept 6, but with a trailing-edge flap to provide greater control of the pressure distribution over the upper surface of the airfoil.

Concept 8 is the most complex of any concept considered, and was modelled after the flat-plate test-section configuration used in the wind-tunnel at Carleton University, upon which the simulations of Chapter 7 were based. This concept consists of two surfaces, a curved upper-surface and a flat lower-surface, through which contraction and expansion of

the flow would provide a pressure distribution similar to that encountered over the suction surfaces of low-pressure-turbine airfoils. As the test configuration would have to be towed through the working medium in the NRC tow-tank facility, the lower surface must be supported by the upper surface while still providing optical access from the side for particle-image capture. As well, the lower surface would have to consist of a transparent material to allow illumination of the seeding material, by the laser light-sheet, in the passage between the two surfaces.

The selected configuration, Concept 6, was chosen based on a weighted trade-study of the eight concepts presented in Figure 8.1. Three criteria were used to assess the capability of the configurations for achieving the desired flow conditions. These criteria were: 1) the ability to provide flow conditions upstream of separation with characteristics similar to those observed over low-Reynolds-number and low-pressure-turbine airfoils, 2) the ability to provide minimal variation in the separation location over a wide operating range, and 3) the ability to provide a wide range of separation-bubble sizes and characteristics. Design and manufacturing considerations were also evaluated for the various configurations. The three criteria assessed in these regards were: 1) the time required to design the test model, 2) the simplicity and cost of manufacturing the test model, and 3) the ease with which the test model could be mounted in the tow-tank facility. As PIV was the intended measurement technique for use in this study, optical-access considerations were also important in the design study. The two criteria assessed in regards to this were: 1) the access and visibility of the LED marker-fixture, and 2) the ease with which the flow region of interest could be illuminated by the laser-light sheet and viewed by the camera. Based on the weighted trade study, Concept 6 was found to best meet the requirements for the design.

Concept 6, from here on referred to as the “unconventional airfoil,” provides the best compromise between achieving the desired flow characteristics and ease of design. As shown by Bao and Dallmann (2004), this configuration can provide minimal movement of the

separation location while providing a large potential variation in separation bubble sizes for the Reynolds-number-range that can be realized in the tow-tank facility. It can also be manufactured in one piece and, as it does not require an elevated angle-of-attack to promote separation, does not require much initial study to select suitable operating conditions.

The shape of the unconventional airfoil differs from that used by Bao and Dallmann, in that it has a much shorter flat-surface section upstream of the curved backward-facing ramp. This change was made because of the following competing requirements: limits in the chord length for ensuring steady-state operating conditions over the measurement length of the tow-tank; and the ability to capture closed separation-bubbles over the aft section of the airfoil. The short working length of the tow tank (3 m) limits the chord length of the airfoil, as a longer chord would require a greater distance of travel before the shear-layers reach a steady-state condition (Schlichting and Gersten, 2000). The selected chord length for the airfoil model is 0.25 m. To ensure that a closed separation bubble forms over the airfoil, the distance of the flat surface downstream of the backward-facing ramp was selected such that transition and reattachment were expected to occur over this surface for any flow Reynolds numbers greater than 10,000. This aft-section sizing was performed using the separation-bubble transition-onset model of Roberts (Equation 2.1, page 33), to predict the length from separation to transition onset, with the momentum-thickness Reynolds-number at separation estimated by assuming the boundary layer upstream of separation develops in the same manner as a zero-pressure-gradient Blasius boundary layer. Based on this analysis, the required aft-surface length reduced the fraction of chord-length available for the forward-section. Although the short forward-section of the airfoil was a result of the above-noted requirements, its short length has provided conditions that better represent the upstream flow conditions over low-Reynolds-number and low-pressure-turbine airfoils. The short length provides conditions such that, for the lower Reynolds numbers examined in this study, an adverse pressure gradient is present over the entire distance between the

leading-edge suction peak and separation. The shape used by Bao and Dallmann provided relaxation of the leading-edge boundary layer to a zero-pressure-gradient Blasius profile prior to being influenced by the ramp.

The height of the backward-facing ramp of the unconventional airfoil is 0.015 m, and was selected such that it is at least twice the expected boundary-layer thickness at separation for any flow Reynolds numbers greater than 10,000. The surface shape parameters, including polynomial coefficients, ellipse lengths, and ellipse axis-ratios, along with excerpts from the engineering drawings of the airfoil, are provided in Appendix B.

8.3 Discussion of Measurement Results

For the range of flow-Reynolds-numbers examined with the unconventional airfoil, separation bubbles are observed on the upper surface of the airfoil over the curved backward-facing ramp. The basic flow characteristics of the separation bubbles are discussed in Section 8.3.1, which includes descriptions of the shear layer growth properties. The mechanisms associated with laminar-to-turbulent transition of the separated shear layers are then described in Section 8.3.2, followed by a discussion of the ensemble-averaged flow statistics in the transition and reattachment regions of the separation bubbles in Section 8.3.3.

8.3.1 Shear-Layer and Flow Characteristics

At all Reynolds numbers examined, a separation bubble develops over the airfoil surface in the region of the backward-facing ramp. Figure 8.2 shows streamlines associated with the ensemble-averaged flow-fields over the airfoil for all Reynolds numbers examined, and provides an indication of the range of separation-bubble shapes and sizes observed in the

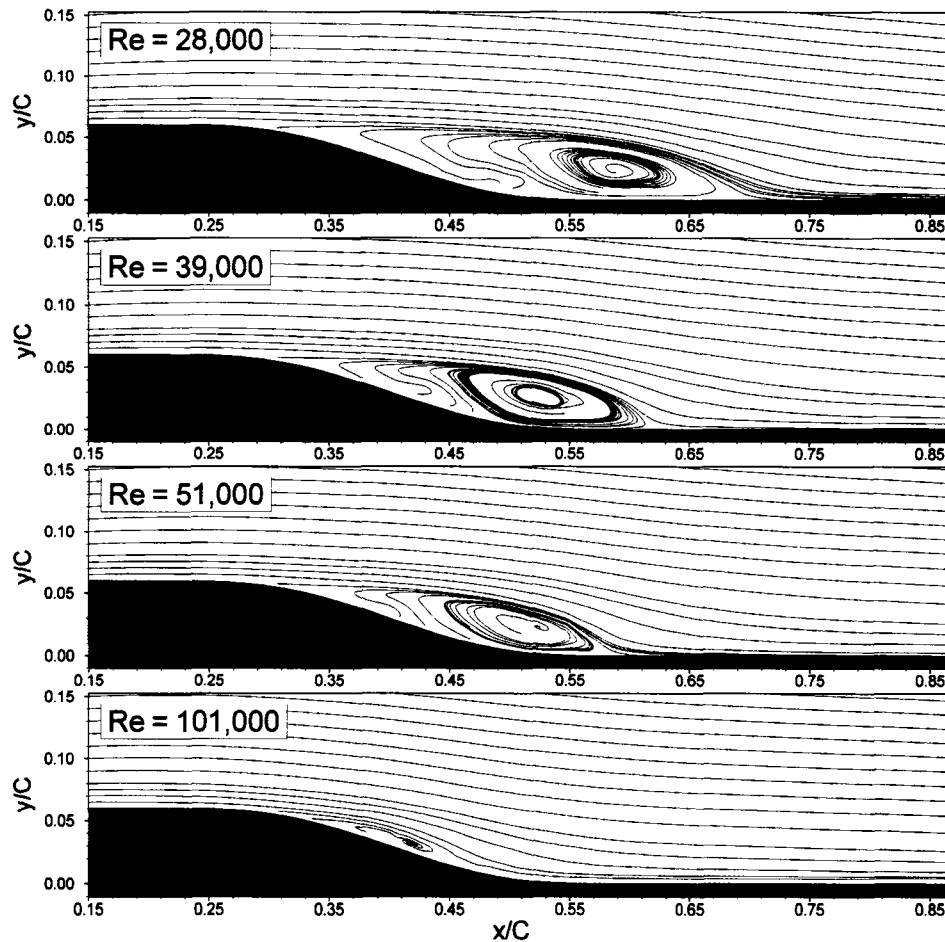


Figure 8.2: Ensemble-averaged streamlines over the unconventional airfoil

present study. Separation occurs around $x/C = 0.3$, and the reattachment length decreases with increasing Reynolds number as expected. Large clockwise recirculation regions are observed in the downstream region of the bubbles. As will be shown, this large-scale reattachment vortex evident in the averaged flow field is not readily identifiable in the instantaneous flow field where the many smaller-scale vortical structures that originate from instability of the separated shear layer prevail. At the three lower Reynolds numbers, a small ensemble-averaged forward-flow region is observed near the surface at the upstream end of the strong recirculation region, and is indicated by streamlines emanating from the surface with a component in the downstream direction. This occurs in the region of the

separation bubble that is often called the “dead-air” or “dead-water” region, where the velocity is much lower than that of the freestream flow, and is not a phenomenon associated with typical separation bubbles that occur over conventional airfoils. This forward flow is associated with a secondary vortex that has been observed in the lower corner behind sharp backward-facing steps (Hall *et al.*, 2003). As with the large-scale reattachment vortex of the separation bubble, this secondary vortex is not discernable in the instantaneous velocity field which is dominated by smaller scale transient flow structures. The strength and size of this secondary vortex are driven by the relative magnitudes of the shear generated by the reattachment vortex and the separated shear layer, and this averaged-vortex phenomenon is generally not observed in separation bubbles that develop over conventional airfoils. Based on comparison of these results with those for the SD7003 airfoil presented in Chapter 6 and the low-freestream-turbulence simulation in Chapter 7, the presence of an ensemble-averaged secondary vortex in the separation bubble does not appear to alter the transition process in the separated shear layer in any significant manner.

For all four Reynolds numbers, the freestream velocity distributions measured at the edge of the shear layer are presented in Figure 8.3a. This edge is easily identified in the laminar part of the shear layer, as the streamline-curvature induced by the airfoil geometry provides a maximum in the velocity profiles at the edge of the shear layer. Over the turbulent part of the shear layer, this edge has been identified as the dividing line outside of which the $\langle u'v' \rangle$ velocity correlation values are negligible. Upstream of separation ($x_s/C \approx 0.3$), the freestream velocity and acceleration magnitudes change over the Reynolds number range examined. As the Reynolds number is reduced, the thicker boundary layer developing over the elliptic leading edge provides reduced streamline curvature and hence a reduced suction-peak velocity magnitude. The change in lift distribution as a result of the Reynolds-number-dependent separation-bubble size also contributes to this effect. It is also noted that, for all cases, freestream acceleration is observed over the aft region of the airfoil.

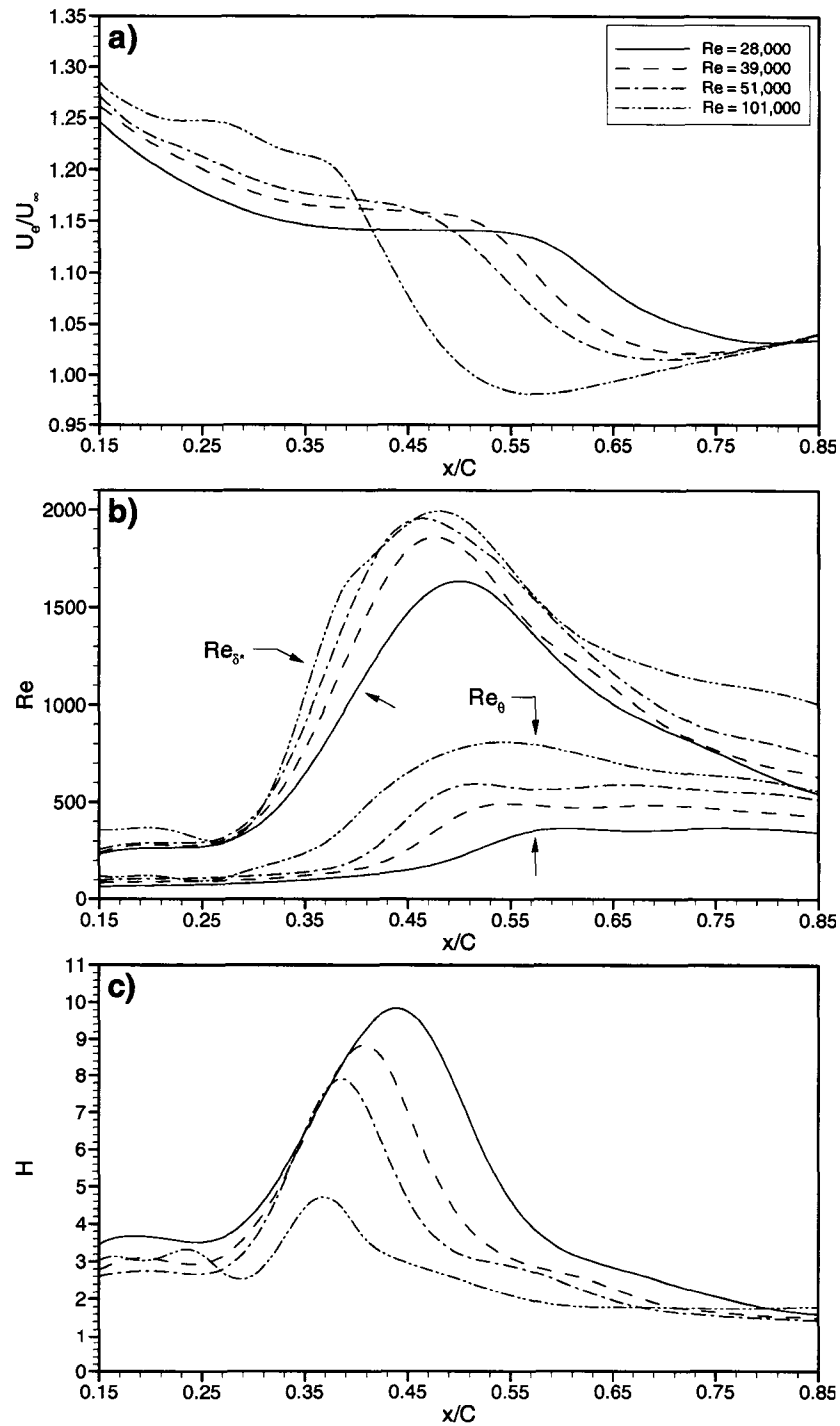


Figure 8.3: Shear layer property distributions over the unconventional airfoil, a) shear layer edge velocity, b) displacement and momentum thicknesses, c) shape factor

The shear-layer integral parameters are presented in Figures 8.3b and 8.3c. Downstream of separation, the displacement thickness increases at a high rate due to the thick “dead-water” region resulting from the the shear layer moving away from the surface. The momentum thickness, however, remains low until the effects of transition in the separated shear layer become pronounced. The high displacement thicknesses prior to transition result in high shape factors, as observed in Figure 8.3c. The peak shape factors for the three lower Reynolds numbers ($H \approx 8 - 10$) are indicative of the separated shear layers being located far from the surface, and are consistent with values observed over the SD7003-airfoil measurements of Chapter 6.

8.3.2 Transition Mechanisms

Transition of shear layers in low-disturbance environments occurs through receptivity of the shear layer to infinitesimal disturbances. According to the classification by Saric *et al.* (2002), regarding receptivity sites over aerodynamic bodies, two distinct receptivity sites are encountered prior to separation over the airfoil. The first receptivity site is the leading-edge region where the boundary layer is thin and grows rapidly, and where streamwise pressure gradients are strong relative to the boundary-layer scales. The second receptivity site is localized at $x/C = 0.12$, where a discontinuity in surface curvature occurs as the leading-edge ellipse, with a major-to-minor axis ratio of 3.333, joins the flat surface segment upstream of the curved ramp. Upon penetrating the boundary layer, the disturbances grow in the shear layer, which is promoted by the inflectional cross-stream velocity distribution owing to the adverse streamwise pressure gradient (Schlichting and Gersten, 2000).

In the present experiments, transition of the separated shear layer occurs in a manner similar to that which occurs in planar free-shear layers and in separation bubbles over

conventional airfoils under low levels of freestream disturbances, such as those documented in Chapters 6 and 7. Under these conditions, the small disturbances that penetrate the boundary layer at the upstream receptivity sites grow up to the point of separation at the beginning of the backward-facing ramp, and amplify further in the separated shear layer which is inviscidly unstable due to the inflectional velocity profile. Amplification of the most unstable frequency associated with this Kelvin-Helmholtz instability mechanism leads to roll-up of the vorticity contained in the shear layer to produce a train of discrete vortices which grow as they convect downstream. Figure 8.4 presents a series of $x - y$ plots of normalized spanwise vorticity ($C_{\Omega_z} = \Omega_z C / U_\infty$) which show the formation and growth of these spanwise-oriented vortices over one period of the dominant instability frequency, at a Reynolds number of 39,000. The plots correspond to a series of instants in time, with time stated in a normalized form ($t^* = t U_\infty / C$). The Strouhal number associated with the formation frequency of the spanwise vortices, based on conditions at separation ($St_{\theta_s} = f \theta_s / U_{es}$), is in the range 0.015 to 0.016 for the three lowest Reynolds numbers examined. This is consistent with the value of 0.016 identified by Ho and Huerre (1984) for an unforced planar free shear layer. A slightly higher value of 0.020 is observed for the highest Reynolds number. However, the uncertainty in this value is approximately 0.005, and is much higher than that for the lower Reynolds numbers due to the relatively thin boundary layer at separation. For this case, a resolution of only six vectors across the boundary layer at separation yields larger uncertainties in the momentum thickness at separation and the inferred frequency of vorticity roll-up.

Once the roll-up of vorticity is initiated in the separated shear layer, the amplification rate is very high in the streamwise direction. As seen in Figure 8.4, over a distance of approximately two wavelengths, the spanwise-oriented vortices grow to a level where the wall-normal extent is approximately equal to that of the streamwise wavelength, and small-scale fluctuations in the vorticity contours near $x/C = 0.5$ indicate that breakdown to

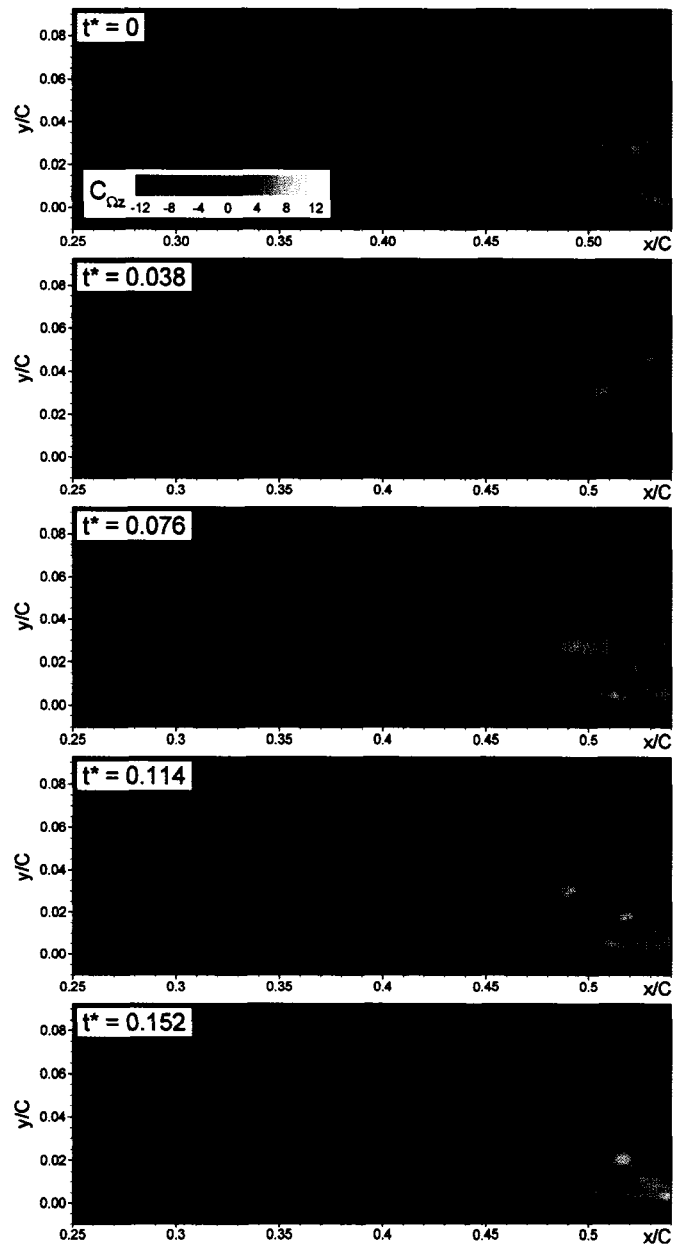


Figure 8.4: Instability growth in the separated shear layer for $Re=39,000$

small-scale turbulence has been initiated. In the region $0.45 < x/C < 0.50$ the vortices grow to a sufficient strength that they provide a significant level of cross-stream momentum exchange and initiate the process of reattachment of the shear layer to the surface.

The transition point in a shear layer can be defined as the location where small-scale fluctuations, smaller than those associated with the dominant instability waves, are initiated and provide a mechanism for dissipation of energy at the Kolmogorov scale. In the simulation results of Chapter 7 for which transition occurred in a separation bubble under low-freestream-turbulence conditions, it was observed that this small-scale breakdown to turbulence is initiated in the high-shear braid region between sequential large-scale spanwise vortices. Due to convection of the vortices through the shear layer, the small-scale breakdown occurs in a time-periodic manner. Through the results of Chapter 7, it was also observed that the most upstream location where small-scale breakdown occurs corresponds with deviation of the fluctuation growth rates from the exponential growth associated with amplification of the dominant instability. This has therefore been used as a means for identifying the transition onset location in the present study, and was also used in the SD7003 study of Chapter 6. Figure 8.5 shows the growth of $\langle v'v' \rangle$ and $\langle u'v' \rangle$ fluctuation correlations in the shear layer for the case presented in Figure 8.4 ($Re = 39,000$). In Figure 8.5, the fluctuation-correlation levels are presented as an integration of the ensemble-averaged values across the shear layer. As compared to the method used in Chapter 6, where data were extracted along the line of maximum amplification within the shear layer, this new method was found to provide lower uncertainty and scatter in the fluctuation growth curves, with the integration acting to filter localized errors in the correlation parameters. This is observed by comparing the fluctuation growth curves in Figure 8.5 with those in Figures 6.6 (page 119) and 6.7 (page 120), for which greater scatter is observed in the latter figures at the upstream end of the exponential-growth regions. In Figure 8.5, deviation from exponential growth occurs at about $x/C = 0.44$, and is identified as the location of transition

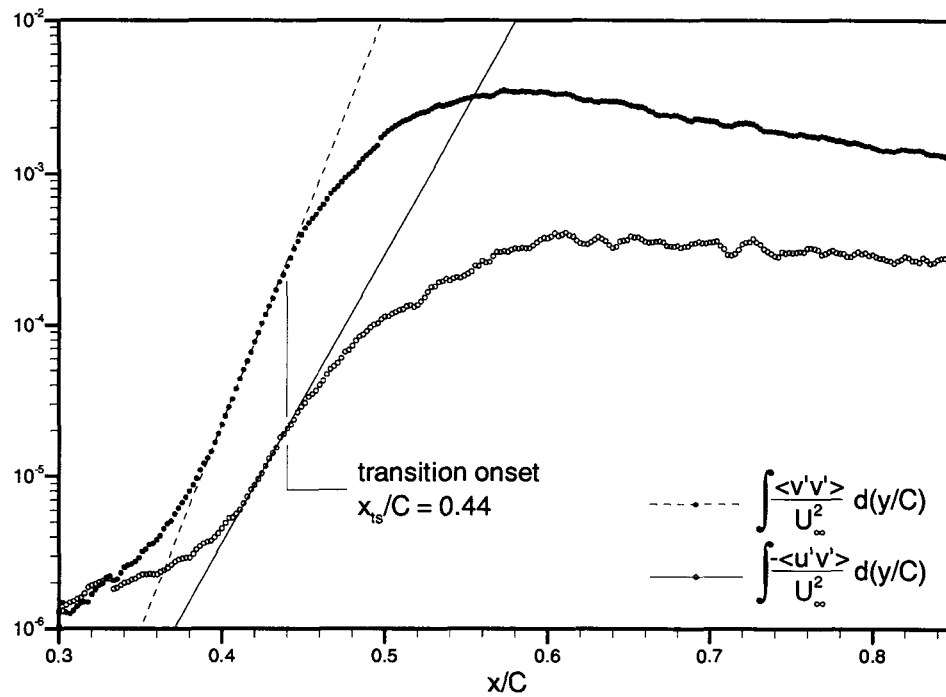


Figure 8.5: Fluctuation growth rates and transition onset location for $Re=39,000$

onset. It was also confirmed that this location corresponds to deviation from exponential growth of data extracted along the line of maximum instability growth of the separated shear layer, thus validating the method using cross-stream-integrated values. Although both the $\langle v'v' \rangle$ and $\langle u'v' \rangle$ distributions deviate from exponential growth at the same streamwise location, the $\langle v'v' \rangle$ curve exhibits exponential growth further upstream than the $\langle u'v' \rangle$ curve, thus providing a greater streamwise extent of observed exponential growth. This has also been identified at all other Reynolds numbers, and therefore the $\langle v'v' \rangle$ distributions have been used in identifying transition onset. Uncertainty in the location of transition onset for the present measurements, and those of the flow-manipulation study presented later in Chapter 9, is $\pm 0.01 C$.

In planar free-shear layers, the spanwise vortices produced by the Kelvin-Helmholtz instability are susceptible to subharmonic disturbances (Kelly, 1967), which results in

a vortex-pairing phenomenon. This pairing phenomenon is observed in the present experiments at all Reynolds numbers, and is shown for $Re = 28,000$ in Figure 8.6 through a series of $x-y$ plots of normalized spanwise vorticity. At $t^* = 0$, a large vortex resulting from roll-up of the separated shear layer is observed at approximately $x/C = 0.55$. In the next frame, at $t^* = 0.0544$, an upstream vortex enters the field of view and the subharmonic instability causes it to shift towards the higher velocity side of the shear layer. As this upstream vortex convects at a higher rate and catches up to the downstream vortex, the two become stretched and elongated as they rotate about each other due to mutual induction of their vorticity fields. The trajectories of the two vortex cores are traced out in Figure 8.6 and clearly show the difference in convection rates of the two vortices due to the subharmonic instability. As the vortices merge, the production of smaller-scale turbulence is observed near the core of the new vortex, indicated by the stronger vorticity fluctuations, and at $t^* = 0.2722$ the new vortex is dominated by small-scale fluctuations. The same vortex-pairing phenomenon has been observed in other studies of separation bubbles (Wissink and Rodi, 2002; Abdalla and Yang, 2004; Malkiel and Mayle, 1996), including that of Chapter 6. However, the presence of pairing has only been observed at lower Reynolds numbers ($Re_\theta O(100)$), similar to those of the present study. It is conceivable that the presence of this subharmonic instability is also dependent on the distance of the separated shear layer from the surface, and the closer proximity of the surface in a thinner bubble, like that of the low-freestream-turbulence simulation of Chapter 7, may suppress its effects.

The new vortices produced as a result of vortex pairing have approximately double the spacing of the primary vortices. As described by Ho and Huang (1982) in regards to planar free-shear layers, the change of the local length scale of the shear layer as a result of the vortex merging makes the original subharmonic become neutrally stable, and the new subharmonic becomes the wave of most rapid amplification. This process leads to a secondary pairing phenomenon, and is suggested as the dominant mechanism

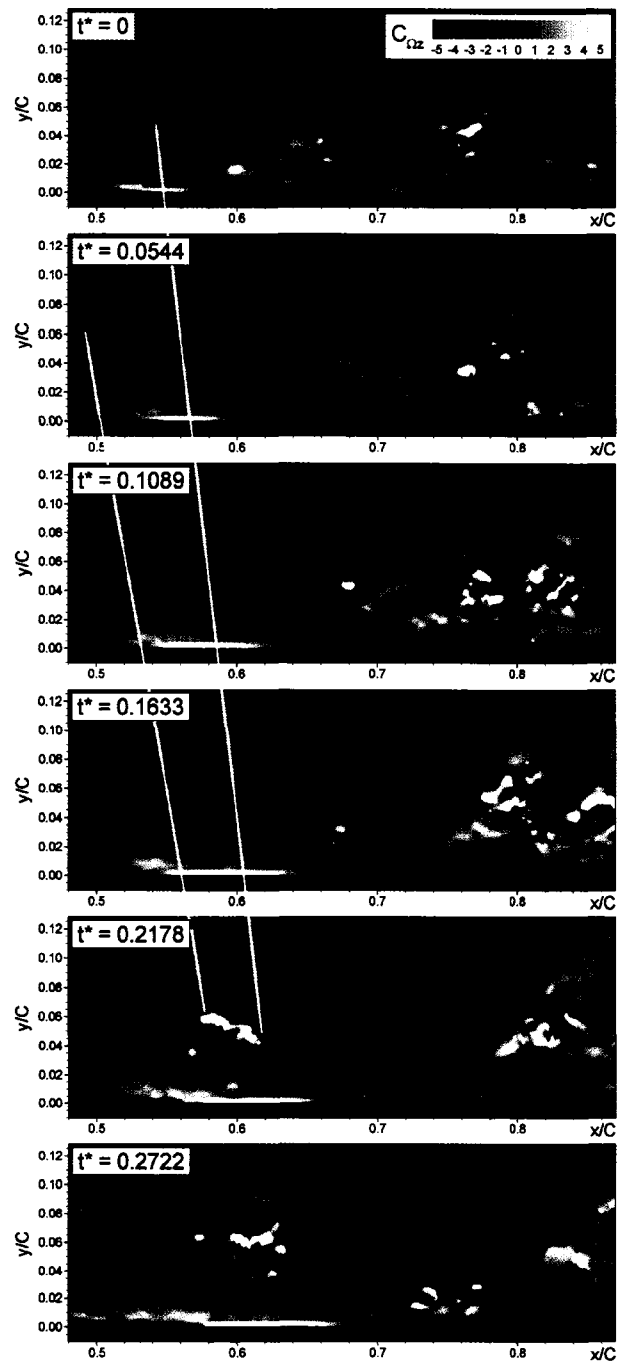
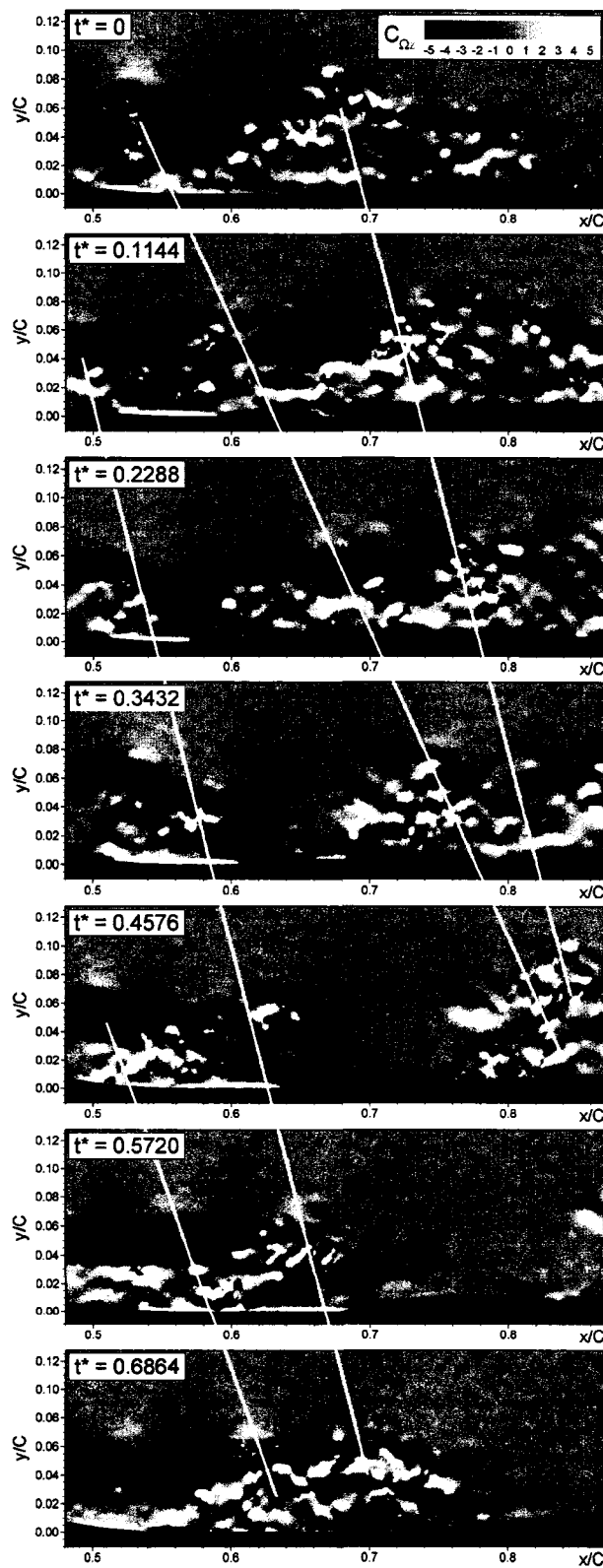


Figure 8.6: Vortex pairing phenomenon observed at $Re=28,000$

associated with growth of planar free-shear layers (Ho and Huerre, 1984). In the present measurements, this secondary pairing is sometimes observed in and downstream of the reattachment region. However this secondary pairing process does not occur in as coherent a manner as that which occurs in free shear layers. Some indications of this secondary pairing are seen in the downstream regions of Figure 8.6, but the process is more distinct at a Reynolds number of 39,000 as shown in Figure 8.7. In this figure, two occurrences of the secondary pairing phenomenon are identified and the trajectories of the pairing vortices are shown. The vortices do not have a distinctive structure but are identified by clusters of strong vorticity fluctuations. The most interesting observation of the current measurements is the inter-vortex regions with negligible velocity and vorticity fluctuations (apparent for $0.3432 \leq t^* \leq 0.6864$ in Figure 8.7). These regions are comprised of freestream fluid entrained towards the surface by the large-scale vortices generated in the transition region. The boundary layers in the inter-vortex regions have velocity profiles similar to time-averaged turbulent profiles, despite the low fluctuation levels, with vorticity concentrated to a thin region near the surface. The occurrence and streamwise extent of this laminar-like inter-vortex region decrease with increasing Reynolds number, and is scarcely observed at a Reynolds number of 101,000.

As observed in some large-eddy and direct-numerical simulations of transition in separation bubbles (Yang and Voke, 2001; Wissink and Rodi, 2002; Abdalla and Yang, 2004), including the results of Chapter 7, the large-scale spanwise vortices generated in the transition region become stretched and reoriented as they convect downstream, due to a secondary spanwise instability, resulting in hairpin-shaped structures similar to the dominant structures observed in turbulent boundary layers (Panton, 2001). Some of the streamwise-elongated turbulent structures observed in the present measurements, such as that observed in the lower plots of Figure 8.7, may be a result of the two-dimensional measurement plane cutting through the upstream-oriented legs of one of these hairpin-

Figure 8.7: Subharmonic pairing phenomenon observed at $Re=39,000$

shaped structures and may not be a result of a secondary pairing instability. Despite this, the more distinct occurrences of large-scale vortex merging, like that observed in the upper plots of Figure 8.7, is a strong indicator that the secondary pairing instability is active. However, the presence of the wall provides damping for this process as the reattached shear layer slowly recovers towards the structure of a turbulent boundary layer. As shown by Alam and Sandham (2000) and the simulation results of Chapter 7, this recovery takes place over a distance of many bubble lengths.

As mentioned above, the secondary pairing process is not a consistent phenomenon, and most often the vortices generated from the primary pairing event remain relatively coherent as they convect downstream of the separation bubble. The dominant streamwise wavelengths associated with the large-scale vortices have been identified by means of a spatial correlation of the wall-normal velocity fluctuation. The correlation coefficient $cc_{v'}$ is defined as:

$$cc_{v'}(x, x + \Delta x) = \frac{1}{N} \sum_{i=1}^N \frac{v'_i(x)}{\sqrt{\langle v'v'(x) \rangle}} \frac{v'_i(x + \Delta x)}{\sqrt{\langle v'v'(x + \Delta x) \rangle}} \quad (8.1)$$

where N is the number of vector fields used in the ensemble average and i is an index identifying the instantaneous vector fields. Normalization of the instantaneous fluctuation values by the local ensemble-averaged RMS values, $\sqrt{\langle v'v' \rangle}$, is required since the fluctuation levels change with streamwise distance and this ensures that the correlation value remains below 1. Figure 8.8 provides an example of the correlation function at a location of $x/C = 0.426$ and $y/C = 0.061$ for $Re = 39,000$. Apart from the autocorrelation peak centered at the location about which the correlation is being performed ($x/C = 0.426$), two distinct correlation peaks are observed in Figure 8.8, and provide estimates for the dominant wavelength prevailing in the separated shear layer. Since the dominant length scale changes with streamwise distance due to changes in the vortex convection rates and the vortex pairing phenomenon, the length scales identified by the correlation function are not

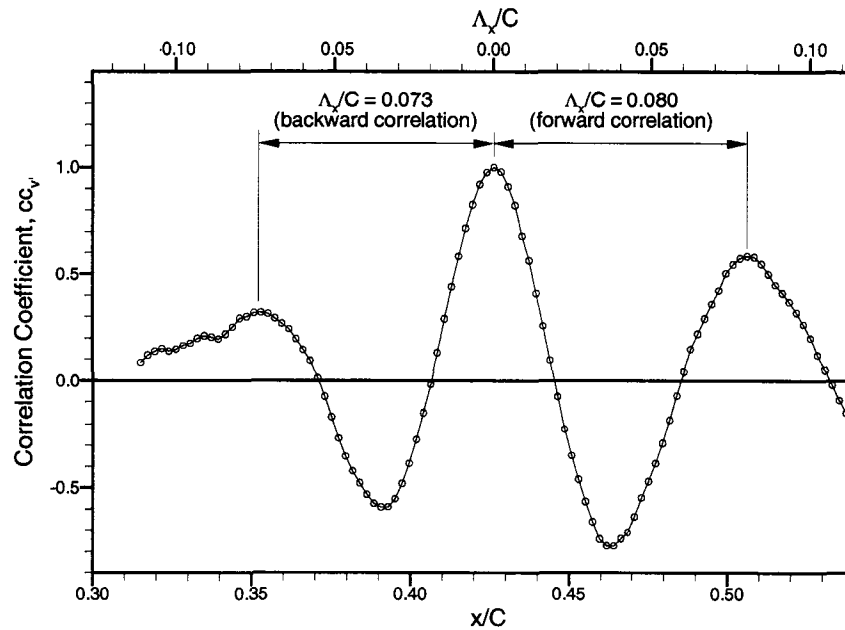


Figure 8.8: Streamwise correlation function of wall-normal velocity fluctuations at $x/C = 0.426$, $y/C = 0.061$ for $Re=39,000$

indicative of the dominant wavelength at the location about which the correlation is being performed. Differences in the forward- and backward-correlated wavelengths in Figure 8.8 provide evidence of this discrepancy. It can be assumed that the observed dominant length scale is more representative of those that occur at a distance half-way between the correlation location and the location of the respective correlation peak. Wavelengths extracted in this manner provide a clear picture of the change in length scale with streamwise distance due to the vortex pairing phenomenon, and are shown in Figure 8.9a. There is a slight discrepancy in the length scales extracted using the forward and backward correlation peaks, but the general trend of increasing length scale is captured well. Over the aft region of the airfoil, the dominant length scale is approximately double that of the primary instability wavelength that develops in the separated shear layer, providing evidence that the primary pairing event is dominant and the inconsistency of the secondary pairing phenomenon provides minimal influence on the spatial correlation. The correlation peak values associated

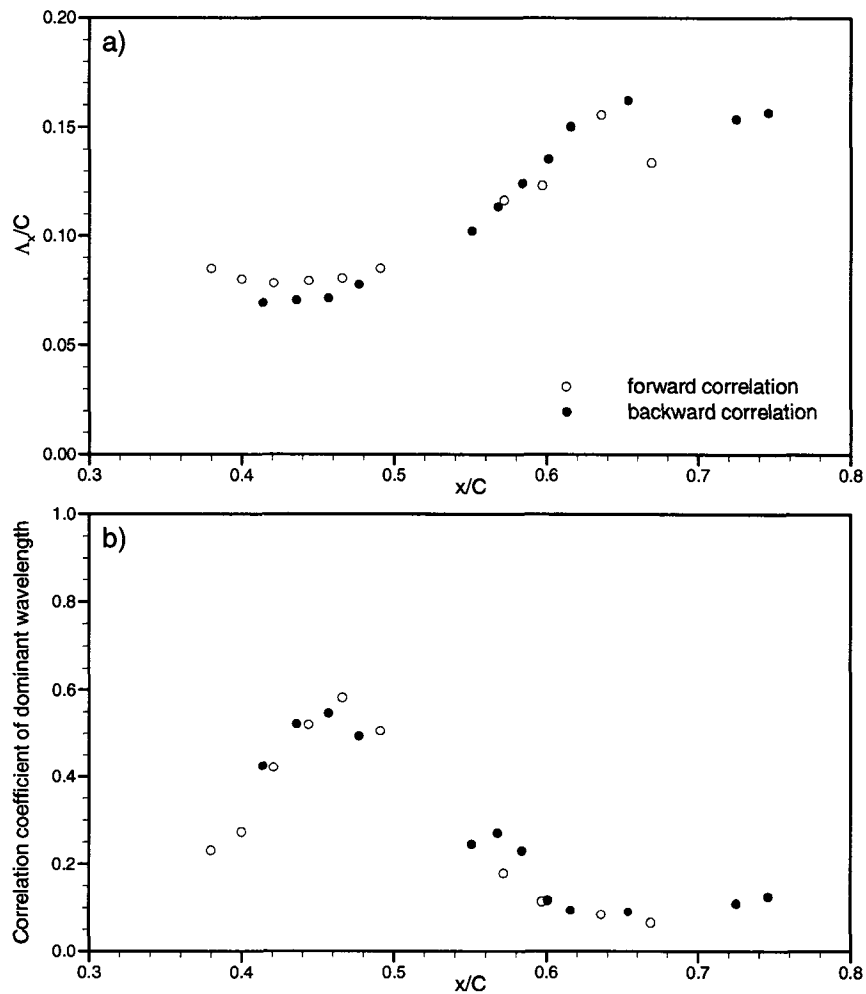


Figure 8.9: Streamwise correlation of dominant wavelengths for $Re = 39,000$, a) wavelength distribution, b) correlation peak distribution

with the dominant wavelengths are shown in Figure 8.9b, and show the decay in coherence of these dominant length scales with downstream distance. The highest level of coherence is observed near transition onset ($x_{ts}/C = 0.44$), downstream of which the combined effect of small-scale breakdown to turbulence and distortion of the large-scale vortices results in lower correlation values.

8.3.3 Ensemble-Averaged Flow Statistics

For practical purposes, the ensemble-averaged statistics associated with the velocity fluctuations in separation bubbles are important, particularly for validation and development of transition models and turbulence-closure models for use in computational fluid dynamics (CFD) software (Roberts, 2005). In Figure 8.10, contour plots of velocity correlations are shown for $Re = 39,000$ with the averaged streamline patterns provided in the upper plot of the figure, and with the dividing streamline that bounds the averaged reverse-flow region overlaid on the subsequent contour plots. On the contour plots of Figure 8.10, a slight discontinuity in the fluctuation fields is observed at $x/C \approx 0.51$ which is at the interface of the two measurement regions from which the data has been processed. Velocity fluctuations are first observed to grow along the line of maximum vorticity in the separated shear layer, which is consistent with growth of vorticity fluctuations by means of the inviscid Kelvin-Helmholtz instability, as observed in Figure 8.4. The highest fluctuation levels are observed near the ensemble-averaged reattachment location, and decay with downstream distance as a result of damping due to the presence of the wall. In the plots of U_{rms} and $\langle u'u' \rangle$, a secondary fluctuation peak is observed inside the bubble along the line of maximum reverse-flow velocity. This is consistent with other measurement and simulation results of separation bubbles (Volino, 2002a; Spalart and Strelets, 2000; Lang *et al.*, 2004) and is predicted by linear stability theory (LST). As discussed in Chapter 7 by means of LST results presented by Rist and Maucher (2002), this inner peak is a result of a viscous instability associated with the reverse-flow below the separated shear layer.

Of the statistical parameters presented in Figure 8.10, the Reynolds shear-stress component $\langle u'v' \rangle$ provides a measure of the wall-normal momentum exchange occurring as a result of the transition process, and also has peak levels near the ensemble-averaged reattachment location. The energy transfer facilitated by the $\langle u'v' \rangle$ Reynolds shear-stress

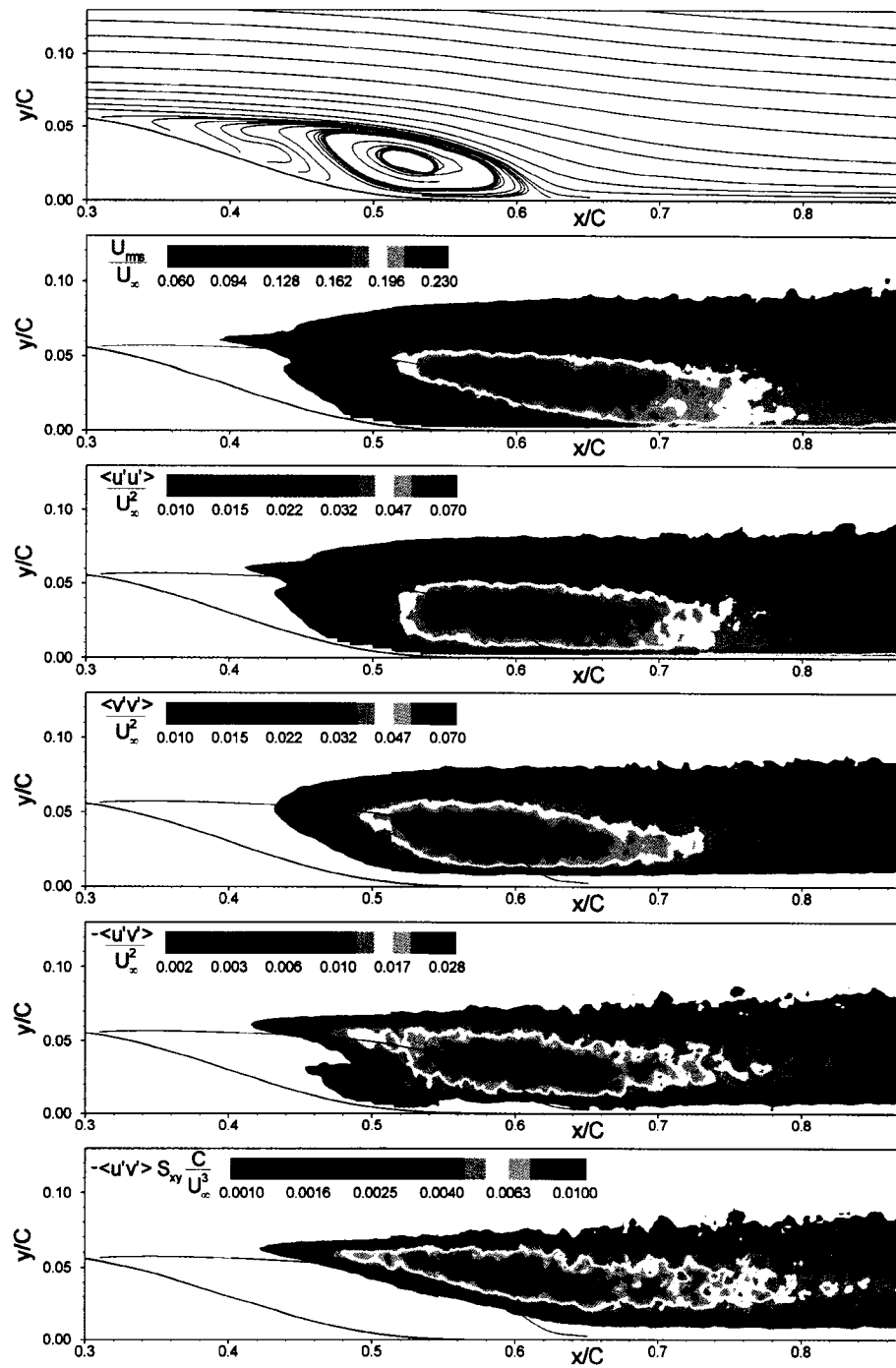


Figure 8.10: Mean streamlines and contour plots of velocity correlations at $Re = 39,000$ (dividing streamline overlaid on contour plots)

component is quantified by $-\langle u'v' \rangle S_{xy}$ which is the work done by this shear stress on the time-mean flow field through the strain rate S_{xy} . This energy transfer is noted to occur predominantly in the outer part of the separated shear layer as a result of the high rates of strain occurring in that region. Downstream of the bubble, significant levels of $-\langle u'v' \rangle S_{xy}$ are observed across the reattached shear layer.

Although not presented in this chapter, for the sake of conciseness, similar velocity-correlation plots to those of Figure 8.10 have been examined for all the measurement cases, including those for the flow-manipulation study presented in the next chapter. The detailed measurement results for each of these cases are included in Appendix D.

8.4 Conclusions

In an effort to further examine the mechanisms and processes involved in transition and reattachment of a separated shear layer, and to provide baseline conditions for the flow-manipulation study of the next chapter, an airfoil has been designed that provides a suction-side pressure distribution similar to that occurring over typical low-Reynolds-number airfoils while minimizing the streamwise movement of separation over a range of operating conditions. Measurements were performed using PIV over the upper surface of this airfoil at four Reynolds numbers, based on chord length, in the range 28,000 to 101,000 and under negligible freestream turbulence conditions.

At all Reynolds numbers, the Kelvin-Helmholtz instability has been observed as the dominant transition mechanism in the separation bubbles measured over the newly-designed, unconventional airfoil. This instability leads to roll-up of the vorticity contained in the shear layer into discrete spanwise-oriented vortices that grow and shed from the shear layer, initiating small-scale breakdown to turbulence. The normalized frequency of shedding

is noted to be consistent with that observed in planar free shear layers. A pairing process has been identified whereby a subharmonic instability causes two sequential vortices to rotate about each other and merge to form a train of larger vortices with double the spacing of the primary vortices. A secondary pairing of these larger vortices is sometimes observed. When this secondary pairing occurs, a region of laminar flow is observed between the large scale vortices. This laminar inter-vortex region consists of freestream fluid entrained towards the surface as a result of the strong circulation associated with the large-scale vortices. A data-processing method based on a spatial-correlation of the velocity fluctuations has been examined, and proven reliable, for extracting the wavelength of the vortical structures originating in the separated shear layer.

The overall structure of the separation bubble developing downstream of the backward-facing curved ramp of the airfoil is noted to be generally consistent with that observed previously on conventional airfoils. In the separation bubble over the curved backward-facing ramp configuration, a secondary recirculation zone is observed to develop ahead of the primary recirculation zone within the time-averaged flow field. This secondary recirculation zone does not appear to be strong enough to modify the base-flow profile in the separated shear layer, such that it would affect the instability and transition characteristics of the layer.

The clear physical picture of the transition and reattachment processes established for the unconventional airfoil provides a sound basis for examining the effects of passive surface modifications applied to the airfoil. The next chapter discusses the results of this flow-control study.

Chapter 9

Passive Manipulation of Separation-Bubble Transition

9.1 Chapter Overview

The feasibility of manipulating the transition process in a separated shear layer through passive forcing is evaluated in this chapter. The newly-designed, unconventional airfoil examined in the previous chapter was used for the study. A series of surface disturbances in the form of two-dimensional surface modifications located upstream of the point of separation are experimentally evaluated in regards to their ability to promote or delay transition and reattachment of the separated shear layer. The tested surface perturbations vary broadly, and include a constant-height step, constant-depth grooves, a backward-facing step followed by a ramp, and a sinusoidal groove, with the goal of identifying the configuration that provides the best trade-off between improved aerodynamic performance at low Reynolds numbers and minimal aerodynamic penalties at higher Reynolds numbers.

Through experiments using two-dimensional particle-image velocimetry (PIV), manipulation of the separation-bubble-transition process by the surface perturbations is examined. The study was conducted under the same flow conditions examined in Chapter 8: low freestream-turbulence over a flow-Reynolds-number range of 28,000 to 101,000 based on airfoil chord.

9.2 Passive Surface Modifications

As noted in Chapter 2, Section 2.5, with regards to the control of transition in separation bubbles, active methods are more effective than passive methods at manipulating the transition process, but the energy expenditure required by these devices could potentially result in a decrease of the overall system performance. Conversely, passive methods which require no energy expenditure can work very well for a specific operating condition, but generally result in performance degradation under flow conditions where control of the transition process is not needed. Of the passive techniques that have previously been employed for control of separation bubbles, surface indentation methods appear to provide the best compromise between improved low-Reynolds-number performance and minimal penalties at higher Reynolds numbers.

Several two-dimensional surface modifications have been examined for the newly-designed, unconventional airfoil, and are shown in Figure 9.1 with their identifying acronyms. They include both surface protrusions (ST configuration) and surface indentations (SG, LG, SN, SR configurations). The indentation configurations have been machined into thin, flexible vinyl strips mounted in a matching groove on the airfoil surface, and the extent of these strips is indicated by the dashed lines in Figure 9.1. The surface modifications have been designed to provide a perturbation to the separating shear layer at a frequency matching that of the dominant instability frequency of the separated shear

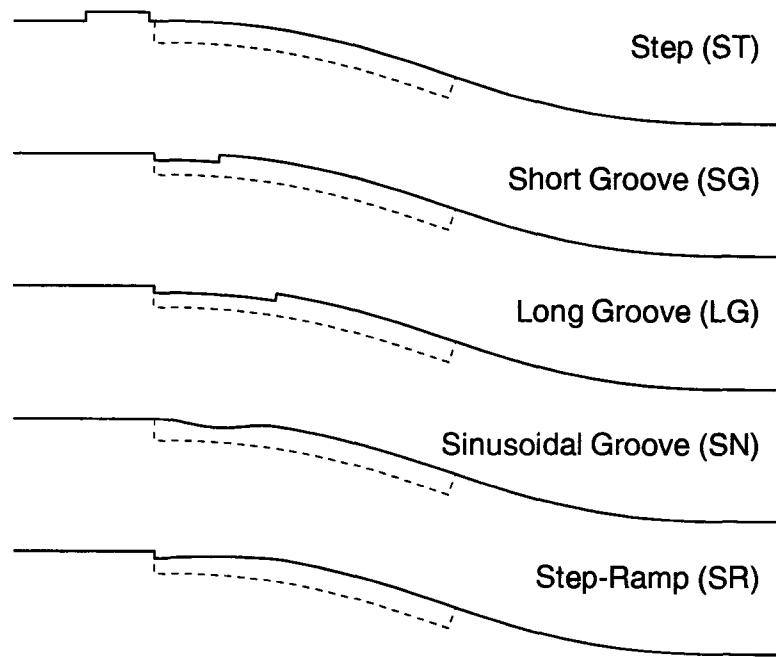


Figure 9.1: **Geometry of surface modifications (dashed line indicates extent of flexible vinyl strip)**

layer. To this effect, the streamwise lengths of the surface modifications have been selected to provide passive forcing at intervals of the instability wavelength, which was observed to be $\Lambda_x = 18$ mm, or 7.2% of chord, for the clean airfoil configuration at a Reynolds number of 39,000.

The protrusion/indentation height of the surface modifications were set to 70% of the displacement thickness at separation, which was based on the results of the passive control studies of Volino (2003), Zhang and Hodson (2005), and Zhang *et al.* (2005) performed on low-pressure-turbine airfoils. This corresponds to 1 mm based on the clean-airfoil configuration at a Reynolds number of 39,000. The above noted studies, in which similar constant-height protrusion/indentation modifications were examined at higher Reynolds numbers, also suggest that instabilities are promoted by the edge of a sharp backward-facing step as this would provide a receptivity site for infinitesimal disturbances. Accordingly,

some of the configurations include such a backward-facing step (ST, SG, LG, and SR) to promote disturbance-initiation in the inflectional boundary layer prior to separation. The steps coincide with the leading edge of the groove that was machined into the airfoil surface ($x/C = 0.232$), which is slightly upstream of the separation location for the clean-airfoil cases ($x_s/C \approx 0.3$).

9.3 Discussion of Measurement Results

In the following discussion on the effects of the surface modifications with regards to the separation-bubble characteristics and boundary-layer losses downstream of reattachment, the acronym CL refers to the clean airfoil configuration that was discussed in the previous chapter. First, a comparison of the general performance of the airfoil with the surface modifications is given in Section 9.3.1, followed by individual discussions of the flow physics for each modification in Sections 9.3.2 through 9.3.6. As the inclusion of all measurement results for each of the 20 additional cases presented herein would unnecessarily lengthen this chapter, only results deemed important for understanding the physics of the flow manipulations are presented. The detailed measurements for each of these cases, along with those of the clean-airfoil configuration presented in the preceding chapter, are included in Appendix D.

9.3.1 Separation Bubble Characteristics and Airfoil Performance

The surface modifications examined have been designed to provide passive forcing of the shear layer at a frequency similar to that of the dominant instability observed in the separated shear layer. Figure 9.2 shows the dominant streamwise wavelengths of the observed instabilities for all configurations examined. These dominant wavelengths have been identified by means of the same spatial correlation of the wall-normal velocity

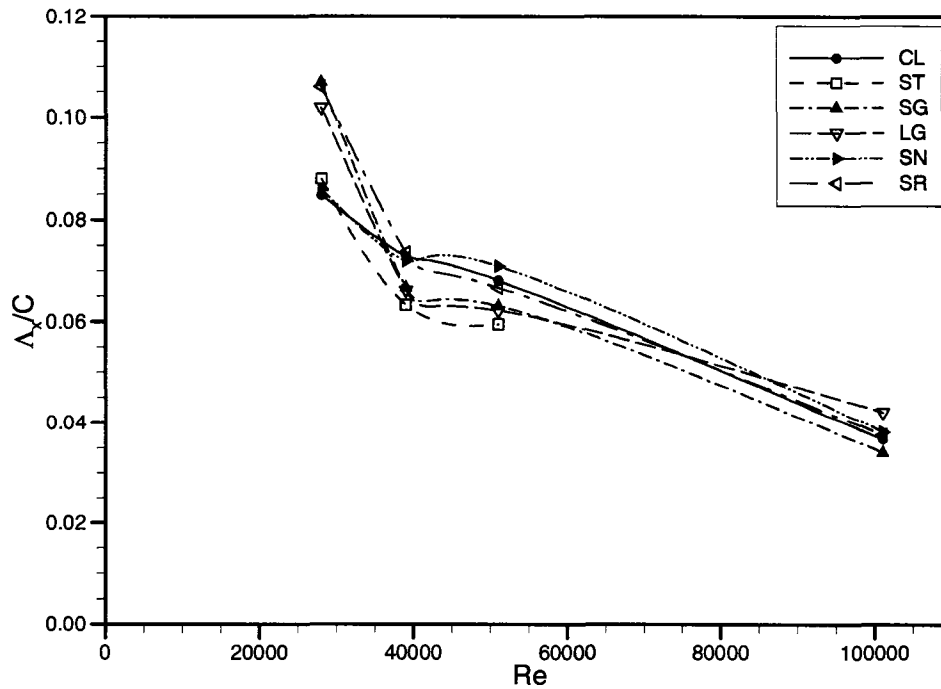


Figure 9.2: Dominant wavelengths observed in the separated shear layer for all configurations

fluctuation described in the previous chapter (Equation 8.1, page 205). Peaks in the correlation distributions provide estimates of the dominant wavelengths in the separated shear layer, as described in Section 8.3.2 on pages 205 and 206.

In Figure 9.2, a distinct change in the dominant instability wavelength is observed for many of the configurations. At a Reynolds number of 28,000, all flow-control configurations show similar or increased wavelengths compared to the clean-airfoil case, whereas at Reynolds numbers of 39,000 and 51,000 the dominant wavelengths are similar or lower than the respective clean-airfoil cases, except for the SN configuration at a Reynolds number of 51,000 which shows a slightly higher wavelength. This trend is contrary to what was expected, in that for a particular configuration the dominant wavelength was expected to be similar at all Reynolds numbers due to the spatial nature of the forcing device. Despite

this, there is a distinct effect of spatial forcing on the instability wavelengths compared to the clean airfoil case.

Important parameters that define the characteristics of the separation bubbles, as well as the reattached turbulent boundary layer, are given in Table 9.1. The maximum expected uncertainties in these parameters were provided in Table 5.2 on page 98. The ensemble-averaged locations of separation, transition onset, and reattachment for all cases are shown in Figure 9.3 with a schematic of the airfoil for reference. The SG and SR configurations show similar separation locations compared to the clean airfoil case, with a greater downstream shift for the SR configuration. For the ST and LG configurations, separation occurs well upstream of the clean airfoil separation point, at the location where a sharp backward-facing step associated with these surface-modification configurations is present. A time-averaged reattachment point is not provided in Table 9.1 and Figure 9.3 for the LG configuration at a Reynolds number of 101,000, the reasons for which will be discussed later. The SN case also shows an upstream movement of the separation location, except at a Reynolds number of 101,000 where separation occurs at the most downstream location of any of the separation-bubble cases examined.

In the present study, transition onset is defined as the location where small-scale fluctuations, smaller than those associated with the dominant instability waves, are initiated and provide a mechanism for dissipation of energy at the Kolmogorov scale. As discussed in Chapter 8, Section 8.3.2, this is identified by the streamwise location at which the growth of fluctuation levels in the shear layer begins to deviate from the exponential growth associated with amplification of the Kelvin-Helmholtz instability. The location of transition onset for the SG and SN cases is almost coincident with that for the clean airfoil at the three lower Reynolds numbers examined, with a slight deviation seen at the highest Reynolds number (Figure 9.3). The ST configuration at the three lower Reynolds numbers, and LG configuration over the full Reynolds number range, show upstream movement of the

Table 9.1: Characteristics of separation bubbles and reattached boundary layers for all configurations

Configuration	Re $\times 10^{-3}$	Separation			Transition			Reattachment		$x/C = 0.85$	
		$\frac{x_s}{C}$	$\frac{U_{es}}{U_\infty}$	Re_{θ_s}	$\frac{x_{ts}}{C}$	$\frac{x_{ts} - x_s}{C}$	Sr_{θ_s}	$\frac{x_r}{C}$	$\frac{x_r - x_s}{C}$	Re_θ	H
CL	28	0.292	1.160	83	0.488	0.196	0.0159	0.684	0.392	342	1.60
	39	0.293	1.180	100	0.438	0.145	0.0159	0.618	0.325	422	1.49
	51	0.297	1.192	120	0.411	0.114	0.0150	0.581	0.284	516	1.43
	101	0.323	1.221	185	0.381	0.058	0.0197	0.456	0.133	562	1.79
ST	28	0.229	1.210	79	0.444	0.215	0.0138	0.673	0.444	364	1.65
	39	0.229	1.221	100	0.403	0.174	0.0172	0.621	0.392	497	1.51
	51	0.229	1.242	118	0.383	0.154	0.0168	0.582	0.353	596	1.43
	101	0.229	1.346	215	0.229	0.000	-	0.240	0.011	457	1.46
SG	28	0.295	1.171	85	0.492	0.197	0.0128	0.689	0.394	301	1.67
	39	0.294	1.181	103	0.439	0.145	0.0176	0.630	0.336	400	1.45
	51	0.304	1.183	125	0.410	0.106	0.0171	0.585	0.281	505	1.43
	101	0.323	1.252	231	0.385	0.062	0.0256	0.418	0.095	636	1.40
LG	28	0.232	1.201	75	0.479	0.247	0.0120	0.664	0.432	336	1.51
	39	0.232	1.218	95	0.418	0.186	0.0143	0.596	0.364	407	1.42
	51	0.232	1.232	108	0.402	0.170	0.0136	0.557	0.325	461	1.40
	101	0.232	1.289	162	0.410	0.178	0.0160	-	-	494	1.45
SN	28	0.247	1.198	83	0.497	0.250	0.0157	0.681	0.434	327	1.54
	39	0.247	1.209	106	0.435	0.188	0.0163	0.619	0.372	396	1.43
	51	0.247	1.221	129	0.413	0.166	0.0146	0.570	0.323	477	1.41
	101	0.350	1.210	225	0.390	0.040	0.0247	0.443	0.093	534	1.39
SR	28	0.300	1.172	86	0.509	0.209	0.0129	0.687	0.387	306	1.68
	39	0.304	1.176	104	0.452	0.148	0.0177	0.635	0.331	368	1.47
	51	0.308	1.186	123	0.418	0.110	0.0159	0.588	0.280	478	1.44
	101	0.330	1.218	201	0.403	0.073	0.0196	0.457	0.127	577	1.74

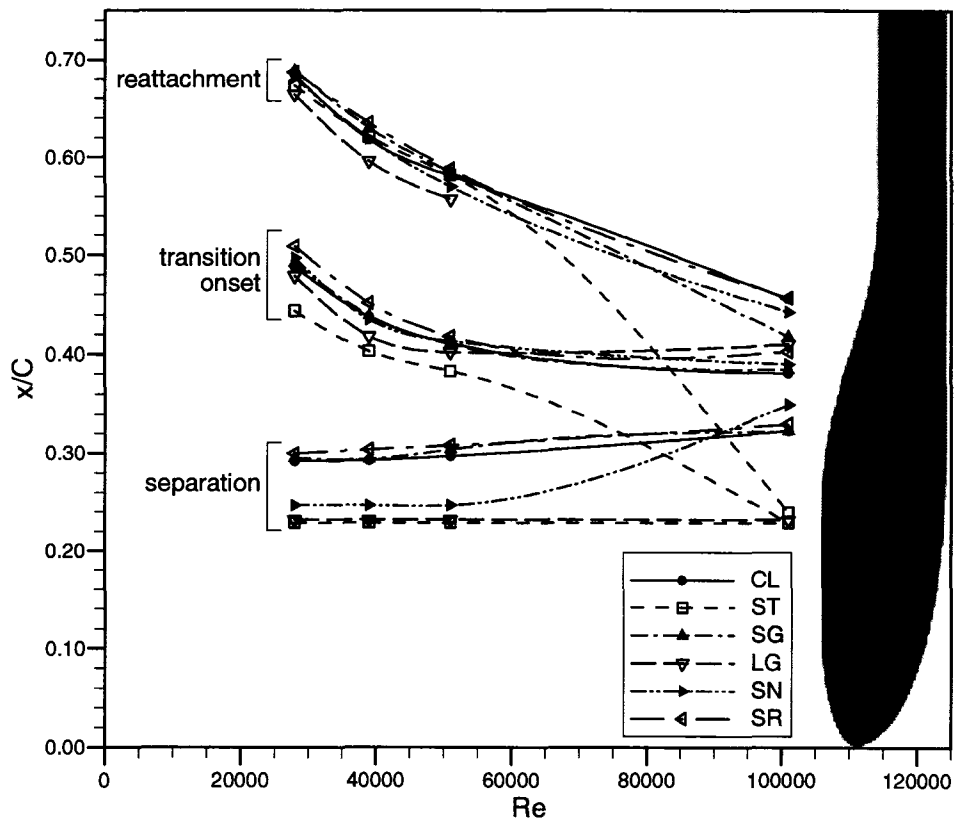


Figure 9.3: Separation, transition onset, and reattachment locations for all configurations

transition onset location, resulting primarily from the upstream movement of the separation point. Similarly, for the highest Reynolds number, the SR case shows downstream movement of transition onset by a distance equivalent to the downstream movement of separation. For the ST configuration at the highest Reynolds number, the protrusion initiates transition near the trailing edge of the step.

Reattachment locations show similar movement, relative to the clean airfoil, to that of the transition onset location, except for the ST configuration which shows similar reattachment locations to the clean airfoil, except at a Reynolds number of 101,000 where reattachment occurs shortly downstream of the step. For this case, transition is initiated at

the trailing edge of the step and occurs in an attached boundary layer over the backward-facing ramp.

The transition onset and reattachment locations, measured relative to the separation location, provide a better measure of the manipulation by the surface modifications on the transition process within the separation bubble. Figure 9.4 shows these relative locations for all configurations, for which three distinct trends are observed. At the three lower Reynolds numbers, the SG and SR configurations show similar relative locations of transition onset and reattachment as those for the clean airfoil. For the LG and SN configurations, the transition onset and reattachment relative locations are further downstream, except at the highest Reynolds number. At the three lower Reynolds numbers, the ST configuration shows delayed transition onset compared to the clean airfoil, but not to the same extent as the LG

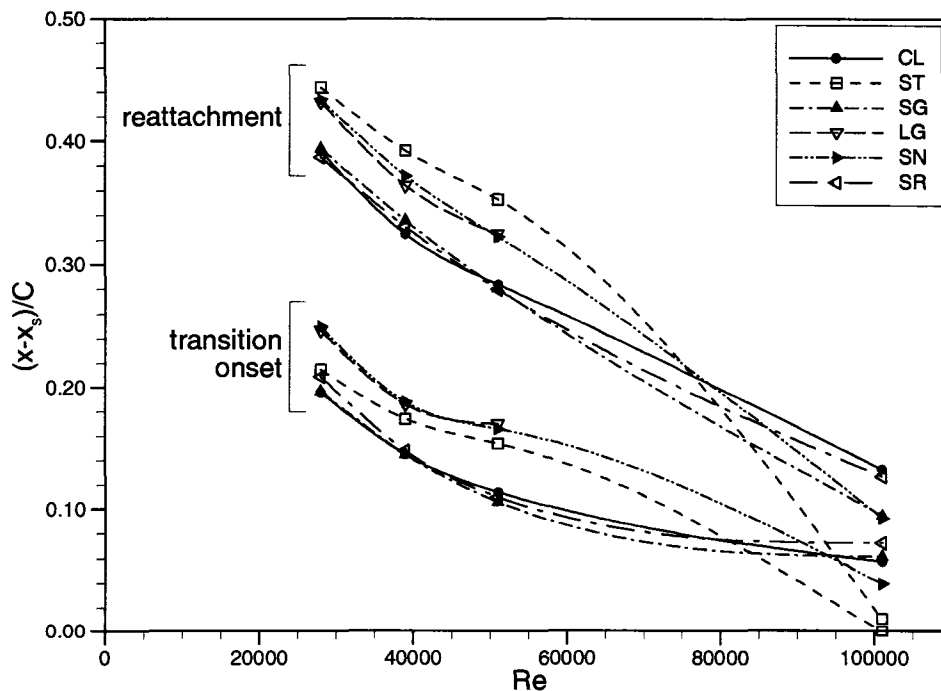


Figure 9.4: Transition onset and reattachment lengths, relative to separation, for all configurations

and SN configurations. However, the reattachment length for the ST configuration is longest of all the configurations examined at the three lower Reynolds numbers and shortest at the highest Reynolds number. It is again noted that reattachment occurs shortly downstream of the step for the ST configuration at the highest Reynolds number, and transition occurs in an attached boundary layer over the backward-facing ramp.

The losses associated with manipulation of the separation bubble through surface modifications can be evaluated by examining the momentum thickness of the boundary layer downstream of reattachment. Figure 9.5 shows momentum-thickness Reynolds numbers for all cases at a location of $x/C = 0.85$, which is downstream of the reattachment location for all conditions. The curve-fits in Figure 9.5 are provided only as a guide for the eye and do not indicate the trends expected at intermediate Reynolds numbers. As would be

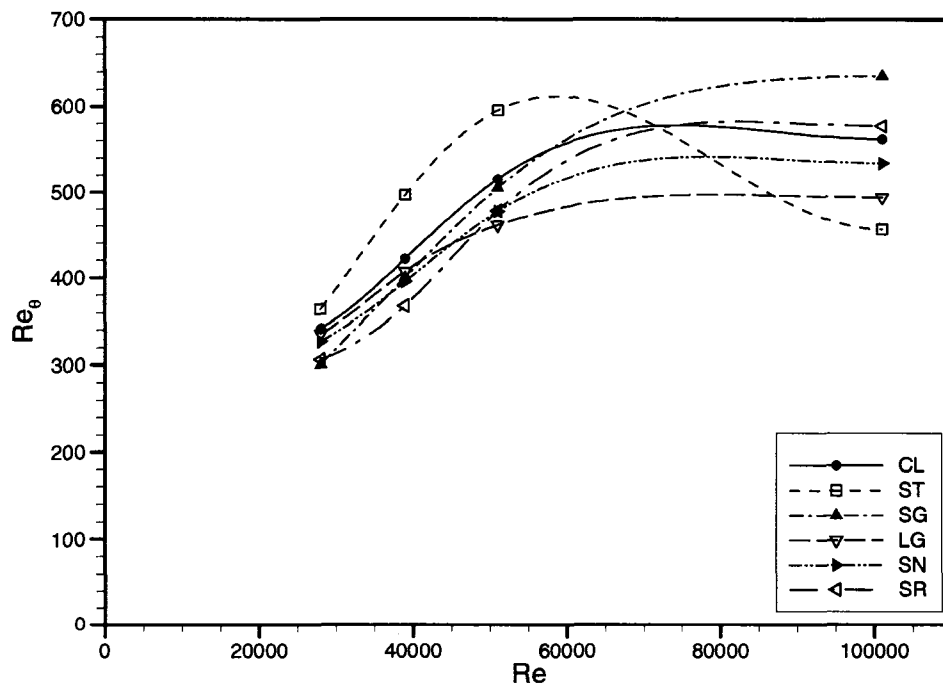


Figure 9.5: Momentum-thickness Reynolds numbers for all surface configurations at $x/C = 0.85$

expected with increasing flow Reynolds number, the momentum-thickness Reynolds number increases for all but the ST configuration which shows lower losses at $Re = 101,000$ than at 39,000 and 51,000. At the three lower Reynolds numbers examined, all configurations except ST provide a decrease in losses. At the highest Reynolds number, the SG and SR configurations show increased losses compared to the clean airfoil, with a decrease observed for all other configurations. The configuration that shows the most consistent improvement in losses at the three lower Reynolds numbers is the SR configuration; however it provides a slight increase in losses at the highest Reynolds number.

In the following, details regarding the ways in which each surface modification affects the separation bubble are discussed to provide a physical explanation of the performance trends observed. The discussions revolve around the performance trends presented in Figures 9.2 through 9.5, without explicit reference to these figures.

9.3.2 ST Configuration

The step associated with the ST configuration provides a disturbance comparable to a trip wire placed upstream of separation. Trip wires generally promote transition in the separated shear layer, resulting in decreased separation-bubble lengths, but often have increased losses for conditions where a separation bubble would not develop in absence of the tripping device. For the present configuration, this trend is reversed and losses are higher than those for the clean airfoil at the three lower Reynolds numbers, with a decrease in losses observed only at the highest Reynolds number.

At the three lower Reynolds numbers, separation occurs at the trailing edge of the surface protrusion providing a separated shear layer at a greater distance from the airfoil surface than all other configurations examined. This is observed in Figure 9.6 through a comparison of the velocity-vector profiles over the backward-facing ramp for the clean-airfoil

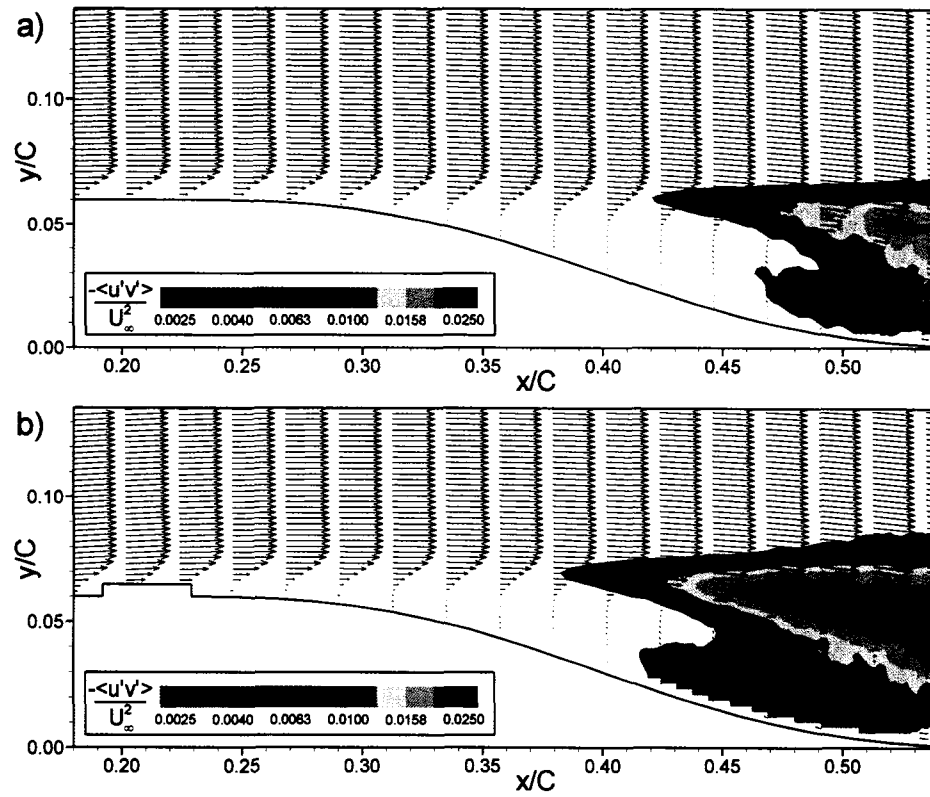


Figure 9.6: Velocity-vector profiles and $\langle u'v' \rangle$ distributions at a Reynolds number of 39,000 for a) the clean airfoil, and b) the ST configuration

and ST configurations at a Reynolds number of 39,000. Despite the higher losses associated with the ST configuration at the three lower Reynolds numbers, transition onset relative to the separation point is delayed. Of all the configurations examined, the highest level of velocity fluctuations within the separated shear layer is observed for this configuration. By examining the instantaneous velocity and vorticity fields, it was observed that the greater distance of the shear layer from the surface reduces the damping effect of the wall. As a result, the large-scale vortical structures as well as the smaller-scale turbulence can spread over a greater transverse, or wall-normal, distance. This greater displacement of the separated shear layer from the surface, as observed in Figure 9.6, also provides the conditions which result in longer reattachment lengths, relative to the location of separation.

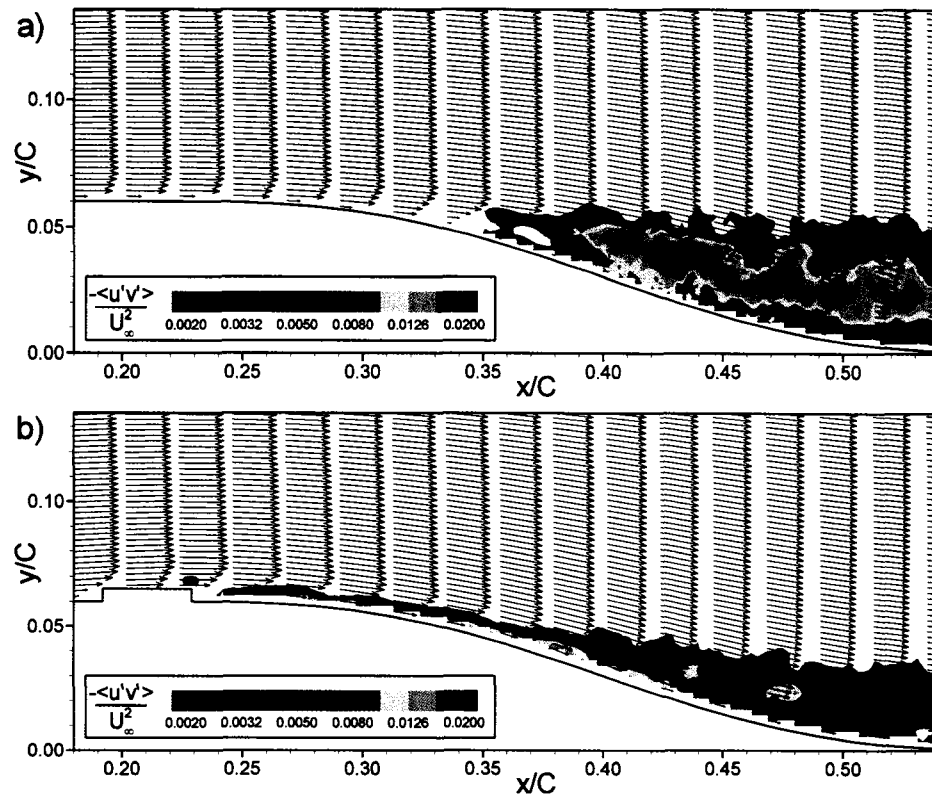


Figure 9.7: Velocity-vector profiles and $\langle u'v' \rangle$ distributions at a Reynolds number of 101,000 for a) the clean airfoil, and b) the ST configuration

The ST configuration provides the greatest loss reduction at a Reynolds number of 101,000. For this case, a small recirculation zone is observed right behind the step, but is not well defined due to the spatial resolution of the PIV measurements. The separated shear layer over this recirculation zone reattaches over a short streamwise distance, yielding a transitional boundary layer downstream of the step, which does not separate over the backward-facing ramp of the airfoil. This is observed in Figure 9.7 through a comparison of the velocity-vector profiles and $\langle u'v' \rangle$ distributions between the clean-airfoil and ST configurations. In Figure 9.7, the presence of elevated $-\langle u'v' \rangle$ at the downstream end of the step provides an indication that transition is initiated by the trailing-edge of the step. This elevated $-\langle u'v' \rangle$ at the step trailing-edge may be a result of errors in the PIV image

analysis due to the thin shear layer in this region, but the elevated values observed shortly downstream of the step provide confidence that transition is initiated in this region.

The absence of a separated shear layer over the backward-facing ramp of the airfoil at $Re = 101,000$ prevents the growth and shedding of large-scale vortical structures, thereby reducing the thickness of the shear layer as well as the fluctuation levels present therein (see Figure 9.7). In a study of a range of disturbance strips over a low-pressure-turbine airfoil in the presence of periodically passing turbulent wakes, Zhang *et al.* (2005) provide similar conclusions regarding the use of a rectangular step upstream of separation. In their case however, separation was still present downstream of the step, but the disturbances promoted by the step hastened the transition process within the separation bubble providing lower losses at the trailing edge of the airfoil. Volino (2003) observed similar effects induced by a rectangular protrusion located upstream of separation.

9.3.3 SG Configuration

The SG configuration provides the greatest reduction in loss at a Reynolds number of 28,000. However, the loss reduction diminishes with increasing Reynolds number and a significant increase in loss is observed at the highest Reynolds number of 101,000.

At a Reynolds number of 28,000 the primary pairing process is suppressed. Figure 9.8 shows the wavelength and associated correlation coefficient distributions for this case compared with those for the clean airfoil at the same Reynolds number. As a result of the higher mean velocities in the outer part of the reattached turbulent boundary layer, the convection rate of the shed vortices is increased over that observed in the separated laminar shear layer, which is what causes the observed increase in dominant length scale for the SG configuration. Conversely, a continual increase in wavelength is observed for the clean airfoil case. The higher correlation levels for the SG configuration also indicate greater coherence

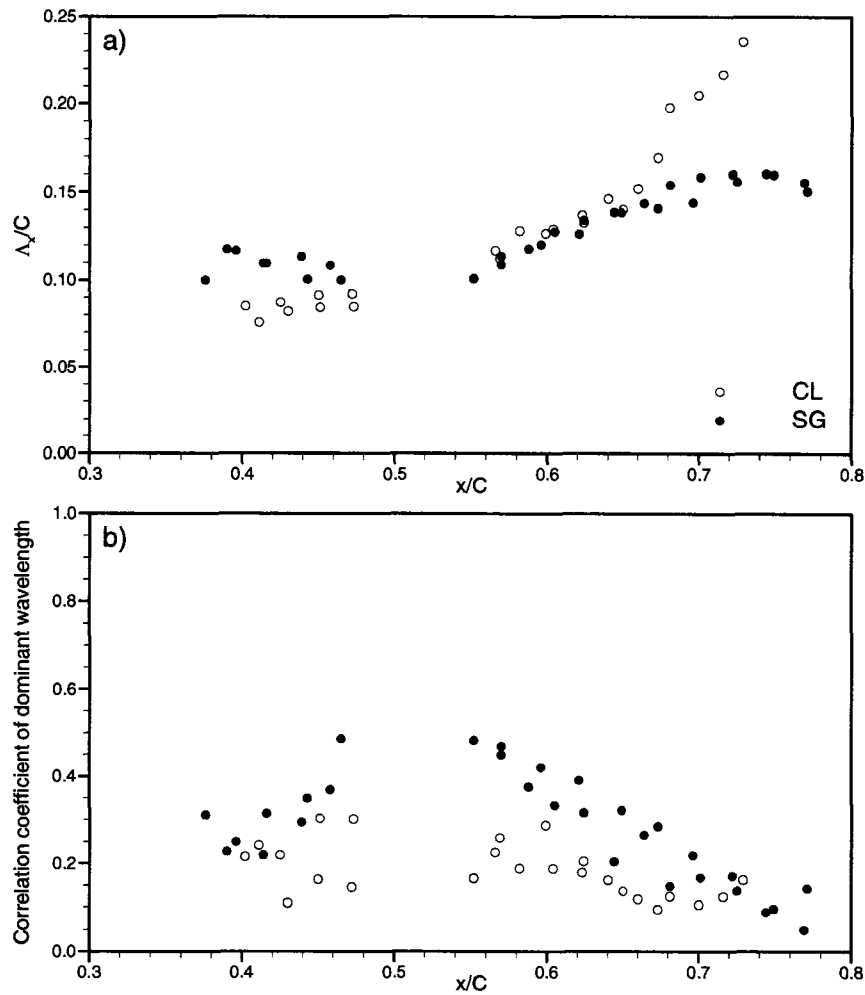


Figure 9.8: Streamwise correlation of dominant wavelengths for SG and CL configurations for $Re = 28,000$, a) wavelength distributions, b) correlation peak distributions

of the shed vortices. The passive forcing appears to promote a frequency lower than that of the natural frequency of the shear layer, indicated by the increased instability wavelength, which according to Ho and Huerre (1984) should result in suppression of the subharmonic that initiates the pairing process. In examining instantaneous velocity and vorticity plots, the primary pairing process is rarely observed and the occurrence of laminar-like inter-vortex regions is significantly reduced from what was observed for the clean airfoil at this Reynolds number.

At Reynolds numbers of 39,000 and 51,000 the transition process and associated flow structures are very similar to those of the clean airfoil, which includes the presence of the primary and secondary pairing events. There are however slight increases in the length-scale correlations observed in the reattached boundary layer, similar to that observed for $x/C > 0.65$ in Figure 9.8, which indicates that the shed vortices remain coherent for a longer streamwise distance. This may provide the mechanism for the slight decrease in losses observed for these two Reynolds numbers, over the respective clean airfoil cases.

At the highest Reynolds number examined, the separation and transition-onset locations are very similar to the clean airfoil case. However, the groove seems to provide a disturbance source that modifies the vortical structures originating from the periodic roll-up of the separated shear layer in a manner that yields earlier reattachment. This modification to the structure of turbulence developing in the separated shear layer also yields a thicker reattached boundary layer, hence higher losses than the clean airfoil case.

9.3.4 SR Configuration

The SR configuration provides the greatest delay in separation of all configurations examined, except at a Reynolds number of 101,000 where the SN configuration provides a greater delay. For all conditions, a small separated-flow region occurs in the leading edge region of the surface modification. Reattachment of this shear layer prior to the larger-scale separation bubble provides a highly-inflectional laminar boundary layer which separates further downstream than the clean airfoil cases. As previously noted, this configuration provides the most consistent reduction in losses at the three lower Reynolds numbers.

At a Reynolds number of 28,000, the SR configuration provides the same manipulation to the transition process as does the SG configuration. The passive forcing promotes a lower instability frequency, which results in suppression of the subharmonic that initiates

the pairing process, and the primary instability wavelength remains the dominant length scale present over the airfoil.

The dominant instability wavelengths at Reynolds numbers of 39,000 and 51,000 are almost identical to those for the clean airfoil, indicating negligible influence of the surface modification on the frequency of maximum amplification in the separated shear layer. Despite this, at a Reynolds number of 39,000 the disturbance appears to suppress the instability growth during some periods of the shear-layer development. Figure 9.9 shows two $x - y$ plots of normalized spanwise vorticity for a Reynolds number of 39,000 at two unrelated moments in time. Visible growth of the instability wave is observed at a more upstream location in the upper plot than in the lower plot. The wavelength of the instability in the upper plot is also larger than that in the lower plot, indicating that a broad range of frequencies are present in the separated shear layer. These trends are also noted to occur for the clean airfoil but not to the same extent. At this Reynolds number, the maximum

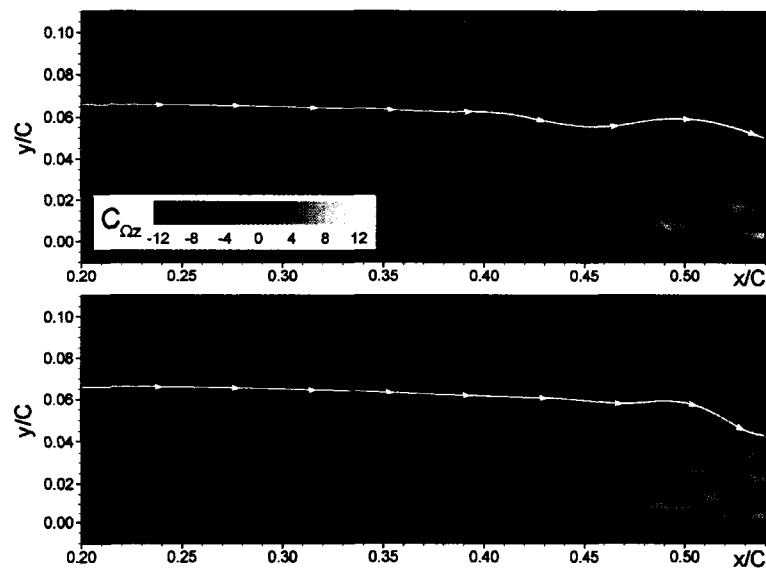


Figure 9.9: Variation in instability growth and wavelength for the SR configuration at $Re = 39,000$ for unrelated instants in time

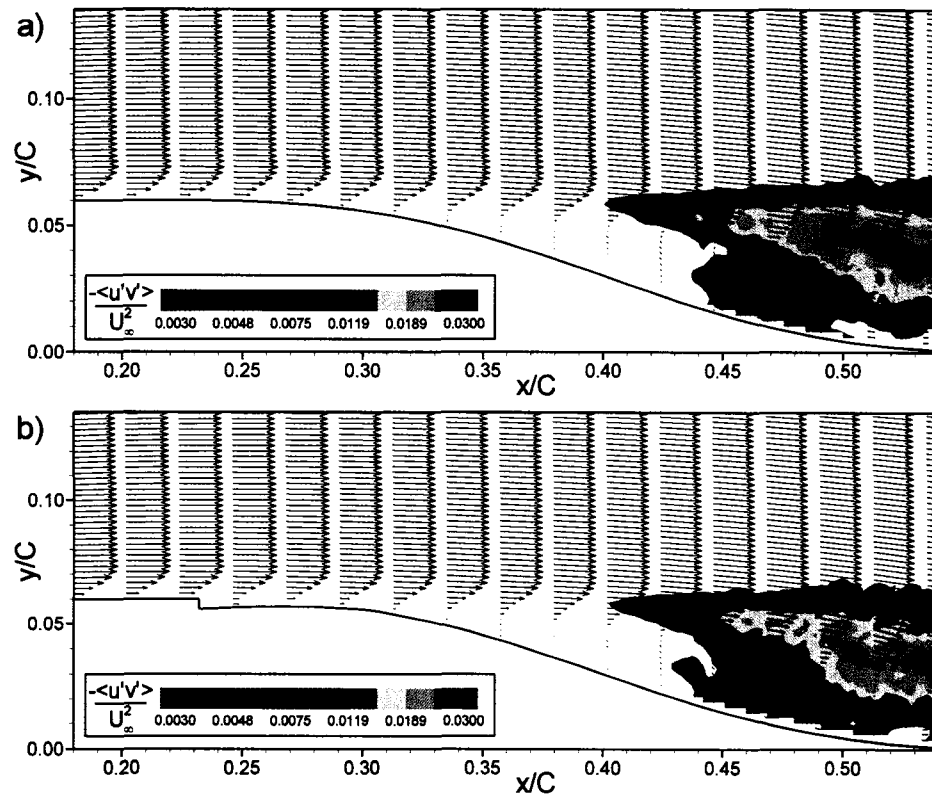


Figure 9.10: Velocity-vector profiles and $\langle u'v' \rangle$ distributions at a Reynolds number of 51,000 for a) the clean airfoil, and b) the SR configuration

wavelength-correlation peak is much lower than that for the clean airfoil (0.35 for SR and 0.6 for CL) which is another indicator of this broader range of frequencies.

A different effect is observed at a Reynolds number of 51,000, where breakdown to small-scale turbulence is promoted by the surface modification, resulting in a shorter bubble length. The reattachment point is almost coincident with the clean-airfoil case despite the delayed separation. Although quicker reattachment is observed, relative to separation, lower peak-fluctuation levels are observed in the transition region, as seen through a comparison of the velocity-vector profiles and $\langle u'v' \rangle$ distributions with the clean airfoil case in Figure 9.10. The shorter bubble length and lower fluctuation levels provide a lower momentum thickness downstream of the bubble, therefore lower losses.

At the highest Reynolds number of 101,000, the SR surface modification has no significant effect on the separation bubble. The velocity fluctuation levels observed in and downstream of the separation bubble are very similar to the clean airfoil case. This results in similar loss levels for the two configurations.

9.3.5 LG Configuration

For the LG configuration, separation occurs off the sharp backward-facing step at the leading edge of the groove. At the three lower Reynolds numbers, transition onset occurs upstream of the corresponding clean-airfoil locations, but the separation-to-transition length is longer due to the lower momentum thicknesses at separation.

The dominant instability wavelengths are very similar to those for the SG configuration, however the trend in losses is opposite to that of the SG case. At the lowest Reynolds number, the losses are equivalent to the clean airfoil case, but a decrease in losses is observed with increasing Reynolds number, and at a Reynolds number of 101,000 this configuration provides greatly reduced losses.

Despite the increased instability wavelength at a Reynolds number of 28,000, the pairing process is not suppressed as was seen for the SG and SR cases at this Reynolds number. There are no distinct differences in the transition and reattachment process from that which occurs over the clean airfoil.

The earlier transition onset (relative to the leading edge of the airfoil) that occurs for this configuration over the clean airfoil is the primary difference that leads to decreased losses at Reynolds numbers of 39,000 and 51,000. As the instability waves grow and develop into discrete large-scale vortices, the closer proximity of the shear layer to the surface due to earlier separation provides a greater level of damping to the growing vortices, which

no longer grow to as great an extent in the transverse direction before being influenced and distorted by the presence of the wall. The vortices shed from the bubble therefore have a lower wall-normal extent and result in a thinner boundary layer downstream of reattachment. At $Re = 51,000$, the downstream edge of the groove provides a greater influence on the disturbance level in the separated shear layer. Disturbances with a smaller length-scale than that of the dominant instability wavelength are observed in the separated shear layer, which also results in lower correlation of the dominant wavelength prior to transition. At this Reynolds number, there is also a greater level of small-scale fluctuations present soon after transition onset, and in the near-wall region below the separated shear layer, which results in a shorter reattachment length relative to transition onset. This is observed in Figure 9.11, which shows velocity-vector profiles and $\langle u'v' \rangle$ fluctuation levels for the LG configuration compared to the corresponding clean-airfoil case.

At a Reynolds number of 101,000, a very different process leads to the significant loss-reduction observed. As with the lower Reynolds number cases, separation occurs off the backward-facing step at the leading edge of the groove. However, instability waves are observed in the separated shear layer upstream of the groove trailing edge. These instability waves interact with the trailing-edge step of the groove to provide an unsteady separated shear layer downstream of the groove. Figure 9.12 presents an example of an instantaneous velocity field in the region downstream of the groove. The disturbed instability waves introduce local regions of reverse flow near the surface as they grow and convect downstream. The ensemble-averaged velocity field shows a highly-inflectional shear layer in this region with no reverse-flow present. However, the fluctuation growth levels show similar trends to the separation-bubble cases, and the instability Strouhal number based on conditions at the leading edge of the groove is 0.0160, which is in good agreement with values that have been observed in separated shear layers. This would indicate that, although no ensemble-averaged separation bubble is present, instability growth occurs in the same manner as

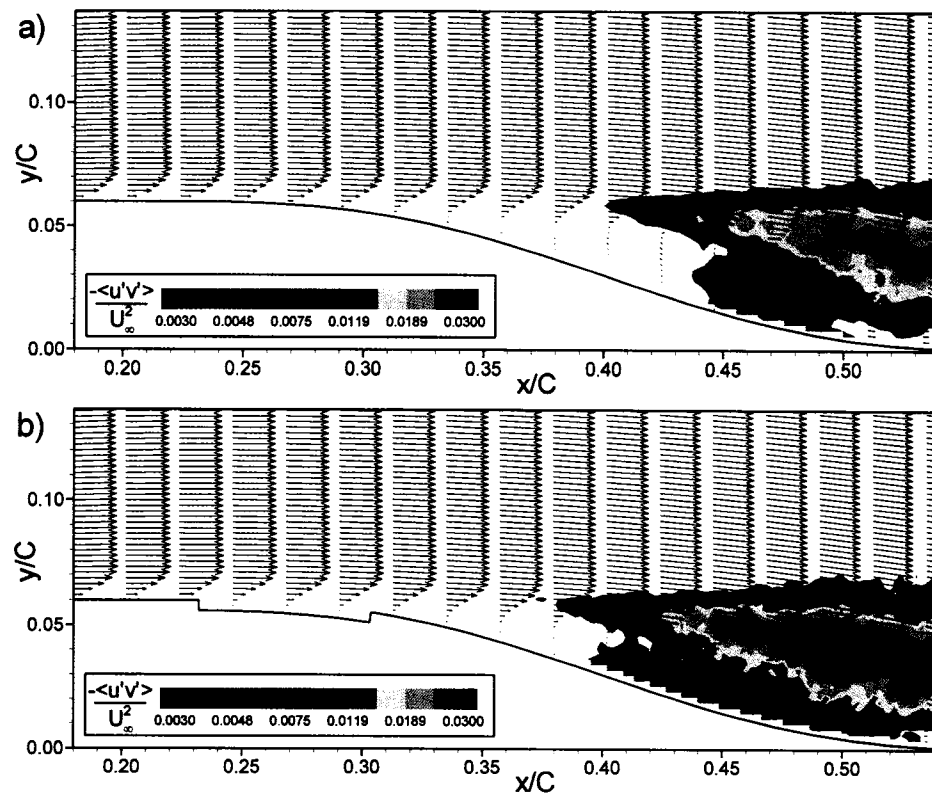


Figure 9.11: Velocity-vector profiles and $\langle u'v' \rangle$ distributions at a Reynolds number of 51,000 for a) the clean airfoil, and b) the LG configuration

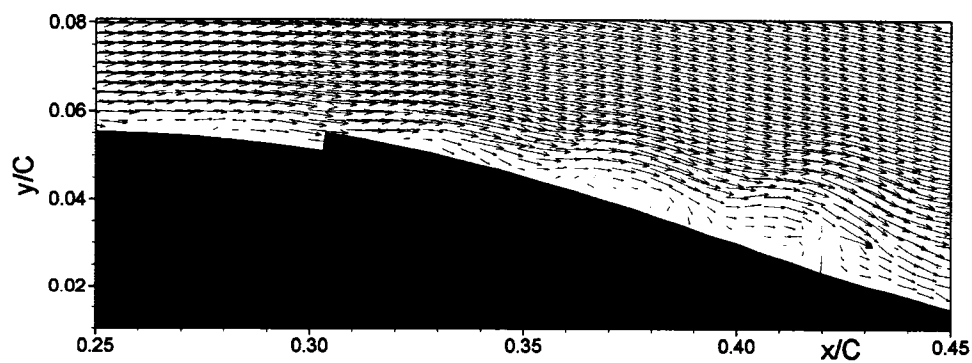


Figure 9.12: Unsteady separation observed downstream of the groove of the LG configuration at $Re = 101,000$

in shear layers that are observed as separated when viewed through time-averaged data. The unsteady nature of the shear layer also reduced the occurrence and size of large-scale vortices shed downstream. This results in the loss reduction observed at this Reynolds number.

9.3.6 SN Configuration

The SN configuration provides transition and reattachment locations (relative to the airfoil leading edge) that closely match those of the clean airfoil; however separation occurs sooner for the three lower Reynolds numbers and losses are reduced over the full Reynolds-number range examined. Separation at the three lower Reynolds numbers occurs slightly downstream of the start of the sine groove, in the region where increase in surface curvature becomes pronounced. The dominant instability wavelengths for this configuration also most closely match those of the clean airfoil.

At the three lower Reynolds numbers examined, there are no distinct differences in the development of the vortical structures observed in and downstream of the separation bubble as compared to the clean airfoil. The only difference is the earlier separation. Downstream of separation, the shear layer remains marginally separated over the length of the groove and as the surface curves back towards the clean airfoil shape near the trailing edge of the groove, the height of the reverse-flow region decreases. At the trailing edge of the groove, the reverse-flow near the surface is almost eliminated, downstream of which the separated shear layer develops in the same manner as that over the clean airfoil. The similarity between the SN and clean-airfoil configurations at a Reynolds number of 28,000 is shown in Figure 9.13.

Despite the negligible manipulation of the shear layer at the lower Reynolds numbers, a significant difference in the separation-bubble characteristics is observed at $Re = 101,000$.

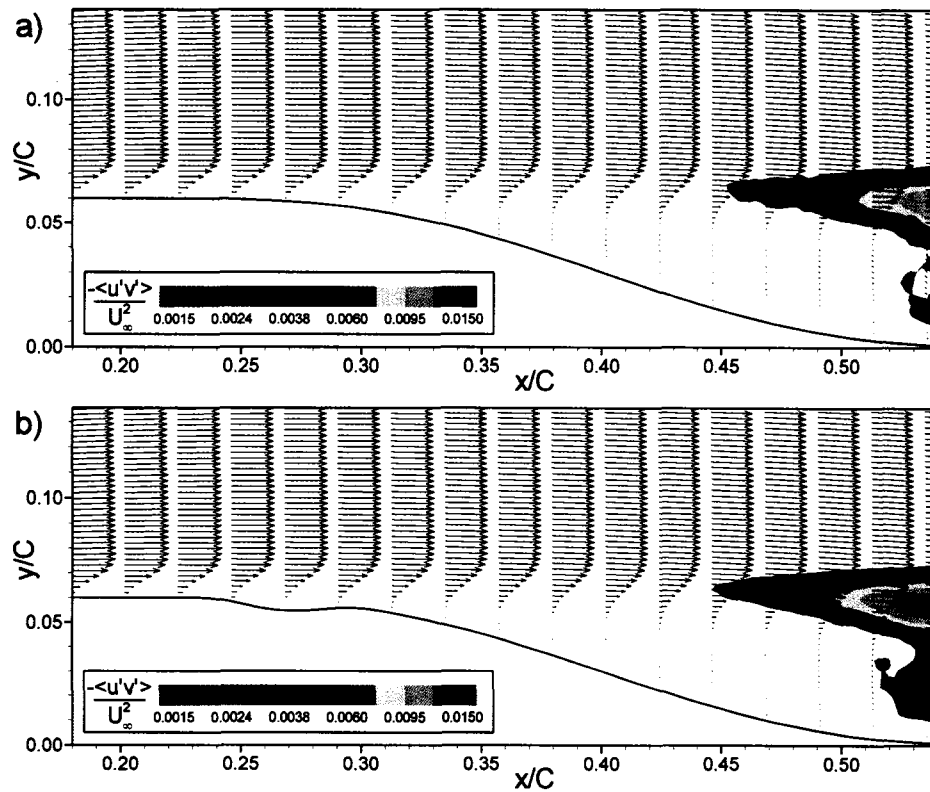


Figure 9.13: Velocity-vector profiles and $\langle u'v' \rangle$ distributions at a Reynolds number of 28,000 for a) the clean airfoil, and b) the SN configuration

As with the LG configuration at this Reynolds number, instability waves begin to develop shortly downstream of the groove leading edge. These instabilities grow quickly and interact with the trailing edge region of the groove providing a highly-unsteady separation process. However, unlike the LG configuration, ensemble-averaged reverse flow is present near the surface. Figure 9.14 provides an example of the instantaneous velocity field downstream of the groove. The instability waves initiate shedding of vortices downstream of the groove, which results in the highly unsteady separation, with a separation location that varies over the range of $0.33 < x/C < 0.38$. The transition length for this case is shortest of any of the configurations for which an ensemble-averaged separation bubble is present over the curved backward-facing ramp, and the shorter separation bubble results in lower losses than the

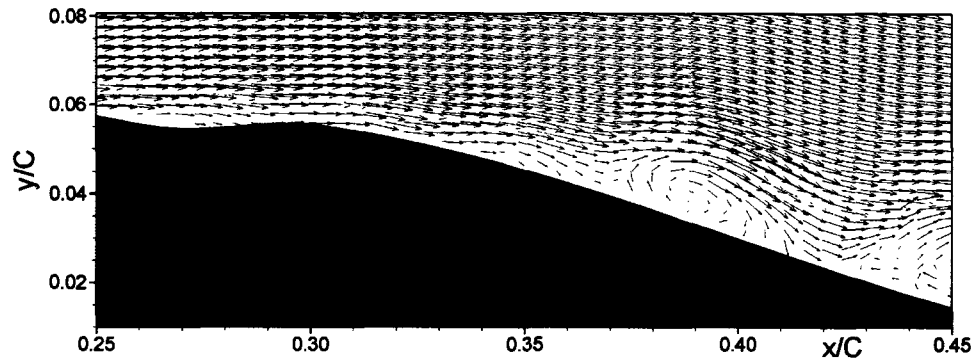


Figure 9.14: Unsteady separation observed downstream of the surface modification for the SN configuration at $Re = 101,000$

clean airfoil at this Reynolds number.

9.4 Conclusions

Passive manipulation of transition in a separation bubble has been examined experimentally using particle-image velocimetry (PIV) in the low-Reynolds-number tow-tank facility at the National Research Council of Canada. The airfoil used for the study provides a suction-side pressure distribution similar to that occurring over typical low-Reynolds-number airfoils while minimizing the streamwise movement of separation over a wide range of operating conditions. Measurements were performed at four Reynolds numbers, in the range of 28,000 to 101,000 based on chord length, and under negligible freestream turbulence conditions. The clean-airfoil measurements against which the flow-manipulation results have been compared were documented in Chapter 8.

Several two-dimensional surface modifications have been made to the airfoil surface to provide passive forcing of the separated shear layer in an effort to manipulate the transition process and mitigate the performance penalties typically associated with separation bubbles.

The tested configurations consist of a constant-height step, constant-depth grooves, a backward-facing step followed by a ramp, and a sinusoidal groove. The various geometries provide variation in the separation, transition onset, and reattachment locations over the airfoil surface. For all but the constant-height step, the boundary-layer losses are reduced downstream of the separation bubble for the three lower Reynolds numbers examined. At the highest Reynolds number examined, only three of the tested geometries result in decreased losses.

The spatial nature of the PIV measurements has allowed a detailed analysis of the manner in which the surface modifications affect the transition process occurring in the separated shear layer. The observed decrease in boundary-layer losses occurs through various manipulation mechanisms. At the lowest Reynolds number of 28,000, two of the configurations provide forcing at a frequency lower than the dominant Kelvin-Helmholtz frequency identified for the clean airfoil. This suppresses the subharmonic instability associated with vortex pairing and results in significantly reduced occurrence of the vortex-pairing phenomenon and a reduced level of small-scale breakdown to turbulence. At the intermediate Reynolds numbers of 39,000 and 51,000, the greatest levels of loss-reduction result from a promotion of the small-scale breakdown providing reduced bubble lengths and thinner boundary layers downstream of reattachment. At the highest examined Reynolds number of 101,000, two different manipulations have been identified for reducing losses. The first, by use of a rectangular surface protrusion upstream of the clean-airfoil separation location, initiates transition earlier and eliminates the separation bubble in the region of strong adverse pressure gradient. The second manipulation, induced by providing a physical disturbance to the instability waves developing in the separated shear layer, results in a highly-unsteady separation process downstream of the disturbance. These two manipulations either eliminate or reduce the size of the large-scale vortical structures that are shed downstream of the bubble and provide a decrease in the boundary-layer thickness

over the aft region of the airfoil.

The results of the flow control study indicate that there is no optimal solution to passive transition control in a separation bubble, at least for the range of passive control techniques considered here. Depending on the flow Reynolds number and pressure distribution present over the airfoil, different physical mechanisms can be manipulated to affect the separation, transition, and reattachment processes. The results presented herein provide some guidelines for developing passive control techniques for use in practical applications for which separation bubbles generate an undesirable level of boundary-layer losses.

Chapter 10

Summary, Contributions and Recommendations

10.1 Summary

Separation of a laminar boundary layer is a common occurrence over airfoils, particularly at low-Reynolds-number operating conditions, and laminar-to-turbulent transition within the separated shear layer may promote reattachment of the layer to the surface, thus forming a separation bubble. Although separation generally reduces the performance of airfoils under such conditions, through decreased lift and increased form drag, this performance reduction can be minimized by ensuring that transition and reattachment of the separated shear layer occur shortly downstream of separation. It is therefore important to understand the transition process in a separated shear layer for the intent of modelling such flows, and for the purpose of designing high-performance airfoils to be used under such conditions. The primary objectives of the research documented in this thesis were to identify the physical mechanisms associated with this transition process under conditions

observed over the surfaces of low-pressure-turbine and low-Reynolds-number airfoils, and to provide further validation of a separated-flow transition model developed at Carleton University. Complementary experimental and computational studies were performed for this purpose, and the results have provided a better understanding of the physics associated with separation-bubble transition. In addition to this, manipulation of such processes can further increase the performance of airfoils over which separation bubbles occur, and several passive control techniques have been examined in this regard.

Separation-bubble transition was examined experimentally using a combination of previously-performed measurements in a closed-circuit wind tunnel at Carleton University and measurements performed by the author in a low-Reynolds-number tow-tank facility at the National Research Council of Canada. As experimental measurements do not provide a complete picture of the transition process in separation bubbles, due to restrictions in the simultaneous availability of the spatial and temporal nature of the process, direct numerical simulation (DNS) was performed using the commercially-available ANSYS-CFX computational fluid dynamics (CFD) software package. The results of DNS provide simultaneous availability of the spatial and temporal scales of the flow, thus allowing detailed analysis of a complete description of the flow.

Separation-bubble transition was examined experimentally under low-Reynolds-number ($Re < 100,000$) and low-freestream-turbulence ($Tu \approx 0$) conditions in the low-Reynolds-number tow-tank facility using particle image velocimetry (PIV). The PIV measurements have provided details regarding the spatial nature of the transition process in separation bubbles. The suction-surface flow over a typical low-Reynolds-number airfoil was first studied in this facility under three combinations of flow-Reynolds-number and angle-of-attack, which provided a range of separation-bubble locations and sizes. The promising results of this study provided confidence in using such experimental methods for studying separation-bubble transition, and a new airfoil was designed to further investigate this

process and to provide controlled conditions under which a parametric study of various passive flow-manipulation techniques could be undertaken. The unconventional airfoil designed for this purpose consisted of a curved backward-facing suction-side ramp, over which a separation bubble forms. The selected airfoil shape provides minimal movement in the separation location over a wide low-Reynolds-number range. The curved backward-facing ramp, which provides a continuous change in surface slope and curvature over the upper surface of the airfoil, ensured that separation occurs through the induced pressure field and not due to a discontinuity in surface curvature. The airfoil also provided boundary-layer and separated-shear-layer characteristics similar to those observed over typical low-Reynolds-number airfoils.

As a follow-up to research regarding transition in attached and separated shear layers performed over the past decade at Carleton University, direct numerical simulation was used to examine the physical mechanisms associated with separation-bubble transition under conditions typical of those encountered over the suction surface of low-pressure-turbine airfoils. Two simulations were performed; both based on experimental test-cases performed in the wind tunnel at Carleton University, with the primary difference between the two being the level of freestream turbulence. Elevated freestream turbulence has been shown in the open literature to promote transition in a separation bubble, providing a shorter reattachment length, and its presence can improve the performance of low-Reynolds-number and low-pressure-turbine airfoils. The freestream turbulence intensities observed at the time-averaged streamwise locations of separation for the two simulations were 0.1% and 1.45%. The simulations represent the flow over a flat-plate test surface over which a streamwise pressure gradient is imposed by means of a contoured test-section ceiling in the experiments. In the simulations, the streamwise pressure gradients were imposed by means of a static pressure distribution applied to an outflow boundary condition defining the upper surface of the computational domain. For the low-freestream-

turbulence simulation, an experimentally-measured velocity profile was used as an inlet boundary condition and the freestream turbulence intensity of 0.1% was allowed to develop through round-off errors associated with the finite-precision computations. Conversely, the elevated-freestream-turbulence simulation made use of a simulated turbulence-generating grid at the inlet boundary, placed a sufficient distance upstream of the plate leading edge, consisting of an array of square, uniform-velocity jets that mix downstream of the inlet plane to provide freestream-turbulence characteristics similar to those in the experiments. Despite small differences in the flow conditions between the simulations and the experiments upon which they were based, experimental hot-wire measurements were used to validate the computational results and provide confidence that they were correctly simulating the physical processes occurring in the transition region of the separation bubbles.

Under conditions of low freestream turbulence, transition in a separation bubble was shown to be initiated by the inviscid Kelvin-Helmholtz (K-H) mechanism. Due to the inviscidly-unstable nature of the inflectional velocity profile associated with the separated shear layer, the K-H mechanism provides conditions under which the spanwise vorticity of the layer becomes unstable to small disturbances resulting in grouping of this spanwise vorticity at a selective streamwise wavelength. The spanwise-oriented vortical structures grow as they convect downstream and a point is reached where small-scale turbulence is initiated in the region of high-shear between sequential vortices. This break-down to small-scale turbulence occurs in a time-periodic manner, as a result of the high-shear regions being convected through the shear layer, and complete breakdown occurs very quickly over a distance corresponding to approximately one wavelength of the primary instability. Prior to this breakdown, packets of amplified instability are observed in the separated shear and their subsequent growth and decay was shown to result from a modification of the shear layer velocity profile during the period of instability amplification, thus providing a mechanism that stabilizes the growth-rate of these instabilities. These packets, or periods, of amplified

instability were also shown to provide enhanced momentum-exchange across the shear layer prior to transition.

The frequency with which the instabilities develop in a separated shear layer are consistent with that seen in planar free-shear layers where the presence of the K-H instability is well documented. Differences in the observed instability frequencies occurring in separation bubbles, compared with that observed in planar free-shear layers, was attributed to the presence of a bounding wall which, according to results of linear stability theory found in the open literature, can affect not only the frequency but the growth rate of the instabilities. The presence of a time-averaged fluctuation peak in the near-wall reverse-flow region of the separation bubble is also consistent with results of linear stability theory and is attributed to a near-wall viscous, or Reynolds-number-dependent instability. For separation bubbles that occur over typical airfoils, it was noted that the inviscid instability of the separated shear layer likely dominates over the near-wall viscous instability.

Under the low-Reynolds-number conditions examined in the tow-tank facility, a vortex-pairing phenomenon was observed in the separated shear layers for both of the airfoils examined, and was identified as a subharmonic pairing instability that is also commonly-observed in planar free-shear layers. This instability results in rotation of two sequential spanwise-oriented vortices about each other, through their mutually-induced vorticity fields, which subsequently merge to form a larger vortex with approximately twice the spacing and strength of the primary vortices, thus initiating a subharmonic of the primary instability frequency. This vortex-pairing phenomenon was not observed in the low-freestream-turbulence simulation, for which the Reynolds number was much higher and the separation bubble was thinner, relative to the boundary-layer thickness at separation, than those in the tow-tank experiments. It is conceivable that the presence of this subharmonic instability is dependent on the distance of the separated shear layer from the surface, and the closer proximity of the surface in a thinner bubble may suppress its effects. In the unconventional-

airfoil experiments, a secondary pairing event was sometimes observed with an associated inter-vortex region consisting of undisturbed laminar flow entrained towards the surface by the strong circulation generated by the large-scale vortices.

Once transition is initiated through small-scale breakdown to turbulence, the large-scale spanwise-oriented vortical structures that develop in the separated shear layer remain coherent for a significant distance downstream of reattachment. However, these structures become distorted and stretched in a manner such that, downstream of reattachment, they resemble the hairpin-vortex structures found in near-wall boundary-layer turbulence, but on a larger scale. The presence of these hairpin-like structures in the reattached boundary layer provides a source of turbulence-kinetic-energy production in the outer part of the layer, which results in a slow recovery towards an equilibrium turbulent-boundary-layer state.

In the presence of elevated freestream turbulence, the nature of the transition process differs from that in a low-disturbance environment. Under such conditions, transition in a separation bubble occurs through the production, growth, and merging of turbulent spots, similar to the process that occurs in attached boundary-layer transition. For the elevated-freestream-turbulence simulation, in which the turbulence intensity level of 1.45% at separation is considered moderate, transition is initiated by a transient-growth mechanism whereby streamwise streaks are generated in the laminar boundary layer and provide the conditions necessary for turbulent spots to form in the separated shear layer. These streaks, which are comprised predominantly of fluctuations in the streamwise component of velocity, are elongated in the streamwise coordinate-direction and have a spanwise width on the order of the boundary layer thickness. The initiation of these streaks, which occurs shortly downstream of the plate leading-edge, is attributed to a shear-filtering effect where the shear in the boundary acts as a low-pass filter to the forcing provided by disturbances in the freestream flow. The streaks are also associated with streamwise vorticity that provides some cross-stream momentum exchange in both the laminar boundary layer and

the separated shear layer prior to breakdown into small-scale turbulence.

Turbulent spots were shown to develop as a result of low-speed streaks convecting through the separated shear layer. The spots consisted of a series of vortex loops that roll-up around such a low-speed streak, due to a secondary inviscid instability that closely resembles the Kelvin-Helmholtz vorticity roll-up. The frequency associated with convection of these vortex loops also closely matched that of the K-H instability. A topological structure of turbulent spots in a separated shear layer was established and identified the spots as consisting of three vortex loops; however there were some occurrences with a greater or lesser number of loops. The primary vortex-loop that defines the leading edge of the spot resembles a hairpin-vortex structure with its legs pointing in the upstream direction. The secondary and tertiary loops have their legs pointing in the downstream direction, as they wrap themselves around a core of low-momentum fluid injected upwards from the surface through the legs of the primary loop. This wrapping and stretching of the secondary and tertiary vortex loops is what provides the spanwise growth of the spots as they convect through the shear layer.

Spectral analysis of the elevated-freestream-turbulence simulation provided evidence that, although transition occurred predominantly through the production and merging of turbulent spots, the Kelvin-Helmholtz mechanism associated with the time-averaged separated shear layer may still be active. This may be the mechanism that provides the observed small-scale breakdown to turbulence in the inter-spot regions.

A distributed-breakdown of turbulent spots was observed along the entire length of the separated shear layer, and transition was completed approximately 50% of the reverse-flow length downstream of time-averaged reattachment. This long transition length, relative to that in the low-freestream-turbulence case, provided more gradual shear-layer growth characteristics through the separation-bubble region. The spots themselves remained coherent

for a long distance downstream of reattachment and, as did the hairpin-like structures of the low-freestream-turbulence case, provided turbulence-kinetic-energy production in the outer part of the shear layer resulting in a slow recovery to an equilibrium turbulent-boundary-layer state.

Apart from developing a better understanding of the possible modes of transition in separation bubbles, an objective of the research was to further validate a semi-empirical transition model developed by a colleague (Roberts, 2005). The range of applicability of Roberts' separated-flow transition-onset model (Equation 2.1 on page 33) was extended to lower Reynolds numbers, as it provided good agreement with experimentally-measured transition-onset locations in the first set of low-Reynolds-number airfoil experiments performed in the tow-tank facility. The model is now recommended for use in the range $57 \leq Re_{\theta_s} \leq 444$, and for the presence of convex surface curvature. The transition-rate prediction scheme of Roberts makes use of previously published models that define the streamwise and spanwise spreading of turbulent spots. The models of Gostelow *et al.* (Equation 2.5 on page 35) and D'Ovidio *et al.* (Equation 2.6 on page 35) for the spot spreading half-angle, α , and the spot propagation parameter, σ , respectively, were developed based on experimental measurements in low-freestream-disturbance environments. Based on good agreement for these parameters with the results of the elevated-freestream-turbulence simulation, these models are further recommended for use under such conditions.

From the improved understanding of separation-bubble transition developed through the complementary experimental and numerical studies, several techniques for passively manipulating this process were examined using the unconventional airfoil. Two-dimensional surface-protrusion and surface-indentation modifications were made to the airfoil for such purposes, and their characteristic streamwise lengths were tailored to provide passive forcing of the shear layer at the frequency of maximum instability amplification observed therein. The results of this study have shown that there is no optimal solution to this problem, but

there are several ways in which the transition process can be manipulated in order to reduce the losses arising from this process. These manipulations include: subharmonic-instability suppression that eliminates the vortex-pairing phenomenon; bubble-length reduction or bubble suppression through the promotion of small-scale turbulence; and suppression of large-scale vortex-shedding through physical disturbance of the primary instability waves.

10.2 Contributions

In regards to the physical mechanisms associated with transition in separation bubbles, the research presented herein has provided additional insight, and a better understanding of this transition process under low and elevated levels of freestream turbulence. Although some of the results provide confirmation of various aspects of separation-bubble transition already noted or theorized in the open literature, the major contributions that provide an extension to the knowledge-base for such flows are the identification of:

- The time-periodic nature of small-scale break-down to turbulence under low-freestream-turbulence conditions.
- The mechanism of cross-stream momentum exchange associated with packets of amplified instabilities during the exponential-growth phase of Kelvin-Helmholtz-induced transition.
- The laminar inter-vortex region associated with the secondary pairing phenomenon at low Reynolds numbers.
- The initiation of turbulent spots in a separated shear layer occurring through an inviscid instability associated with low-speed streaks convecting through the shear layer.

- The vortex loop structure of turbulent spots in a separated shear layer under elevated-freestream-turbulence conditions.
- The shedding of large-scale coherent structures from the transition region being the source of elevated turbulence-kinetic-energy in the outer part of the reattached shear layer, thus providing the source for delayed establishment of an equilibrium turbulent-boundary-layer.
- Various physical mechanisms through which passive manipulation of separation-bubble transition can be achieved.

There are still, however, many outstanding issues to address regarding separation-bubble transition in order to provide a full understanding of such flows.

10.3 Recommendations for Future Work

Many avenues of future research related to transition in separation bubbles have been identified and some that the author deem most promising are discussed in the following.

In regards to the low-Reynolds-number studies performed in the tow-tank facility using the unconventional airfoil, the three-dimensional nature of the primary and secondary vortex-pairing events has not been identified, as the two-dimensional PIV measurements have only been performed in a single $x - y$ plane. It is likely that the larger-scale paired vortices become stretched and reoriented, as were the primary spanwise-oriented vortices observed in the low-freestream-turbulence simulation. The flow-manipulation techniques may also provide some modification to the spanwise development of these structures. Such phenomena could potentially be examined through various means. One such means is a possible redesign of the support-stem in the tow-tank such that the airfoil can be mounted vertically, instead of horizontally, so that the laser light sheet can be oriented in an $x - z$

plane through the separated shear layer. The major difficulty to overcome in doing this is the provision of markers in the particle images that are required for camera-model-tracking correction. This may not be an issue in the new full-scale facility currently under construction, as it has been decided to mount the camera traverse system to the side of the tow-tank instead of the adjacent wall. This will not only provide a shorter distance from the lens to the model, but will also eliminate the need for the heavy, high-magnification lenses that are cantilevered off the camera support-stand, thus providing a potentially greater reduction in the tracking errors. The use of DNS to study the flow over the unconventional airfoil is also a possibility. This was attempted by the author using a setup similar to that presented in Chapter 7 for the flat-plate test-cases. However it was very quickly realized that due to the nature of the isolated airfoil configuration, a much greater extent of the surrounding freestream flow-field would have to be modelled, and the computational resources for such a simulation were not available at the time. In particular, the flow-field upstream of the leading edge would have to be modelled, as the uncertainty associated with PIV measurements in the thin boundary-layer near the suction peak of the airfoil negate the use of such measurements for specification of a velocity-based inlet boundary condition.

With the computational resources now available at Carleton University (as seven additional processors have recently been added to the simulation-cluster), the potential for examining the physics associated with transition using DNS methods has been greatly improved. Some recommended studies are discussed in the following.

Some of the experimental test-cases examined by Roberts (2005) involving elevated-freestream-turbulence provide conditions where transition is initiated much farther downstream of separation than the case examined in this thesis, as a result of a different pressure distribution. The greater distance of the separated shear layer from the surface in such cases may alter the structure of the resulting turbulent spots, and this can be examined using DNS. The attached-boundary-layer transition cases of Roberts can also be simulated

to examine the nature of freestream-turbulence-induced turbulent spots in adverse pressure gradients. In regards to the turbulent spots themselves, many of the experimental studies that have been aimed at identifying the structure of such spots made use of phase-averaged data that can smear-out details of the vortical structures generated within the spots. Such artificially-generated turbulent spots can also be examined using DNS, from which details regarding the spot-to-spot variations in internal structure can be identified. The possibility even presents itself for simulating surface-roughness-induced transition in the context of DNS. The computational mesh on the lower boundary of the domain can be modified to simulate surface roughness, as long as the spatial nature of the roughness pattern can be resolved by the near-wall mesh resolution.

The transient-growth instability mechanism that has resulted in streamwise streaks developing in the laminar boundary layer of the elevated-freestream-turbulence simulation is a potential avenue for future research. The development of such streaks in separated shear layers could potentially be examined using DNS by itself, or complemented with experiments for which artificially-generated streaks are studied.

With regard to the transition model developed by Roberts (2005), there is only one outstanding issue that has not been addressed: that is the potential influence of spanwise pressure gradients on the transition process. Spanwise pressure gradients are observed over compressor and turbine airfoils, as well as over swept wings, and their effect on the transition process has been documented in the open literature for low-freestream-turbulence conditions. The effects of spanwise pressure gradients on the transition process under elevated-freestream-turbulence conditions is also a recommended avenue for research. In fact, such a study has already been initiated at Carleton University and will make use of complementary hot-wire measurements and DNS results. These studies can be used to validate, or further modify, Roberts' model for the effects of spanwise pressure gradients.

Although several passive transition-manipulation techniques have been examined in the context of the present work, and have been shown to provide some potential performance improvements for low-Reynolds-number airfoils, further studies can be initiated to examine additional configurations. Three-dimensional surface indentations may provide the desired spatial forcing in not only the streamwise direction, through manipulation of the spanwise oriented vortices, but also the spanwise direction to promote the re-orientation of spanwise-oriented vorticity into the streamwise direction and provide a quicker reattachment process. This study would require an assessment of the three-dimensional nature of the coherent structures that develop in the transition region, through either $x - z$ plane measurements or through DNS.

References

- Abdalla, I. E. and Yang, Z. (2004), "Numerical Study of the Instability Mechanism in Transitional Separating-Reattaching Flow," *International Journal of Heat and Fluid Flow*, **25**, pp. 593–605.
- Abdeljabar, R. and Safi, M. J. (2001), "Shear Flow Induced Interface Instability," *Experiments in Fluids*, **31**, pp. 13–18.
- Abu-Ghannam, B. J. and Shaw, R. (1980), "Natural Transition of Boundary Layers - The Effects of Turbulence, Pressure Gradient and Flow History," *Journal of Mechanical Engineering Sciences*, **22**, pp. 213–228.
- AEA-Technology (2001), *CFX-TASCflow Computational Fluid Dynamics Software - Theory Documentation, Version 2.11.1*, AEA Technology Engineering Software Ltd.
- Alam, M. and Sandham, N. D. (2000), "Direct Numerical Simulation of 'Short' Laminar Separation Bubbles with Turbulent Reattachment," *Journal of Fluid Mechanics*, **403**, pp. 223–250.
- ANSYS (2004), *CFX-5.7.1 User Manual*, ANSYS Canada Ltd.
- Arena, A. V. and Mueller, T. J. (1980), "Laminar Separation, Transition, and Turbulent Reattachment Near the Leading Edge of Airfoils," *AIAA Journal*, **18**, pp. 747–753.

- Asai, M., Minagawa, M. and Nishioka, M. (2002), "The Instability and Breakdown of a Near-Wall Low-Speed Streak," *Journal of Fluid Mechanics*, **455**, pp. 289–314.
- Bao, F. and Dallmann, U. C. (2004), "Some Physical Aspects of Separation Bubble on a Rounded Backward-Facing Step," *Aerospace Science and Technology*, **8**, pp. 83–91.
- Batill, S. M. and Mueller, T. J. (1981), "Visualization of Transition in the Flow Over an Airfoil Using the Smoke-Wire Technique," *AIAA Journal*, **19**, pp. 340–345.
- Bearman, P. W. (1971), "Corrections for the Effect of Ambient Temperature Drift on Hot-Wire Measurements in Incompressible Flow," *DISA Information*, **11**, pp. 25–30.
- Brear, M. J. and Hodson, H. P. (2003), "The Response of a Laminar Separation Bubble to 'Aircraft Engine Representative' Freestream Disturbances," *Experiments in Fluids*, **35**, pp. 610–617.
- Chandrasekhar, S. (1961), *Hydrodynamic and Hydromagnetic Stability*, Dover Publications, New York.
- Cherry, N. J., Hillier, R. and Latour, M. E. M. P. (1984), "Unsteady Measurements in a Separated and Reattaching Flow," *Journal of Fluid Mechanics*, **144**, pp. 13–46.
- Davis, R. L., Carter, J. E. and Reshotko, E. (1987), "Analysis of Transitional Separation Bubbles on Infinite Swept Wings," *AIAA Journal*, **25**, pp. 421–428.
- Denton, J. D. (1993), "Loss Mechanisms in Turbomachines," *ASME Journal of Turbomachinery*, **115**, pp. 621–656.
- Dhawan, S. and Narasimha, R. (1958), "Some Properties of Boundary-Layer Flow During the Transition from Laminar to Turbulent Motion," *Journal of Fluid Mechanics*, **3**, pp. 418–436.

- Dovgal, A. V., Kozlov, V. V. and Michalke, A. (1994), "Laminar Boundary Layer Separation: Instability and Associated Phenomena," *Progress in Aerospace Sciences*, **30**, pp. 61–94.
- D'Ovidio, A., Harkins, J. A. and Gostelow, J. P. (2001*a*), "Turbulent Spots in Strong Adverse Pressure Gradients Part 1 - Spot Behavior," ASME Paper No. 2001-GT-0194.
- D'Ovidio, A., Harkins, J. A. and Gostelow, J. P. (2001*b*), "Turbulent Spots in Strong Adverse Pressure Gradients Part 2 - Spot Propagation and Spreading Rates," ASME Paper No. 2001-GT-0406.
- Emmons, H. W. (1951), "The Laminar-Turbulent Transition in a Boundary Layer - Part 1," *Journal of the Aeronautical Sciences*, **18**, pp. 490–498.
- Estevadeordal, J. and Kleis, S. J. (1999), "High-Resolution Measurements of Two-Dimensional Instabilities and Turbulence Transition in Plane Mixing Layers," *Experiments in Fluids*, **27**, pp. 378–390.
- Gad-el-Hak, M. (2000), *Flow Control: Passive, Active, and Reactive Flow Management*, Cambridge University Press, Cambridge, UK.
- Gad-el-Hak, M. (2001), "Flow Control: The Future," *AIAA Journal of Aircraft*, **38**, pp. 402–418.
- Gilbert, R. and Johnson, D. (2003), "Evaluation of FFT-Based Cross-Correlation Algorithms for PIV in a Periodic Grooved Channel," *Experiments in Fluids*, **34**, pp. 473–483.
- Gostelow, J. P., Melwani, N. and Walker, G. J. (1996), "Effects of Streamwise Pressure Gradients on Turbulent Spot Development," *ASME Journal of Turbomachinery*, **118**, pp. 737–743.

- Gostelow, J. P. and Thomas, R. L. (2006), "Interactions Between Propagating Wakes And Flow Instabilities In The Presence Of A Laminar Separation Bubble," ASME Paper No. GT2006-91193.
- Hall, S. D., Behnia, M., Fletcher, C. A. J. and Morrison, G. (2003), "Investigation of the Secondary Corner Vortex in a Benchmark Turbulent Backward-Facing Step Using Cross-Correlation Particle Imaging Velocimetry," *Experiments in Fluids*, **35**, pp. 139–151.
- Hanff, E. S. (2004), "PIV Application in Advanced Low Reynolds Number Facility," *IEEE Aerospace and Electronic Systems*, **40**, pp. 310–319.
- Hanff, E. S., ed. (2006), *AVT-101 Final Report: Some Experimental and Computational Investigations in Low Reynolds Number Aerodynamics, with Applications to Micro Air Vehicles*, North Atlantic Treaty Organization (NATO) Research and Technology Organization (RTO).
- Hatman, A. and Wang, T. (1998a), "Separated-Flow Transition. Part 1 - Experimental Methodology and Mode Classification," ASME Paper No. 98-GT-461.
- Hatman, A. and Wang, T. (1998b), "Separated-Flow Transition. Part 2 - Experimental Results," ASME Paper No. 98-GT-462.
- Hatman, A. and Wang, T. (1998c), "Separated-Flow Transition. Part 3 - Primary Modes and Vortex Dynamics," ASME Paper No. 98-GT-463.
- Hatman, A. and Wang, T. (1999), "A Prediction Model for Separated-Flow Transition," *ASME Journal of Turbomachinery*, **121**, pp. 594–602.
- Hinze, J. O. (1975), *Turbulence*, 2nd ed., McGraw-Hill, New-York.
- Ho, C. and Huang, L. S. (1982), "Subharmonics and Vortex Merging in Mixing Layers," *Journal of Fluid Mechanics*, **119**, pp. 443–473.

- Ho, C. and Huerre, P. (1984), "Perturbed Free Shear Layers," *Annual Review of Fluid Mechanics*, **16**, pp. 365–424.
- Hodson, H. P. and Howell, R. J. (2005), "The Role of Transition in High-Lift Low-Pressure Turbines for Aeroengines," *Progress in Aeronautical Sciences*, **41**, pp. 419–454.
- Howell, R. J., Ramesh, O. N., Hodson, H. P., Harvey, N. W. and Schulte, V. (2001), "High Lift and Aft-Loaded Profiles for Low-Pressure Turbines," *ASME Journal of Turbomachinery*, **123**, pp. 181–188.
- Huang, L. S. and Ho, C. M. (1990), "Small-Scale Transition in a Plane Mixing Layer," *Journal of Fluid Mechanics*, **210**, pp. 475–500.
- Hutchinson, B. R. and Raithby, G. D. (1986), "A Multigrid Method Based on the Additive Correction Strategy," *Numerical Heat Transfer*, **9**, pp. 511–537.
- Jacobs, R. G. and Durbin, P. A. (2001), "Simulations of Bypass Transition," *Journal of Fluid Mechanics*, **428**, pp. 185–212.
- Johnson, M. W. and Ercan, A. H. (1999), "A Physical Model for Bypass Transition," *International Journal of Heat and Fluid Flow*, **20**, pp. 95–104.
- Kalitzin, G. (2003), "DNS of Fully Turbulent Flow in a LPT Passage," *International Journal of Heat and Fluid Flow*, **24**, pp. 636–644.
- Kelly, R. E. (1967), "On The Stability of an Inviscid Shear Layer Which is Periodic in Space and Time," *Journal of Fluid Mechanics*, **27**, pp. 657–689.
- Kerho, M., Hutcherson, S., Blackwelder, R. F. and Liebeck, R. H. (1993), "Vortex Generators Used to Control Laminar Separation Bubbles," *AIAA Journal of Aircraft*, **30**, pp. 315–319.

- Kiya, M. and Sasaki, K. (1985), "Structure of Large-Scale Vortices and Unsteady Reverse Flow in the Reattaching Zone of a Turbulent Separation Bubble," *Journal of Fluid Mechanics*, **154**, pp. 463–491.
- Klebanoff, P. S. (1971), "Effect of Free-Stream Turbulence on a Laminar Boundary Layer," *Bulletin of the American Physical Society*, **16**.
- Lake, J. P., King, P. I. and Rivir, R. B. (2000), "Low Reynolds Number Loss Reduction on Turbine Blades with Dimples and V-Grooves," AIAA Paper No. 00-0738.
- Lang, M., Rist, U. and Wagner, S. (2004), "Investigations on Controlled Transition Development in a Laminar Separation Bubble by Means of LDA and PIV," *Experiments in Fluids*, **36**, pp. 43–52.
- Liebeck, R. H. (1978), "Design of Subsonic Airfoils for High Lift," *AIAA Journal of Aircraft*, **15**, pp. 547–561.
- Lin, H. J. and Perlin, M. (1998), "Improved Methods for Thin, Surface Boundary Layer Investigations," *Experiments in Fluids*, **25**, pp. 431–444.
- Lin, J. C. (2002), "Review of Research on Low-Profile Vortex Generators to Control Boundary-Layer Separation," *Progress in Aerospace Sciences*, **38**, pp. 389–420.
- Lin, J. C., Howard, F. G., Bushnell, D. M. and Selby, G. V. (1990), "Investigation of Several Passive and Active Methods for Turbulent Flow Separation Control," AIAA Paper No. 90-1598.
- Lin, J. C., Howard, F. G. and Selby, G. V. (1989), "Turbulent Flow Separation Control Through Passive Techniques," AIAA Paper No. 89-0976.
- Lou, W. and Hourmouziadis, J. (2000), "Separation Bubbles Under Steady and Periodic-Unsteady Main Flow Conditions," *ASME Journal of Turbomachinery*, **122**, pp. 634–643.

- Mahallati, A. (2003), "Aerodynamics of a Low-Pressure Turbine Airfoil Under Steady and Periodically Unsteady Conditions," Ph.D. Thesis, Carleton University, Ottawa, Canada.
- Mahallati, A., McAuliffe, B. R., Sjolander, S. A. and Praisner, T. J. (2007), "Aerodynamics of a Low-Pressure Turbine Airfoil at Low-Reynolds Numbers Part 1: Steady Flow Measurements," ASME Paper No. GT2007-27347.
- Malkiel, E. and Mayle, R. E. (1996), "Transition in a Separation Bubble," ASME Journal of Turbomachinery, **118**, pp. 752–759.
- Marxen, O., Lang, M., Rist, U. and Wagner, S. (2003), "A Combined Experimental/Numerical Study of Unsteady Phenomena in a Laminar Separation Bubble," Flow, Turbulence and Combustion, **71**, pp. 133–146.
- Matsubara, M. and Alfredsson, P. H. (2001), "Disturbance Growth in Boundary Layers Subjected to Free-Stream Turbulence," Journal of Fluid Mechanics, **430**, pp. 149–168.
- Mayle, R. E. (1991), "The Role of Laminar-Turbulent Transition in Gas Turbine Engine," ASME Journal of Turbomachinery, **113**, pp. 509–537.
- Mayle, R. E., Dullenkopf, K. and Schultz, A. (1998), "The Turbulent That Matters," ASME Journal of Turbomachinery, **120**, pp. 402–409.
- McAuliffe, B. R. (2003), "An Experimental Study of Flow Control Using Blowing For a Low-Pressure Turbine Airfoil," M.A.Sc. Thesis, Carleton University, Ottawa, Canada.
- McMichael, J. M. and Francis, M. S. (1997), "Micro Air Vehicles - Toward a New Dimension in Flight," www.fas.org/irp/program/collect/docs/mav_auvsi.htm, Accessed Aug. 2004 .
- Meunier, P. and Leweke, T. (2003), "Analysis and Treatment of Errors Due to High Velocity Gradients in Particle Image Velocimetry," Experiments in Fluids, **35**, pp. 408–421.

- Michelassi, V., Wissink, J. and Rodi, W. (2002), "Analysis of DNS and LES of Flow in a Low Pressure Turbine Cascade with Incoming Wakes and Comparison with Experiments," *Flow, Turbulence and Combustion*, **69**, pp. 295–330.
- Morkovin, M. V. (1993), "Bypass-Transition Research: Issues and Philosophy," *Instabilities and Turbulence in Engineering Flows*, edited by D. E. Ashpis, T. B. Gatski, and R. Hirsh, pp. 3–30, Kluwer Academic Publishers, Boston, pp. 3–30.
- Murawski, C. G. and Vafai, K. (1999), "Effect of Variable Axial Chord on a Low-Pressure Turbine Blade," *Journal of Propulsion and Power*, **15**, pp. 667–674.
- Muti Lin, J. C. and Pauley, L. L. (1996), "Low-Reynolds-Number Separation on an Airfoil," *AIAA Journal*, **34**, pp. 1570–1577.
- Na, Y. and Moin, P. (1998), "Direct Numerical Simulation of a Separated Turbulent Boundary Layer," *Journal of Fluid Mechanics*, **374**, pp. 379–405.
- Panton, R. L. (2001), "Overview of the Self-Sustaining Mechanisms of Wall Turbulence," *Progress in Aerospace Sciences*, **37**, pp. 341–383.
- Pierrehumbert, R. T. and Widnall, S. E. (1982), "The Two- And Three-Dimensional Instabilities of a Spatially Periodic Shear Layer," *Journal of Fluid Mechanics*, **114**, pp. 59–82.
- Pope, S. B. (2000), *Turbulent Flows*, Cambridge University Press, New-York.
- Praisner, T. J. and Clark, J. P. (2007), "Predicting Transition in Turbomachinery, Part I - A Review and New Model Development," *ASME Journal of Turbomachinery*, **129**, pp. 1–13.
- Praisner, T. J., Grover, E. A., Rice, M. J. and Clark, J. P. (2007), "Predicting Transition in Turbomachinery, Part II - Model Validation and Benchmarking," *ASME Journal of Turbomachinery*, **129**, pp. 14–22.

- Qui, S. and Simon, T. W. (1997), "An Experimental Investigation of Transition as Applied to Low Pressure Turbine Suction Surface Flows," ASME Paper No. 97-GT-455.
- Raffel, M., Willert, C. and Kompenhans, J. (1998), *Particle Image Velocimetry: A Practical Guide*, Series: Experimental Fluid Mechanics, Springer-Verlag, Berlin.
- Raw, M. (1996), "Robustness of Coupled Algebraic Multigrid for the Navier-Stokes Equations," AIAA Paper No. 96-0297.
- Redford, J. A. and Johnson, M. W. (2004), "Predicting Transitional Separation Bubbles," ASME Paper No. GT2004-53353.
- Ripley, M. D. and Pauley, L. L. (1993), "The Unsteady Structure of Two-Dimensional Steady Laminar Separation," *Physics of Fluids A (Fluid Dynamics)*, **5**, pp. 3099–3106.
- Rist, U. and Maucher, U. (2002), "Investigations of Time-Growing Instabilities in Laminar Separation Bubbles," *European Journal of Mechanics, B/Fluids*, **21**, pp. 495–509.
- Roach, P. E. (1987), "The Generation of Nearly Isotropic Turbulence by Means of Grids," *International Journal of Heat and Fluid Flow*, **8**, pp. 82–92.
- Roberts, S. K. (2005), "Boundary Layer Transition in Attached and Separated Flows at Low Reynolds Numbers," Ph.D. Thesis, Carleton University, Ottawa, Canada.
- Roberts, S. K. and Yaras, M. I. (2003), "Effects of Periodic Unsteadiness, Free-Stream Turbulence and Flow Reynolds Number on Separation-Bubble Transition," ASME Paper No. GT2003-38626.
- Roberts, S. K. and Yaras, M. I. (2005a), "Boundary-Layer Transition Affected by Surface Roughness and Free-Stream Turbulence," *ASME Journal of Fluids Engineering*, **127**, pp. 449–457.
- Roberts, S. K. and Yaras, M. I. (2005b), "Modeling Transition in Separated and Attached Boundary Layers," *ASME Journal of Turbomachinery*, **127**, pp. 402–411.

- Roberts, S. K. and Yaras, M. I. (2006a), "Effects of Surface Roughness Geometry on Separation-Bubble Transition," *ASME Journal of Turbomachinery*, **128**, pp. 349–356.
- Roberts, S. K. and Yaras, M. I. (2006b), "Large-Eddy Simulation of Transition in a Separation Bubble," *ASME Journal of Fluids Engineering*, **128**, pp. 232–238.
- Roberts, W. B. (1975), "The Effects of Reynolds Number and Laminar Separation on Axial Cascade Performance," *Journal of Engineering for Power*, **97**, pp. 261–274.
- Rohaly, J., Nakajima, T. and Ikeda, Y. (2000), "Identification of True Particle Image Displacement Based on False Correlation Symmetry at Poor Signal Peak Detectability," *Experiments in Fluids*, **Suppl.**, pp. S23–S33.
- Saric, W. S., Reed, H. L. and Kerschen, E. J. (2002), "Boundary-Layer Receptivity to Freestream Disturbances," *Annual Review of Fluid Mechanics*, **34**, pp. 291–319.
- Scarano, F. (2003), "Theory of Non-Isotropic Spatial Resolution in PIV," *Experiments in Fluids*, **35**, pp. 268–277.
- Scarano, F. and Reithmuller, M. L. (1999), "Iterative Multigrid Approach in PIV Processing with Discrete Window Offset," *Experiments in Fluids*, **26**, pp. 513–523.
- Scarano, F. and Riethmuller, M. L. (2000), "Advances in Iterative Multigrid PIV Image Processing," *Experiments in Fluids*, **Suppl.**, pp. 51–60.
- Schlichting, H. and Gersten, K. (2000), *Boundary Layer Theory*, 8th ed., Springer-Verlag, Berlin.
- Schmidt, G. S. and Mueller, T. J. (1989), "Analysis of Low Reynolds Number Separation Bubbles Using Semiempirical Methods," *AIAA Journal*, **27**, pp. 993–1001.
- Schröder, A. and Kompenhans, J. (2004), "Investigation of a Turbulent Spot Using Multi-Plane Stereo Particle Image Velocimetry," *Experiments in Fluids*, **36**, pp. 82–90.

- Schubauer, G. B. and Klebanoff, P. S. (1955), "Contributions on the Mechanics of Boundary-Layer Transition," NACA Report No. 1289.
- Selig, M. S. (1995), *Summary of Low-Speed Airfoil Data - Volume 1*, Soartech.
- Shyne, R. J., Sohn, K.-H. and DeWitt, K. J. (2000), "Experimental Investigation of Boundary Layer Behavior in a Simulated Low Pressure Turbine," ASME Journal of Fluids Engineering, **122**, pp. 84–89.
- Sieverding, C. H., Bagnera, C., Boege, A. C., Anton, J. A. C. and Luere, V. (2004), "Investigation of the Effectiveness of Various Types of Boundary Layer Transition Elements of Low Reynolds Number Turbine Bladings," ASME Paper No. GT2004-54103.
- Solomon, W. J., Walker, G. J. and Gostelow, J. P. (1996), "Transition Length Prediction for Flows With Rapidly Changing Pressure Gradients," ASME Journal of Turbomachinery, **118**, pp. 744–751.
- Spalart, P. R. and Strelets, M. K. (2000), "Mechanisms of Transition and Heat Transfer in a Separation Bubble," Journal of Fluid Mechanics, **403**, pp. 329–349.
- Stieger, R. D. and Hodson, H. P. (2004), "The Transition Mechanism of Highly Loaded Low-Pressure Turbine Blades," ASME Journal of Turbomachinery, **126**, pp. 536–543.
- Talan, M. and Hourmouziadis, J. (2002), "Characteristic Regimes of Transitional Separation Bubbles in Unsteady Flow," Flow, Turbulence and Combustion, **69**, pp. 207–227.
- Tani, I. (1964), "Low Speed Flows Involving Bubble Separation," Progress in Aeronautical Sciences, **5**, pp. 70–104.
- Tennekes, H. and Lumley, J. L. (1972), *A First Course in Turbulence*, MIT Press, Massachusetts.

- Volino, R. J. (2002*a*), "Separated Flow Transition Under Simulated Low-Pressure Turbine Airfoil Conditions: Part 1 - Mean Flow and Turbulence Statistics," ASME Journal of Turbomachinery, **124**, pp. 645–655.
- Volino, R. J. (2002*b*), "Separated Flow Transition Under Simulated Low-Pressure Turbine Airfoil Conditions: Part 2 - Turbulence Spectra," ASME Journal of Turbomachinery, **124**, pp. 656–664.
- Volino, R. J. (2003), "Passive Flow Control on Low-Pressure Turbine Airfoils," ASME Journal of Turbomachinery, **125**, pp. 754–764.
- Volino, R. J. and Bohl, D. G. (2004), "Separated Flow Transition Mechanism and Prediction with High and Low Freestream Turbulence Under Low Pressure Turbine Conditions," ASME Paper No. GT2004-53360.
- Volino, R. J. and Hultgren, L. S. (2001), "Measurements in Separated and Transitional Boundary Layers Under Low-Pressure Turbine Airfoil Conditions," ASME Journal of Turbomachinery, **123**, pp. 189–197.
- Volino, R. J. and Murawski, C. G. (2003), "Separated-Flow Transition in a Low Pressure Turbine Cascade - Mean Flow and Turbulence Spectra," ASME Paper No. GT2003-38727.
- Volino, R. J., Schultz, M. P. and Pratt, C. M. (2001), "Conditional Sampling in a Transitional Boundary Layer Under High Free-Stream Turbulence Conditions," ASME Paper No. 2001-GT-0192.
- Walker, G. J. (1989), "Transitional Flow On Axial Turbomachine Blading," AIAA Journal, **27**, pp. 595–602.
- Walker, G. J. (1993), "The Role of Laminar-Turbulent Transition in Gas Turbine Engines: A Discussion," ASME Journal of Turbomachinery, **115**, pp. 207–217.

- Watmuff, J. H. (1999), "Evolution of a Wave Packet Into Vortex Loops in a Laminar Separation Bubble," *Journal of Fluid Mechanics*, **397**, pp. 119–169.
- Westerweel, J. (2000), "Theoretical Analysis of the Measurement Precision in Particle Image Velocimetry," *Experiments in Fluids*, **Suppl.**, pp. 3–12.
- White, F. M. (1991), *Viscous Fluid Flow*, 2nd ed., McGraw-Hill, Boston.
- White, F. M. (1994), *Fluid Mechanics*, 3rd ed., McGraw-Hill, Boston.
- Wilson, P. G. and Pauley, L. L. (1998), "Two- and Three-Dimensional Large-Eddy Simulations of a Transitional Separation Bubble," *Physics of Fluids*, **10**, pp. 2932–2940.
- Wissink, J. G. and Rodi, W. (2002), "DNS of Transition In a Laminar Separation Bubble," *Advances in Turbulence IX; Proceedings of the Ninth European Turbulence Conference*, edited by I. P. Castro and P. E. Hancock, Southampton, UK.
- Wissink, J. G. and Rodi, W. (2003), "DNS of a Laminar Separation Bubble in the Presence of Oscillating External Flow," *Flow, Turbulence and Combustion*, **71**, pp. 311–331.
- Wu, X., Jacobs, R. G., Hunt, J. C. R. and Durbin, P. A. (1999), "Simulation of Boundary Layer Transition Induced by Periodically Passing Wakes," *Journal of Fluid Mechanics*, **398**, pp. 109–153.
- Yang, Z. and Voke, P. R. (2001), "Large-Eddy Simulation of Boundary-Layer Separation and Transition at a Change of Surface Curvature," *Journal of Fluid Mechanics*, **439**, pp. 305–333.
- Yaras, M. I. (2001), "Measurements of the Effects of Pressure-Gradient History on Separation-Bubble Transition," ASME Paper No. 2001-GT-0193.
- Yaras, M. I. (2002), "Measurement of the Effects of Freestream Turbulence on Separation-Bubble Transition," ASME Paper No. GT-2002-30232.

-
- Yaras, M. I. (2007), "An Experimental Study of the Effects of Free-Stream Turbulence on Turbulent Spots in Boundary Layers," ASME Journal of Fluids Engineering, **129** In Press.
- Zhang, X.-F. and Hodson, H. (2005), "The Combined Effects of Surface Trips and Unsteady Wakes on the Boundary Layer Development of an Ultra-High-Lift LP Turbine Blade," ASME Journal of Turbomachinery, **127**, pp. 479–488.
- Zhang, X.-F., Vera, M. and Hodson, H. (2005), "Separation and Transition Control on an Aft-Loaded Ultra-High-Lift LP Turbine Blade at Low Reynolds Numbers: Low-Speed Investigation," ASME Paper No. GT2005-68892.

Appendix A

The Particle Image Velocimetry (PIV) Measurement Technique

Particle Image Velocimetry (PIV) has become a common measurement technique in experimental fluid dynamics. This appendix is intended to provide a brief overview of the technique, such that it can be used as a starting point for other students planning to use PIV for their studies. Although PIV has been in practice since the early part of the 20th century, most of the important advances were made in the nineteen-eighties with regard to analog PIV, and the nineteen-nineties with regard to digital PIV. The basic principles of PIV are discussed in Section A.1, and digital processing techniques are described in Section A.2.

A.1 Principles of PIV

The earliest techniques for studying fluid-dynamic phenomena were primarily of a qualitative nature, and focused on flow visualization methods. PIV developed from a form of flow visualization for which the flow of interest was seeded with tracer particles and the

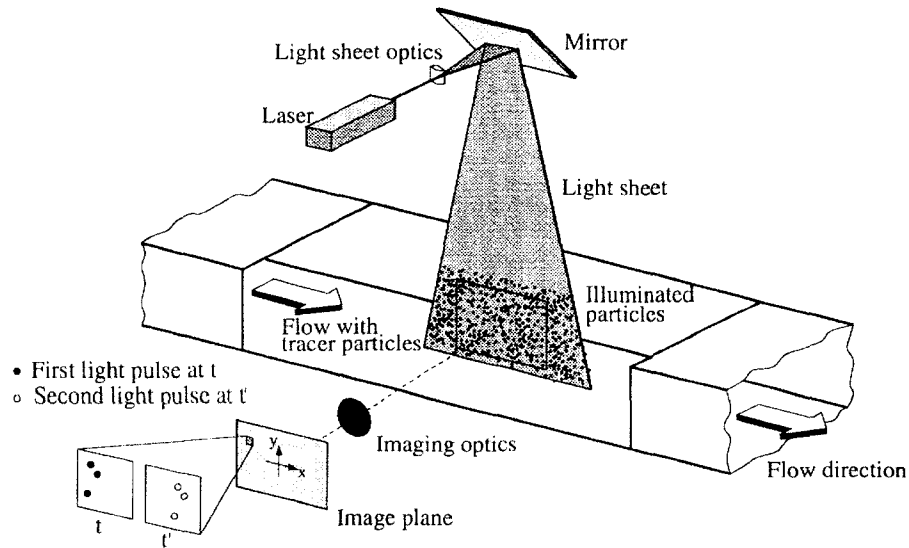


Figure A.1: Typical arrangement for a PIV measurement system (reproduced from Raffel *et al.*, 1998)

flow behaviour was documented based on visual observation of the particle motion. The basic principle of PIV is to capture images of a seeded flow field at two instants in time from which the displacement of the seeds, or “particles”, can be evaluated. The particle velocity is then calculated from the displacement and the time delay between images. To accomplish this, several subsystems are required. Only the digital PIV technique will be discussed herein. For details regarding analog PIV, the reader is referred to the book by Raffel *et al.* (1998). Figure A.1 shows a typical PIV arrangement including all of the important subsystems, and is presented as an aid to the following description of the PIV measurement technique.

In an experimental PIV setup, tracer particles are introduced into the flow of interest. A plane light sheet is used to illuminate the particles twice in a very short time and the light scattered from the particles is recorded on an image plane by use of a high-quality optical lens. The time delay required between light sheet pulses depends on the velocity of the flow,

the magnification factor of the lens, and the spatial resolution of the desired velocity field. The image plane can be either a photographic film or a digital CCD (charge-coupled device) sensor. If a photographic technique is used, the developed film images must be digitized using a scanner. For the digital technique, the image recordings are stored directly to the memory of a digital computer.

PIV has two major benefits over other measurements techniques. The first is that PIV is a “non-intrusive” velocity measurement technique. Unlike hot-wires or pressure probes, PIV does not introduce a measurement device into the flow, enabling reliable measurements in flows with shock waves and in near-wall regions of boundary layer flows. This being said, it must be ensured that the tracer particles do not affect the flow behaviour. Therefore, it is desired that the tracer particles have a material density the same as that of the fluid medium and that they be small in relation to the scale of flow structures, such that they closely follow the motions of the fluid particles. The second major benefit of PIV over other measurement techniques is the ability to capture instantaneous planar flow fields, rather than single-point measurements. This allows a quantitative measure of the flow structure at a given time. This is particularly useful in shear flows where the identification and quantification of coherent structures is becoming increasingly important.

Digital PIV recordings are evaluated by dividing the images into small “interrogation windows”, each of which are used to calculate a particle displacement vector. Each interrogation window is evaluated using one of two statistical methods, depending on the method in which the images were recorded. An auto-correlation technique is used if both light pulses were recorded on the same image frame. A cross-correlation technique is used if each light pulse was recorded on a separate image frame. The inherent problem with the auto-correlation technique is that the sign of the particle displacement cannot be evaluated, only the magnitude and the directional line. The cross-correlation technique does not suffer from this problem since the order in which the frames were recorded is known. Therefore,

the cross-correlation technique is most often used, and any mention of PIV processing henceforth will refer to this technique. The mathematical background of the digital cross-correlation evaluation method is described in the next section.

Raffel *et al.* (1998) present detailed descriptions of all of the important PIV subsystems, including tracer particle light scattering properties, laser types, light sheet and lens optics, and image recording devices. They also discuss processing techniques that were state-of-the-art at the time. More sophisticated processing techniques have been developed since then, and are described in the following sections.

A.2 Digital Cross-Correlation Evaluation for PIV

Modern digital PIV evaluation is based on a discrete cross-correlation between two particle images, or frames. In general, many particles are present within each interrogation window, and these particles are represented by image pixels of high intensity. Therefore, particle displacement evaluation is based on the motion of a cluster of particles, or high intensity pixels, within an interrogation window which are assumed to move homogeneously within the time separation of the two images. The cross-correlation algorithm does not “track” the motion of individual particles. Particle Tracking Velocimetry (PTV) is another technique used for flows with low-seeding density, where the location of discrete particles is identified and the motion of the particles are tracked. In the following description of the discrete cross-correlation PIV technique, it is assumed that only one pair of interrogation windows is being evaluated.

The intensity distribution, $I(x, y)$, defines the recorded pixel intensity at location (x, y) within the interrogation window. The discrete cross-correlation of the intensity values of

frame 1, $I(x, y)$, with those of frame 2, $I'(x, y)$, is given as follows:

$$R(x, y) = \sum_{i=-K}^K \sum_{j=-L}^L I(i, j)I'(i + x, j + y) \quad (\text{A.1})$$

where $K = M/2$ and $L = N/2$, with M and N being the interrogation window pixel size in the x and y directions, respectively. A correlation plane is formed by applying Equation A.1 for a range of shifts ($-K \leq x \leq +K$, $-L \leq y \leq +L$). This correlation plane has dimensions of $(M+1) \times (N+1)$, and requires that $I'(x, y)$ have dimensions twice that of the desired interrogation window. An example of this process is shown in Figure A.2. The cross-correlation function, $R(x, y)$, will have a maximum value at the location within the correlation plane where the two images most closely match in their intensity distributions. The location of this correlation peak represents an estimate of the particle displacement between the two image frames. Since the correlation plane is a discrete set of correlation

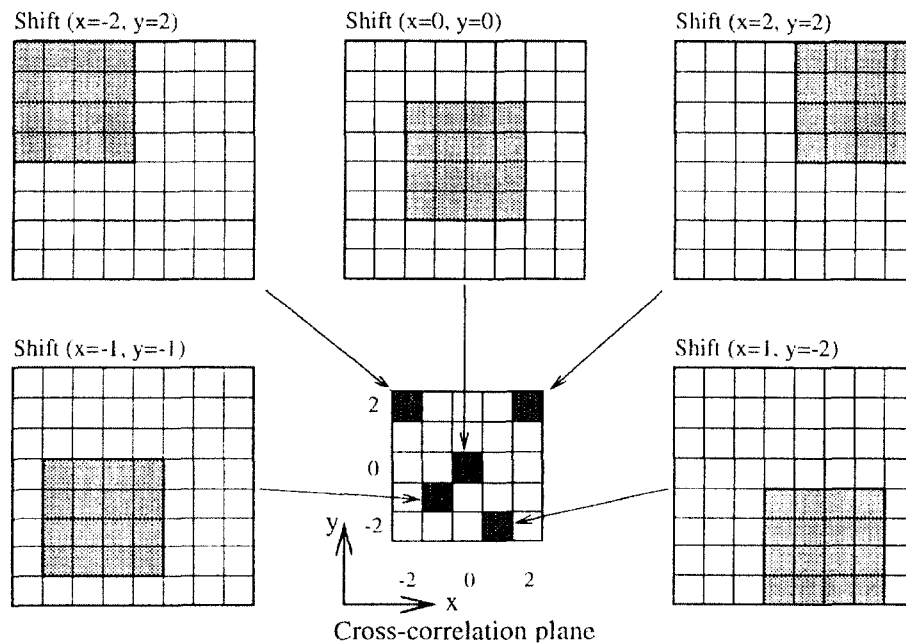


Figure A.2: **Example of Cross Correlation Evaluation for a 4x4 Pixel Interrogation Window (shaded region is window 1, reproduced from Raffel *et al.*, 1998)**

values, this estimate of particle displacement is an integer value, in units of pixels, and therefore has an uncertainty of ± 0.5 pixels.

The direct calculation of the discrete cross-correlation of Equation A.1 can be computationally expensive, especially for large interrogation window sizes. For a two-dimensional cross-correlation, $O(N^4)$ operations are required to evaluate Equation A.1 directly, where N is the pixel width of a square interrogation window. This can be reduced significantly by recognizing that the cross-correlation of two functions is equivalent to a complex conjugate multiplication of their Fourier transforms:

$$R(x, y) \iff \hat{I}' \cdot \hat{I}'^* \quad (\text{A.2})$$

where \hat{I} and \hat{I}' are the Fourier transforms of $I(x, y)$ and $I'(x, y)$, respectively. The use of a fast Fourier transform (FFT) can reduce the number of operations to $O(N^2 \log_2 N)$. Most modern PIV methods employ an FFT-based cross-correlation algorithm.

Modern PIV evaluation methods can detect a correlation peak to sub-pixel accuracy. This is achieved by fitting an appropriate curve or surface to the correlation data in the vicinity of the correlation peak, and selecting the maximum of the fit as the correlation peak. The three-point Gaussian fit is most often used as a fit for the correlation plane data (Westerweel, 2000).

The accuracy of PIV depends greatly on the quality of the recorded images, the selection of the time delay between images, the desired spatial resolution, and the characteristics of the flow itself. For various reasons, an incorrect displacement vector is sometimes calculated and these incorrect vectors are called “outliers” or are sometimes referred to as “spurious vectors”.

It is important to select an appropriate interrogation window size to ensure accurate

estimation of the particle displacements. The particle density should be such that at least 10 particles are present in the interrogation window in order to achieve a high signal-to-noise ratio in the correlation plane, and that the particle diameter be no less than two pixels to prevent a low-pass filtering effect (Scarano and Riethmuller, 2000). It should also be ensured that a sufficient number of particles remain within the boundaries of both windows during the elapsed time between image recordings. One of the major sources of uncertainty in shear flows is the presence of a displacement gradient across the interrogation window. Displacement gradients result in a bias towards lower displacement magnitudes, as discussed by Raffel *et al.* (1998). To reduce the effect of this bias, small interrogation windows are desired.

To avoid some of the problems associated with the above-mentioned restriction, modern PIV methods incorporate additional techniques to increase the accuracy of the particle displacement estimates. Some of these techniques include Window Overlap, Window Shifting, Adaptive Multi-Pass, and Window Deformation, each of which are described in the following paragraphs.

Window Overlap describes the overlapping of interrogation windows to increase the spatial resolution of the resultant vector field. The Window Overlap technique is most easily explained with a visual example. Figure A.3(a) shows examples of 0% window overlap and 50% window overlap. 50% overlap increases the spatial resolution by a factor of two in each direction ($4\times$ total increase in spatial resolution). The number of pixels in each interrogation window remains the same for any level of overlap.

Window Shifting is a technique whereby the two interrogation windows can be selected with a relative offset such that both windows contain approximately the same group of particles (Scarano and Reithmuller, 1999). For a given offset $(\Delta x, \Delta y)$, most PIV methods will use a centroidal shift $(I(x - \Delta x/2, y - \Delta y/2), I'(x + \Delta x/2, y + \Delta y/2))$ such that the

calculated displacement vector represents the displacement at the centre of the desired interrogation window (see Figure A.3(b)). The resultant displacement then consists of the calculated correlation peak displacement and the relative window offset. The relative offset can be set as a constant prior to the cross-correlation evaluation, but most PIV methods utilize Window Shifting with an Adaptive Multi-Pass approach.

Adaptive Multi-Pass is an iterative method of PIV evaluation. Each subsequent evaluation of a specific window is based in part on the previous evaluation of the same window. The evaluated particle displacement of the previous iteration is used as an offset for Window Shifting. This method requires no initial guess of the particle displacement for selecting the level of window shift. It is also possible to use a decreasing window size with an Adaptive Multi-Pass technique which enables the evaluation of displacements greater than the desired window size.

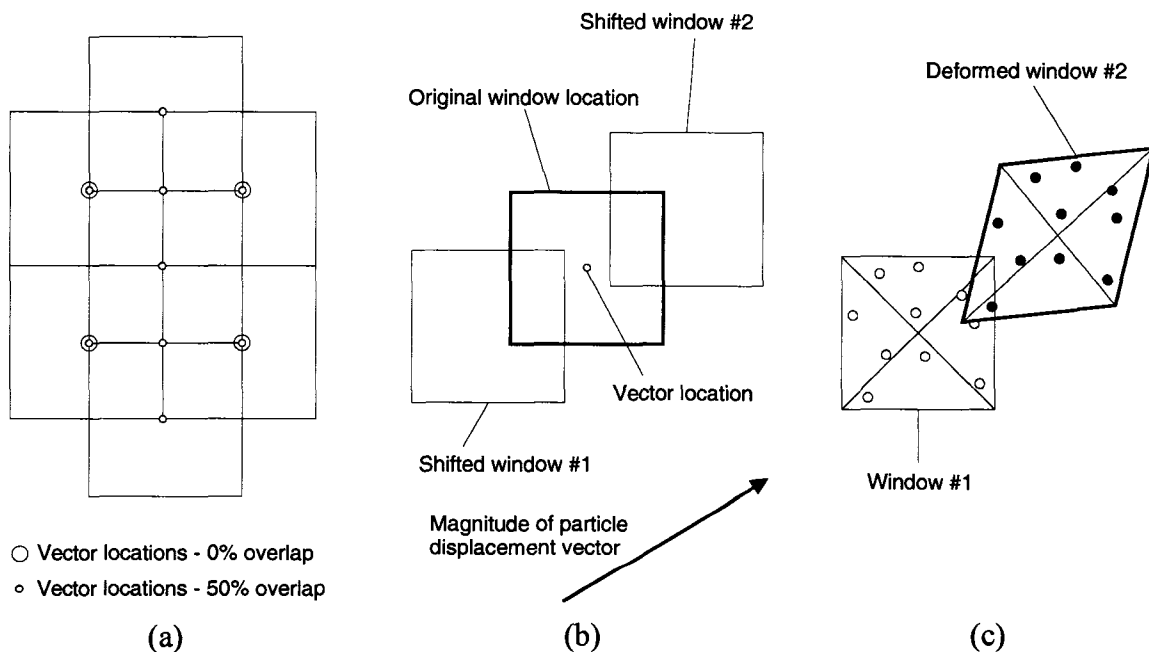


Figure A.3: **Advanced Techniques for PIV Cross-Correlation Evaluation, (a) Window Overlap, (b) Window Shifting, (c) Window Deformation**

As mentioned previously, small interrogation windows must be used for flows with high displacement gradients, or shear. A method of Window Deformation has been developed to alleviate this problem (described in Meunier and Leweke, 2003). The purpose of the Window Deformation technique is to account for the effects of continuum deformation, including translation, rotation, shearing, and dilation. This technique requires the use of an Adaptive Multi-Pass evaluation method. Once an initial estimate of the displacement vectors is established, the local continuum deformation can be estimated, and an appropriate image transformation is performed on the second window such that both windows contain approximately the same distribution of particles. This technique is shown schematically in Figure A.3(c).

In the literature, most of the above-mentioned techniques are characterized as Iterative Multigrid techniques, and many papers discuss their various theories, validations, applications, and advances (e.g. Lin and Perlin, 1998; Scarano and Reithmuller, 1999; Scarano and Riethmuller, 2000; Rohaly *et al.*, 2000; Westerweel, 2000; Scarano, 2003; Meunier and Leweke, 2003; Gilbert and Johnson, 2003).

Appendix B

Unconventional Airfoil Geometry

This appendix provides the geometric description of the unconventional airfoil designed for the studies documented in Chapters 8 and 9. Excerpts from the engineering drawings from which the airfoil was manufactured are also provided.

B.1 Surface Geometry

The unconventional airfoil consists of simple geometric surface shapes, including flat-segments, ellipses, and a polynomial shape. The airfoil is shown schematically in Figure B.1. The upper leading-edge quarter-ellipse has a major-to-minor axis ratio of 3.333, with a corresponding major-axis dimension of 3 cm. The lower leading-edge quarter-ellipse has major-to-minor axis ratios of 3.0, with a corresponding major-axis dimension of 7 cm. The trailing-edge half-ellipse has a major-to-minor axis ratio of 2.274 with a major-axis dimension of 2 cm.

The curved backward-facing ramp on the upper surface of the airfoil has a shape corresponding to a seventh-order polynomial. This polynomial, which provides a continuous

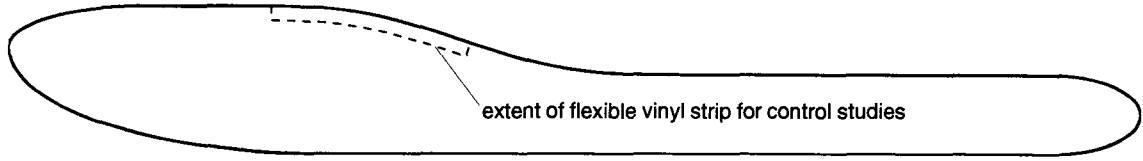


Figure B.1: Schematic of unconventional airfoil

change in surface slope and curvature over the upper surface of the airfoil, is defined as:

$$\frac{y}{C}(x) = \frac{h}{C} \left[20 \left(\frac{x - x_0}{L_r} \right)^7 - 70 \left(\frac{x - x_0}{L_r} \right)^6 + 84 \left(\frac{x - x_0}{L_r} \right)^5 - 35 \left(\frac{x - x_0}{L_r} \right)^4 + 1 \right] \quad (\text{B.1})$$

where h is the ramp height, x_0 is the location of the upstream-end of the ramp, and L_r is the length of the ramp. Equation B.1 is defined such that $y/C = 0$ at the downstream end of the ramp. For the ramp over the unconventional airfoil, which extends over the range $0.2 \leq x/C \leq 0.4$, the important parameters for defining the shape using Equation B.1 are $h/C = 0.06$, $x_0/C = 0.2$, and $L_r/C = 0.4$.

The surface coordinates of the unconventional airfoil are provided in Table B.1, neglecting the groove in which the flexible vinyl strips were inserted for the flow control study. The coordinates corresponding to this groove are provided in Table B.2.

Table B.1: Unconventional airfoil surface coordinates

x [m]	y [m]	x [m]	y [m]	x [m]	y [m]
0.000000	0.006000	0.102000	0.006845	0.249254	-0.011172
0.000080	0.006658	0.106000	0.005559	0.247871	-0.012742
0.000778	0.008036	0.110000	0.004347	0.245623	-0.014284
0.002260	0.009427	0.114000	0.003250	0.243620	-0.015233
0.003290	0.010098	0.118000	0.002302	0.241187	-0.016083
0.005844	0.011337	0.122000	0.001524	0.238195	-0.016815
0.008885	0.012393	0.126000	0.000925	0.236344	-0.017133
0.012208	0.013246	0.130000	0.000500	0.233978	-0.017412
0.015674	0.013908	0.134000	0.000229	0.231546	-0.017561
0.019284	0.014406	0.138000	0.000081	0.230000	-0.017588
0.023325	0.014774	0.142000	0.000018	0.090000	-0.017588
0.025885	0.014915	0.146000	0.000001	0.080000	-0.017588
0.030000	0.015000	0.150000	0.000000	0.070000	-0.017588
0.050000	0.015000	0.230000	0.000000	0.059243	-0.017307
0.054000	0.014999	0.231546	-0.000026	0.052618	-0.016849
0.058000	0.014982	0.233978	-0.000176	0.042372	-0.015673
0.062000	0.014919	0.236344	-0.000454	0.033526	-0.014133
0.066000	0.014771	0.238195	-0.000772	0.025377	-0.012174
0.070000	0.014500	0.241187	-0.001504	0.017933	-0.009765
0.074000	0.014075	0.243620	-0.002354	0.011461	-0.006933
0.078000	0.013476	0.245623	-0.003303	0.006292	-0.003774
0.082000	0.012698	0.247871	-0.004846	0.004278	-0.002119
0.086000	0.011750	0.249254	-0.006415	0.001450	0.001223
0.090000	0.010653	0.249895	-0.007895	0.000149	0.004464
0.094000	0.009441	0.250000	-0.008794		
0.098000	0.008155	0.249895	-0.009692		

Table B.2: Coordinates of groove on upper surface of the unconventional airfoil

x [m]	y [m]
0.058000	0.014982
0.057973	0.011807
0.061922	0.011745
0.065838	0.011600
0.069728	0.011337
0.073599	0.010925
0.077462	0.010347
0.081329	0.009595
0.085210	0.008675
0.089115	0.007604
0.093048	0.006412
0.097014	0.005137
0.101014	0.003827
0.102000	0.006845

B.2 Engineering Drawings

Excerpts from the engineering drawings of the airfoil and the bottom-surface cover-plates are provided in Figures B.2 through B.6. The airfoil components were manufactured from a machinable fibreglass material (Green Glass G-10), with a surface-finish level of 16.

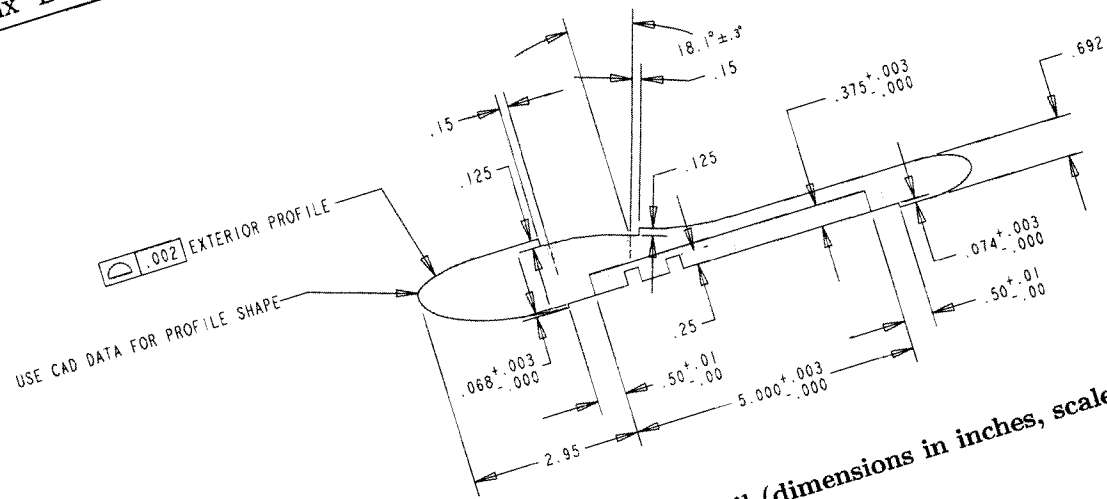


Figure B.2: Side view of the unconventional airfoil (dimensions in inches, scale=0.30)

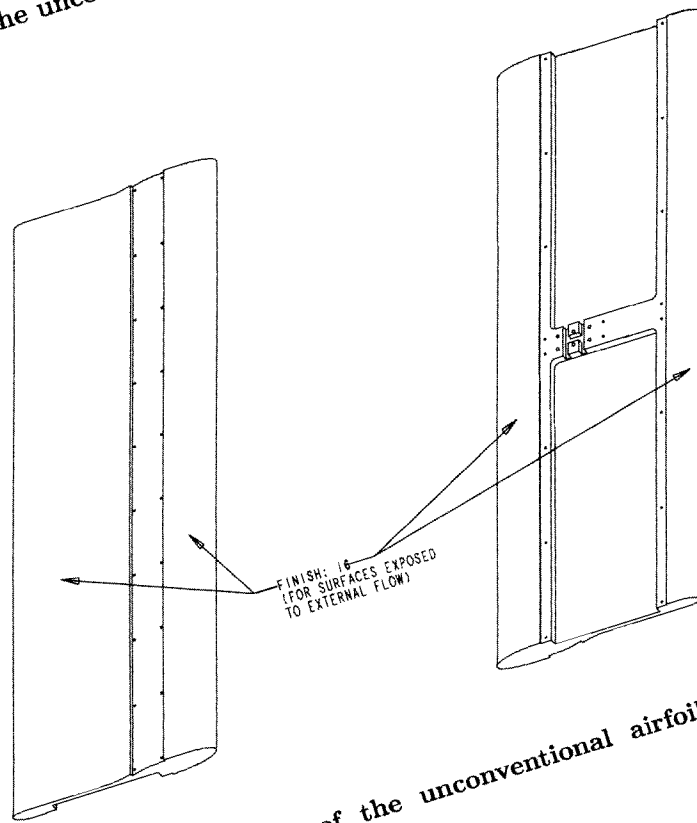


Figure B.3: Isometric views of the unconventional airfoil (dimensions in inches, scale=0.125)

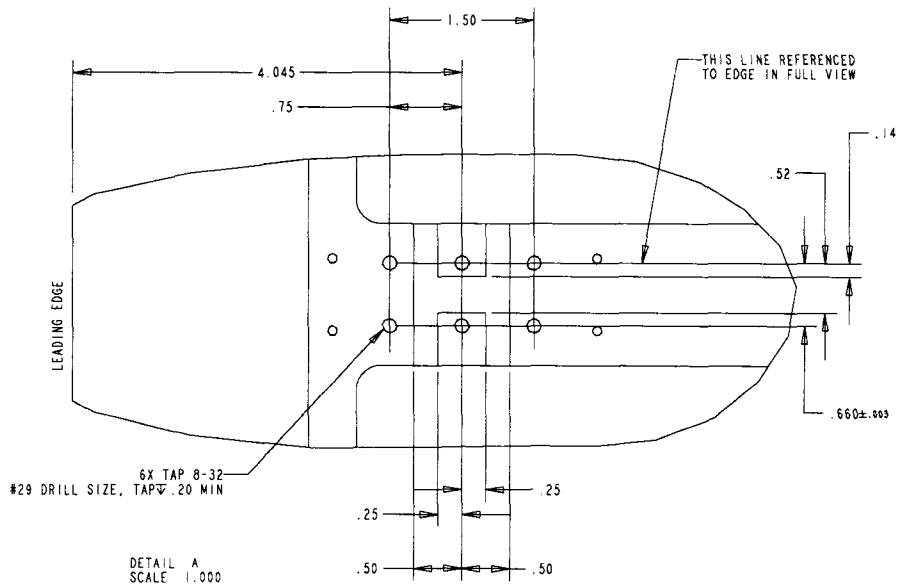


Figure B.5: Detail for the mounting-hole and wire-passage arrangements of the unconventional airfoil (dimensions in inches, scale=0.50)

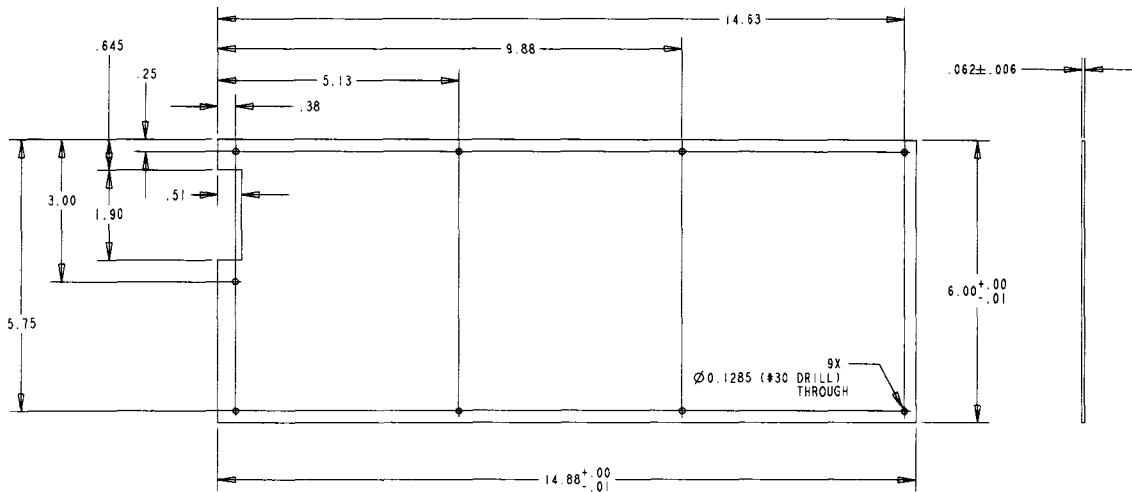


Figure B.6: Lower-surface cover plate for the unconventional airfoil; two required (dimensions in inches, scale=0.125)

Appendix C

Simulation Boundary Details

This appendix provides the upper-domain shapes and the boundary conditions used for the direct numerical simulations documented in Chapter 7. The polynomials that define the upper-domain shapes are provided in Section C.1, the inlet-velocity boundary conditions are provided in Section C.2, and the pressure distributions applied to the upper-domain boundaries are provided in Section C.3.

C.1 Upper Domain Shapes

As described in Chapter 4, the shapes of the upper-domain surfaces for the two simulations were selected to ensure outflow over the domain length, and consist of various flat and polynomial-shaped segments. Tables C.1 and C.2 provide the polynomial coefficients for these shapes, corresponding to the following equation:

$$y = c_0 + c_1x + c_2x^2 + c_3x^3 + \dots + c_nx^n \quad (\text{C.1})$$

where n is the polynomial order. The domain shapes for the low- and elevated-freestream-turbulence simulations were shown in Figures 4.3 (page 68) and 4.4 (page 70), respectively.

Table C.1: Upper-surface polynomial coefficients for low- Tu simulation in units of metres

Segment	$0.40 \leq x \leq 0.45$	$0.45 \leq x \leq 0.56$	$0.56 \leq x \leq 0.71$	$0.71 \leq x \leq 0.78$
c_0	0.117	0.036	-2769.475945016	0.030
c_1	-0.360	0	31046.04330950	0
c_2	0.400	0	-148743.6976074	0
c_3	0	0	394810.1799511	0
c_4	0	0	-627002.2347829	0
c_5	0	0	595768.1086624	0
c_6	0	0	-313611.9253012	0
c_7	0	0	70553.88345707	0

Table C.2: Upper-surface polynomial coefficients for elevated- Tu simulation in units of metres (segments for $0.45 \leq x \leq 0.78$ same as those in Table C.1)

Segment	$-0.325 \leq x \leq 0.12$	$0.12 \leq x \leq 0.45$
c_0	0.072	0.053642841
c_1	0	0.315178514
c_2	0	-1.662168885
c_3	0	1.943660092

C.2 Inlet Velocity Conditions

An experimentally-measured velocity profile was used for the inlet boundary condition of the low-freestream-turbulence simulation, with a slight modification. The profile corresponds to a distance of $x = 0.40$ m from the flat-plate leading edge in the experiments. Figure C.1 shows the velocity profile used for specification of the streamwise velocity component, u , at the domain inlet, and the corresponding values are tabulated in Table C.3. The ANSYS-CFX solver linearly interpolates the specified distribution over the boundary mesh. A constant velocity was specified between the boundary-layer edge and the upper domain surface, as the velocity profile was measured only up to a height of 5.5 mm from the surface.

Although streamline curvature of the accelerating and decelerating freestream flow would provide a component of wall-normal velocity, v , at the plane for which the inlet boundary is located, the wall-normal velocity was specified as zero over this inlet plane. The use of single-point hot-wire measurements provide only the velocity magnitude and not the flow direction,

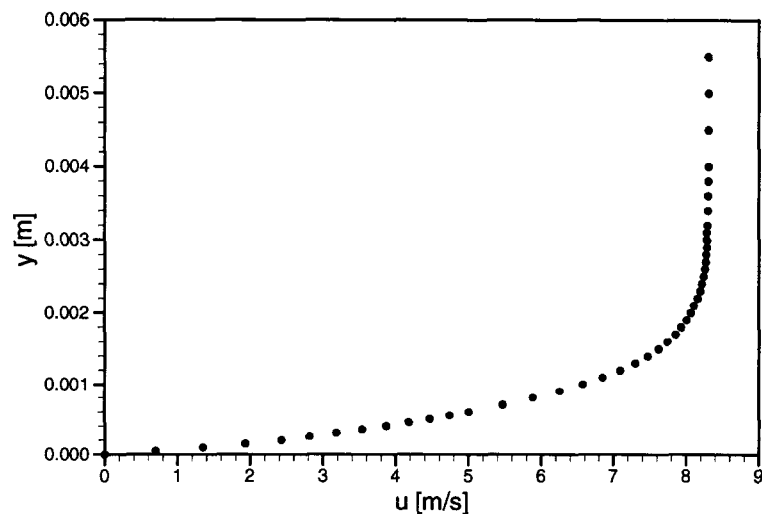


Figure C.1: Velocity distribution specified on inlet boundary for low- Tu simulation

Table C.3: Velocity distribution specified on inlet boundary for low- Tu simulation

y [mm]	u [m/s]	y [mm]	u [m/s]	y [mm]	u [m/s]
0.00	0.00000	1.00	6.57214	2.60	8.25664
0.05	0.70000	1.10	6.85119	2.70	8.26775
0.10	1.35000	1.20	7.09183	2.80	8.27270
0.15	1.93000	1.30	7.30044	2.90	8.28227
0.20	2.42757	1.40	7.47080	3.00	8.28383
0.25	2.81282	1.50	7.61810	3.10	8.28627
0.30	3.18129	1.60	7.74093	3.20	8.29531
0.35	3.53358	1.70	7.85105	3.40	8.30148
0.40	3.86505	1.80	7.93267	3.60	8.30051
0.45	4.17814	1.90	8.00810	3.80	8.30297
0.50	4.47003	2.00	8.06598	4.00	8.30428
0.55	4.74402	2.10	8.10879	4.50	8.30785
0.60	5.00626	2.20	8.15946	5.00	8.30836
0.70	5.47223	2.30	8.19365	5.50	8.30836
0.80	5.88567	2.40	8.21564	38.00	8.30836
0.90	6.25309	2.50	8.23825		

therefore the measurements themselves could not provide evidence to support this zero- v assumption. To ensure that this assumption would provide a reasonable approximation to the actual velocity profile in the experiments, a two-dimensional simulation representing the flow from the plate leading-edge to a location slightly downstream of the suction peak was performed. The use of a streamwise pressure distribution applied to the upper domain surface was used in the same manner as the full simulation. Results of this two-dimensional simulation showed that the wall-normal velocity expected within the boundary layer is no greater than 0.14% of the streamwise component, with a direction away from the wall. This simulation also provided evidence that the wall-normal velocity expected near the

upper domain boundary would be on the order of 1% of the streamwise component, in the downward direction. Thus, it was concluded that the specification of zero- v over the domain inlet plane should provide a good approximation to the true flow-field.

The experimental velocity profile used for specification of the inlet boundary condition was measured over the range 0.25 mm to 5.5 mm. The two-dimensional simulation described above was used to verify whether or not a linear distribution between the wall and 0.25 mm (approximately 5% of the boundary-layer thickness) would provide a reasonable approximation to the velocity profile in this region, which it did not. The two-dimensional simulation results were then used to approximate the profile in this region and provide a more representative velocity distribution near the wall for the three-dimensional simulation.

For the elevated-freestream-turbulence simulation, a constant velocity was specified for each of the 16 openings at the inlet plane of the computational domain. The reference inlet velocity measured above the plate leading-edge in the experiments was 4.24 m/s, which required a velocity of 8.13 m/s at each of the openings to provide this mixed-out velocity downstream of the simulated turbulence grid.

C.3 Streamwise Pressure Distributions

As discussed in Section 4.4.2, the upper domain boundary was set as an outflow boundary-condition with a specified streamwise pressure distribution. The distributions of static pressure applied to the upper domain boundaries are shown in Figure C.2, and tabulated for the two simulations in Tables C.4 and C.5. The reference pressure, p_{ref} , used in the simulations corresponds to 1 atm (101,325 Pa). The static pressure applied to the domain outlet boundaries are those at corresponding streamwise location ($x = 0.78$ m) from Tables C.4 and C.5.

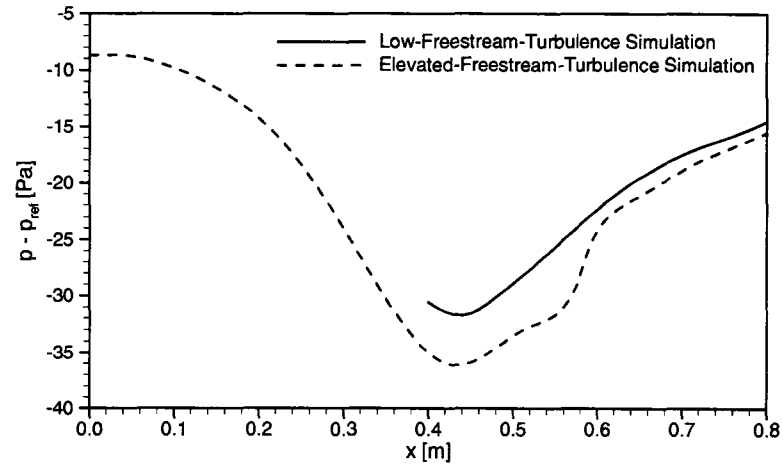


Figure C.2: Static pressure distributions specified on upper domain boundaries

Table C.4: Static pressure distribution specified on upper boundary for low- Tu simulation (gauge pressure)

x [m]	p [Pa]						
0.40	-30.5411	0.50	-28.9100	0.60	-22.3126	0.70	-17.5232
0.41	-31.0188	0.51	-28.2925	0.61	-21.7056	0.71	-17.2002
0.42	-31.4154	0.52	-27.6360	0.62	-21.1234	0.72	-16.8978
0.43	-31.6595	0.53	-26.9657	0.63	-20.5684	0.73	-16.6114
0.44	-31.7084	0.54	-26.2871	0.64	-20.0424	0.74	-16.3357
0.45	-31.5481	0.55	-25.6053	0.65	-19.5466	0.75	-16.0644
0.46	-31.1935	0.56	-24.9253	0.66	-19.0818	0.76	-15.7901
0.47	-30.6879	0.57	-24.2518	0.67	-18.6480	0.77	-15.5048
0.48	-30.1075	0.58	-23.5892	0.68	-18.2447	0.78	-15.1989
0.49	-29.5200	0.59	-22.9416	0.69	-17.8704		

Table C.5: Static pressure distribution specified on upper boundary for elevated- T_u simulation (gauge pressure)

x [m]	p [Pa]						
0.00	-8.7110	0.20	-14.2710	0.40	-34.9846	0.60	-24.2045
0.01	-8.7110	0.21	-14.9752	0.41	-35.5322	0.61	-23.1836
0.02	-8.7110	0.22	-15.7409	0.42	-35.9126	0.62	-22.5016
0.03	-8.6917	0.23	-16.5678	0.43	-36.1026	0.63	-21.9985
0.04	-8.7227	0.24	-17.4444	0.44	-36.0853	0.64	-21.5700
0.05	-8.8088	0.25	-18.3878	0.45	-35.8791	0.65	-21.1555
0.06	-8.9402	0.26	-19.4029	0.46	-35.5198	0.66	-20.7264
0.07	-9.1100	0.27	-20.4868	0.47	-35.0539	0.67	-20.2764
0.08	-9.3134	0.28	-21.6315	0.48	-34.5323	0.68	-19.8129
0.09	-9.5471	0.29	-22.8263	0.49	-34.0042	0.69	-19.3501
0.10	-9.8094	0.30	-24.0586	0.50	-33.5109	0.70	-18.9034
0.11	-10.0995	0.31	-25.3144	0.51	-33.0790	0.71	-18.4852
0.12	-10.4177	0.32	-26.5792	0.52	-32.7148	0.72	-18.1023
0.13	-10.7651	0.33	-27.8377	0.53	-32.3974	0.73	-17.7544
0.14	-11.1438	0.34	-29.0735	0.54	-32.0730	0.74	-17.4343
0.15	-11.5564	0.35	-30.2696	0.55	-31.6480	0.75	-17.1294
0.16	-12.0067	0.36	-31.4079	0.56	-30.9833	0.76	-16.8249
0.17	-12.4986	0.37	-32.4691	0.57	-29.8874	0.77	-16.5077
0.18	-13.0368	0.38	-33.4329	0.58	-28.1109	0.78	-16.1730
0.19	-13.6261	0.39	-34.2783	0.59	-25.7949		

Appendix D

Detailed Results of Flow Control Study

This appendix provides the ensemble-averaged results for all cases examined in the flow control study of Chapter 9, along with parameters of interest regarding separation, transition onset, reattachment, and the turbulent boundary layer downstream of reattachment. The clean airfoil results are first provided (CL configuration) followed by all other configurations (ST, SG, LG, SN, SR).

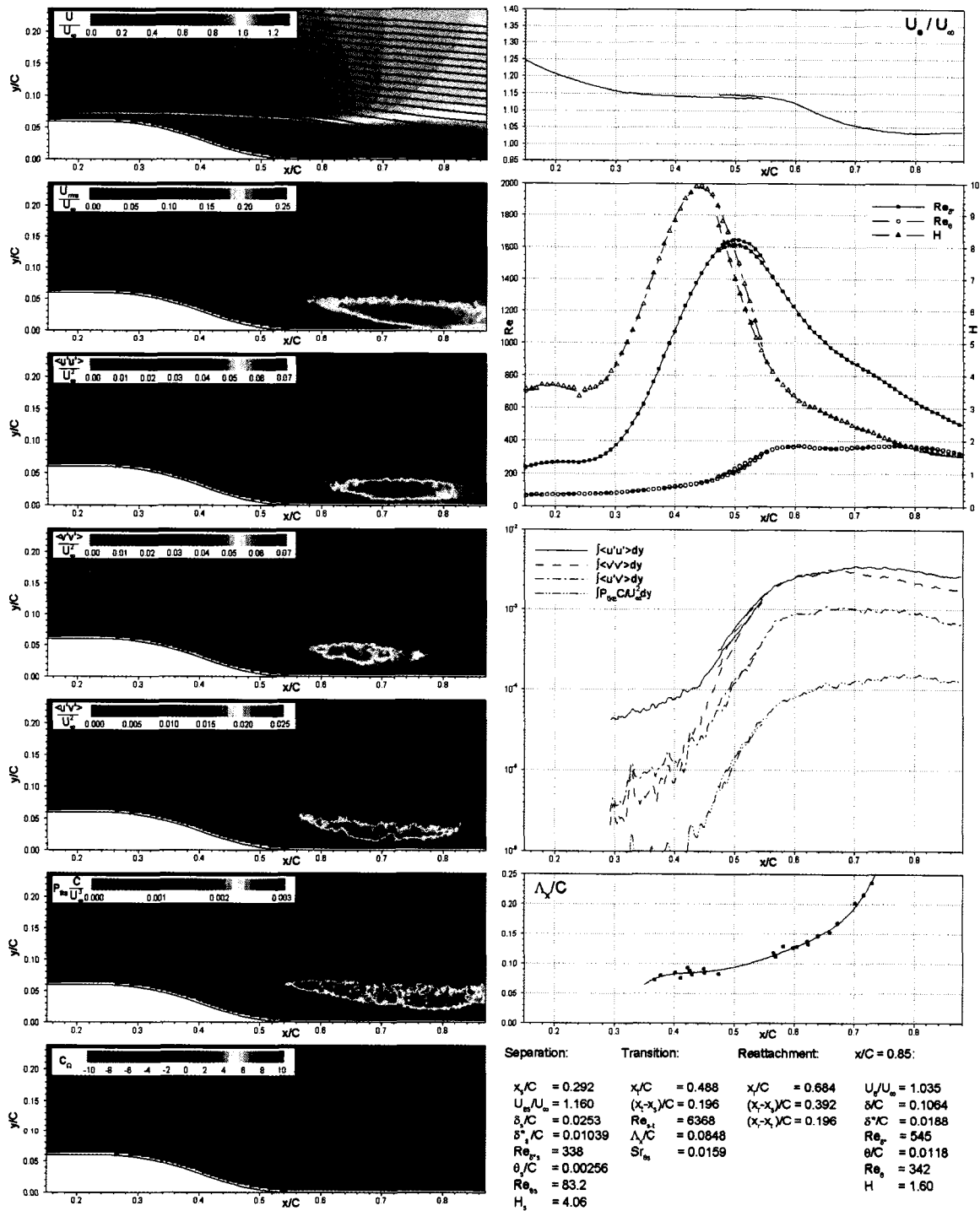


Figure D.1: Detailed results for CL configuration at $Re=28,000$

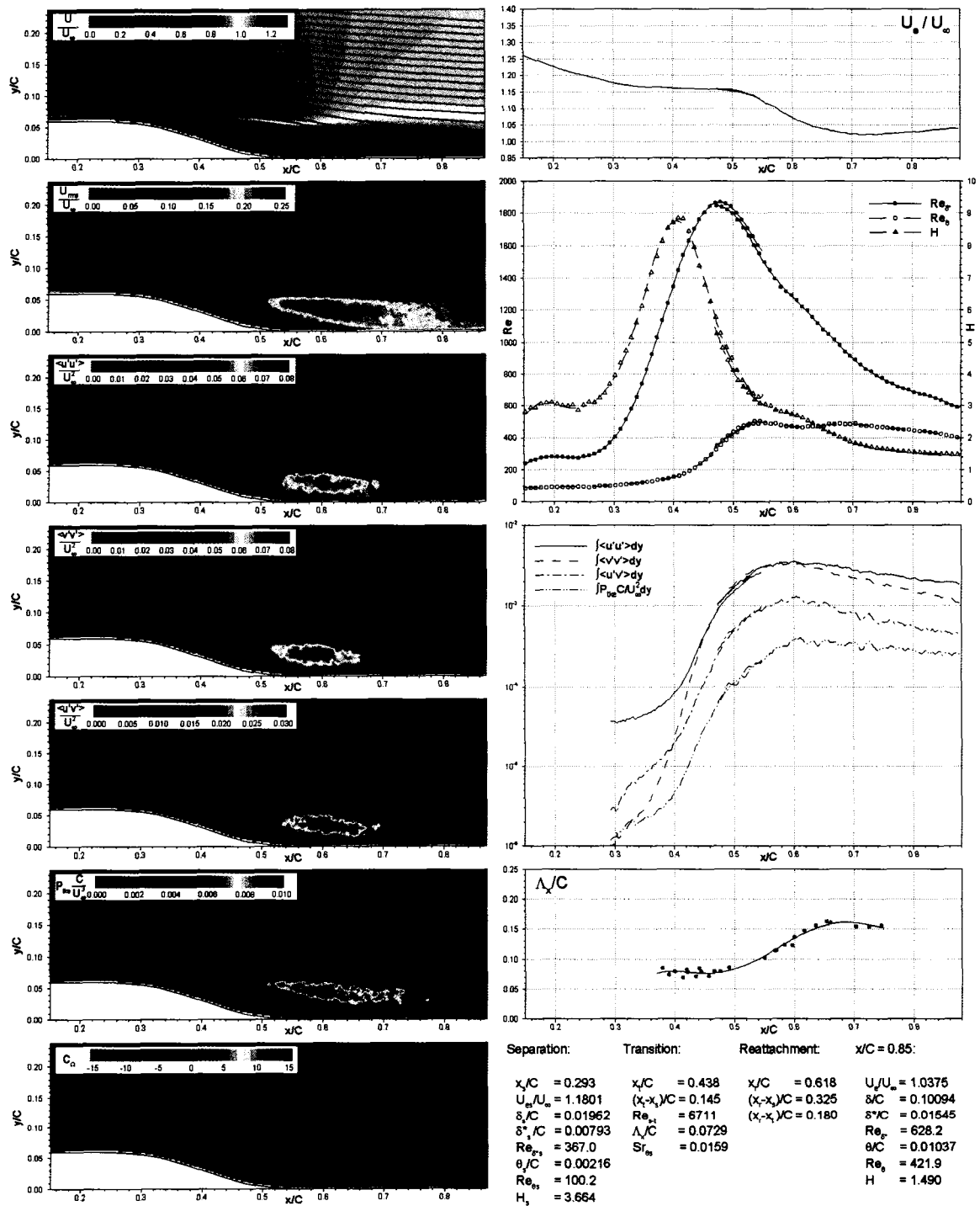


Figure D.2: Detailed results for CL configuration at $Re=39,000$

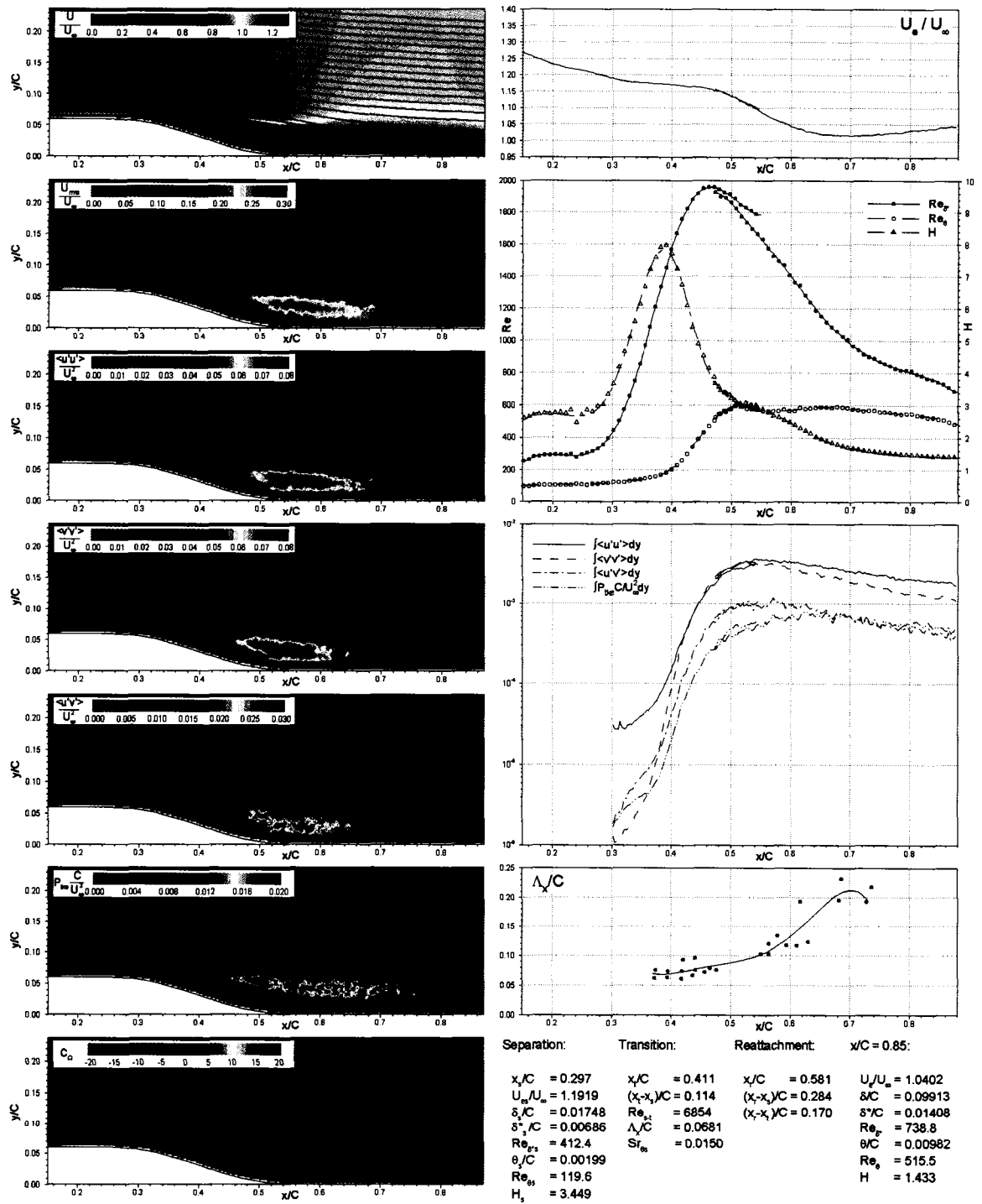


Figure D.3: Detailed results for CL configuration at $Re=51,000$

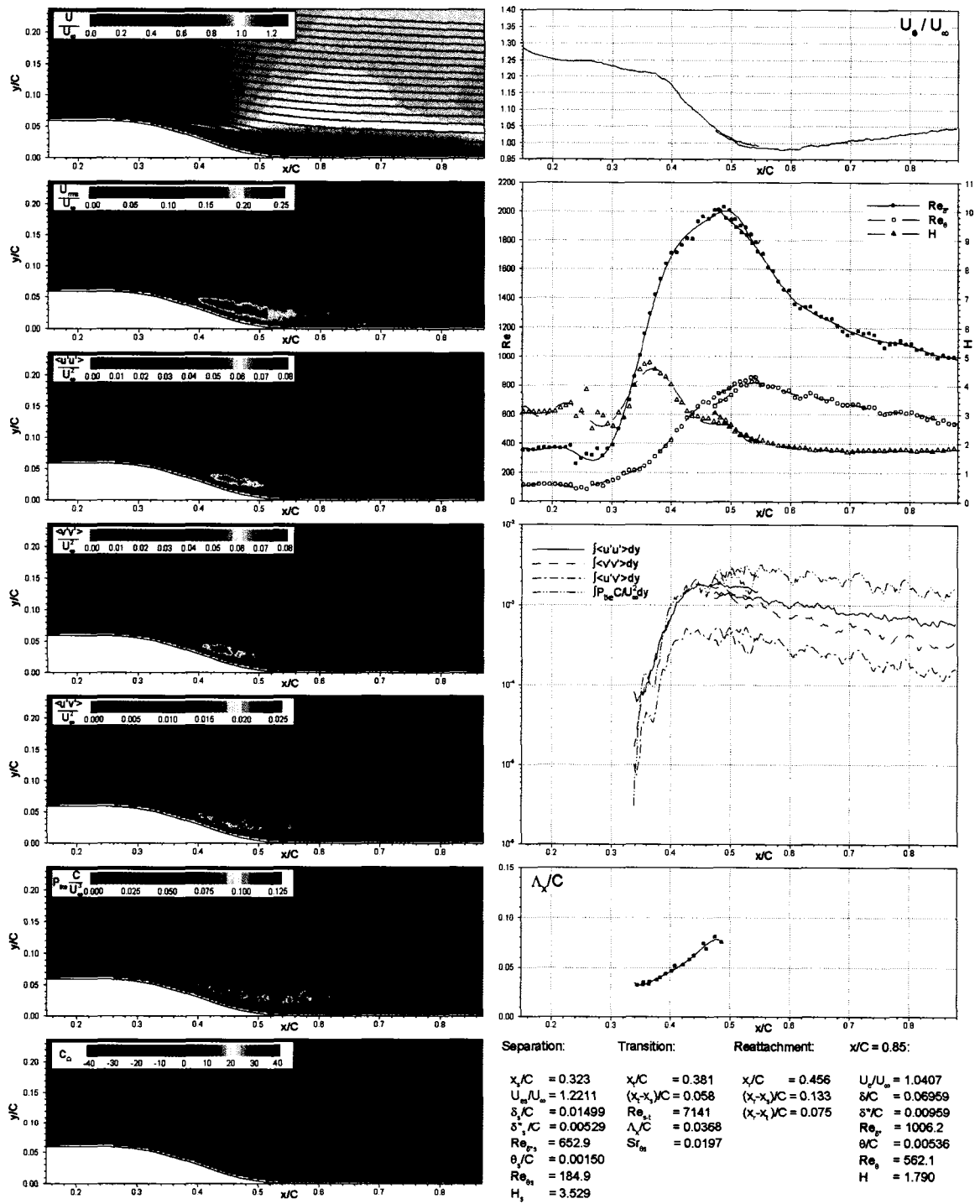


Figure D.4: Detailed results for CL configuration at $Re=101,000$

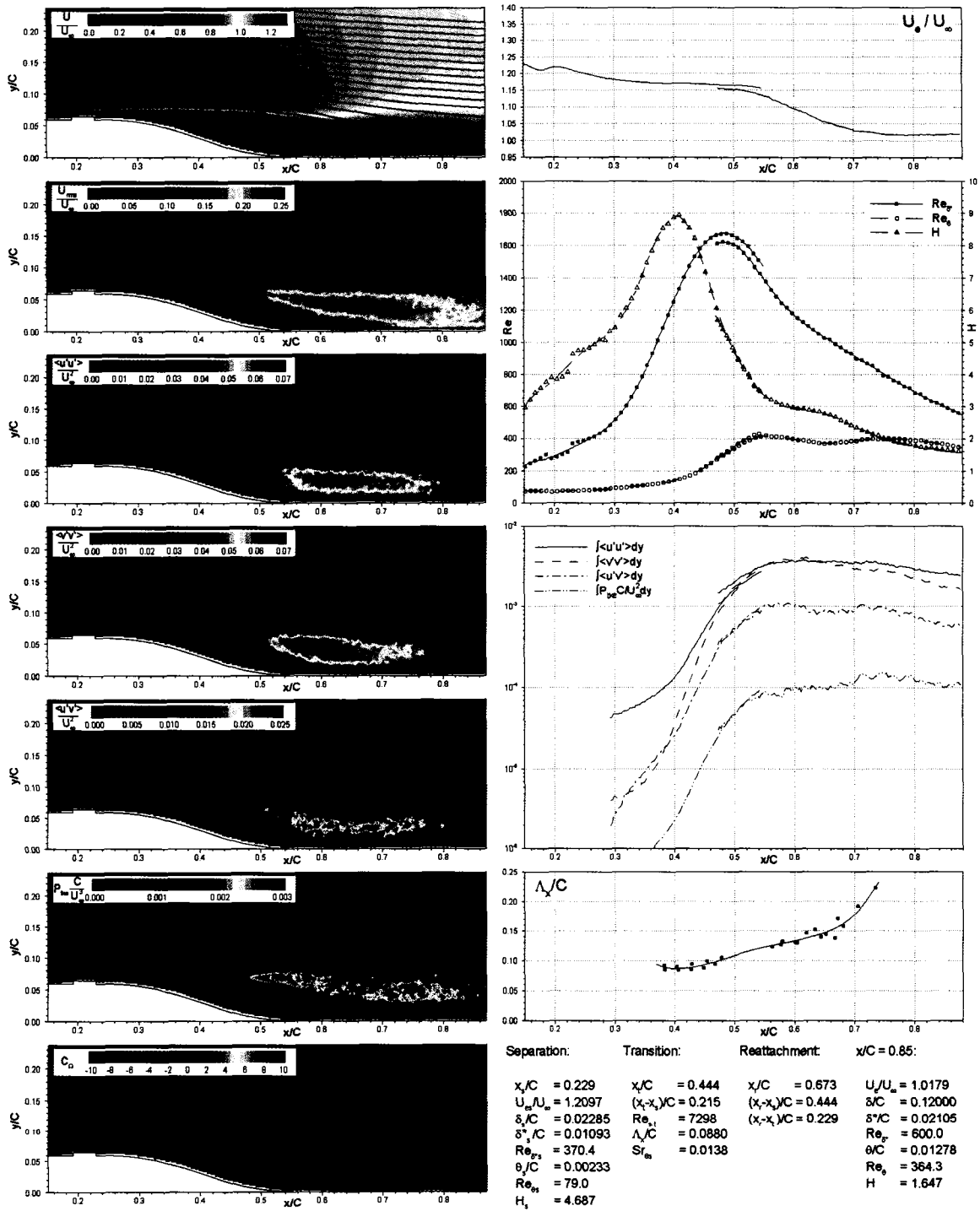


Figure D.5: Detailed results for ST configuration at $Re=28,000$

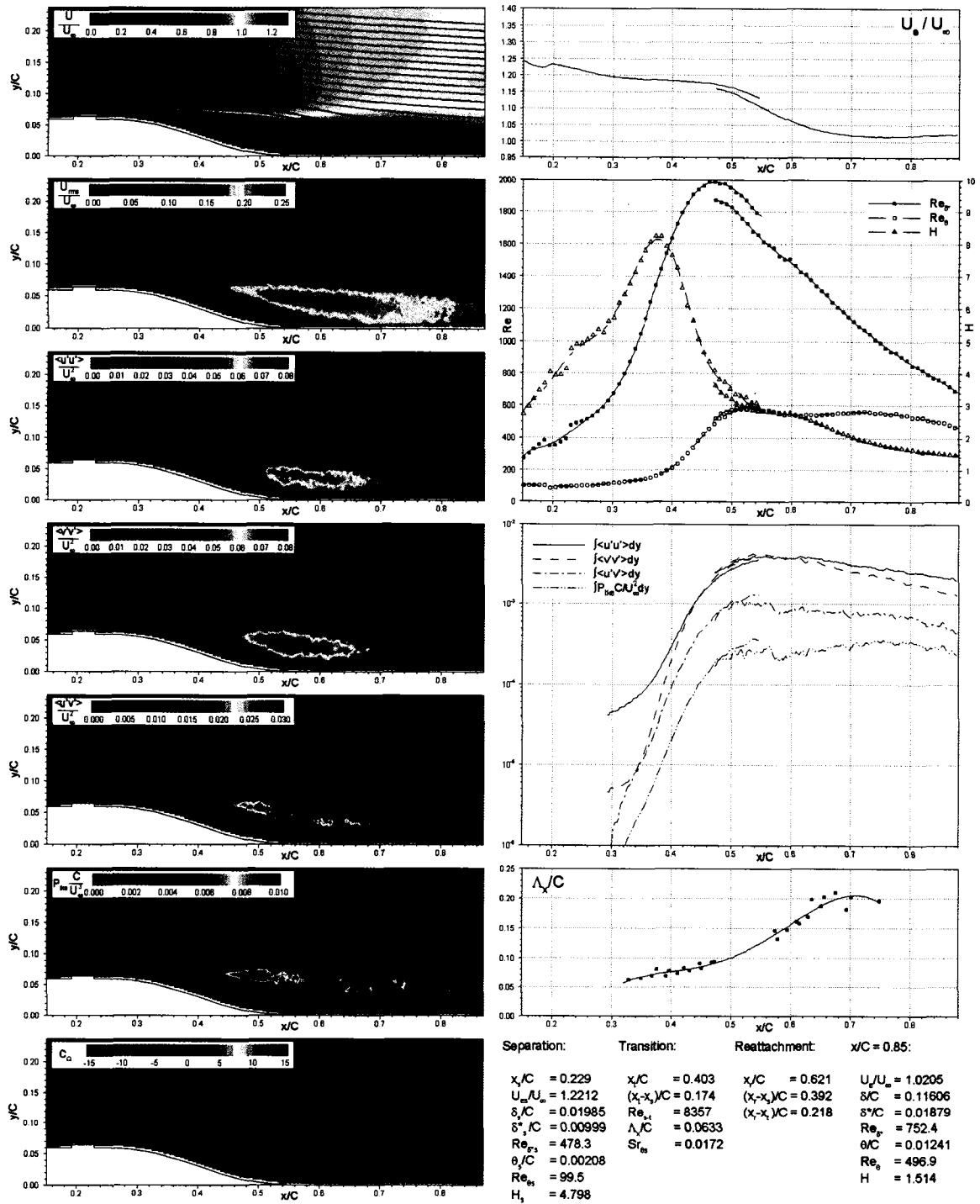


Figure D.6: Detailed results for ST configuration at $Re=39,000$

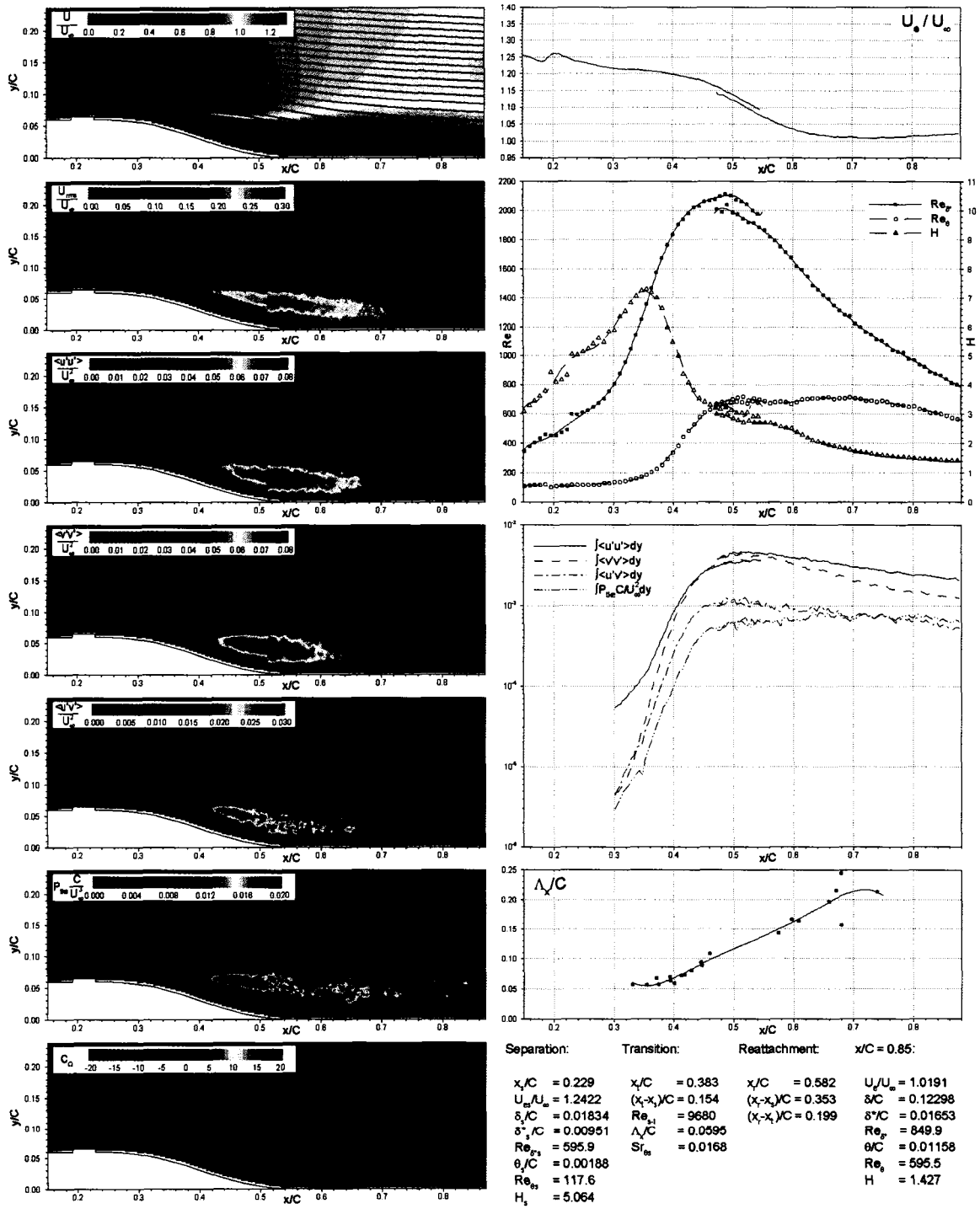


Figure D.7: Detailed results for ST configuration at $Re=51,000$

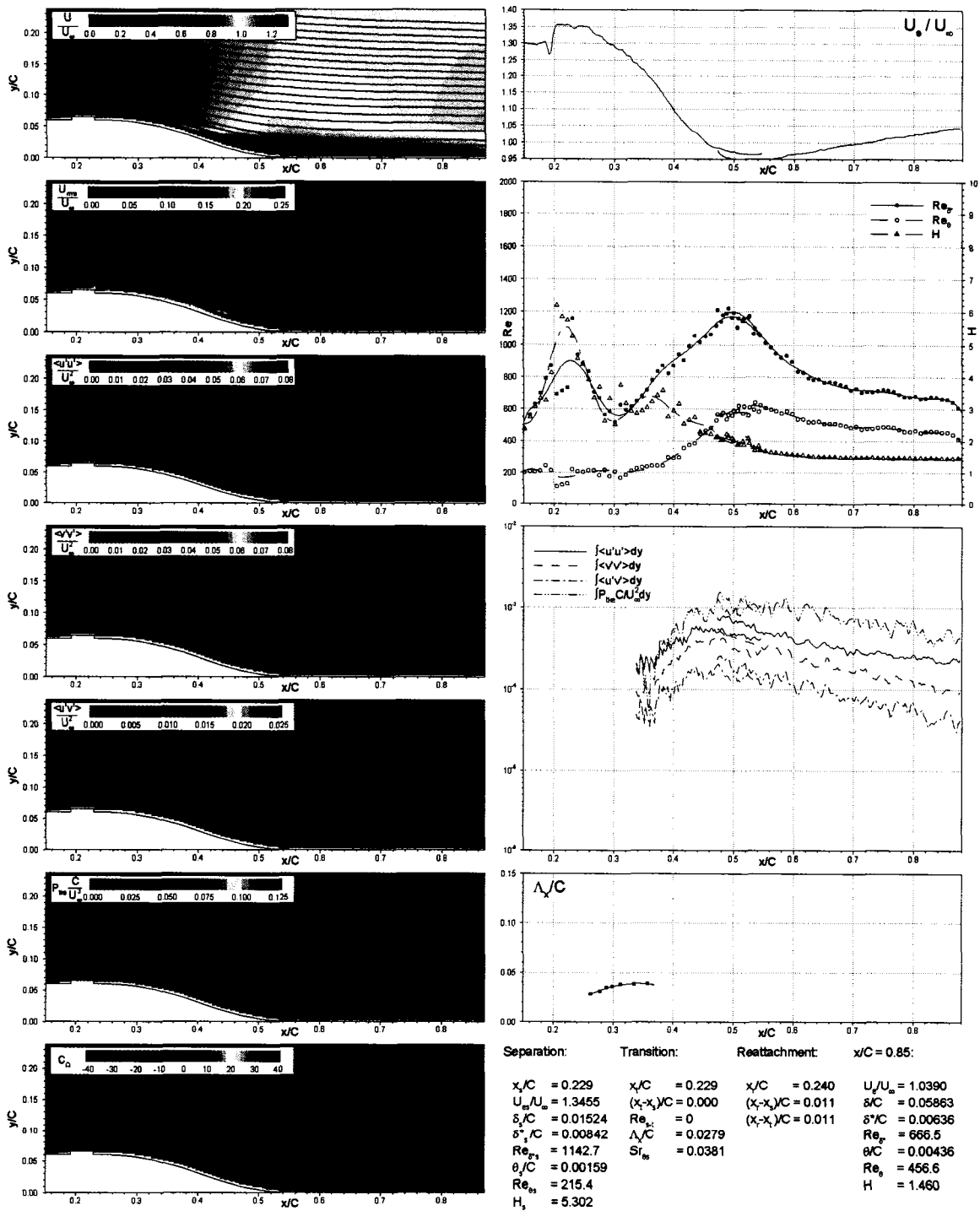


Figure D.8: Detailed results for ST configuration at $Re=101,000$

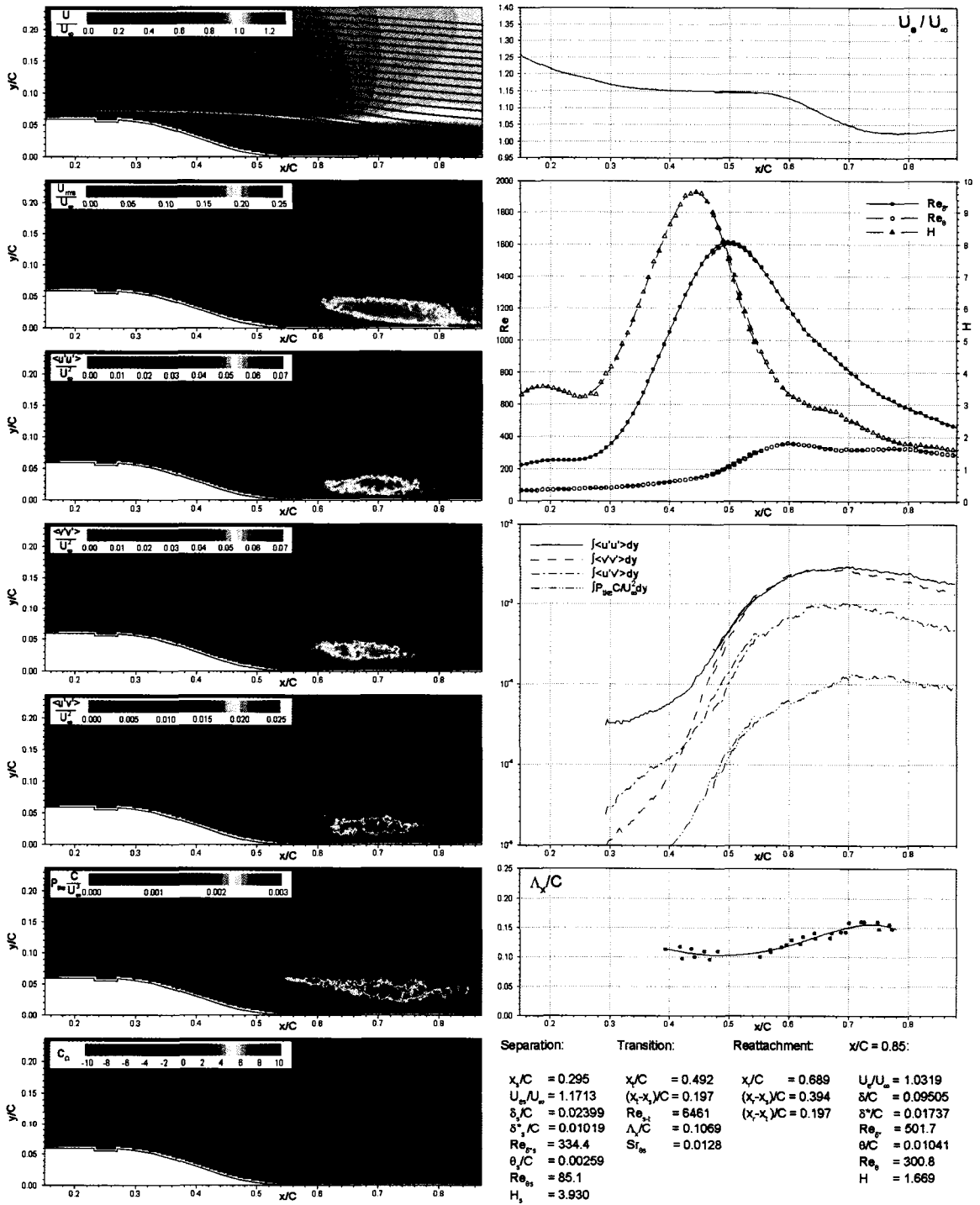


Figure D.9: Detailed results for SG configuration at $Re=28,000$

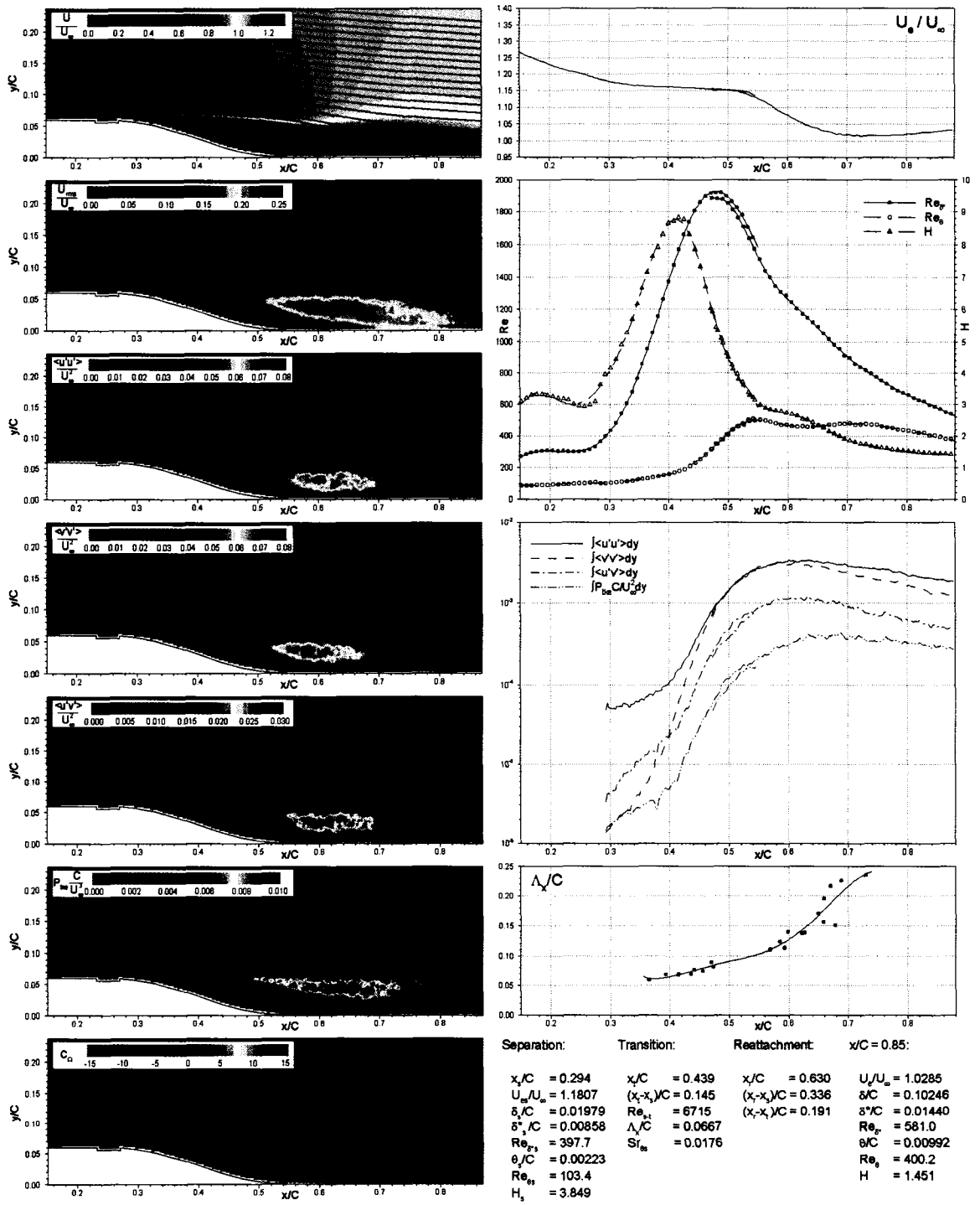


Figure D.10: Detailed results for SG configuration at $Re=39,000$

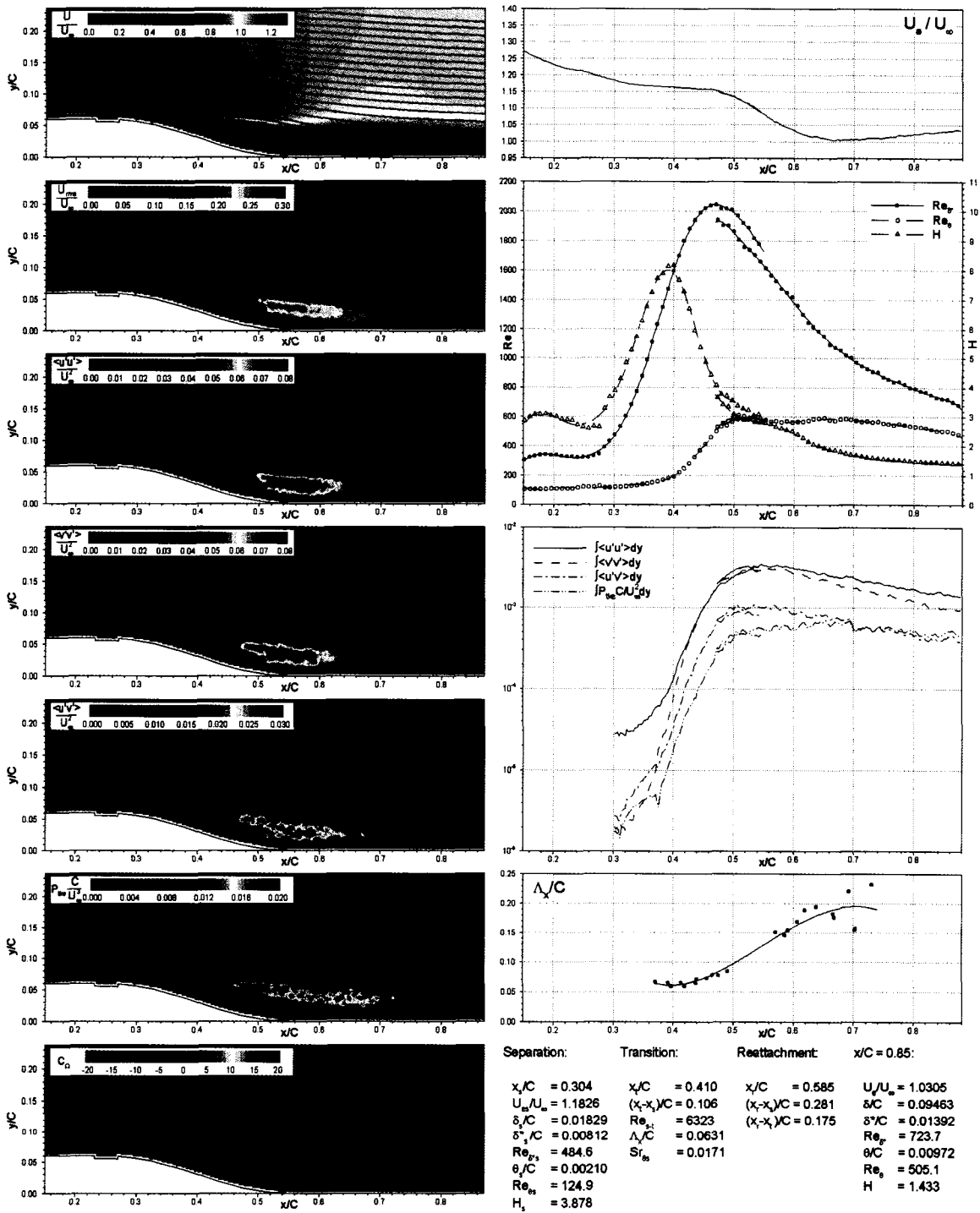


Figure D.11: Detailed results for SG configuration at $Re=51,000$

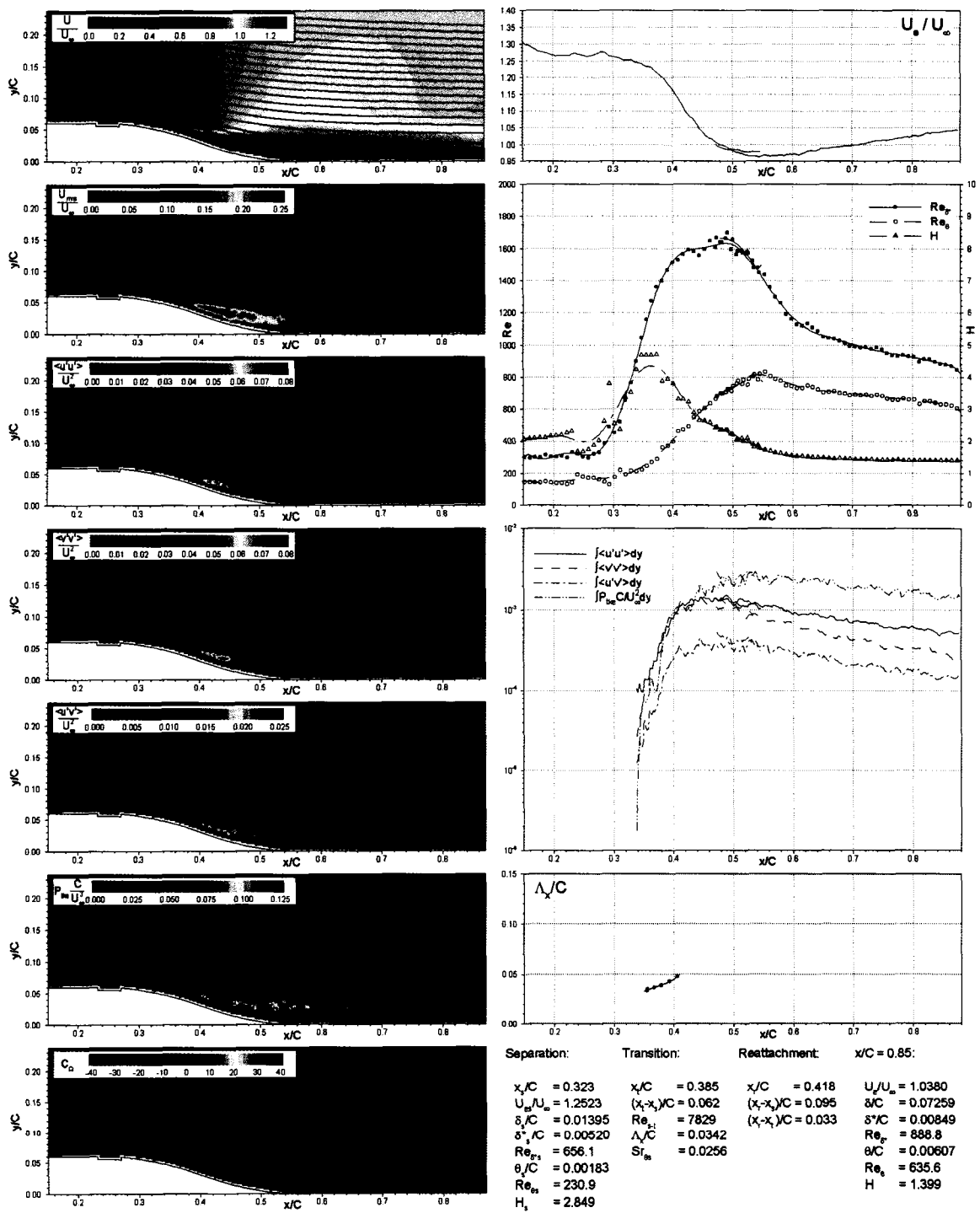


Figure D.12: Detailed results for SG configuration at $Re=101,000$

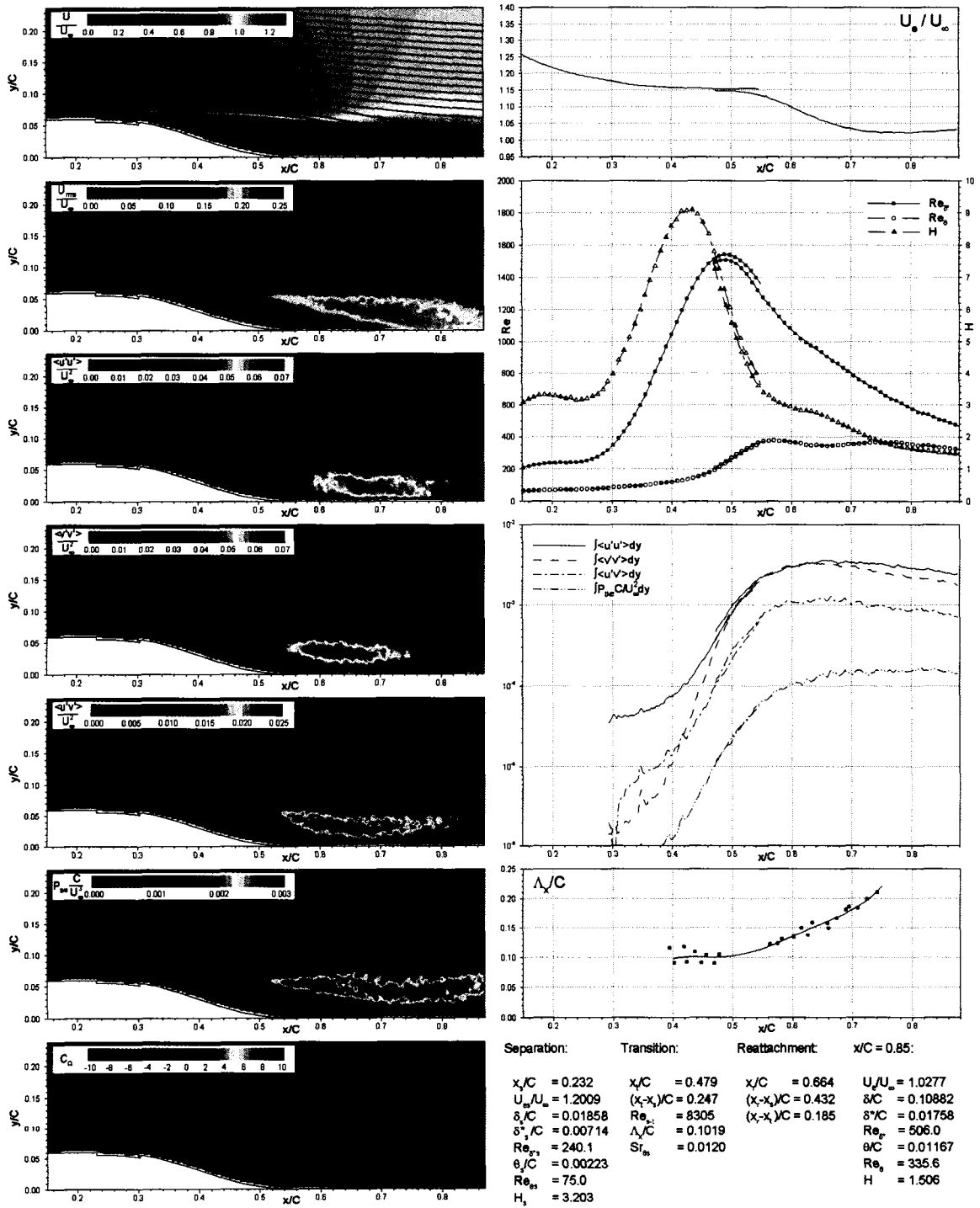


Figure D.13: Detailed results for LG configuration at $Re=28,000$

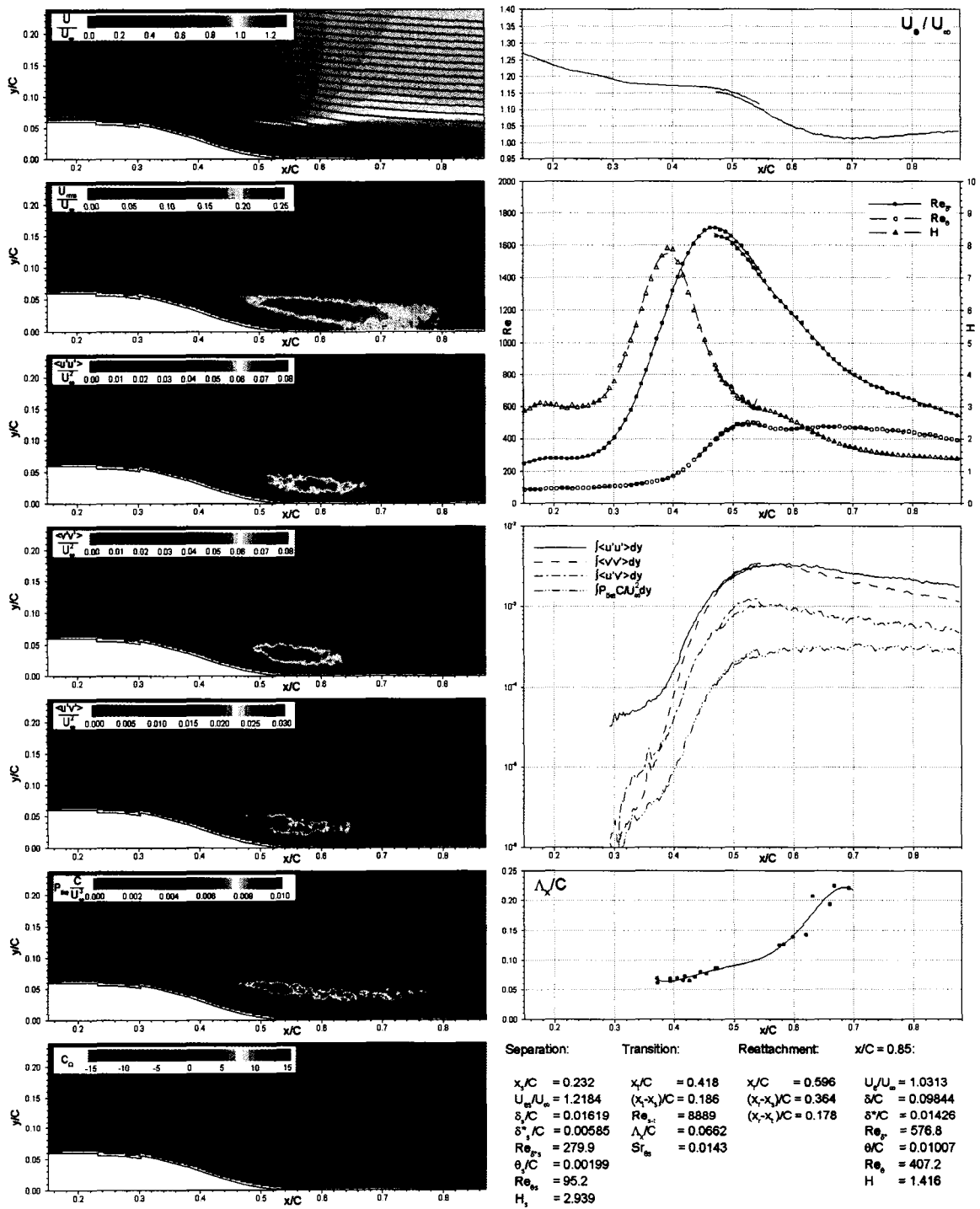


Figure D.14: Detailed results for LG configuration at $Re=39,000$

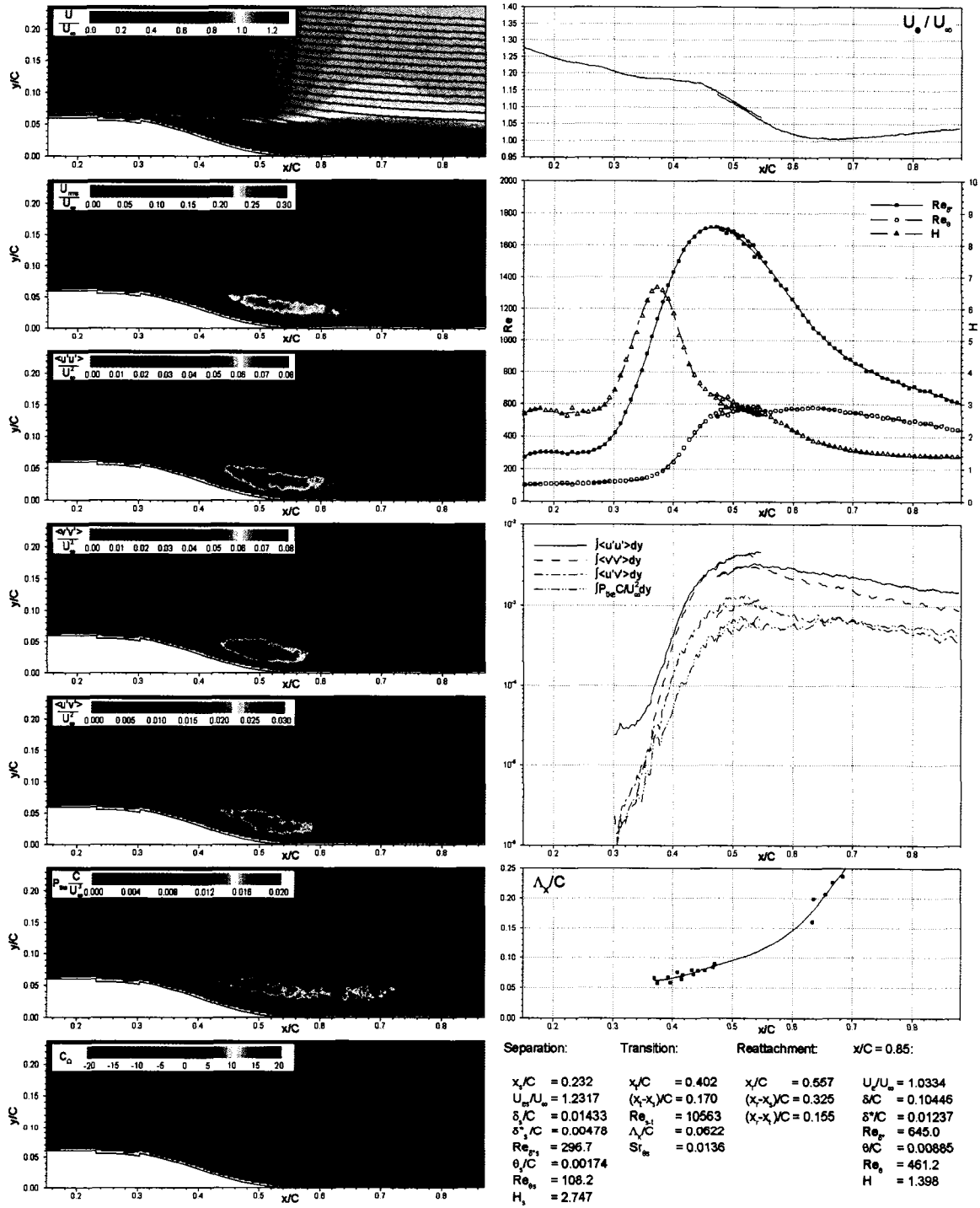


Figure D.15: Detailed results for LG configuration at $Re=51,000$

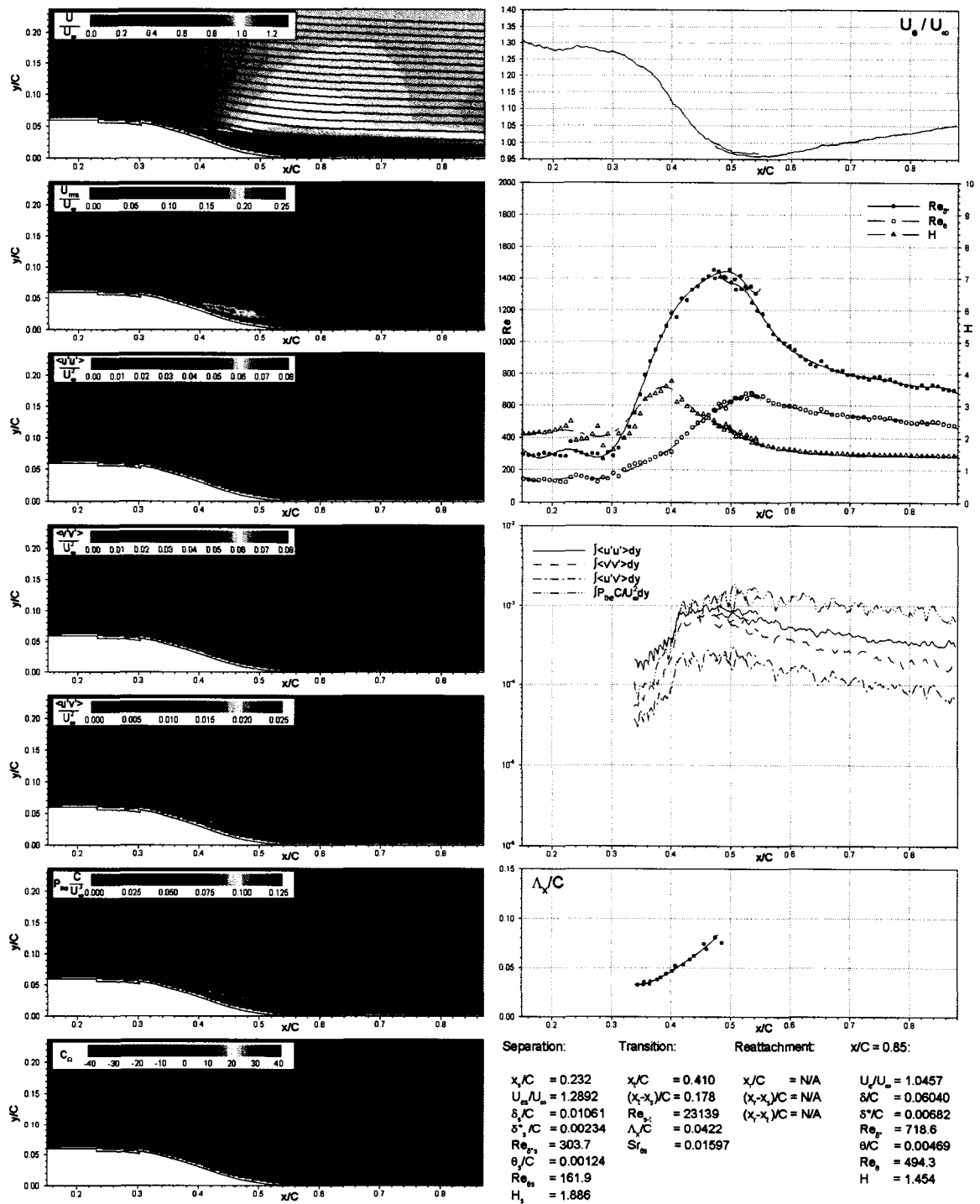


Figure D.16: Detailed results for LG configuration at $Re=101,000$

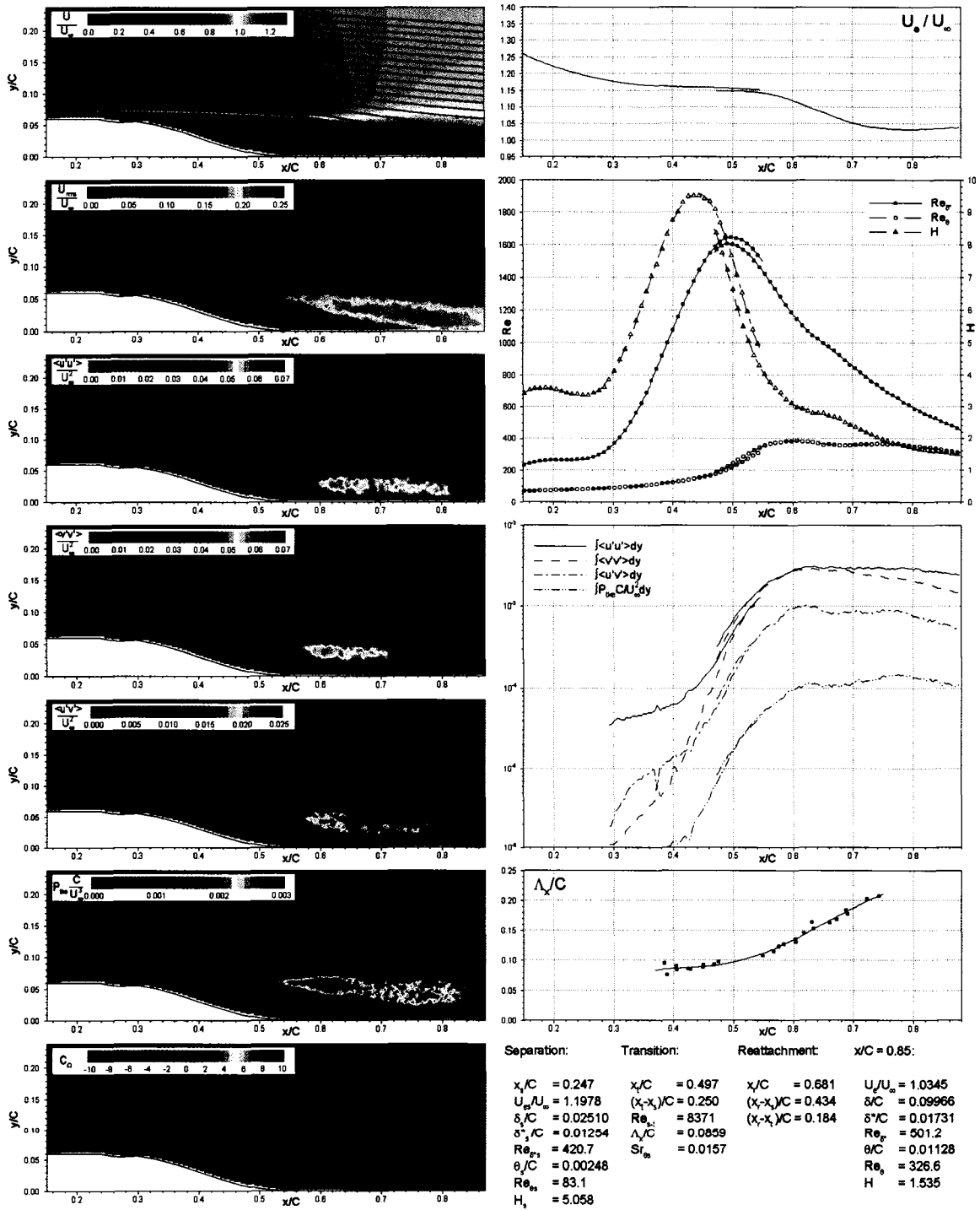


Figure D.17: Detailed results for SN configuration at $Re=28,000$

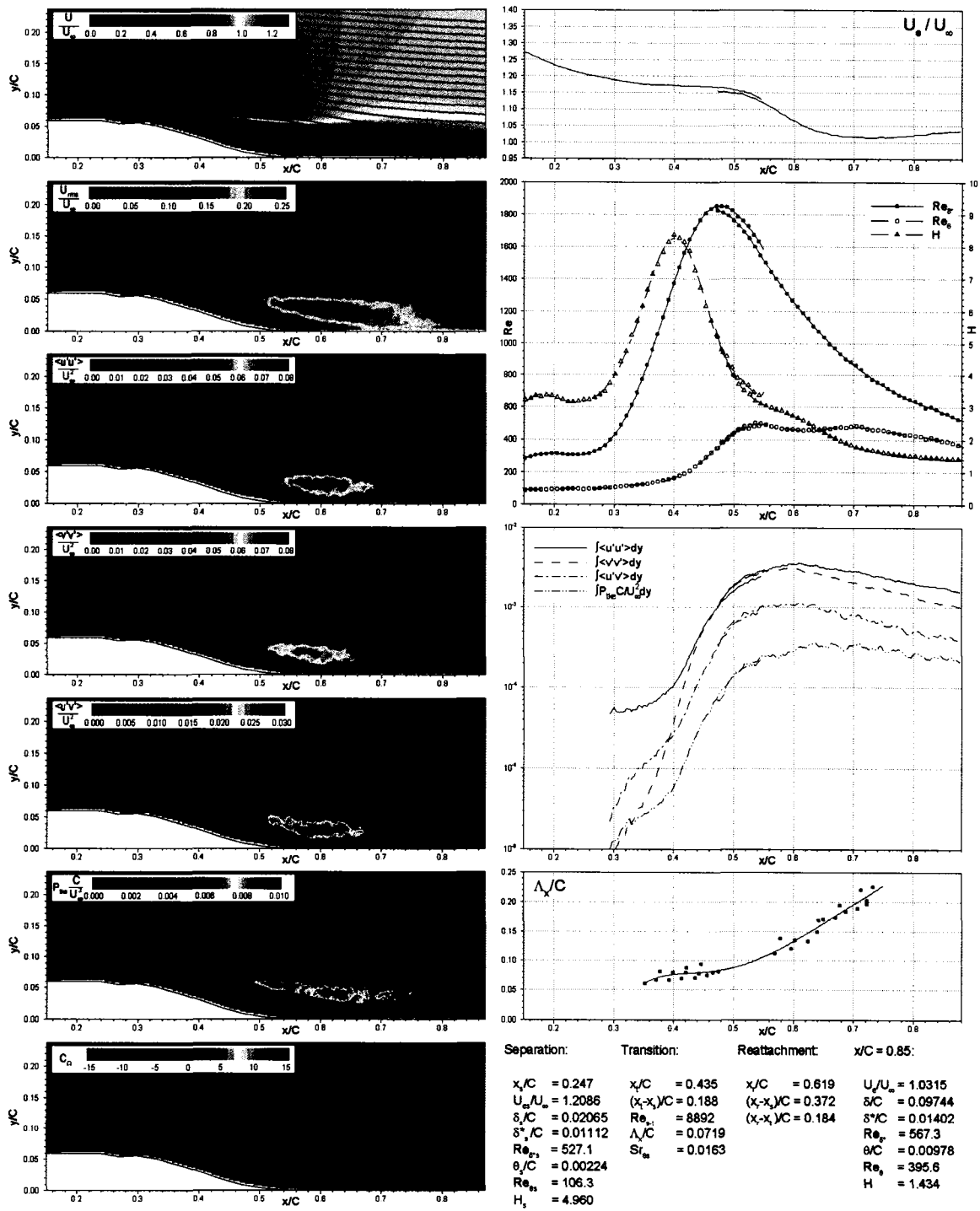


Figure D.18: Detailed results for SN configuration at $Re=39,000$

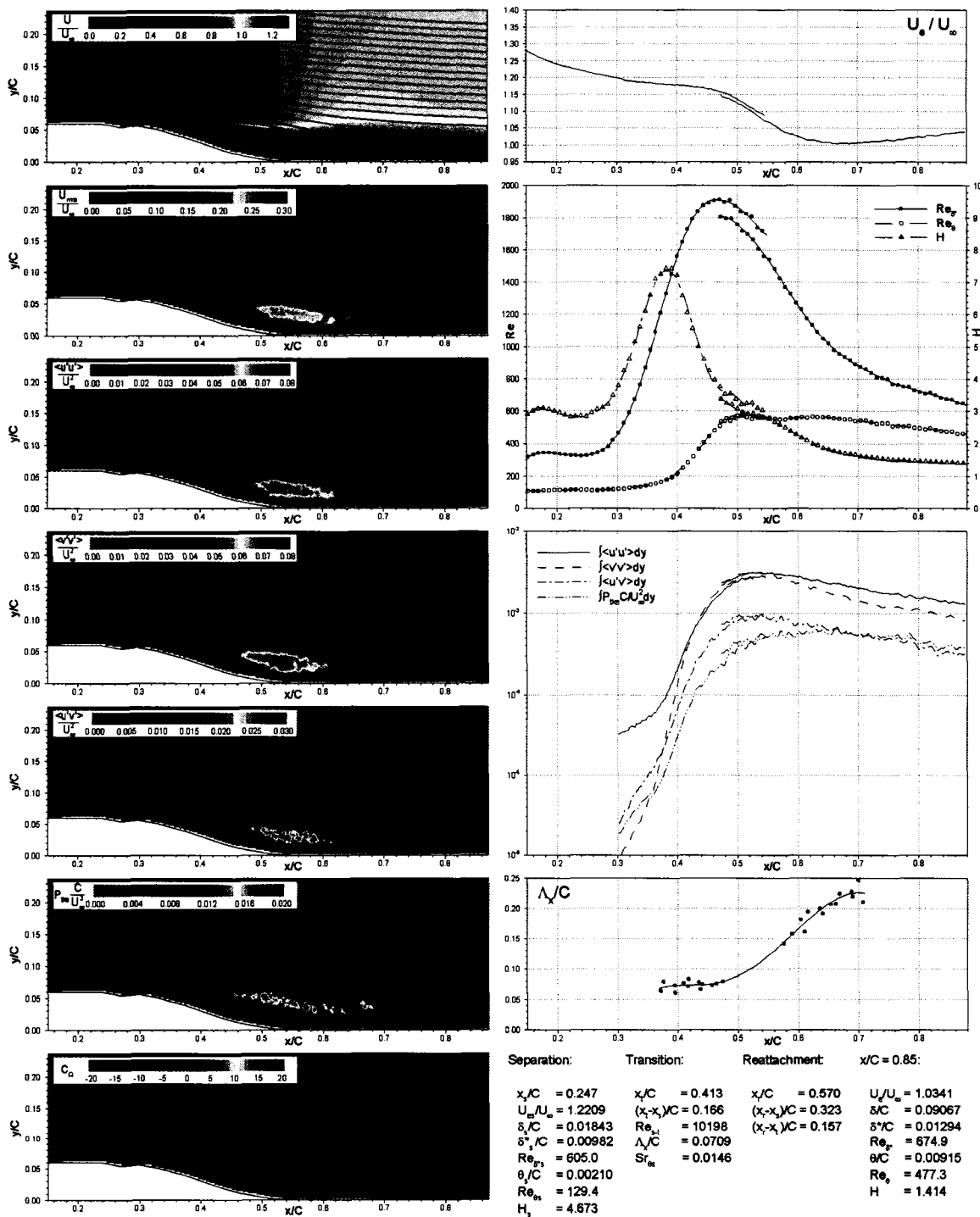


Figure D.19: Detailed results for SN configuration at $Re=51,000$

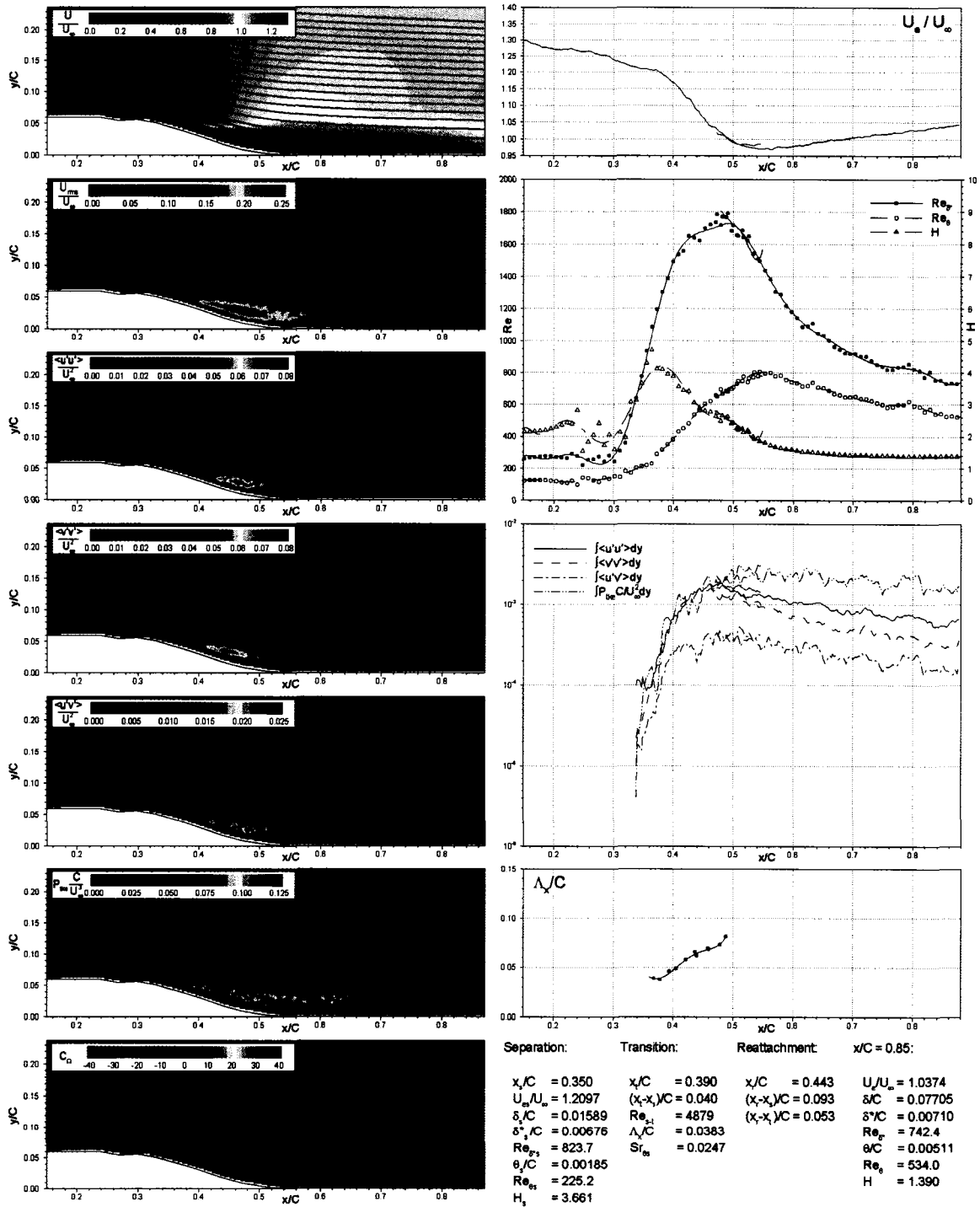


Figure D.20: Detailed results for SN configuration at $Re=101,000$

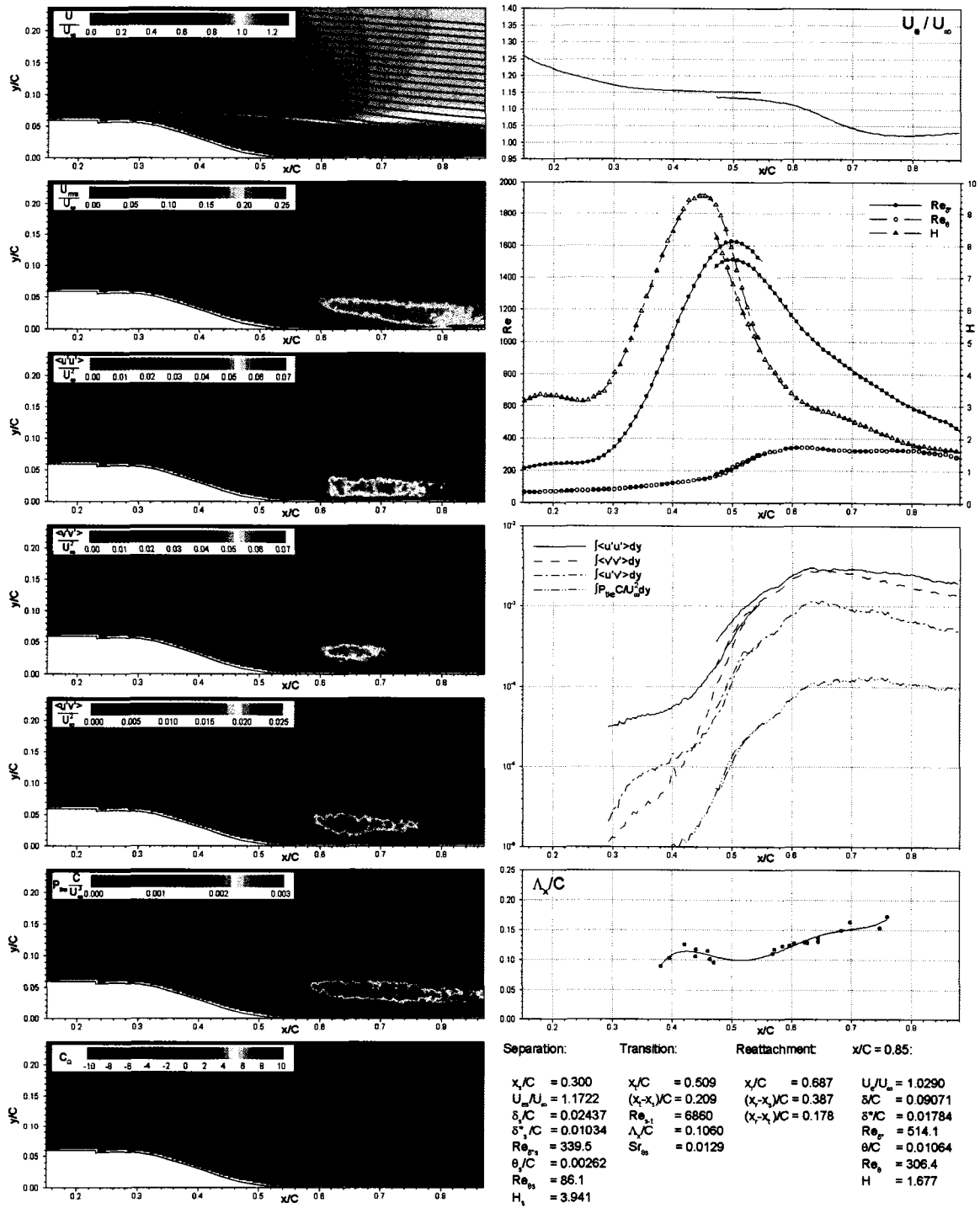


Figure D.21: Detailed results for SR configuration at $Re=28,000$

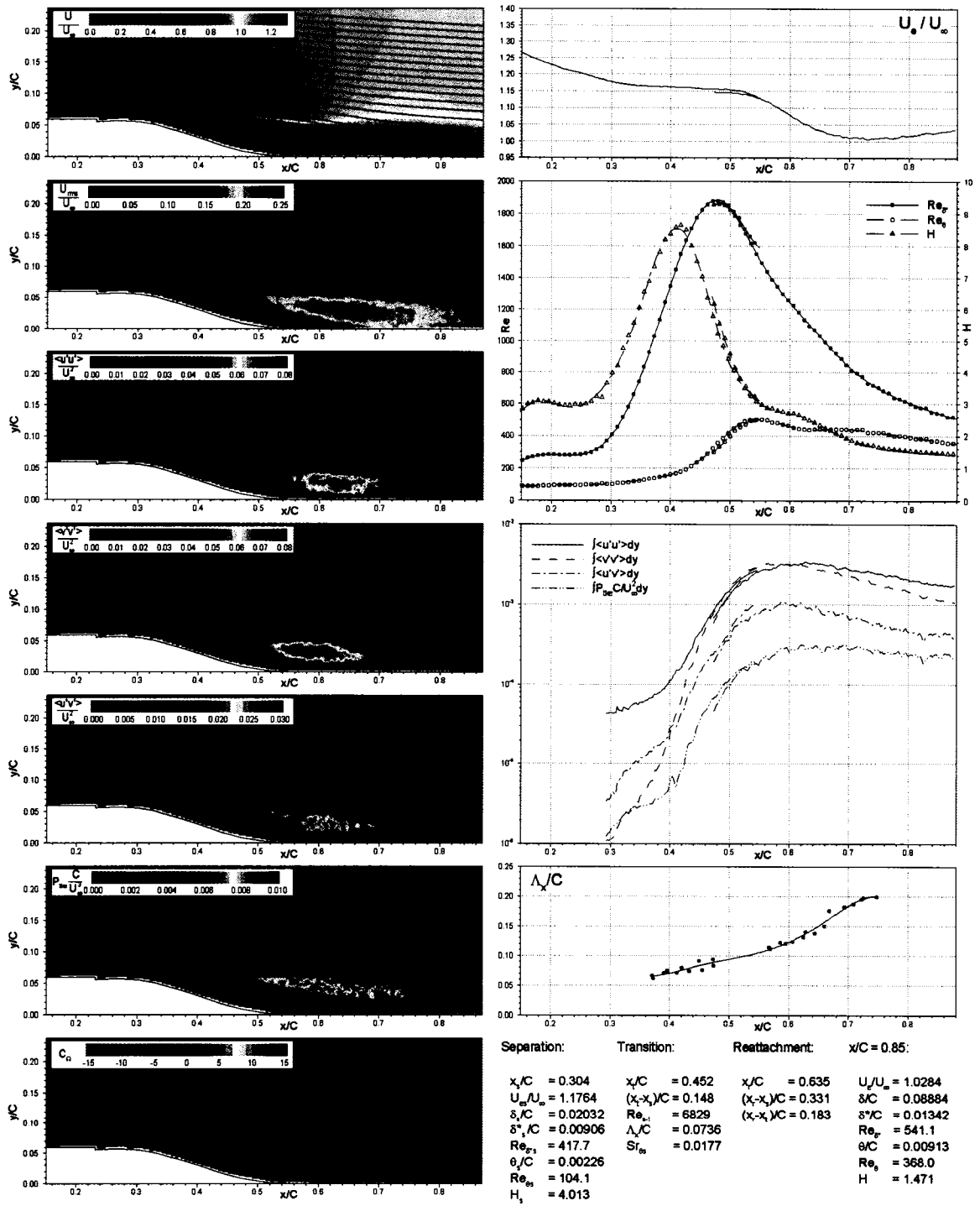


Figure D.22: Detailed results for SR configuration at $Re=39,000$

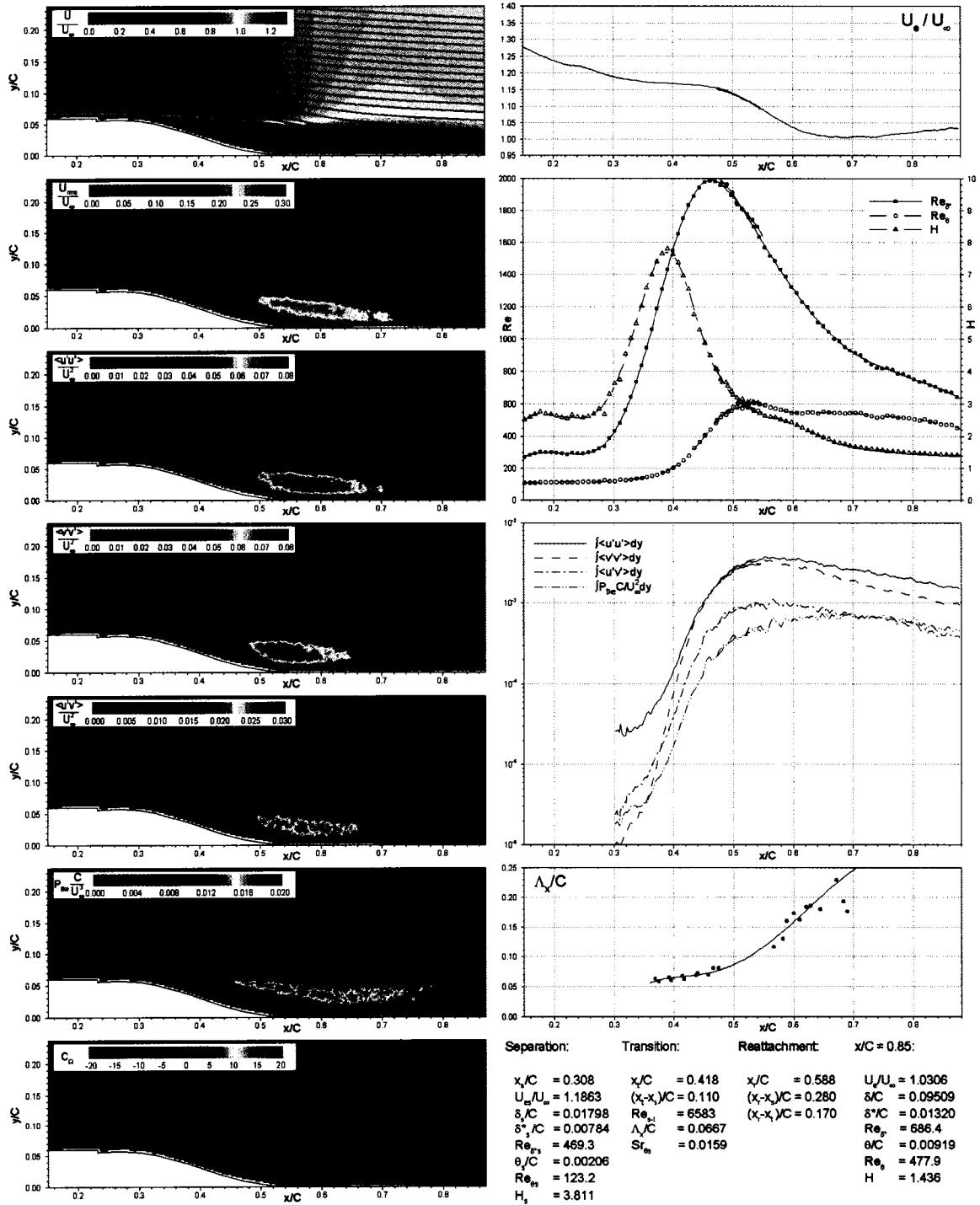


Figure D.23: Detailed results for SR configuration at $Re=51,000$

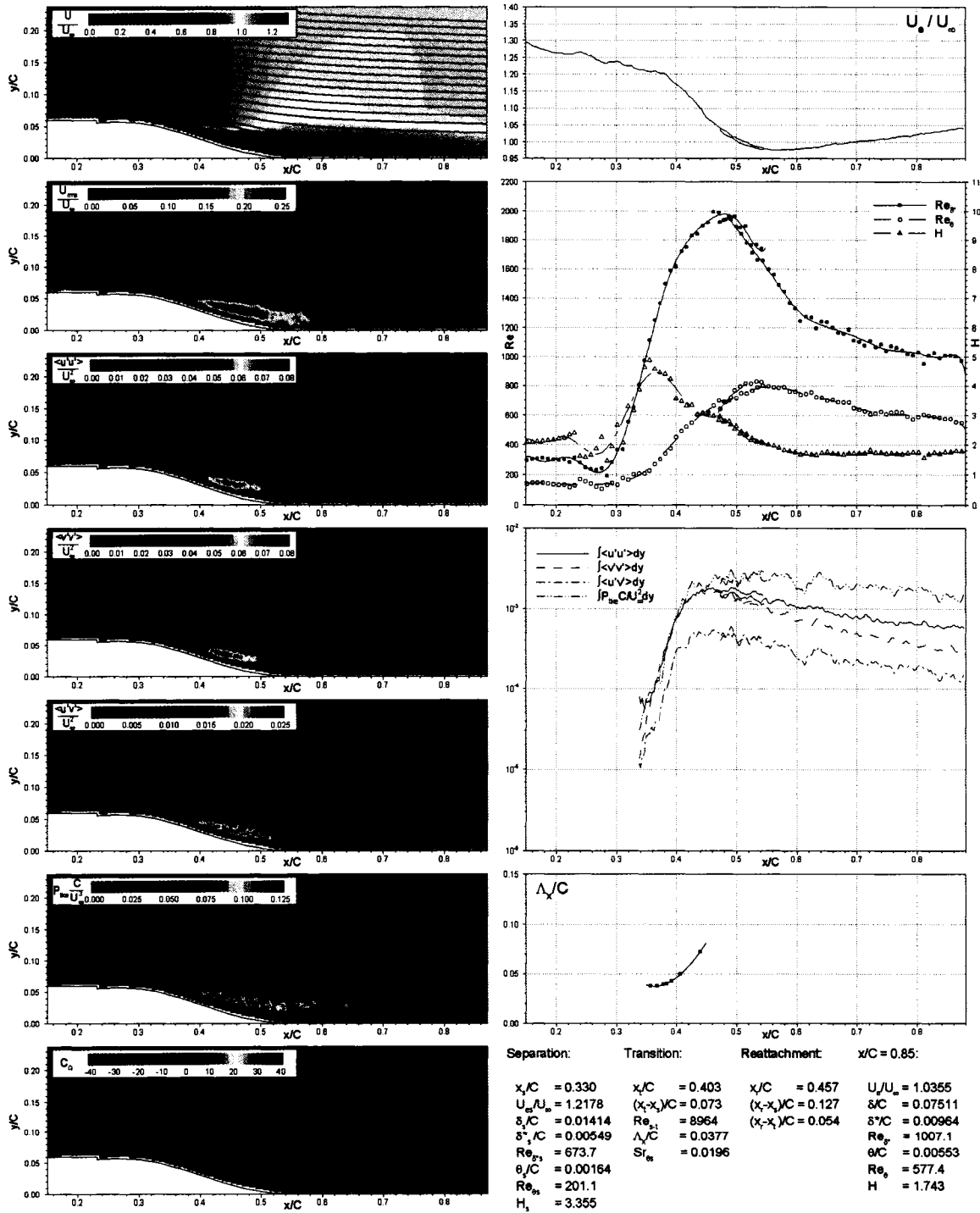


Figure D.24: Detailed results for SR configuration at $Re=101,000$